Wake Dynamics in the Atmospheric Boundary Layer Over Complex Terrain

A THESIS
SUBMITTED TO THE FACULTY OF THE GRADUATE SCHOOL
OF THE UNIVERSITY OF MINNESOTA
BY

Corey D. Markfort

IN PARTIAL FULFILLMENT OF THE REQUIREMENTS
FOR THE DEGREE OF
DOCTOR OF PHILOSOPHY

Fernando Porté-Agel and Heinz G. Stefan

August, 2013

Acknowledgements

I have immense gratitude for all those who have supported me during the years leading to the completion of this thesis. In particular, I was fortunate to be advised by Professor Fernando Porté-Agel and Professor Heinz Stefan. Their infectious curiosity and endless encouragement led me to seek out interesting questions. They taught me not only about how to conduct good research, but also how to strive for excellence. I also thank Efi Foufoula-Georgiou and Tim Griffis for serving on my committee. This thesis would not be possible without their support.

Thanks to the researchers and staff at the St. Anthony Falls Laboratory (SAFL) and at École Polytechnique Fédérale de Lausanne (EPFL) in Switzerland. First and foremost, I am grateful to Wei Zhang, who joined our lab at a critical time and with whom I shared a very productive time in the SAFL wind tunnel. I am thankful for the friendships and efforts of Rob Stoll, Matt Carper, Leo Chamorro, and Jim Tucker, who contributed to building up the capabilities of the wind tunnel making it possible to conduct thermally stratified boundary layer experiments. To those who moved on to EPFL, Yu-Ting Wu and Hao Lu, as well as those who have joined since, thank you for stimulating discussions. I also would like to thank the SAFL community for all their support over these years. Starting during my pursuit of the MS in 2003, when I was first welcomed. Then, again when I returned in 2008 to begin study toward the PhD after working in consulting. Particularly, I want to thank Heinz for encouraging me to return and for teaching me that if one works to solve important problems, interesting research questions will inevitably abound. I cannot thank him enough for all the time he spent with me, encouraging me to pursue my passions. I also thank the members of our research group, Bill Herb, Craig Taylor, Ben Janke and Eric Novotny. I especially want to thank Emily Resseger for agreeing to work on the Trout Lake field campaign

for her MS project. Our collaboration has been a very rewarding experience.

I had the privilege to be supported by and to work with a great group of researchers in the NSF IGERT – *Non-equilibrium dynamics across space and time*. I am grateful to Efi Foufoula-Georgiou for graciously agreeing to mentor our group. She was extremely generous, leading many interesting discussions from which I learned many details of stochastic processes, spatial statistical methods and multiscale dynamics. Out of the IGERT experience emerged a very rewarding collaboration between myself, Casey Godwin (Ecology, Evolution and Behavior) and Patrick McNamara (Civil Engineering) that culminated with the BOREAS fen study. I greatly appreciate all of their hard work and their resolve to pursue the research to a satisfying conclusion.

I would like to acknowledge financial support from the NSF IGERT (Grant DGE-0504195) and the NASA Earth and Space Science Fellowship (Grant NNX10AN52H). Additional support was provided by the Swiss National Foundation (grant 200021-132122), the National Science Foundation (grant ATM- 0854766), and NASA (grant NNG06GE256). Support for field research conducted at Trout Lake was provided by the USGS as part of the Minnesota DNR Sentinel Lakes project. Computing resources were provided by the Minnesota Supercomputing Institute (MSI). Special thanks for the support provided by the Anderson Family in the form of the Anderson Award and to Frank and Julie Tsai for the travel award.

Thank you to my friends and family who have provided support throughout my academic career. Their love and encouragement gave me strength in the challenging times and reason to celebrate in the good times. Special thanks to my parents, brother and sister (who is mother to my wonderful niece and nephew). To each I wish all success in following their dreams. To my grandmother whose love and support gives me strength. To my mother-in-law and family, and in particular the Walters' family for supporting the pursuit of knowledge.

Finally, I could never have completed this thesis without the support and prayers of my wife and best friend, Crystal. She has been the strongest motivation in this endeavor. Thank you for her love, moral support and patience. Without my family, none of this would be possible.

Dedication

This thesis is dedicated to my family, teachers and friends.

"*God could cause us considerable embarrassment by revealing all the secrets of nature to us: we should not know what to do for shear apathy and boredom.*"

- Goethe

...to Crystal for joining me on this journey

Ad majorem Dei gloriam

Abstract

Wake Dynamics in the Atmospheric Boundary Layer Over Complex Terrain

Corey D. Markfort

The goal of this research is to advance our understanding of atmospheric boundary layer processes over heterogeneous landscapes and complex terrain. The atmospheric boundary layer (ABL) is a relatively thin (~ 1 km) turbulent layer of air near the earth's surface, in which most human activities and engineered systems are concentrated. Its dynamics are crucially important for biosphere-atmosphere couplings and for global atmospheric dynamics, with significant implications on our ability to predict and mitigate adverse impacts of land use and climate change. In models of the ABL, land surface heterogeneity is typically represented, in the context of Monin-Obukhov similarity theory, as changes in aerodynamic roughness length and surface heat and moisture fluxes. However, many real landscapes are more complex, often leading to massive boundary layer separation and wake turbulence, for which standard models fail. Trees, building clusters, and steep topography produce extensive wake regions currently not accounted for in models of the ABL. Wind turbines and wind farms also generate wakes that combine in complex ways to modify the ABL. Wind farms are covering an increasingly significant area of the globe and the effects of large wind farms must be included in regional and global scale models. Research presented in this thesis demonstrates that wakes caused by landscape heterogeneity must be included in flux parameterizations for momentum, heat, and mass (water vapor and trace gases, e.g. CO_2 and CH_4) in ABL simulation and prediction models in order to accurately represent land-atmosphere interactions. Accurate representation of these processes is crucial for the predictions of weather, air quality, lake processes, and ecosystems response to climate change.

Objectives of the research reported in this thesis are: 1) to investigate turbulent boundary layer adjustment, turbulent transport and scalar flux in wind farms of varying configurations and develop an improved modeling framework for wind farm - atmosphere interaction, 2) to determine how heterogeneous patches of forest affect the structure of the ABL and its interactions with clearings and water bodies, 3) to investigate how landscape heterogeneity, including wakes, may be parameterized in regional-scale weather and climate models to improve the representation of surface fluxes, e.g. from lakes/wetlands and forest clearings. To achieve these objectives, this research employs an interdisciplinary strategy, utilizing concepts and methods from fluid mechanics, micrometeorology, ecosystem ecology and environmental sciences, and combines laboratory and field experiments. In particular, a) wind tunnel experiments of flow through and over model wind farms and model forest canopies were used to improve our fundamental understanding of how wakes affect land-atmosphere coupling, including surface fluxes, after wind farm installation and for heterogeneous landscapes of canopies and clearings or lakes, and b) extensive field studies over lakes and wetlands were undertaken to study the effects of wakes downwind of forest canopies and the effect of wind sheltering on lake stratification dynamics and gas fluxes. These experiments were also used to improve and validate numerical simulation techniques for the atmospheric boundary layer, specifically the large eddy simulation technique, which is used to simulate flow in wind farms and flow over heterogeneous terrain.

Keywords: Atmospheric boundary layer · Air - water exchange processes · Biosphere–atmosphere exchange processes · Canopy flows · Carbon cycling · Ecosystems structure and dynamics · Land–atmosphere interaction · Turbulence · Wind energy

Advisors:
Professor Fernando Porté-Agel and Professor Heinz G. Stefan

Contents

List of Tables

List of Figures

Chapter 1

Introduction

This thesis concerns the interaction between the earth's surface and the atmosphere in non-ideal conditions. Knowledge of the turbulent fluxes of momentum, sensible and latent heat fluxes and mass is critical in weather, climate, hydrologic and ecosystem models. The goal of this research is to advance our understanding of transport processes within the atmospheric boundary layer (ABL) and improve measurements and modeling of ABL processes including surface fluxes. The ABL is the lowest layer of the atmosphere directly in contact with Earth's surface. The ABL has a depth that varies from tens of meters to a few kilometers depending on surface heating/cooling, and it directly influences human life through weather and air quality. ABL turbulence mediates transport and is important for ecological and hydrological processes at the biosphere–atmosphere interface, including the exchange of water vapor and trace gases (e.g. CO_2 and CH_4). ABL turbulence is characterized by a wide range of space-time scales, from one millimeter to kilometers, and from less than a second to hours. Turbulence is generated by surface shear stress and is either enhanced or suppressed by thermal stratification due to solar heating or cooling of the earth's surface, respectively. Existing models of the ABL, e.g. Monin–Obukhov similarity theory [1], are generally appropriate for homogeneous and stationary flow, which require vast expanses of flat and homogeneous land covers to be applicable. However most landscapes are more complex. The current state of the art for land–atmosphere models is to parameterize complex land surfaces as differences in aerodynamic roughness length as well as

heat and moisture fluxes. Empirical adjustments to the standard models are then employed to account for interactions between different landscapes (Avissar and Pielke [2]). However, real landscapes with trees, building clusters, steep topography, and lakes are more complex, often leading to boundary layer separation and, consequently, producing large–scale coherent eddies and wake turbulence. Wind farms, consisting of clusters of wind turbines, are a special land cover, which is becoming more widespread. These large engineered structures are the largest rotating turbomachines, extending over 100 m above the ground, and strongly affecting the ABL flow by extracting wind energy and generating wakes that extend hundreds of meters downwind from the machines.

Significant regions of the ABL are affected by wakes causing the standard similarity theory formulations for mean momentum and heat fluxes to fail and strongly affecting surface fluxes. This is because wakes near the land surface cause a variable vertical distribution of kinematic fluxes, causing the constant stress assumption, for which similarity theory is based, to be invalid. The goal of this research is to develop improved models of the ABL that can account for complex terrain, where the flow separates due to abrupt changes in land cover and topography. Wakes caused by wind turbines in large wind farms and the transition between, for example, canopies of tall trees and clearings covered by shorter vegetation or open water have, to date, not been systematically studied. The resulting downwind wake turbulence persists for long distances, affecting surface fluxes and turbulent transport. This research, for the first time, quantifies the turbulent dynamics and resulting surface fluxes for common landscape configurations that are affected by wake flows.

Wind energy is becoming a significant source of electricity world-wide and wind farms are becoming increasingly widespread features on the landscape that generate significant wakes that may change the local climate (see Fig. 1.1). As seen in the images, taken from a service helicopter under ideal meteorological conditions, low pressure and enhanced vertical mixing behind turbines can generate fog, which highlights the turbine wake structure. The details of the meteorologic conditions leading to the phenomena in this image were analyzed by Hasager et al. [3]. Wind turbine wakes grow with downwind distance until the wakes from rows of turbines thoroughly mix laterally and the flow within the wind farm can be considered fully developed. The momentum is significantly depleted in the flow compared to the freestream wind, leading to reduced

Figure 1.1: Images of the Horns Rev 1 offshore wind farm in the North Sea, off the coast of Denmark, taken on 12 February 2008 at approximately at 10:10 UTC. Top: view from the southeast, Bottom: subsequent view from the south (photo by Christian Steiness, courtesy of Vattenfall)

power production by waked turbines. Additionally, the increased turbulence buffet the downwind turbines leading to enhanced fatigue loads and more frequent maintenance and potentially reduced service life. Currently, models of wind farm performance do not accurately predict energy production due to the challenges of modeling the complex nonlinear turbine-wake interactions. The environmental impacts, including effects on evaporation and fluxes of other scalars, is also unknown. It is crucial to determine how wind turbine configurations affect wake-turbine interaction in wind farms, and including the effect of the underlying landscape, to improve wind farm designs and power prediction (e.g. Calaf et al. [4], Porté-Agel et al. [5]). Experiments were conducted to investigate these interactions and develop a new model for large-scale wind farms based on observed similarities between the fluid dynamics of wind farms and forest canopies.

A notorious example of complex terrain, which has revealed significant challenges for accurate climate prediction, is the deforestation of the Amazon rainforest near Rondônia, Brazil, known for the "fishbone" pattern of forests and clearings (Fig. 1.2). Current climate models for the region result in vastly different and therefore unreliable forecasts of evaporation and precipitation due to varying amounts of patterned deforestation (Baidya Roy [6]). The subgrid-scale heterogeneity of the forest patches has been found to significantly alter the atmospheric dynamics. Coarse scale climate models represent deforestation in a bulk sense, leading to reduced evapotransporation and decreased convective precipitation. However, higher resolution models, which resolve the dominant scales of land cover variability, revealed the existence of enhanced convective storm development, due to complex nonlinear interactions between forests and pastures. This phenomenon is termed the "vegetation breeze" effect and is similar to a coastal sea-breeze. Ultimately, continued deforestation will lead to reduced rainfall and potentially the degradation of the rainforest remnant. Identification of a critical scale of deforestation, in terms of canopy patch size and organization, is needed. The results will have significant management implications for forested ecosystems not only in Amazonia. To address this problem new experiments were conducted to investigate the effects of abrupt transitions between forest canopies and clearings. It was discovered that wake turbulence downwind of canopy edges strongly affect surface fluxes and lead to new challenges for modeling and measurements. The turbulence in the wake has similarities to that of a classic backward-facing step. However, the separation does

not occur at the top of the canopy as with a solid step, the reattachment of the mean flow generally occurs closer to the canopy edge and shear recovery occurs much farther downwind of the canopy. Unlike a step change in aerodynamic roughness, wake turbulence causes the development of a new surface layer to be delayed, and a new constant flux layer may not form for potentially more than a kilometer downwind.

Figure 1.2: Remotely sensed images of the patterned deforestation in Rondnia, Brazil in the Amazon rainforest. This MODIS series shows the deforestation that took place on the frontier in the northwestern part of the state between 2000 and 2010. (Images taken with the Moderate Resolution Imaging Spectroradiometer (MODIS) on NASA's Terra satellite, Credit: NASA/MODIS.)

Forest canopy fragmentation also exists naturally in landscapes with lakes and wetlands (e.g. in the boreal forest of Canada, Scandinavia, and Russia, as well as nearby in the temperate forests of Minnesota and Wisconsin). The ABL transition from a forest to a lake or wetland is particularly complex due to coupling between the wind and surface waves. Wind sheltering, due to trees and complex topography affects heat, moisture and gas flux (e.g. CO_2 and CH_4) to the atmosphere, which impact climate processes. Sheltering also affects lake processes, including the depth of the warm surface mixed layer and the transfer of oxygen into the water column, which are critical for sustaining a healthy aquatic ecosystem. The salient feature of wind sheltering is a region of reduced wind speed and surface shear stress as well as increased turbulence. Wind sheltering

Figure 1.3: Aerial image of light reflection by surface waves of a small lake. Wind is blowing from the land onto the lake, from the right to the left. The image is the result of the wind sheltering effect of trees on the wave-field on the surface of the lake. A wind-sheltered zone is clearly visible (Image copy-right GeoEye, obtained through Google Earth (www.google.com.)

leads to reduced mechanical mixing of the surface layers in the water column and affects the transport of heat, water vapor and gases such as CO_2 and O_2 across the air-water interface in complex ways, depending on whether the constituent transport is air-side or water-side controlled. (see Fig. 1.3). Wake flows behind canopies and topography can have an impact for distances on the order of 1 km downwind from the shoreline. This makes it difficult to accurately simulate or measure fluxes across the air-water interface of lakes due to uncertainty, arising from a lack of models that can account for wind sheltering. Additionally, the measurement of representative meteorological data over small wind-sheltered lakes is fraught with difficulty because standard flux-gradient and eddy-covariance theories do not account for wake effects. This results in inaccurate flux

measurements, or estimates that are not representative of the entire lake.

Wakes caused by complex terrain including canopies, topography and wind farms must be parameterized to account for their effect on momentum, heat, and mass (including water vapor and trace gases) fluxes in ABL simulation and prediction models for climate, weather, lake ecosystems, and wind energy. Beyond understanding the localized details of wake flows on transport in the ABL, it is useful to develop parameterizations which provide corrections to the standard 1-D models currently in operational use. An example of a simple model useful for the prediction of energy flux to a small lake is presented in Chapter 6. The new wind sheltering model is a physics-based model that can be easily employed to correct the standard surface layer model. Similar parameterizations may be developed for evaporation and gas fluxes.

1.1 Specific Research Questions

This thesis focuses on the following research questions:

- What are the effects of wind turbine wakes on the structure of the atmospheric boundary layer and surface fluxes?
- Do wind farms lead to fluid dynamics similar to rough wall-bounded flow or obstructed shear flow (i.e. canopy flow)?
- Can a canopy-type model be formulated that can accurately represent the mean flow and account for the partitioning of momentum flux between the wind turbines and the ground or sea?
- How does wake turbulence due to an abrupt transition from a forest canopy to a clearing or lake affect measurements and models of land-atmosphere interactions, including turbulent flow physics and surface fluxes?
- Can a simple model be developed to correct standard 1-D ABL models to determine wind shear stress on small lakes due to forest and topographic sheltering?
- How does canopy sheltering affect lake stratification and air-water exchange of momentum, water vapor and trace gases?

- Can wind sheltering explain the observed diurnal pulse of methane from a wetland?

1.2 Outline of the Thesis

The thesis presents research that utilizes a synergistic approach, including field and laboratory experiments as well as theoretical methods in a research strategy that is optimized, based on the strengths and weaknesses of each method. Field studies have the advantage of including all of the "real world" complexity, where the natural physical processes that affect the system can be observed. Wind tunnel experiments take advantage of similarity phenomena in fluid mechanics, which allows for the isolation of key controlling factors and highly detailed observations. In addition, numerical techniques are useful for providing full three dimensional data for the flow of interest and can be used to help identify target locations where measurements will most likely detect the phenomena of interest. In this approach field-scale observations are used to identify key phenomena of interest. Then highly controlled wind tunnel experiments are conducted to develop functional relationships that may be used to create new or improve existing models. The new models are then validated against new field data and high resolution flow models, e.g. large-eddy simulation. The integration of multiple techniques represents a holistic approach to solving environmental problems.

This thesis is divided into two parts. Part I focuses on the interactions between wind farms and the atmospheric boundary layer. Part II explores the effects of abrupt transitions from forest canopies to clearings of low vegetation or water bodies. The following lists the specific topics covered in this thesis. Each chapter is written in manuscript format and constitutes a standalone publication that has appeared or has been accepted for publication in the peer-reviewed literature.

- Chapter 2 Turbulent flow and scalar transport through and over aligned and staggered wind farms [7].
- Chapter 3 Experimental study of the impact of large-scale wind farms on land-atmosphere exchanges [8].
- Chapter 4 A canopy-type model for wind farm-atmosphere interaction [9].

- Chapter 5 Canopy wake dynamics and sheltering effects on surface fluxes [10].
- Chapter 6 Wind sheltering of a lake by a tree canopy or bluff topography [11].
- Chapter 7 Wind sheltering effects on methane flux from wetlands [12].

This thesis is the product of collaborations between researchers from the fields of engineering, ecology, and earth sciences. For Chapters 2, 4, 5, and 6, I was the primary author, while for Chapters 3 and 7, I provided significant contributions, but was not the first author. The research presented in Chapter 3 extended the findings of Chapter 2, improving our understanding of how wind farms affect surface scalar flux. The research presented in Chapter 7 was completed as part of an NSF IGERT interdisciplinary research project. It presents new analyses and results from the NASA BOREAS experiment at a boreal wetland in northern Manitoba, Canada. I developed the hypothesis that the observed evening pulses of methane, released to the atmosphere, were not an error in the measurement method, but were due to thermal destratification in the hollow pools of the wetland during evening transition. My analysis of the data supported the hypothesis. The coauthors established that the release of methane could not have been caused by other biogeochemical or ecological processes.

Part I

Wind Farm-Atmosphere Interaction

Chapter 2

Turbulent Flow and Scalar Transport in Wind Farms[†]

[†] **This chapter was published as Markfort CD, W Zhang and F Porté-Agel. 2012. Turbulent flow and scalar transport through and over aligned and staggered wind farms. *Journal of Turbulence*. 13(1) N33:1-36. doi: 10.1080/14685248.2012.709635**

2.1 Abstract

Wind farm-atmosphere interaction is complicated by the effect of turbine array configuration on momentum, scalar and kinetic energy fluxes. Wind turbine arrays are often arranged in rectilinear grids and, depending on the prevailing wind direction, may be perfectly aligned or perfectly staggered. The two extreme configurations are end members with a spectrum of infinite possible layouts. A wind farm of finite length may be modeled as an added roughness or as a canopy in large-scale weather and climate models. However, it is not clear which analogy is physically more appropriate. Also surface scalar flux, including heat, moisture and trace gas (e.g. CO_2), are affected by wind farms, and need to be properly parameterized in large-scale models. Experiments involving model wind farms, in aligned and staggered configurations, were conducted in a thermally controlled boundary-layer wind tunnel. Measurements of the turbulent flow were made using a custom x-wire/cold-wire probe. Particular focus was placed on studying the effect of wind farm layout on flow adjustment, momentum and scalar fluxes, and turbulent kinetic energy distribution. The flow statistics exhibit similar turbulent transport properties to those of canopy flows, but retain some characteristic surface layer properties in a limited region above the wind farms as well. The initial wake growth over columns of turbines is faster in the aligned wind farm. However, the overall wake adjusts within and grows more rapidly over the staggered farm. The flow equilibrates faster and the overall momentum absorption is higher for the staggered compared to the aligned farm, which is consistent with canopy scaling and leads to a larger effective roughness. Surface heat flux is found to be altered by the wind farms compared to the boundary-layer flow without turbines, with lower flux measured for the staggered wind farm.

Keywords
Atmospheric boundary-layer (ABL); Canopy turbulence; Roughness transition; Scalar transport; Wake-turbine interaction; Wind farm layout; Wind-tunnel experiment

2.2 Introduction

With increased interest in developing sustainable renewable energy, wind farms are being built larger and in more locations. Whether onshore or offshore, wind farms now occupy a significant amount of the earth's surface and invariably have an impact on surface-atmosphere fluxes of momentum, moisture, and trace gases (e.g. CO_2). To account for wind farm-atmosphere interaction in large-scale weather and climate models, new or improved parameterizations need to be developed. As the interaction between the atmospheric boundary layer (ABL) and wind farms are multi-scale and fully coupled, it is also necessary to develop improved methods for designing wind farms to optimize the power output and minimize fatigue loads on the turbines for different wind-farm configurations, atmospheric stability, and complex land cover and terrain characteristics. Energy converted to power by a wind farm is derived from the available energy of the wind. This energy is primarily available as total kinetic energy in the atmospheric boundary layer, and is extracted in two primary ways, from the incoming wind at the leading edge of the wind farm and from above the farm. For very large wind farms where the distance across the farm is much larger than the characteristic flow development length scale, nearly all of the energy must be extracted from flow above the farm [13, 4, 14, 15].

A challenging problem for the design of wind farms is balancing the need for adequate spacing between turbines to extract the maximum amount of energy per turbine, while at the same time limiting the amount of land used for power production and ensuring that wakes-turbine interaction does not lead to fatigue failure [16]. The most important aerodynamic considerations in the design of wind farms is the velocity deficit within the farm and the enhancement of turbulence intensity, which primarily occurs near the top-tip height of the farm [17]. The velocity deficit within the farm is linked to the amount of power which can be extracted from the flow, while turbulence generated by strong shear and tip vortex shedding at the top of the farm can lead to structural fatigue and possibly failure of wind turbine components. Additionally, it has been found that the current models used for wind farm design tend to over-predict the power that a farm will generate [18, 19]. This is likely due to incomplete and/or incorrect turbine parameterizations of wake–turbine interactions within wind farms as well as

errors in representations of the effect of atmospheric stability [20]. Individual wind turbine efficiency and turbine spacing are parameters which engineers control in the design of wind farms. Therefore it is important to understand how wind-turbine wakes interact and combine, and how wind farm layout may affect the velocity deficit and turbulence intensity in the farm. When there are multiple turbines aligned with the wind, it has been observed that while the first row of turbines produces the maximum power, similar to standalone turbines, there is a significant decrease in power production for the second row of turbines downwind, with limited additional losses for successive turbines [21]. Vermeulen and Builtjes [22] found that turbulence intensity increases to a maximum behind the second row of turbines and then relaxes until reaching an equilibrium by the third or fourth rows.

Large wind farms can affect local meteorology and possibly even the global climate system. First attempts to predict the effect of wind farms on regional-scale weather patterns assumed wind farms increase the effective surface roughness and turbulent kinetic energy (TKE) in the logarithmic layer, resulting in a measurable response in regional weather and climate [23, 24, 25]. The surface-layer approximation for modeling wind-farms was introduced by Frandsen [26]. Alternatively wind-farms may be modeled using a distributed drag approach, taking into account the large vertical extent of turbines and treating the wind farm as a tall canopy [27]. This can be incorporated into Reynolds Averaged Navier Stokes (RANS) simulation frameworks, or at even finer scales, high-resolution large-eddy simulations (LES), using turbine parameterizations based on blade element momentum theory (e.g. drag disc or actuator line models), are able to resolve detailed fluid dynamics in the wakes of turbines and provide important information about how multiple turbines and wakes interact in a turbulent flow, as shown by Lu and Porté-Agel [14], Porté-Agel et al. [5], and Wu and Porté-Agel [28].

Much work has been done recently by a number of researchers to understand wind farm-atmosphere interactions and in-farm fluid dynamics. Research by Frandsen et al. [13], Frandsen et al. [27], Cal et al. [29], Chamorro and Porté-Agel [17], Porté-Agel et al. [5] and others, involve theoretical model development, laboratory experiments, and field scale experiments and simulation of flow in wind farms. All have provided insights into how wind turbines affect the ABL, and how they may be parameterized in wind turbine siting models as well as large scale weather and climate models. In particular, Corten et

al. [30] presented an early wind tunnel experiment measuring the flow through a scaled-down wind farm. Studying boundary layer interaction with a wind farm consisting of 28 turbines for both onshore and offshore conditions, they found that it takes far more than five rows of turbines for the flow to reach equilibrium. Recently Chamorro and Porté-Agel [31] showed the importance of an incoming boundary layer with varying surface roughness on the wake of a single wind turbine. Zhang et al. [32] revealed the effect of the boundary layer on near wake turbulence for a similar wind turbine. Additionally, Chamorro and Porté-Agel [33] and Zhang et al. [34] showed the effects of stable and convective incoming boundary layers, respectively, on the wake recovery for a single turbine. Hancock and Pascheke [35] also investigated the effect of a moderately stable ABL on wind-turbine wake recovery. Cal et al. [29] presented wind tunnel experiments for a 3 by 3 wind turbine array and argued that large wind farms extract most of the energy from the flow above the farm. Chamorro and Porté-Agel [17] presented wind tunnel experimental results describing the flow in and around an aligned wind turbine array, and Chamorro et al. [36] studied the flow through a staggered wind turbine array, both in isothermal conditions. However, it is still not clear if current parameterizations accurately represent wind farm-atmosphere interaction, and development and testing of improved parameterizations are needed to increase confidence in our ability to accurately represent wind farms in models. It is also not well understood how wind turbine array arrangement and wake-turbine interactions affect the overall absorption of momentum, the distribution of added turbulence and turbulent transport, nor the distribution of TKE within large wind farms.

To date, results have not been reported directly comparing the flow within and over aligned and staggered wind farms, nor has there been work to examine whether flow through and over a wind farm is best represented as a rough surface layer or as a canopy flow. Also experimental measurements of passive scalar transport in wind farms have not been performed. This study presents wind tunnel experiments to examine the turbulence characteristics in and over aligned and staggered model wind farms, consisting of 12 rows of horizontal axis wind turbines, in a deep turbulent boundary layer flow. We characterize the wake development within and over the wind farms as well as the horizontally averaged vertical momentum flux and effective roughness for

the quasi-fully-developed flow in wind farms. We also characterize the overall momentum absorption, heat flux, turbulent kinetic energy budget and the scaling parameters of canopy turbulence to assess the appropriateness of the rough surface layer versus canopy model analogies for describing large wind farm flows. The paper is organized as follows: added roughness and canopy models are presented in Sec. 2.3 as an underlying framework for the analysis; the experimental facility, the measurement methods, and the experimental conditions are then described in Sec. 2.4; Sec. 2.5 compares the flow development within the two wind farm configurations, characterization of the wake expansion above the wind farms, and presents the spanwise-averaged flow statistics of the developed flow, including the mean velocity, turbulence intensity, momentum flux, turbulent kinetic energy and passive scalar transport. Sec. 2.6 discusses observed characteristics of the flow and assesses models for added roughness and canopy flows. Finally, Sec. 2.7 provides a summary of the key results and conclusion.

2.3 Wind Farm Models

2.3.1 Added roughness model

The added roughness model is commonly used to describe flow over wind farms [13, 20, 4]. A general model proposed by Lettau [37] is based on the geometry of roughness elements and a drag coefficient. Reformulating the model utilizing properties of wind farms, including the turbine thrust coefficient C_T and the streamwise and spanwise wind turbine spacing $S_x \times S_y$, in terms of multiples of the rotor diameter D, is

$$z_{0,\mathrm{L}} = C_T \frac{Z_{hub}\pi}{4S_xS_y} = c_{ft} Z_{hub}, \tag{2.1}$$

where the important vertical length scale for describing momentum extraction from the flow is assumed to be the hub height Z_{hub} and $c_{ft} = \frac{\pi C_T}{4S_xS_y}$ is the drag coefficient for the wind farm-drag per-unit surface area of ground or ocean.

Frandsen et al. [13] introduced the hypothesis that wind farms can be modeled as a combination of two log-layers intersecting at the hub height, which takes into account the roughness of the surface as well as the momentum extracted by the wind farm, resulting in an effective roughness due to the turbine array. The resulting roughness

$z_{0,\mathrm{F}}$ model follows as,

$$z_{0,\mathrm{F}} = Z_{hub} \exp\left(-\kappa \left[\frac{1}{2}c_{ft} + \left(\frac{\kappa}{\ln(Z_{hub}/z_{0,gnd})}\right)^{-2}\right]^{-1/2}\right), \tag{2.2}$$

where $z_{0,gnd}$ is the roughness of the underlying surface.

A recent refinement of the model was developed, supported by LES results for a suite of 14 hypothetical wind farms using a drag disc wind turbine parameterization, that incorporates a rotor induced wake region buffering the two log layers [4]. The resulting model takes the form,

$$z_{0,\mathrm{C}} = Z_{hub}\,(1+B)^{\beta} \exp\left(-\left[\frac{c_{ft}}{2\kappa^2} + \left(\ln\left[\frac{Z_{hub}}{z_{0,gnd}}\,(1-B)^{\beta}\right]\right)^{-2}\right]^{-1/2}\right). \tag{2.3}$$

The additional parameters in this model are $B = D/2Z_{hub}$, the exponent $\beta = \nu_w^*/(1+\nu_w^*)$ and ν_w^* is a wake eddy viscosity estimated by Calaf et al. [4] as $\nu_w^* \approx 28\sqrt{c_{ft}/2}$. To estimate roughness using the above models, an accurate thrust coefficient must be determined for wind turbines within a farm. Typically a single representative value of C_T is used, based on the performance of individual turbines and invariant of wind turbine array configuration. This is problematic because C_T is expected to depend on the configuration of the turbines within the farm, due to in-farm flow organization resulting in variable degrees of wake interaction and sheltering from upwind turbines.

2.3.2 Wake growth model

For wind farms of a finite length, the flow transitions from the upwind water or land surface to the wind farm leading to the expansion of interacting wakes. Frandsen et al. [13] suggested the flow through and over wind farms can be separated into two distinct layers, the flow inside the farm and the internal boundary layer above due to the transition from a relatively smooth to a rougher surface. Wake development within the wind farm can be characterized by the velocity deficit, and the level of turbulence can be characterized as added turbulence intensity due to the wind farm.

To represent the wind farm as a roughness transition, lateral ensemble averaged velocity profiles are required to track the internal boundary layer adjustment. However,

due to the large distance between roughness elements leading to a long drag development scale, which is a measure of the distance required for the flow to adjust to the imposed drag inside the wind farm, the roughness transition model may break down as an equilibrium sublayer cannot develop above the wind farm until the flow within the farm reaches equilibrium. This means the flow within the wind farm is co-evolving with the flow above and is characterized by complex three-dimensional wake interactions (cf. Dupont and Brunet [38]). It may be more important, from the standpoint of wake-turbine interaction, to determine the rate of wake growth along columns of turbines. The flow adjustment above a wind farm can be characterized using mean and turbulence flow statistics. Wake expansion is typically modeled using one of two approaches: empirically with a power law following, e.g. Elliott [39] and Wood [40], or the more complex model based on the diffusion analogy following Panofsky and Dutton [41]. The diffusion analogy is based on the principle of limited diffusion of momentum. The model proves useful for modeling complex wake expansion and will be used to evaluate the wake growth rate over the wind farm. The wake growth rate is controlled by the relative level of shear stress or vertical turbulence intensity within the wake. A proportional relationship between wake growth and shear or vertical turbulence intensity follows as

$$\frac{d\delta_{wake}}{dx} \propto \frac{\sigma_w}{U(\delta_{wake})} \propto \frac{u_*}{U(\delta_{wake})}. \tag{2.4}$$

2.3.3 Canopy model

An alternative to the added roughness model is the canopy-type model, which resolves the effect of the vertical extent of the wind farm. Wind farms are fundamentally made up of distributed momentum-absorbing elements, that have a significant vertical extent, distorting the flow. Such complex flows can be described as canopy turbulence or as obstructed shear flows [42, 43, 44]. They are common in the atmospheric boundary layer as well as other engineering and environmental flows. The salient feature of a canopy flow is an inflection point in the mean velocity profile, which consequently results in dynamically different transport process from that of surface-layer type flows. The resulting inviscid instability leads to enhanced turbulence and two integral length scales to emerge, including the shear length scale L_s that describes the characteristic scale of

coherent Kelvin-Helmholtz (K-H) type eddies at the top of the canopy, and the canopy drag development length scale L_c. The shear length scale can be defined as

$$L_s = \frac{U_H}{(dU/dz)_{z=Z_H}}, \tag{2.5}$$

where U_H is the mean velocity at the top of the canopy, Z_H is the aerodynamic canopy height, defined by the height of the inflection point in the mean velocity profile. The shear length scale L_s is the characteristic depth K-H type eddies penetrate into a canopy. If present in a wind farm, K-H eddies may represent a significant potential source of turbulent loading on the wind turbines. The drag development length scale is defined as

$$L_c = (C_d a)^{-1}, \tag{2.6}$$

where C_d is the drag coefficient, and a is the canopy area density or projected frontal area per unit volume, which is proportional to the distance required for the momentum within the wind farm to come into balance with the drag force. Coceal and Belcher [45] estimated that the flow within a canopy is fully developed when the drag force is balanced by the vertical momentum flux at approximately $3L_c$. However, the flow development length has been shown to depend on the configuration and drag characteristics of obstacles in the flow, as well as the turbulence statistics being considered. Higher order flow statistics may require a longer distance to adjust. Cheng and Castro [46] and Coceal et al. [47] presented results from wind tunnel experiments and large-eddy simulations, respectively, for flow in and above a model urban canopy. They found the flow in a staggered array of cubes adjusted more rapidly than in the aligned array due to the effect of wake sheltering. It is expected that similar results may be found for wind farms. The drag coefficient is difficult to know *a priori* for a complex array of roughness elements like turbines in a wind farm. Coceal et al. [47] showed that the drag characteristics of the aligned and staggered cube arrangements were quite different because of distinct differences in the three-dimensional structure of the flow.

Frandsen et al. [27] presented a framework for modeling wind-farm flow in terms of a canopy-type flow following theoretical work on urban canopies by Belcher et al. [48], and found good results comparing with field data from an offshore wind farm. The

linearized model and scaling relies on a relatively sparse canopy to ensure that nonlinear terms may be considered negligible. As identified by Frandsen et al. [27], the linearized canopy model is particularly useful as an intermediate model for accurately representing the mean velocity deficit within the relatively sparse wind farm array (intermediate in the sense that it is between the complexity of the added roughness model and more detailed explicitly resolved turbine modeling employed in CFD models). The canopy model has not been rigorously tested for sparse canopies or for wind farms. This is particularly true with regard to second order moments and turbulent transport. The flow over a wind farm may behave similar to a canopy flow, however in general canopies are denser than the typical wind farm. Wind farms may be considered sparse canopies, however research on sparse canopies to date is limited, and it is unresolved whether length scales (e.g. L_s) for dense canopies apply to sparse canopies and by extension to wind farms.

The momentum equation for a fully developed canopy flow residing within the surface layer of the atmospheric boundary layer, with zero longitudinal pressure gradient, and horizontal averaging simplifies to the form

$$-\frac{d}{dz}\left(\left\langle \overline{u'w'} \right\rangle_{xy} + \left\langle \bar{u}''\bar{w}'' \right\rangle_{xy} \right) = \left\langle \bar{f}_x \right\rangle_{xy} . \tag{2.7}$$

The meteorological convention is used where x_i is the direction in Cartesian coordinates with $i = (1, 2, 3)$ or (x, y, z), the z-coordinate oriented vertically, and with the corresponding velocity u_i. The overbar signifies time averaging, $\langle \cdot \rangle_{xy}$ represents spatial averaging in the streamwise and spanwise directions, as identified by the subscripts, and f_x is the turbine induced force. The total wall-normal shear stress is defined as

$$\tau_{xz} = \left\langle \overline{u'w'} \right\rangle + \left\langle \bar{u}''\bar{w}'' \right\rangle , \tag{2.8}$$

where we assume viscous effects are negligible and $\langle \bar{u}''\bar{w}'' \rangle$ is the dispersive flux of momentum. The dispersive flux or stress is the horizontally unresolved subgrid-scale quantity that arises from horizontal spatial filtering of the momentum equation and represents the contribution to momentum transfer from correlations between spatial variations in the time-averaged flow where $\bar{u}_i'' = \bar{u}_i - \langle \bar{u}_i \rangle$ [49]. The turbine induced

drag force is

$$F = \frac{1}{2}\rho C_T A_r U \left|U\right|, \tag{2.9}$$

where ρ is the density of the air, A_r is the rotor swept area and U is the mean streamwise velocity. The force, per unit mass, distributed over the unit volume occupied by turbines in a wind farm is

$$\langle \overline{f}_x \rangle_{xy} = \frac{F}{Z_H A_f}, \tag{2.10}$$

where Z_H is the representative height of the wind farm and $A_f = S_x S_y D^2$ is the unit ground area per turbine. The distributed force is the volume average force in Eqn. 2.7, which can be modeled as the square of the mean velocity divided by the canopy drag length scale,

$$\langle \overline{f}_x \rangle_{xy} = \frac{U\left|U\right|}{L_c}, \tag{2.11}$$

where L_c can be re-written in terms of wind farm parameters as

$$L_c = \frac{2Z_H A_f}{C_T A_r} = \frac{8Z_H S_x S_y}{\pi C_T} = \frac{2Z_H}{c_{ft}}. \tag{2.12}$$

An accurate C_T is required to make predictions of the distance for the flow to develop inside a wind farm. Additionally the shear penetration length scale has been found for many obstructed shear layer flows to be $L_s \approx 1/3 L_c$ [43]. The dispersive flux is generally not important in canopy flows as it has typically been found to be about 1% of the shear stress [50, 51]. However it is likely significant for sparse, heterogeneous canopies or wind farms and is known to be important near the leading edge $x \lesssim O(L_c)$ of a canopy where advective flux is significant [52].

2.4 Experimental Setup

2.4.1 Atmospheric boundary layer wind tunnel

Experiments were conducted at the St. Anthony Falls Laboratory (SAFL) thermally stratified boundary layer wind tunnel at the University of Minnesota. The low speed

tunnel has a plan length of 37.5 m and was operated in closed loop return mode. The main test section is approximately 16 m long, has a cross section of 1.7m $\times$ 1.7m, and a 6.6:1 area contraction ratio. A 200 HP fan drives the flow and turning vanes along with screens and honeycomb flow straighteners help train the flow. The resulting free-stream turbulence intensity is less than 1% at 3.2 m s^{-1}. The flow was tripped by a 4 x 8 cm picket fence, which initiates the growth of a deep turbulent boundary layer, and an adjustable roof allows for zero pressure gradient conditions. The surface layer exhibits good statistical properties with logarithmic mean and linear stress profiles.

The air temperature was controlled with an automated water heater/chiller and heat exchanger at the expansion region downwind of the fan. Aluminum panels on the floor are thermally controlled to maintain the floor temperature independent of the air, within $\pm 0.25^{\circ}$C, using automated valve controllers. Nominally a 60°C differential can be maintained, which allows for well controlled simulation of neutral, stable and convective boundary layers. Secondary false walls were installed along the inner sides of the test section to reduce heat transfer with the outside and prevent secondary circulations from forming. A similar approach was employed by Ohya and Uchida [53] to study stratified boundary layer dynamics in the wind tunnel at Kyushu University, Japan. More details about the SAFL wind tunnel configuration and operation can be found in Carper and Porté-Agel [54] and Chamorro and Porté-Agel [55].

2.4.2 Model wind farm

The model wind turbine arrays consisted of 36 (aligned) and 30 (staggered) miniature wind turbine models (see Fig. 2.1) with three-blade, GWS EP-5030$\times$3, rotors attached to adjustable load resistance SGST DC micro generators (model SRF-1220CA-15085) which were immersed in a turbulent boundary layer. The nacelle around the generator has a 12 mm diameter and extends 3 cm behind the rotor hub. The maximum rated power output from the generator was 0.6 W. The rotor diameter $D = 12.8$ cm with the bottom tip of the turbine at a height of 3.8 cm ($0.3D$) and the top-tip at $z = 16.8$ cm ($1.3D$). The hub height was 10.4 cm, resulting in the turbine rotor swept area within the lowest 1/3 of the turbulent boundary layer, ensuring geometric similarity with prototype scale wind farms. Specific details about the blade geometry are provided in Table 2.1, including chord length (c), max thickness (t_{max}) and twist angle (α_r) at

various positions along the radius (r/R), where R is the rotor radius (6.4 cm). At a free-stream velocity of 3.2 m s^{-1}, the turbine operated at 1710-1760 rpm. The resulting tip speed ratio ($\lambda = \Omega(2\pi/60)(D/2)/U_{hub}$) is approximately 4.2. The tip speed ratio generally falls within the values of previous experiments involving 3-blade wind turbine models (between 3 and 6.7) reported by Vermeer et al. [56]. Typical field scale wind turbines operate at an optimal λ between 6 and 8. Experiments using similar turbines include, Chamorro and Porté-Agel [31, 17], and Zhang et al. [32, 34].

Table 2.1: Rotor blade characteristics as a function of distance from the hub.

	Chord length	Max Thickness	Twist angle
r/R	c/R	t_{max}/c	α_r (deg.)
0.16	0.222	0.092	14.8
0.31	0.235	0.084	18.0
0.47	0.235	0.075	19.6
0.63	0.219	0.067	17.6
0.79	0.183	0.060	12.4
0.94	0.135	0.051	8.7
0.99	0.105	0.048	8.2

Note: Twist angle is relative to the rotor plane.

Two wind farm layouts, with perfectly aligned and staggered configurations, were investigated. The aligned layout consists of a rectilinear grid of turbines with 13 rows and 3 columns. The rows have a streamwise spacing of $S_x = 5D$ and the columns are separated in the spanwise direction by $S_y = 4D$ resulting in a unit turbine area density of $S_x S_y = 20D^2$. The staggered array has the same spacing, however the even numbered rows have only two turbines and are laterally staggered by $2D$ with respect to the aligned configuration (see Fig. 2.2). A similar 2-3 column arrangement was investigated in [36]. The equal turbine density allows for direct comparison of the turbine layout effect on the wind farm performance, flow and turbulent transport characteristics. Solid blockage effects are estimated based on the ratio of the rotor disk area and projected area of the tower to the wind tunnel cross-sectional area. For the aligned case, three turbines span the tunnel resulting in a blockage of 1.3%. For the staggered case, a total of five turbines span the tunnel resulting in a blockage of 2.1%. Many investigators have assessed the

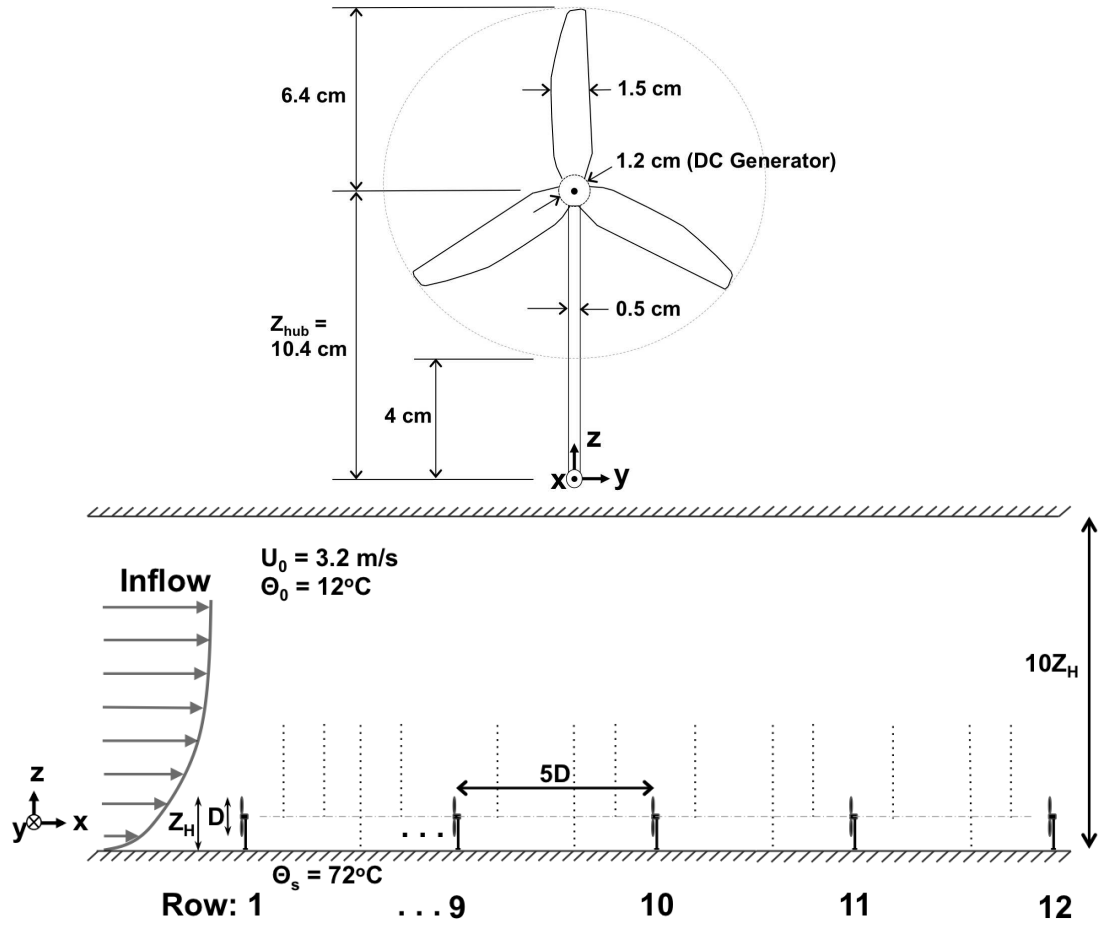

Figure 2.1: Schematic diagram of the wind turbine model (top), and side view of the wind farm layout in the wind tunnel (bottom). Vertical dotted lines indicate where profiles were taken, and the horizontal dash-dotted line indicates the hub height level. (Note, the schematic is not drawn to scale. In particular, the vertical scale of the wind turbines are exaggerated relative to the height of the wind tunnel.)

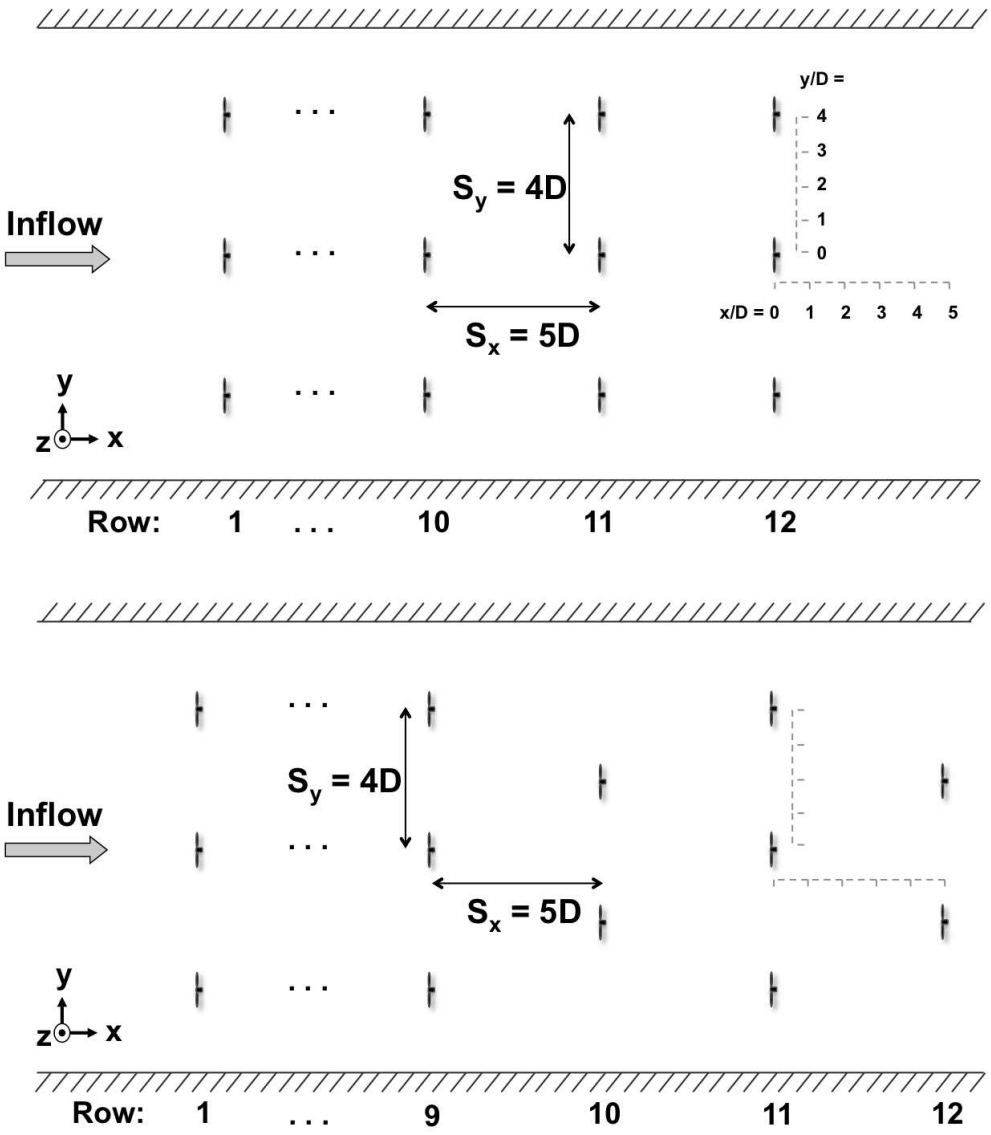

Figure 2.2: Schematic diagram of the aligned (top) and staggered (bottom) wind farm layouts. Profiles collected behind the 12th and 11th row, respectively, at selected spanwise locations were used to characterize the quasi-developed flow. Note that the even numbered rows in the staggered farm have 2 turbines, while the odd-numbered rows have 3 turbines.

effect of blockage and found that solid blockage should be less than 5 - 10% to insure unimpeded expansion of wakes [57].

2.4.3 Hot-wire anemometry

High-resolution turbulence measurements were made using a custom 3-wire (x-wire and cold wire) probe. The x-wire is a standard type, which allows for measurements of instantaneous streamwise and vertical velocities as well as evaluate the wall normal momentum fluxes. The hot-wires are 5.0 μm diameter platinum-coated tungsten wires separated by 0.7 mm and the cold wire is a 2.5 μm diameter wire, 1.7 mm in front of the x-wires. An A.A. Lab System AN-1003 10 channel CTA/CCA system was used to capture the voltage signal with an overheat ratio of 1.2 to minimize interference between the x-wire and cold-wire sensors. The collocation of a cold-wire and x-wire sensor allowed for point-by-point temperature correction of the x-wire measurements as well as wall normal heat flux to be measured. The sensor was calibrated in a custom calibration unit against a Pitot-static tube and a copper-constantan thermocouple at four temperatures, seven inclination angles and seven velocities. A look-up table calibration method, using cubic spline interpolation, was used to determine the two instantaneous velocity components from the two instantaneous voltage signatures. Calibration was performed at the beginning of the experiment and a post-experiment calibration was carried out to check the validity of the calibration throughout the experiment. During the calibration and measurements the air and floor temperatures were maintained within a range of $\pm 0.25^{\circ}$C to avoid bias errors caused by thermal drift of the voltage signal. More details on the calibration procedure can be found in [58] and [59]. The sensor was mounted on a traversing system (Velmex, Inc), controlled with a custom Labview program, so that multiple locations could be precisely measured. Measurement uncertainty for mean velocities is within 1%, while turbulence statistics are accurate to approximately $3\% - 5\%$ depending on turbulence level in the flow and distance to the wall or to the wind turbine models.

Measurements were taken at selected locations within the wind farm to characterize the flow development along the centerline y = 0 inside and over the two wind farm configurations. The profiles have a vertical spacing Δz = 1 cm, and a streamwise

spacing $\Delta x = 1D$. Profiles were also taken at various span-wise locations y/D = -1, 0, 1 and 2 within the wind turbine arrays, at $x/D = 3$ behind the 12th row of the aligned layout and the 11th row of the staggered layout (Fig. 2.2). These measurements characterize the spatially averaged flow statistics within and over the wind farms. Time series of u, w and θ were collected at each point for 90 s to 120 s at a frequency of 2000 Hz.

2.4.4 Boundary layer characterization

A thick turbulent boundary layer is generated in the wind tunnel test section. Over a homogeneous flat surface, the mean velocity in the surface layer (the lowest 10-15% of a fully developed turbulent boundary layer) follows a log-law profile modified with a stability correction, and is written as

$$U(z) = \frac{u_*}{\kappa}\left[\ln\frac{z-d}{z_0} + \Psi_m\left(\frac{z-d}{L}\right)\right], \tag{2.13}$$

where u_* is the friction velocity defined as $u_* = (-\overline{u'w'})_s^{1/2}$, the surface kinematic shear is taken as the minimum value at the surface, κ is the von Karman constant (≈ 0.4), z_0 is the roughness length, d is the zero-plane displacement and

$$\Psi_m((z-d)/L) = -2\ln\left(\frac{1+\mathrm{X}}{2}\right) - \ln\left(\frac{1+\mathrm{X}^2}{2}\right) + 2\tan^{-1}(\mathrm{X}) - \pi/2 \tag{2.14}$$

is the diabatic term. In Equation 2.14, $\mathrm{X} = (1-15((z-d)/L))^{1/4}$ is a function of the Obukhov length, $L = -(u_*^3\Theta_0)/(\kappa g Q_s)$ [60]. The Obukhov length scale corresponds to the height where buoyancy production of turbulence overcomes the shear production, Θ_0 is the reference temperature, often taken as the mean value measured in the surface layer, g is gravitational acceleration, and $Q_s = (\overline{w'\theta'})_s$ is the surface heat flux. Q_s is taken as the maximum value at the surface. Thermal stability can be quantified by the Richardson number Ri, the ratio of the buoyancy production to shear production terms of the TKE budget. It is more common to use the bulk Richardson number $\mathrm{Ri_b} = g\delta\Delta\Theta/(\Theta U_0^2)$ as the measure of atmospheric stability for complex boundary layers with surface heterogeneity and topography. It is negative for the unstable or convective boundary layer, zero for neutral conditions and positive for stable conditions.

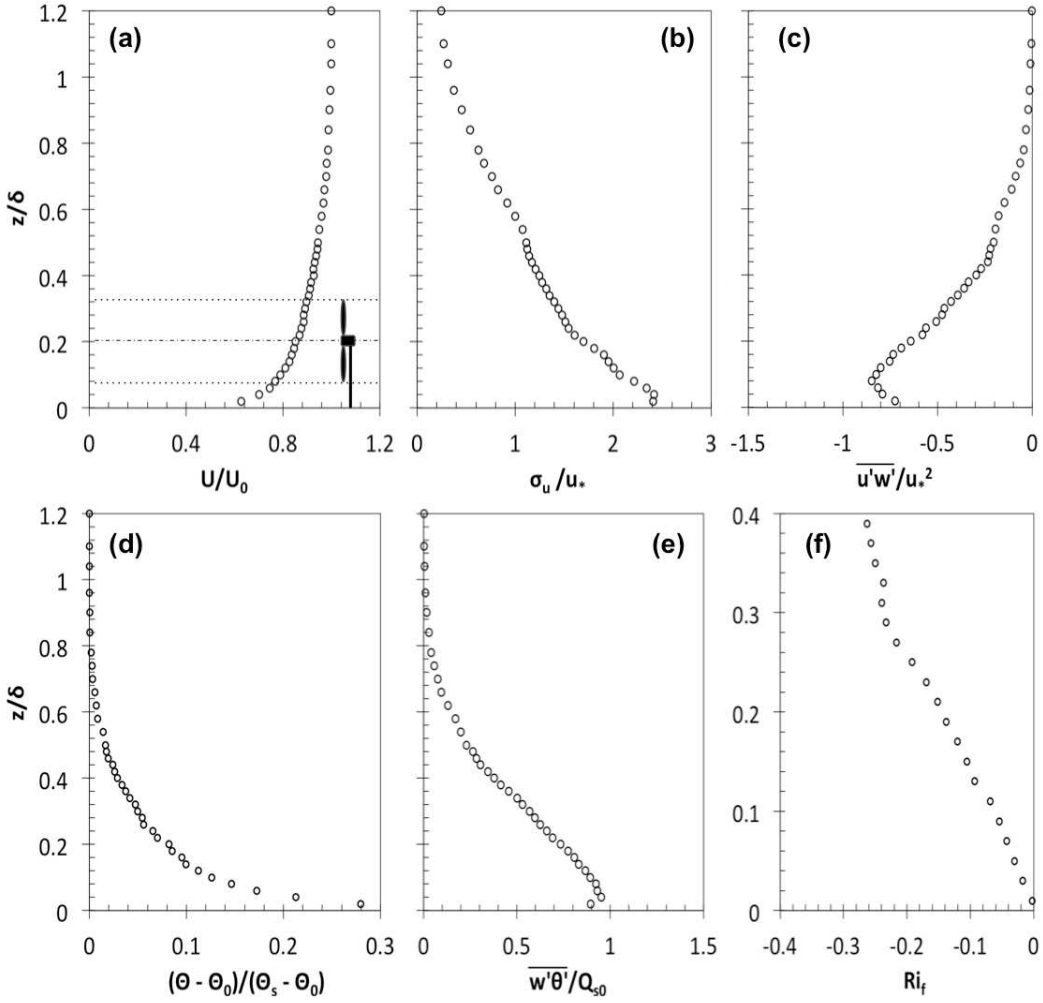

Figure 2.3: Turbulent boundary layer profiles; (a) normalized mean stream-wise velocity, (b) turbulence intensity, (c) kinematic shear stress, (d) mean temperature, (e) kinematic heat flux, and (f) flux Richardson number.

In this study, a nearly neutral boundary layer was developed over a smooth surface and grew to a depth of $\delta = 50$ cm where $U(\delta) = 0.99U_0$. The aerodynamic roughness and friction velocity were $z_0 = 0.08$ mm and $u_* = 0.12$ ms^{-1} respectively. The heat source was achieved by maintaining the floor temperature at 72 °C and a freestream temperature at 12 °C. Fig. 2.3 shows the profiles of the mean velocity, turbulence intensity and fluxes as well as the flux Richardson number profile in the surface layer. The velocity profiles with and without a heat source were measured and were found to be very similar with the same boundary layer thickness, roughness and friction velocity. The bulk Richardson number $\mathrm{Ri_b} = -0.09$ and Obukhov length $L = -0.4$ m. Therefore L is 80% of the boundary layer thickness for the flow entering the wind farm. The diabatic term in the Monin-Obukhov profile was evaluated and found to be negligible. There still may be a small buoyancy enhancement effect on the turbulent dynamics of the first couple of rows of turbines, however shear and wake generation of TKE quickly overwhelm any buoyancy effect within the wind farms, as will be shown in Sec. (2.5.4). Therefore it follows that the heat source does not have an affect on the dynamics of the flow within the wind farms, which allows for the examination of the effect of the wind farm on the flux of heat as a passive scalar quantity.

The Reynolds number, based on free-stream velocity and boundary layer thickness is approximately $\mathrm{Re}_\delta = 1 \times 10^5$, and based on turbine height is approximately $\mathrm{Re}_{Z_H} = U_0 Z_H/\nu = 3.6 \times 10^4$. Reynolds numbers in the field are typically two to three orders of magnitude larger. Despite a mismatch in dynamic scaling between model and prototypical wind farms, the detailed physics characterized in these experiments provide valuable information about the flow behavior within wind farms immersed in a turbulent boundary layer, and high-resolution spatial and temporal data that can be used to validate CFD frameworks including RANS and LES models with turbulent transport and wind turbine parameterizations. It has been shown that, although it is not possible to reproduce the Reynolds numbers of field-scale flows in a wind tunnel, using the selected wind turbine it is possible to reproduce key characteristics of the wakes, including wake rotation, and the tip/root helicoidal vortex system [61, 32].

2.5 Results

2.5.1 Angular velocity

The angular velocity of a wind turbine rotor is a surrogate for power generation. Angular velocity was evaluated as a function of row number for the aligned and staggered wind farms. It is well known that power generation decreases with successive downwind rows of turbines and the rate of decrease depends on the spacing between downwind turbines [20, 13]. Fig. 2.4 shows a comparison between the results for the aligned and staggered wind farms. It is notable that the rotation rate drops quickly for the aligned case by the second row, however the staggered case exhibits a more gradual decrease. At approximately 10 rows, the staggered case exhibits greater rotation rate than the aligned farm, while at 13 rows they are nearly equal. Therefore the overall power generated by the staggered wind farm is greater than that of the aligned farm.

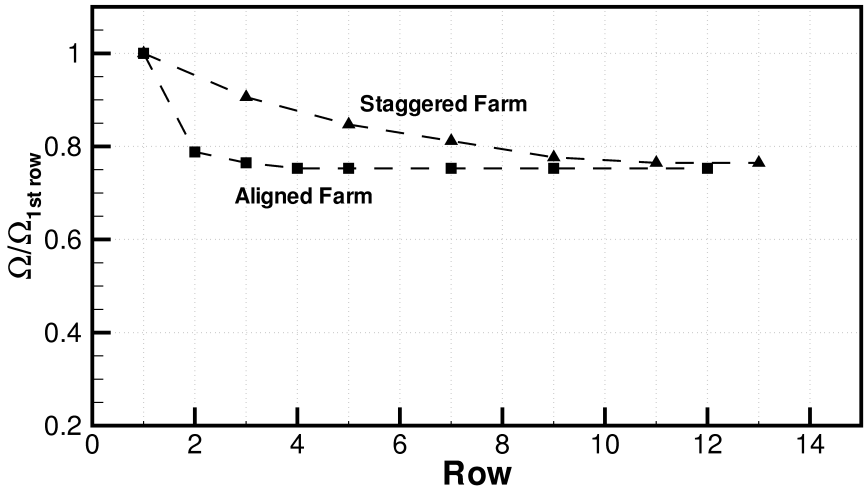

Figure 2.4: Angular velocity of each row of wind turbines in the aligned and staggered wind farm, normalized with the first row.

2.5.2 In-farm wake development

Mean velocity

Wind turbines extract kinetic energy from the incoming flow, which results in a wake of reduced velocity behind the turbines. To examine the development of the flow within the wind farms, velocity profiles were measured at selected positions ($x/D = 3$) downwind of each row of turbines along the center span ($y/D = 0$). Vertical profiles of the mean stream-wise velocity U compared with the undisturbed incoming flow are shown in Fig. 2.5. For even numbered rows, the closest direct upwind turbine in the staggered configuration is $x/D = 8$. The velocity profiles follow a similar trend, including large departures from the inflow in the two cases between the bottom-tip and top-tip heights. A key difference between the two cases is that there is a significant wake recovery behind the even number rows in the staggered farm, due to a larger distance along streamlines between turbines and funneling of the flow between the staggered turbines.

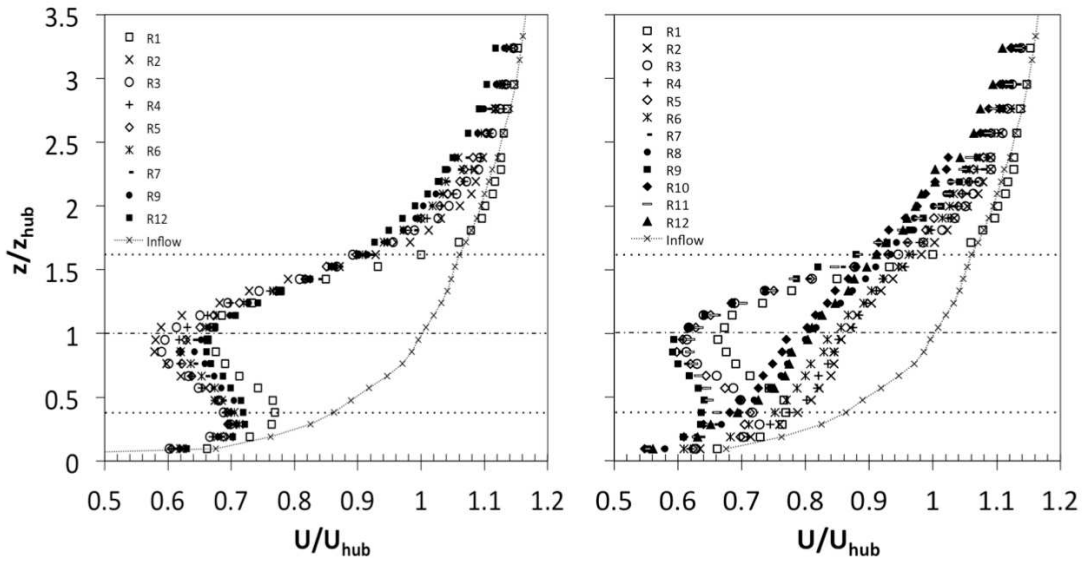

Figure 2.5: Normalized mean streamwise velocity profiles (U/U_{hub}) at center-span $y = 0$ and $x/D = 3$ behind consecutive rows: Aligned (left), Staggered (right). Horizontal dotted lines represent the top and bottom rotor tip heights. The dash-dotted line indicates the hub height level.

The velocity deficit at the center of the wake (around the hub height) is an important parameter to estimate power production and predict overall wake development characteristics. With the assumption of self-similar behavior, the wake profile can be expressed as a function of the velocity deficit at the hub height and radial distance away from the wake center (cf. Frandsen et al. [13], Chamorro and Porté-agel [31], and Zhang et al. [34]). The velocity deficit is calculated by

$$-\frac{\Delta U_x}{U_{hub}} = \frac{U_0(z) - U(x,z)}{U_{hub}}, \tag{2.15}$$

where $U_0(z)$ is the incoming mean stream-wise velocity, and U_{hub} is the incoming mean wind speed at the hub height.

Fig. 2.6 shows the velocity deficit in the wake behind each row of turbines in the wind farm. In the aligned farm case, the velocity deficit at hub height quickly increases to the maximum deficit by the second row and decreases until about the 11th row where it stabilizes. The trend in the velocity deficit within the staggered farm is nearly constant after the third row, and is greater than the aligned case. Because there is no turbine at the centerline for the second nor subsequent even numbered rows in the staggered arrangement, the flow has a greater distance to recover before the next immediately downwind turbine extracts momentum. Additionally, due to the lateral offset of turbines in the second and to a lesser extent in subsequent rows, a Venturi effect is created causing more momentum to recover in front of the second and subsequent rows of turbines. This allows the staggered farm to extract more momentum from the flow. In contrast, in the aligned farm for which the turbines are effectively closer together along streamlines, the wakes shed from upwind rows of wind turbines have less distance to recover. This is significant because it limits the amount of energy the turbines in the aligned case can extract from the flow and conversely optimizes the amount of energy that can be extracted in the staggered case for a given turbine density. The results agree with the rotor angular velocity measurements compared in Sec. 2.5.1. Based on the results we can conclude that for a given turbine density, the configuration of wind turbines controls the amount of kinetic energy the wind farm can extract from the flow.

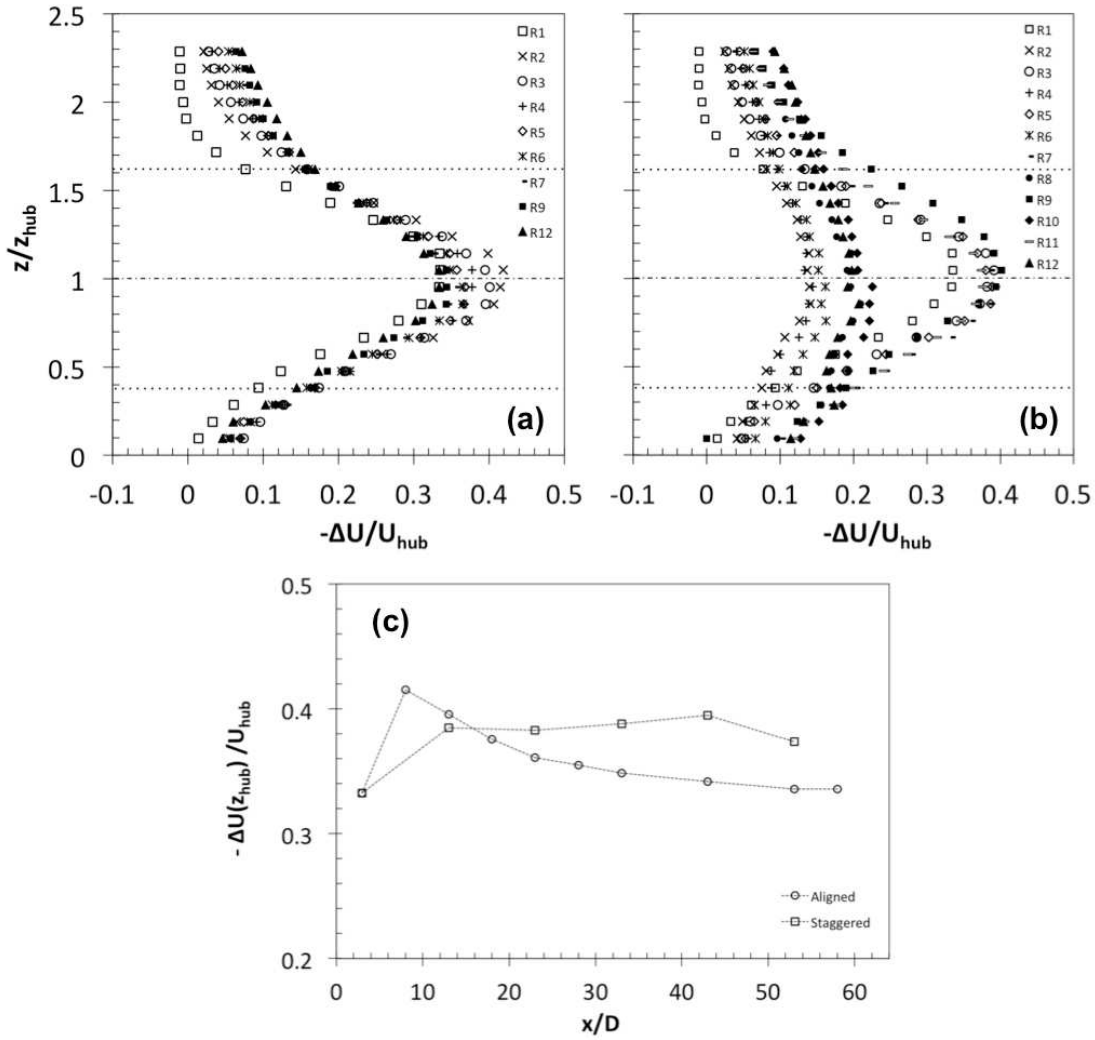

Figure 2.6: Streamwise mean velocity deficit ($-\Delta U/U_{hub}$) within the wind farm at center-span $y = 0$ and $x/D = 3$ behind consecutive rows; (a) Aligned, (b) Staggered. Horizontal dotted lines represent the top and bottom rotor tip heights. The dash-dotted line indicates the hub height level. (c): Streamwise velocity deficit ($-\Delta U_{hub}/U_{hub}$) at the hub height within the wind farm.

Turbulence intensity

As pointed out by Rosen and Sheinman [62] and Thomsen and Sørensen [63], turbulence intensity is the primary cause of fatigue failure and is commonly used as a surrogate measure of the fatigue loads on wind turbines. Turbulence intensity I_u is commonly defined as the standard deviation of the wind velocity in the primary wind direction σ_u divided by the mean velocity at the turbine hub height:

$$I_u = \frac{\sigma_u}{U_{hub}}. \tag{2.16}$$

The stream-wise turbulence is caused by several coupled mechanisms, including the ambient boundary layer turbulence I_{u0}, turbulence generated by the shear layer of the turbine wakes, coherent tip vortex shedding from turbine blades and potentially turbulence generated or suppressed by thermal stratification, *i.e.*, positive or negative buoyancy, respectively.

It is common practice to consider turbulence intensity at the hub height as representative of the whole rotor. However possibly more important is the region around the top-tip height, where shear generation and tip vortex shedding are significant. Fig. 2.7 shows the turbulence intensity profiles at the center span, at $x/D = 3$, behind consecutive rows of wind turbines in the aligned case and behind the odd numbered rows for the staggered case. It is clear that the turbulence intensity is highest near the top tip height throughout both wind farms. It reaches an equilibrium between the third and fourth rows for the aligned case and is increasing throughout the farm in the staggered case. There is a secondary peak just above the bottom tip height as well, with lower turbulence intensity at the center of the wakes and near the surface. The turbulence intensity is higher for the aligned case compared to the staggered case. This is likely due to greater wake recovery behind consecutive turbines in the staggered compared to the aligned case. Overall, wind turbines in the staggered configuration experience less turbulence than in the aligned case.

It is useful to understand how the added turbulence intensity compares in the two wind farm configurations. The effective wake or added turbulence intensity I_{add} is defined as a function of the ambient turbulent intensity I_0, and the turbulence intensity

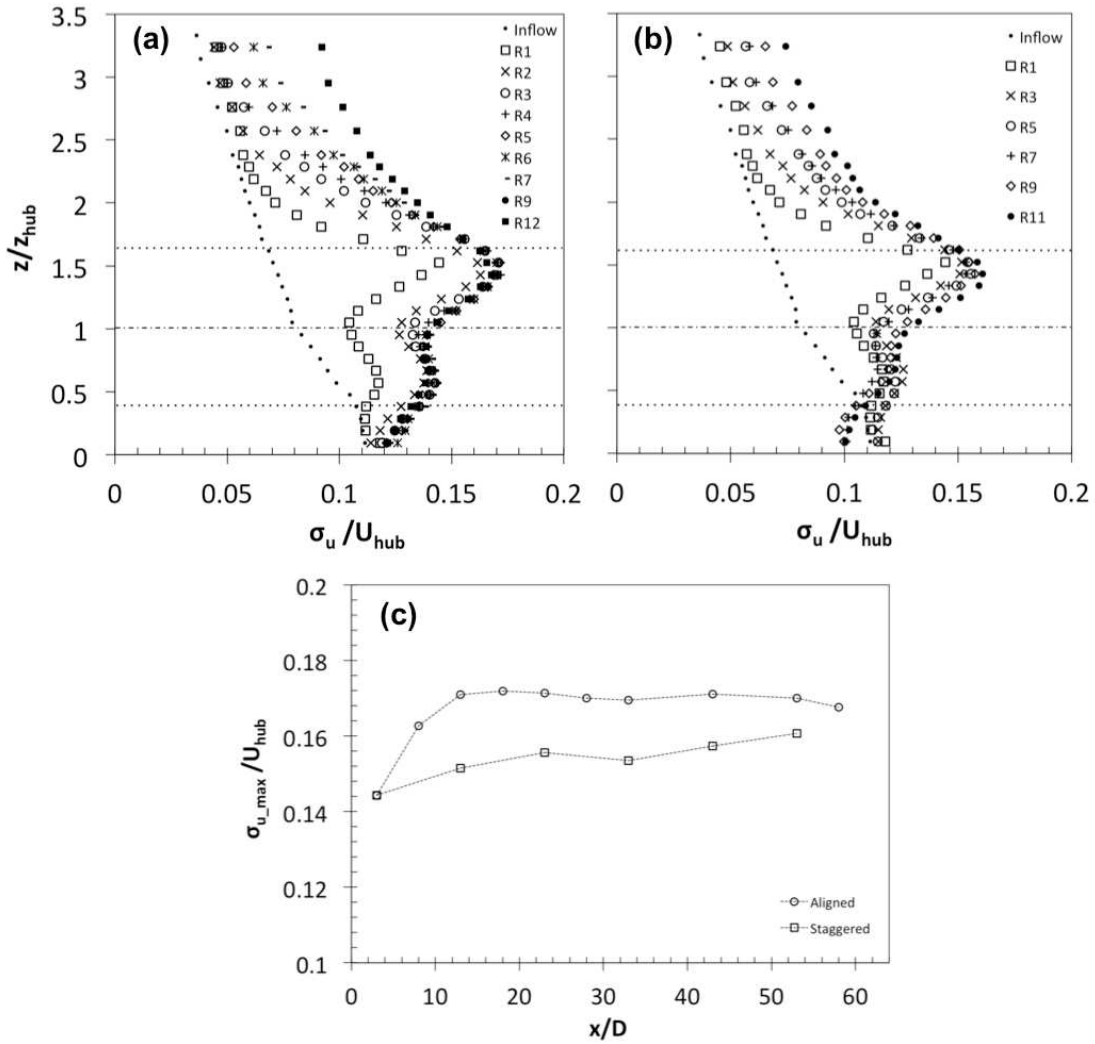

Figure 2.7: Turbulence intensity ($I_u = \sigma_u/U_{hub}$) at center-span $y = 0$ and $x/D = 3$ behind consecutive rows; (a) Aligned, (b) Staggered. Horizontal dotted lines represent the top and bottom rotor tip heights. The dash-dotted line indicates the hub height level. (c) Stream-wise maximum turbulence intensity relative to inflow hub-height mean velocity.

in the wind farm I_{wf} as

$$I_{add} = \sqrt{I_{wf}^2 - I_0^2}. \tag{2.17}$$

Frandsen and Thogersen [64] proposed a model for the added turbulence that takes into account wind-farm density, but does not consider the effects of configuration. The model is based on the geostrophic drag law and takes into account the additional surface roughness generated by the turbines:

$$I_{add,F} = \frac{a\sqrt{C_T}}{b\sqrt{C_T} + \sqrt{S_x S_y}}, \tag{2.18}$$

where a and b are generic empirical coefficients. Fitting the model to data from various unpublished field experiments, cited in [64], the following relationship has been found to be an adequate approximation,

$$I_{add,F} = \frac{0.36}{1 + 0.2\sqrt{S_x S_y / C_T}}, \tag{2.19}$$

where the model applies above the hub height.

In the current experiments I_{add} adjusts with the same trend as the turbulence intensity shown in Fig. 2.7. Previous experiments have shown that the maximum turbulence intensity occurs near the top tip height and about $x/D = 3$ behind turbines *i.e.*, [17, 36]. Taking the maximum value near the top tip, at the centerline, and a distance $x/D = 3$ behind the 11th row turbine as the representative added turbulence for the wind farms, $I_{add} = 0.15$ for the aligned farm and 0.14 for the staggered farm. As will be shown in Sec. 2.6 the thrust coefficient, C_T required to test Eqn. 2.19 is 0.18 for the aligned case and 0.47 for the staggered case. The model predicts $I_{add,F} = 0.12$ for the aligned case and 0.16 for the staggered case. The model generally gives good estimates considering experimentally determined values for C_T. Since the aligned case is the limiting scenario, practitioners should design for this case. However, while turbines are closer together in the aligned case, the added turbulence experienced by turbines in the wind farm will be higher than in the staggered configuration. The current models do not account for how configuration effects turbulence levels in wind farms. Additionally, to understand and model transport of momentum, moisture and other trace gases within the wind farm, more work is required to accurately predict the turbulence levels, taking

into consideration wind farm configuration. There are other similar empirical models summarized in [56], but currently there is no theoretical model for the prediction of turbulence intensity inside wind farms that has been well-validated against data from wind farms with varying turbine density and configuration [65].

Helicoidal tip vortices

Wind turbines induce a complicated wake vortex system, including coherent helicoidal tip vortices within the ambient turbulence of a turbulent boundary layer. These vortices are associated with enhanced turbulence level, noise generation and structural fatigue due to vortex induced vibration. Coherent tip vortex structures were characterized for a stand-alone wind turbine wake within a turbulent boundary layer by Zhang et al. [32] and Hu et al. [66]. Tip vortices are strongest near the top tip level behind turbines where background turbulence is lowest, and were only apparent in velocity power spectra to about two to three rotor diameters downwind of the turbine. Here we examine the persistence of and compare the signature of tip vortices in the aligned and staggered wind farms.

Power spectra of the velocity fluctuations (u' and w') were analyzed for time-series measured at the top-tip height at $x/D = 1$ behind selected rows of turbines. Figure 2.8 displays the spectra behind the first row, which are the same for both the aligned and staggered wind farms. The power spectra show the classical production and inertial subranges with -1 and -5/3 slopes, respectively, for boundary layer turbulence. However, superimposed is a concentration of energy at a specific frequency, which is associated with tip vortices at the top-tip height. Multiple spectral peaks are detected, including the primary frequency of the top-tip vortex shedding ($3f_t$) and the first harmonic frequency ($6f_t$), where f_t is the rotation frequency of the 3-blade turbine.

Some clear differences can be seen between the two wind farm layouts after the second and third rows as well as deep within the wind farms (Fig. 2.9). Particularly in the staggered case, the spectra behind the second row, R2, (measured at $x = 6D, y = 0$, and $z = Z_H$, referenced to the leading edge of the wind farm) exhibits no peak in energy due to the longer distance to the closest upwind turbine ($6D$) compared to the aligned case ($1D$). However, due to lower turbulence at the next closest downwind turbine, in row R3, the peak is larger for the staggered compared to the aligned case. This result

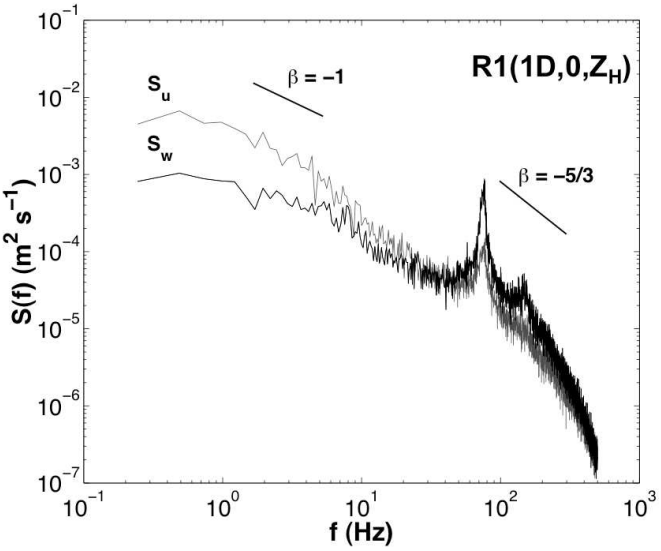

Figure 2.8: Power spectrum of the stream-wise and vertical velocity fluctuating components at the top-tip height, center-span $y = 0$ and $x/D = 1$ behind the 1st row of turbines.

is consistent with earlier findings that higher turbulence intensity leads to a weaker tip vortex signature [34]. This pattern continues throughout the farm and leads to stronger tip vortex signatures behind turbines in the staggered configuration, even far within the wind farm, *e.g.* behind the ninth row. Additionally, the peak signature for both configurations is muted compared to the first row and the second harmonic frequency of the tip vortex signature is undetectable without filtering out the background turbulence signal. This is likely due to the increase in the overall energy concentrated around the peak, exhibited by a wide range of scales and spectral slope that deviates from the inertial $-5/3$ scaling. This may be related to the formation of a shear layer at the top of the wind farm, which may lead to coherent vortex structures and higher turbulence levels compared to boundary layer turbulence. This behavior is similar to that in and above canopies, as the peak frequency often occurs due to complex fluid-structure interaction involving wake shedding, and the movement of canopy elements, leading to a short-circuiting of the energy cascade [42]. In the case of a wind farm, the

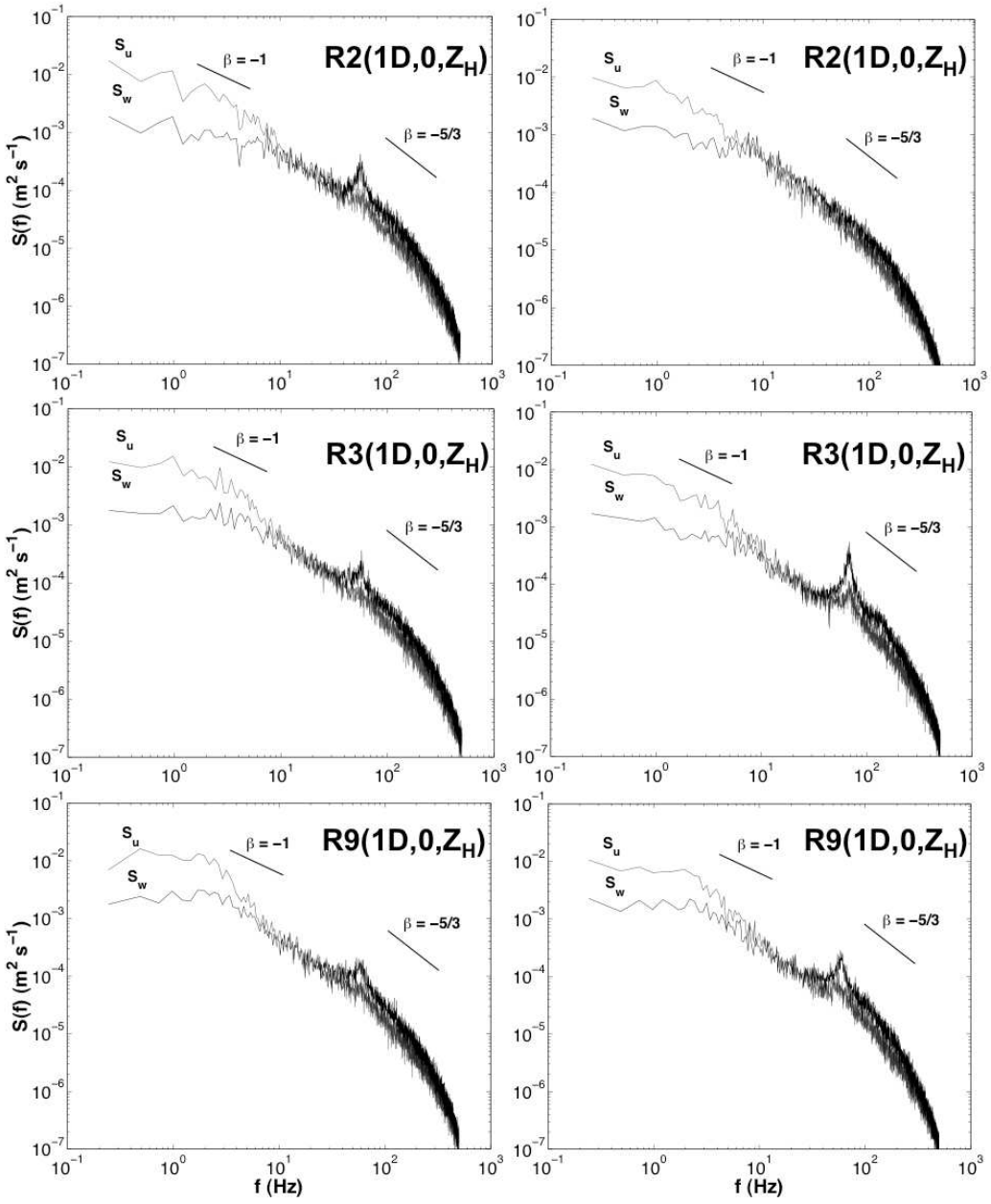

Figure 2.9: Power spectrum of the stream-wise and vertical velocity fluctuating components at the top-tip height, center-span $y = 0$ and x/D= 1 behind the 2nd, 3rd and 9th rows: Aligned (left) and Staggered (right).

fast moving turbines blades chop the air, shedding relatively smaller vortices compared to inertial scale eddies in the flow, expected for a flat boundary layer.

2.5.3 Vertical wake expansion

The mean velocity just above the two wind-farm configurations decreases with downwind distance, however the rate of decrease is greater for the staggered farm. This reduction in velocity above the wind farms is an indication of a growing wake region as the wakes of consecutive downwind turbines interact (see Fig. 2.5). Wake expansion is characterized to compare the rate of flow development over the wind farms. Here we focus on turbulence measurements taken along the centerline $y = 0$, over the central column of wind turbines, at a streamwise spacing of $\Delta x = 1D$ and at four heights above the wind farms, from the top tip $z/Z_H = 1$ to $z/Z_H = 2$.

As introduced in Sec. 2.3.2, an expanding wake can be modeled as proportional to the vertical turbulence intensity and kinematic shear stress (Eqn. 2.4). Fig. 2.10 shows the streamwise distribution of wall-normal turbulence intensity above the centerline of the two wind farms. The wake growth is evident by the increase in turbulence intensity, compared to the inflow, at each level with increasing downwind distance. As expected for a growing wake, there is a delay in the growth downstream with increasing height. This same pattern holds true for shear stress as well as the streamwise turbulence intensity.

Turbulence levels exhibit clear adjustment from inflow conditions to an equilibrium at varying rates. The wake growth rate can be characterized either by the inception of disturbance or the point of equilibrium. The point downstream where the turbulence or shear stress reaches equilibrium can be defined as the distance where the turbulence reaches 99% of the final equilibrated value. However, the flow over the sparsely spaced turbine arrays is not monotonic from point to point, as the wakes adjust significantly between turbines, making it difficult to identify where equilibrium occurs. One option to aid in the quantification is to smooth or filter the data, however the specific filter can affect the results. Another option is to fit a smooth function to the data that characterizes the process and assess equilibrium based on adjustment of that function. An appropriate model to describe the growth of wakes is a logistic growth model. Since the wake growth rate is dependent on the amount of turbulence present (Eqn. 2.4), a

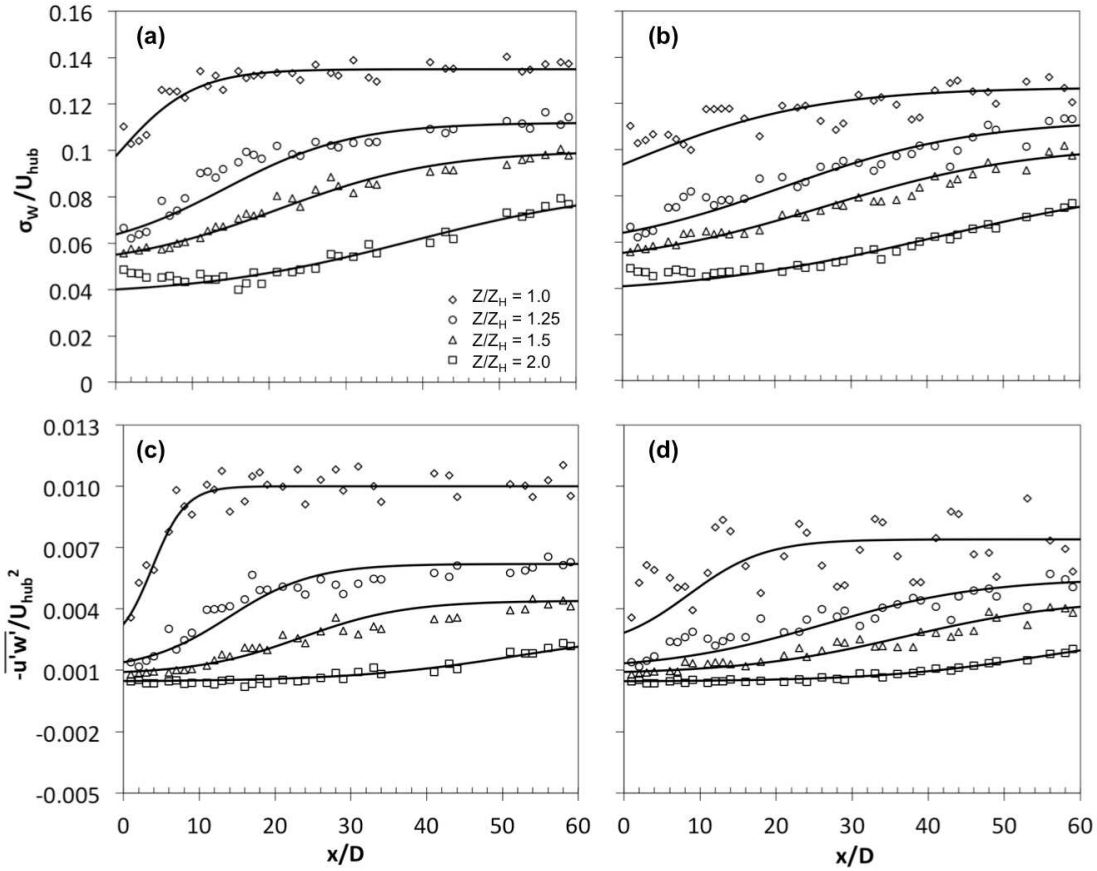

Figure 2.10: Wall-normal turbulence intensity adjustment at four heights above the center-span of the wind farm; (a) Aligned and (b) Staggered. Normalized wall-normal kinematic shear stress adjustment at four heights above the wind farm; (c) Aligned and (d) Staggered.

logistic growth model is a physically realistic representation to describe the wake growth process. Fitting the growth model to measurements of vertical wake growth, we can determine the wake growth rate, $d\delta_{wake}/dx$.

The general form of the logistic growth model, considering the turbulent stress as the characteristic of the flow that is growing, follows as

$$d(\overline{u_i'u_j'})/dx = b\overline{u_i'u_j'}(1 - \overline{u_i'u_j'}/K), \tag{2.20}$$

and integrating results in

$$\overline{u_i'u_j'} = K/(1 + exp[-(a + bx)]), \tag{2.21}$$

with three parameters: K is the asymptotic maximum value and a and b are generic coefficients that shift and rescale the x variable. By algebraic manipulation this model can be transformed into

$$ln[\overline{u_i'u_j'}/(K - (\overline{u_i'u_j'}))] = a + bx. \tag{2.22}$$

Knowing K based on the initial inflow profile and the equilibrium values of the turbulence stresses, we can analyze the log ratio to estimate the parameters a and b using a least squares approach. The result provides a realistic and quantitative approach for determining the wake expansion rate.

Fig. 2.11 shows the equilibrium wake growth over the two wind farm configurations. Regression of the wake layer growth for the three turbulence quantities provides an estimate of the growth rate, $d\delta_{wake}/dx = 0.016$ for the aligned case and 0.024 for the staggered case. The growth rate over the center column of turbines is initially faster over the aligned case compared to the staggered configuration. However, after the initial growth at the leading edge, the growth rate is subsequently faster over the staggered farm as exhibited by the steeper slope of the growth curve.

2.5.4 Characterization of wind-farm turbulence

The spanwise ensemble average profiles collected within and over the aligned and staggered wind farms are compared, and characterized to determine key turbulence properties of the wind farms, including the aerodynamic roughness and friction velocity. Also

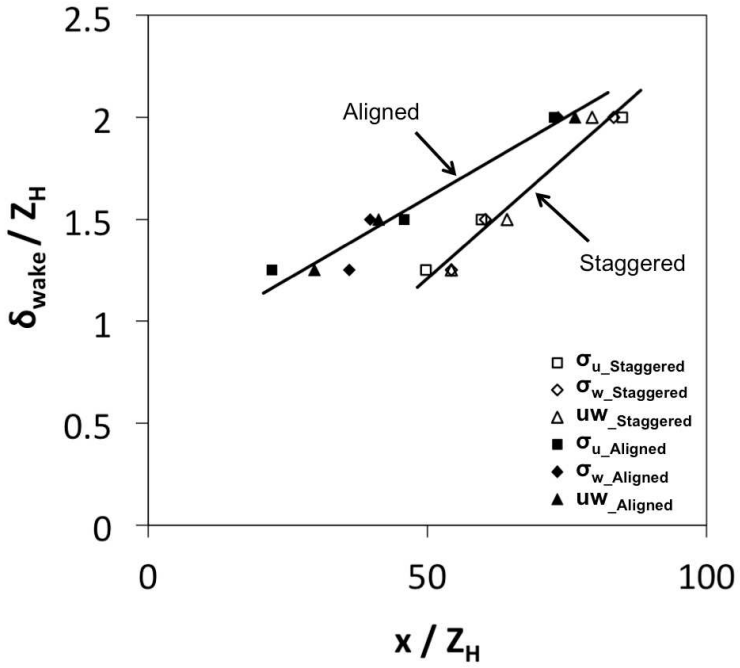

Figure 2.11: Over-farm wake height based on turbulent stress adjustment characterized with a logistic function for aligned and staggered farms. The slope of the regressed linear functions reveal the rate of wake growth over the farms.

presented are the turbulence intensity, kinematic shear stress, dispersive stress, scalar flux, turbulent momentum and heat transport efficiency, as well as key TKE terms. The data were collected at selected locations within the quasi-developed region of the wind farms as presented in Sec. 2.4. To summarize, the spanwise averaged vertical profiles used to characterize the wind-farm flow were collected at four locations along the span ($y/D = -1, 0, 1, 2$) and at the streamwise position $x/D = 3$ behind the wind turbines of the corresponding targeted row, the 11th and 12th row of turbines for the staggered and aligned cases, respectively. These profiles were averaged horizontally and deemed to be representative of the horizontally averaged flow. This strategy was determined initially by trial and error, as we tested averaging various combinations of profiles taken at different locations to determine the optimum number and location of

profiles required. A challenge for collecting true spatially averaged data in complex flows is that it is not feasible to collect data everywhere. This is particularly true close to turbines where errors of the measurement technique make data unreliable. This is also an issue in the field, where often a limited number of sampling stations are available. We have investigated this strategy further using a validated LES framework to similate wind farms with similar characteristics and found averaging the four selected profiles represented the spatially averaged data well, see Wu and Porté-Agel [67]. The results from this section will be employed in Sec. 2.6 to determine the thrust coefficient for the wind farms, and evaluate the models outlined in Sec. 2.3. Additionally, turbulent flow properties of wind farms will be compared to those of surface layer and typical canopy-type flows, to assess which flow type is physically more similar to turbulent flow in and above wind-farms.

Mean flow properties

Spanwise, ensemble averaged streamwise velocity and temperature profiles are shown in Fig. 2.12 for the aligned and staggered wind farms. The mean velocity is normalized by the velocity at the top of each wind farm. For the same free-stream velocity, the velocity is higher in the aligned versus the staggered farm, and an inflection point in the profile is evident just below the top tip height. This is characteristic of canopy-type flows where inviscid instability typically leads to the generation of a mixing layer, with K-H type eddies [68]. The temperature profiles are similar between the two configurations, with a variation of about 7 °C between the bottom-tip height of the wind farm and the free-stream flow. Therefore there is a 53 °C change between the surface and the bottom tip height.

A thick boundary layer over the wind farm ($\delta/Z_H \approx 3$) allows for a limited log-layer to develop over the farm, as can be identified from the mixing length profile in Fig. 2.13, where the mixing length is defined as

$$L_m \equiv -\langle\overline{u'w'}\rangle^{1/2}/(dU/dz). \tag{2.23}$$

The linear region of the L_m profile corresponds to a log-linear region in the velocity profiles, which is only present in a limited region near the top of the wind farms, from

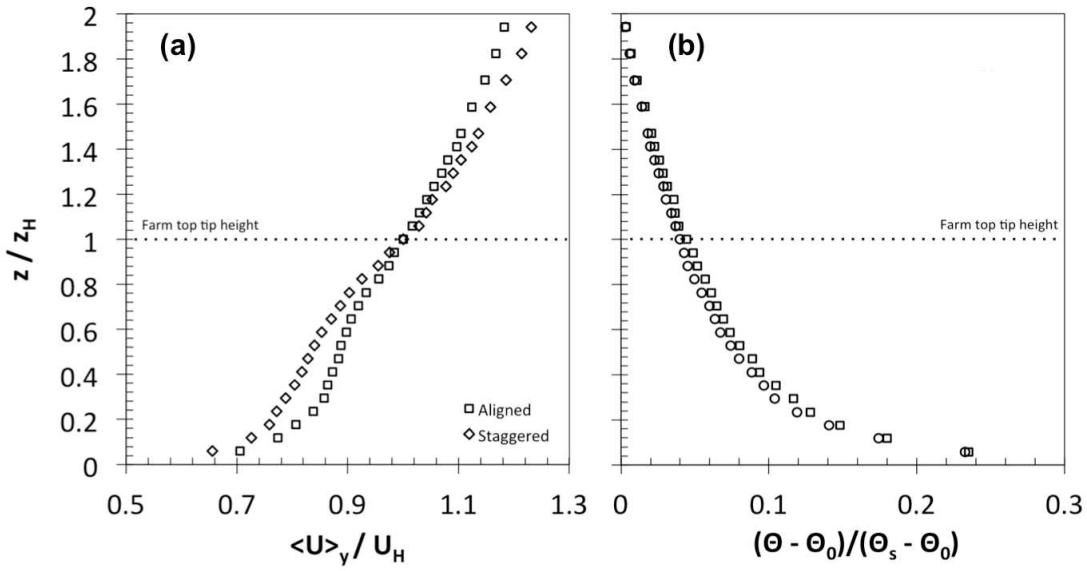

Figure 2.12: Laterally averaged vertical profiles of (a) mean stream-wise velocity and (b) mean temperature in the aligned and staggered wind farm.

$z/Z_H = 0.8$ to 1.0 for the aligned farm and $z/Z_H = 1$ to 1.2 for the staggered farm. The linear variation of the mixing length may be written as

$$L_m = \kappa(z - d). \tag{2.24}$$

Extending the linear fit of the mixing length to the ordinate axis, the zero-plane displacement d is determined. The aligned case exhibits a small displacement $d = 0.005$ m, while the staggered case has a significant displacement $d = 0.065$ m. Based on the log-linear fit of the velocity profiles, following Equation (2.13), the effective roughness for the aligned case is found to be $z_{0(aligned)} = 1.5$ mm with a corresponding friction velocity $u_* = 0.20$ m s^{-1}, and for the staggered case the roughness is $z_{0(staggered)} = 2.5$ mm with a friction velocity of $u_* = 0.26$ m s^{-1}.

A summary of the mean wind farm flow characteristics for the aligned and staggered configurations are listed in Table 2.2. The momentum flux is about 1.7 times greater for the staggered compared to the aligned case. The resulting effective roughness for the staggered case is about 70% greater than that of the aligned wind farm, and the

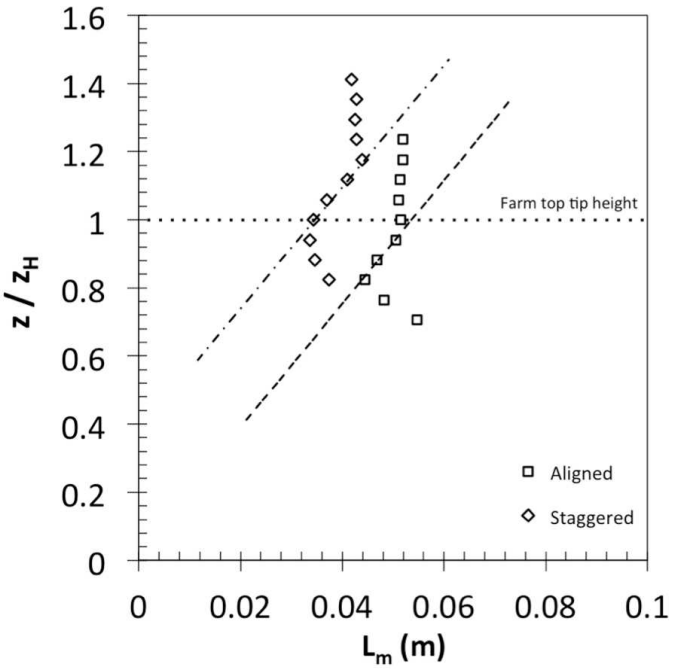

Figure 2.13: Effective mixing length profiles for the aligned and staggered wind farms, used to determine the region of the flow that satisfies linear mixing length scaling. Dashed lines are linear fits extrapolated to determine the zero-plane displacement.

roughness length relative to wind farm height is 1% and 1.5% for the aligned and staggered wind farms, respectively. This is within the range simulated in the study by Calaf et al. [4]. The effective wind farm roughness is 18 to 31 times that of the roughness of the surface below the turbines, respectively. The resulting stability effect on the flow is characterized for the wind farm cases by $L_{(aligned)} = -1.3$ m and $L_{(staggered)} = -1.4$ m, or $-L/Z_H$ is 7.7 for the aligned case and 8.3 for the staggered case. Since the boundary layer only extends up to approximately $3Z_H$, we can reason buoyancy has a negligible effect on the flow in the wind farm cases. Therefore although the flow for the case without a wind farm may be slightly convective, buoyancy is negligible for the wind farm cases.

Table 2.2: Comparison of wind farm flow characteristics and effective roughness for the aligned and staggered wind farms.

Wind farm configuration	U_H (m s^{-1})	d (cm)	d/Z_H –	u_* (m s^{-1})	u_*/U_H –	z_0 (mm)	z_0/Z_H –	$z_0/z_{0,gnd}$ –
Aligned	2.4	0.5	0.03	0.20	0.08	1.5	0.009	18
Staggered	2.2	6.5	0.38	0.26	0.11	2.5	0.015	31

Turbulence and flux characteristics

Fig. 2.14 shows the streamwise and vertical normal stress profiles, which are maximum just below the top tip height of the wind farms. Near the top of the wind farm, the profiles collapse when normalized by u_*. The maximum streamwise value is about 1.7, and the maximum vertical value is 1.5 in both cases. It is notable that the turbulence levels within the wind farms are different likely due to the configuration of the turbines. Fig. 2.15 shows the normalized kinematic shear stress profiles, the dispersive stress component, and total stress profiles. The total stress profiles collapse well with a maximum near the top of the aligned and staggered wind farms. The shear stress reduces quickly below the top of the farm to about 40% of the maximum value at about the hub height and near zero close to the bottom tip height for the aligned farm and 20% for the staggered farm. There is significant dispersive stress measured for the two wind farms. The dispersive stress is 40% of the max shear stress near the hub height for the aligned wind farm, and 10% for the staggered wind farm. The lower dispersive stress in the staggered farm is due to the wakes of offset turbines which aid to homogenize the mean flow and lead to more efficient lateral mixing compared to the aligned case.

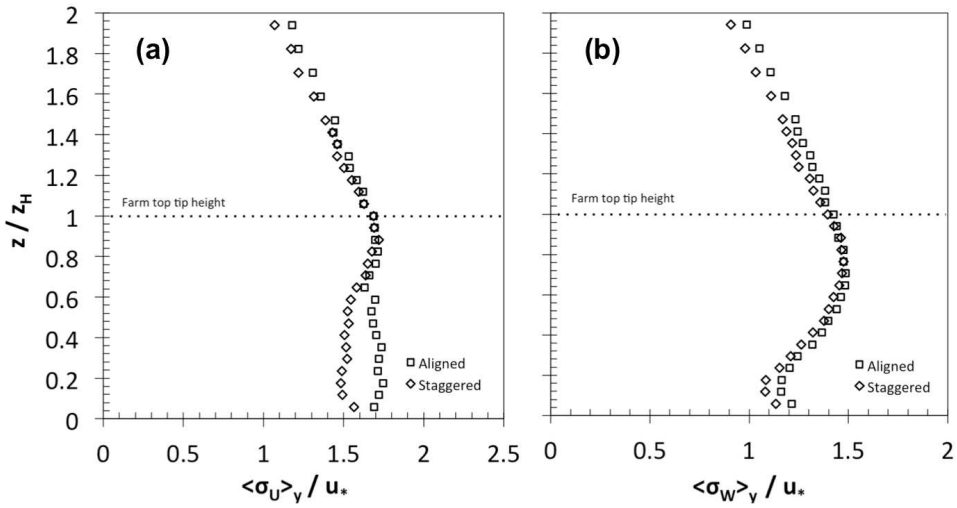

Figure 2.14: Vertical profiles of the (a) streamwise and (b) wall-normal turbulence for the aligned and staggered wind farms.

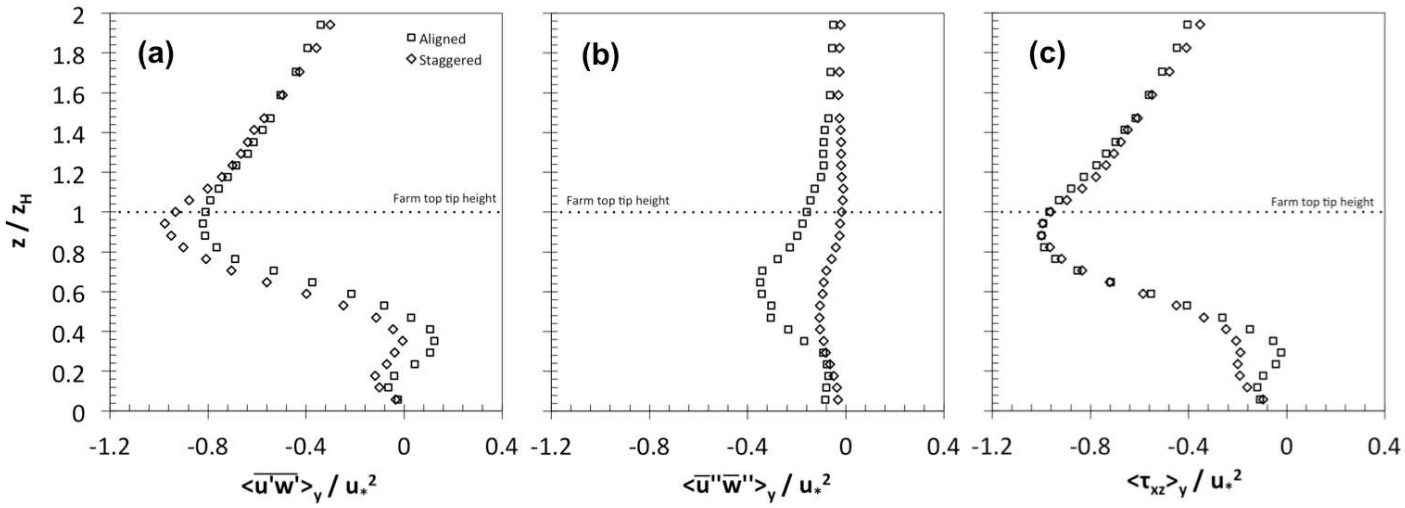

Figure 2.15: Vertical profiles of (a) kinematic shear stress (b) dispersive stress and (c) total stress for the aligned and staggered wind farms.

Figure 2.16 shows the scalar flux profiles, which are the sum of kinematic heat flux and the dispersive heat flux $Q = \langle \overline{w'\theta'} \rangle + \langle \bar{w}''\bar{\theta}'' \rangle$ normalized by the surface flux Q_{s0} in the boundary layer without a wind farm. In both wind farm cases, the heat flux is higher in the region above the hub height and lower in the region below the hub height of the wind farms, compared to the case without a wind farm. Near the surface, the profiles diverge slightly, with the staggered case exhibiting the lowest flux. Lu and Porté-Agel [14] showed similar decreasing behavior in LES cases under stable conditions, while Calaf et al. [69] reported enhanced surface flux for LES cases with scalar source at the surface. The dispersive flux is less than 10% of the total flux. Further study is planned to investigate the surface scalar flux in more detail, but we can infer notable differences in the surface heat flux for the two farms and also note an important difference compared to the flat boundary layer case.

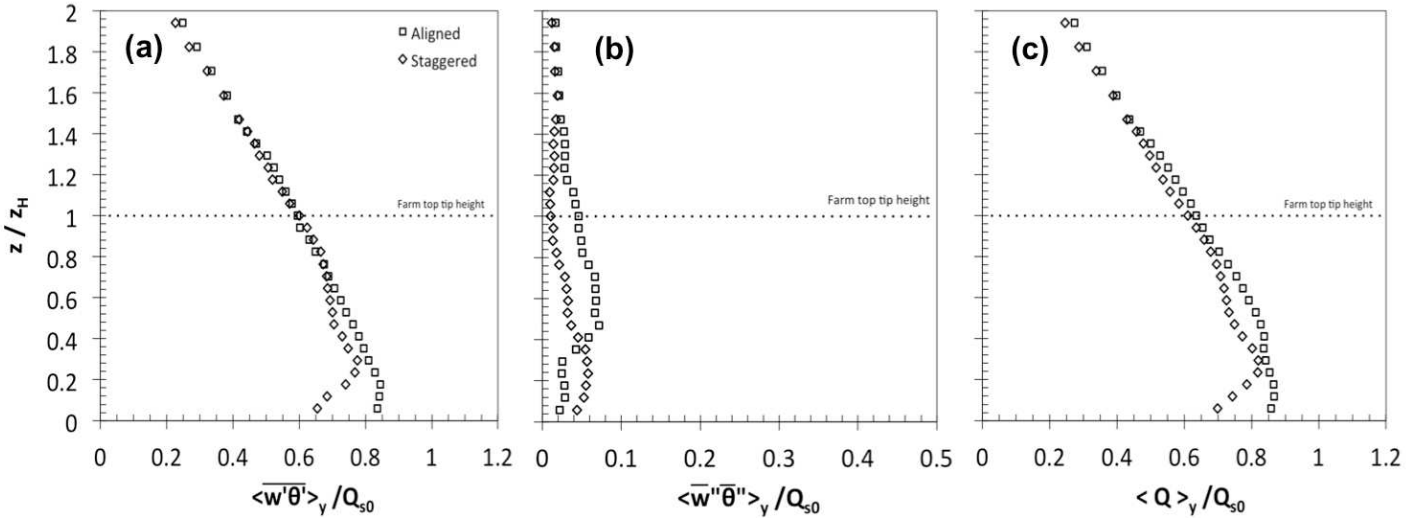

Figure 2.16: Vertical profiles of (a) kinematic heat flux (b) dispersive heat flux and (c) total heat flux for the aligned and staggered wind farms.

Profiles of the spatially averaged correlation coefficient $r_{uw} = \overline{u'w'}/(\sigma_u \sigma_w)$ in the wind farms are shown in Fig. 2.17. The correlation coefficient is a measure of the efficiency of the turbulence in transporting momentum relative to the absolute amount of turbulence present. The profiles follow similar trends, with magnitudes near the top of the wind farms between 0.3 to 0.4 for the aligned and staggered cases, respectively. In flat boundary layer type flows, it is expected to be around 0.3. Therefore flow over the staggered wind farm is more efficient at absorbing momentum than a flat boundary layer, while the aligned case is similar to a flat boundary layer. Fig. 2.17 also shows Prandtl number profiles for the two wind farm configurations. The values are similar near the top tip height of the wind farm at approximately 0.7. This means that the wind farm is about 1.5 times as efficient at transporting heat compared to momentum. For a flat boundary layer under neutral conditions, Pr_t is expected to be about 1.0, while for mixing layers and canopy flows Pr_t is approximately 0.5.

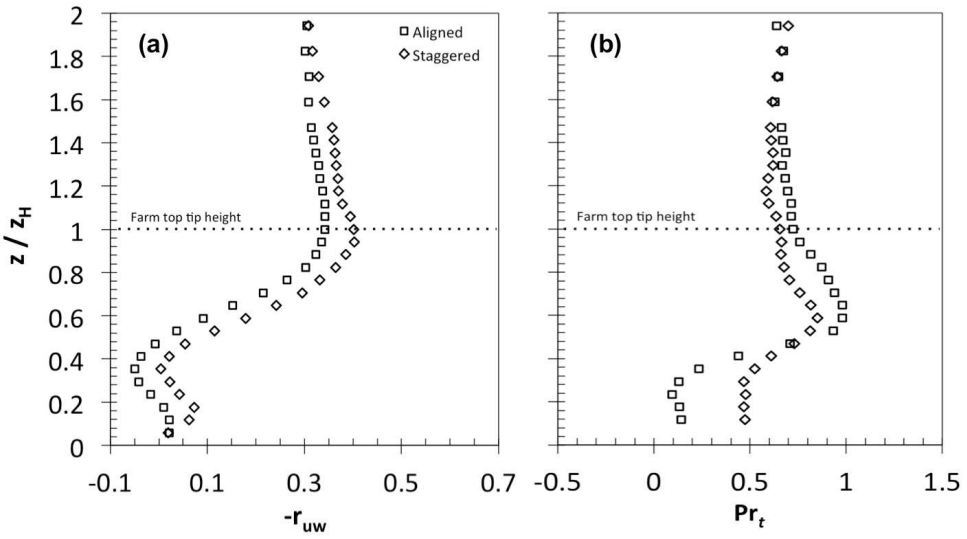

Figure 2.17: Vertical profiles of (a) $u-w$ correlation coefficient and (b) turbulent Prandtl number for the aligned and staggered wind farm.

Turbulent kinetic energy (TKE) budget

The TKE budget consists of the different physical mechanisms contributing to turbulence generation, consumption, and transport of TKE and follows as

$$\left\langle \frac{g}{\overline{\theta}_0}(\overline{w'\theta'}) \right\rangle - \left\langle \overline{u'w'}\frac{\partial \bar{u}}{\partial z} \right\rangle - \left\langle \frac{\partial \overline{kw'}}{\partial z} \right\rangle - \left\langle \frac{1}{\rho}\frac{\partial \overline{p'w'}}{\partial z} \right\rangle + \left\langle \frac{1}{\rho}\overline{d_i' u_i'} \right\rangle - \left\langle \frac{\partial \bar{k}''\bar{w}''}{\partial z} \right\rangle - \left\langle \left(\overline{u_i' u_j'}\right)'' \frac{\partial u_i''}{\partial x_j} \right\rangle - \langle \varepsilon \rangle = 0, \quad (2.25)$$

where $\bar{k} = \frac{1}{2}\overline{u_i'^2}$ is the time-averaged turbulent kinetic energy, p' is pressure fluctuation, ρ is fluid density, d_i' is fluctuations of the drag, and ϵ is dissipation. Index notation is only used for terms where all components are likely significant. From left to right, the terms represent (1) production due to buoyancy, (2) shear production, (3) turbulent transport, (4) pressure transport, (5) waving production, (6) dispersive transport, (7) wake production and (8) viscous dissipation. In canopies, waving production is associated with moving canopy elements. Here waving production is due to the moving blades of wind turbines. Wake production has the same form as shear production but depends on local variation in shear stress doing work against local variations in mean strain rates. In a wind farm this is caused by vortex shedding from wind turbine components, including the tower, nacelle, and blades (e.g. tip vortices). For a homogeneous array of turbines and steady flow conditions, wake production simplifies to

$$P_w = -\langle \bar{u} \rangle \frac{\partial}{\partial z}\left(\langle \overline{u'w'} \rangle + \langle \bar{u}''\bar{w}'' \rangle \right) \quad (2.26)$$

(cf.[70, 50]).

Here we are able to compare the shear, vertical turbulence transport, wake production, and buoyancy production terms of the TKE budget for the aligned and staggered cases (Fig. 2.18). The profiles are normalized by u_*^3/Z_H. The shear production is maximum near the top tip height where mean velocity gradients are greatest, and the profiles are similar between the two wind farm configurations with higher shear near the top tip height in the staggered case. There is a significant sink in vertical turbulent transport for which the maximum of both cases is near the top tip height and is approximately the same magnitude as the shear production. The transport sink is greater for the

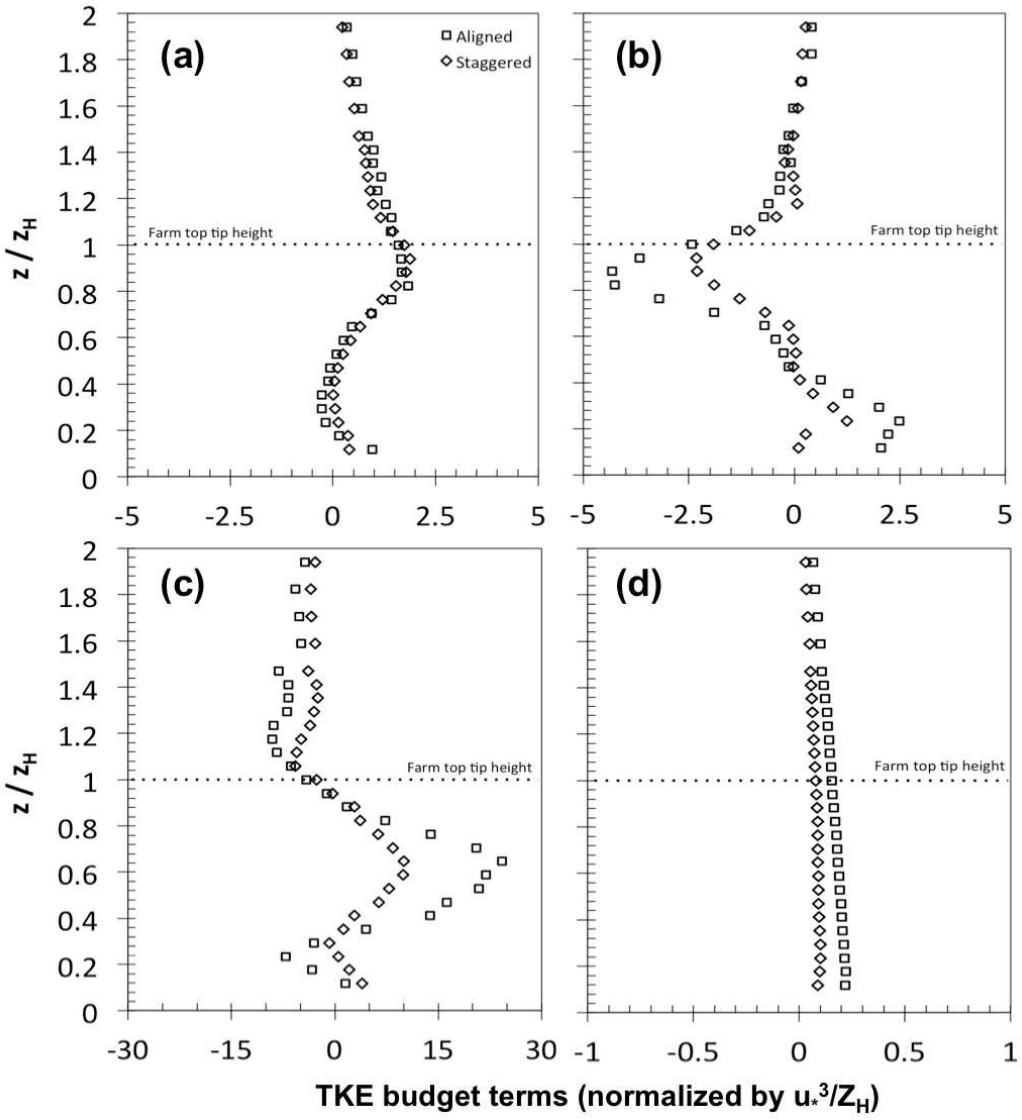

Figure 2.18: TKE budget term profiles in the aligned and staggered wind farm. (a) shear production, (b) vertical turbulent transport, (c) wake production, and (d) buoyancy production.

aligned compared to the staggered configuration. Wake production is the largest of the measured components, and is greatest between Z_{hub} and Z_H. Due to the large pressure drop across wind turbines it is expected that the pressure redistribution term balances the wake production term. However, the pressure term was not measured in this study. Wake and waving production tend to short circuit the spectral energy cascade by converting larger scale eddy motion, with length and time scales in the energy containing range to smaller eddies. The result is an increase in dissipation rate compared to the flat boundary layer flow without wind turbines [42]. This can be seen in the energy spectra far within the wind farms, in Fig. 2.9. The buoyancy production is very small for both cases, less than an order of magnitude compared to shear production. The aligned case has higher buoyancy production than the staggered case, possibly due to more efficient wake interaction in the staggered farm leading to a reduction in surface flux, as seen in Fig. 2.16.

2.6 Discussion

The models for added aerodynamic roughness and canopy length scales require an estimate of the drag due to the wind farm, and the related thrust coefficient C_T. One method to determine the turbine induced drag force is to measure and take an ensemble average of all of the terms in the momentum equation and set their sum equal to the drag term. However we lack adequate three dimensional data coverage to ensure a good estimate. Another approach involves using a well-known canopy model, which relates the exponential decay of mean velocity within a canopy to the momentum flux, developed by Inoue [71] and recently revisited by Yi [72]. The model follows as

$$U(z) = U_H \exp\left[\alpha\left(\frac{z}{Z_H} - 1\right)\right], \tag{2.27}$$

where $\alpha = \beta' Z_H/\lambda$, $\beta' = u_*/U_H$, and $\lambda = 2\beta'^3/L_c$. Fitting the exponential model to the ensemble streamwise velocities, presented in Fig. 2.12, leads to an estimate of the overall drag within the wind farms. The model fits the profiles, with an $R^2 = 0.99$ across the rotor swept region, between $z/Z_H = 0.3$ and 1.0. With direct measurements of β' and fitting a regression to the mean velocity profiles, we can determine L_c and

calculate C_T following Equation 2.12. We find that the thrust coefficient C_T for the aligned farm case is 0.18 and for the staggered case is 0.47. The difference in C_T between the two configurations is remarkable. However, this is not unexpected since the array configuration has a significant effect on the 3-D flow within the wind farms, and the aligned array exhibits greater wake sheltering from upwind turbines compared to the staggered farm. This is supported by Nepf [73] who studied the effect of layout pattern on the drag coefficient of cylinder arrays. A similar effect was reported for arrays of blocks in the study by Coceal et al. [47]. The estimation of C_T is sensitive to measurements of mean velocity, friction velocity and the representativeness of the horizontally averaged profiles. We estimate the uncertainty of C_T to be approximately 5% based on estimated measurement uncertainty (Sec. 2.4) and evidence that the profiles represent horizontally averaged profiles (Sec. 2.5.4). The drag development length scale $L_c = 43$ m was determined for the aligned case and 16 m for the staggered case. Therefore the flow within the staggered case adjusts, on a spanwise averaged bases, much faster than the aligned case. This is due to the more efficient mixing of wakes horizontally and vertically within the staggered farm, and is in agreement with the results of the velocity deficit, wake growth rate, and the vertical transport of momentum and TKE budget.

Using the estimates of C_T, we compare the effective roughness lengths of the two wind farm configurations with the added roughness models introduced in Sec. 2.3.1 as well as with previous experiments. As determined in Sec. 2.5.4, the effective roughnesses for the two wind farm configurations were $z_{0(aligned)} = 1.5$ mm and $z_{0(staggered)} = 2.5$ mm. By comparison, in previous experimental studies of aligned wind farms, Cal et al. [29] found a roughness, $z_0 = 0.4$ mm, for a 3×3 array of model turbines with a spacing of $S_x = 7D$ and $S_y = 3D$, and Chamorro and Porté-Agel [17] found the same roughness, $z_0 = 36$ mm, for two model wind farms with $S_x = 5D$, $S_y = 4D$ and $S_x = 7D$, $S_y = 4D$. Cal et al.'s [29] result is based on spatially averaged velocity measured with particle image velocimetry (PIV) around the third row. However the wind farm extent was much smaller than the drag development length scale and, as pointed out by the authors, an adjusted surface layer was unable to developed over the wind farm. This supports the need to characterize the flow for very large wind farms in order to determine the effective roughness. Chamorro and Porté-Agel [17], on the other

hand, determined the roughness based on velocity profiles collected at the centerline of the two turbine arrays, albeit after 10 rows of turbines. The combination of wakes along the centerline of a turbine array results in a very different velocity profile, which is not representative of the spanwise averaged profile required to characterize the flow using a top-down approach [15]. Only considering the velocity profile at the centerline results in an artificially large apparent roughness.

Comparing our experimental results to model predictions, we can evaluate the performance of the various roughness models (see Sec. 2.3.1). The results from the three added roughness models, Equations (2.1), (2.2), and (2.3) [37, 13, 4], are summarized in Table 2.3. Overall the models produce a large range of effective roughness estimates, with the model by Calaf et al. [4] providing the closest estimates to the experimental results for the aligned farm, while the model by Frandsen et al. [13] is closest for the staggered farm. The results reveal the sensitivity of the models especially to C_T. Deviations of model predictions from experimental results may be due to a number of factors. Although the experimental results reflect flow in and above large wind farms, the flow may not be fully developed, indicated by the large estimated drag development length scales L_c. This is particularly important with regard to the aligned farm for which the estimated L_c is a factor of four greater than the length of the model wind farm. The flow within the farm must be fully developed for the flow above to reach equilibrium. Another possible reason for errors in effective roughness estimations may be due to assumptions made in the model formulations, including the existence of two log layers that intersect at the hub height and simplification of the wake eddy viscosity model. Additionally the models do not explicitly account for wind turbine array configuration. As shown in Sec. 2.5.4, dispersive flux is significant in wind farms, making up as much as 40% of the total momentum flux for the aligned case. Strong and varying levels of inhomogeneity of the flow, which depends on wind farm configuration (*i.e.*, wind direction) and leads to variable momentum flux, presents a challenge for developing a robust model for effective roughness independent of flow information.

In addition to the drag development length scale, the shear penetration scale is a key length scale that describes mixing processes inherent to canopy flows. It has been proposed that the ratio between the height of the roughness elements and the drag length scale $C_d a h$ needs to be greater than 0.1 for canopy flow properties to emerge

Table 2.3: Results for effective roughness models compared with experimental data.

Wind farm configuration	$z_{0,exp}$ (mm)	$z_{0,L}$ (mm)	$z_{0,F}$ (mm)	$z_{0,C}$ (mm)
Aligned	1.5	1.2	0.8	1.3
Staggered	2.5	3.2	2.9	4.5

[74, 75, 76]. This includes characteristics, such as an inflected mean velocity profile, and mixing-layer (shear layer) type K-H eddies near the top of the array. In this study the canopy scales are both well below this criterion with $C_d ah = 0.004$ for the aligned case and $C_d ah = 0.009$ for the staggered case. Ghisalberti [43] reports that flows with such low canopy scales should not exhibit canopy flow characteristics, but instead can be characterized as rough surfaces. Evidence based on the turbulence and transport statistics presented here suggest this limit may not hold. Both wind farm configurations exhibit an inflection point in the ensemble averaged velocity profiles near the top tip height Z_H. The length scale for the penetration of K-H eddies into a canopy is based on the ratio of the mean velocity and the velocity gradient at the top of the wind farm (Eqn. 2.5). The result for the aligned case is $L_s = 0.6$ m, and for the staggered case is $L_s = 0.4$ m. In both cases, the scale of eddy penetration is larger than Z_H. This implies that eddies generated by the shear layer at the top of the wind farms, for the turbine distribution density studied here, directly interact with the surface, likely distorting any K-H eddy development.

We find that some properties of the flow follow characteristics of a surface layer while others are similar to canopy flows. It is evident, based on the mixing length profiles (Fig. 2.13), that the mixing length is proportional to vertical distance within a limited region, which depends on turbine configuration. Conversely, many bulk turbulence statistics more closely resemble typical values reported for canopy turbulence. Table 2.4, partially reproduced from Raupach et al. [68] and Finnigan [42], summarizes a comparison between standard flow properties of surface layers and canopies with those observed from the two wind farm configurations studied here. It is clear that, based on the classical turbulence statistics for surface layer and canopy flows, wind farm flows

are more similar to canopy flows. Additionally, many terms of the TKE budget, which have been shown to be important in canopy flows, are also significant in wind farm flows. However, the integral scales, drag development length scale and shear length scales, examined earlier, do not strictly exhibit typical behavior of a dense canopy flow. The wind farms appear to have integral scale turbulence characteristics that exhibit a combination of surface layer and canopy flow characteristics, while the bulk turbulence statistics and transport behavior more closely follow the characteristics of canopy flows.

Table 2.4: Comparison of statistical flow properties for the flow at $z = Z_H$ of the aligned and staggered wind farms, surface layer, and canopy flow near $z = h$.

Property	Surface layer	Canopy	Wind farm
Inflection in U profile	No	Yes	Yes
σ_u/u_*	2.5 – 3.0	1.8 – 2.0	1.7
σ_w/u_*	1.2 – 1.3	1.0 – 1.2	1.5
$-r_{uw} = -\left\langle \overline{u'w'} \right\rangle / (\sigma_u \sigma_w)$	∼0.3	∼0.5	0.3 – 0.4
$Pr_t = K_M/K_H$	∼1.0	∼0.5	∼0.6 – 0.7
Integral length scale	$\propto (z-d)$	$\propto L_s$	$\propto Z_H$ and L_c
TKE budget	$Ps = \epsilon$	large Ps, Tt, and Tp	large Ps, Tt, Tp and Pw

Note: the TKE budget terms are shear production (Ps), turbulence transport (Tt), pressure transport (Tp), and wake/waving production (Pw).

2.7 Summary and Conclusions

Wind-tunnel experiments were performed to study the effect of wind-farm configuration on flow development in and over wind farms, and to investigate the validity of surface layer versus canopy-flow type models for wind farms. The addition of a heat source at the surface, while maintaining neutral conditions, allowed for the study of scalar transport through the wind farms. High-frequency hot-wire/cold-wire anemometry was used to quantify mean wind velocity, turbulence intensity, turbulent stress and kinematic scalar fluxes within the flow development region as well as deep within the quasi-developed

wind farms flows. Focus was put on revealing the difference in the magnitude and spatial distribution of the velocity deficit and the turbulence intensity in the turbine wakes, characterization of wake expansion above the wind farms and on characterization of the spatially averaged wind-farm turbulent flow, including mean velocity, normal and shear stresses, momentum and heat flux, and key terms of the TKE budget.

The effective aerodynamic roughness of the wind farms, canopy drag length scale, shear layer thickness and bulk turbulence statistics were compared to determine whether flow in and over wind farms is more appropriately modeled as a surface layer with added roughness or as a canopy. We conclude that neither flow paradigm strictly typifies wind-farm flows. Many flow properties follow those of canopy-type flows, however, a well-defined shear layer with Kelvin-Helmholtz type eddies is not observed and unlike most canopy flows, the drag development length scale is very long. The length-scale was on the order of 100 - 250 times the height of the wind farms, compared to forest canopies where the length scale is on the order of the canopy height. The implication is that the thrust force on individual turbines within a wind farm may vary for many rows downwind of the first row and strongly depends on wind farm configuration. This was the first comprehensive study to experimentally examine wind farm turbulence in such detail, which fills an important gap in our knowledge about how wind farm flows behave and provides valuable information from which to improve wind farm parameterizations. The data are also useful for validation of existing parameterizations.

Additionally, key differences in the three-dimensional flow field indicate the momentum absorption and therefore energy generation characteristics are very different in the two wind farms. The main differences found between aligned and staggered wind-farm flows are summarized as follows:

1. The staggered wind farm turbines operate with higher angular velocity than those in the aligned wind farm. This leads to a greater overall power generation potential in the staggered wind farm.

2. The mean velocity profiles exhibit strong wake regions behind wind turbines. The velocity deficit is greater within the staggered wind farm due to more efficient absorption of momentum.

3. The turbulence intensity is greatest around the top tip region for both wind farms.

The peak turbulence intensity is greater within the aligned farm. Available empirical models to estimate added turbulence are sensitive to estimates of C_T and cannot account for different wind farm configurations.

4. The velocity spectral signature of tip vortices behind turbines is stronger in the staggered wind farm than in the aligned farm. However, due to the larger distance to successive downwind turbines, allowing greater dissipation of coherent structures, turbines experience lower turbulence-induced fatigue loads in the staggered configuration.

5. The wake growth over the wind farms can be modeled using a logistic growth model. The wake growth rate is initially faster over turbines in the aligned farm, however the overall wake growth rate is greater over the staggered wind farm due to increased momentum absorption and turbulence production.

6. The spanwise-averaged mean velocity profiles of the quasi-developed wind-farm flow exhibit an inflection point instability, commonly seen in canopy flows. The staggered wind-farm flow has lower mean velocity within and just above the wind farm caused by greater momentum absorption compared to the aligned farm case.

7. The effective roughness of the staggered wind farm is 1.7 times greater than that of the aligned wind farm. The staggered wind farm exhibits a significant zero-plane displacement, whereas there is only a small displacement for the aligned case. The log-layer region, exhibited by a region of linear mixing length is limited to a region near the top of the wind farms, which is approximately 20% of the total wind farm height.

8. Similar turbulence intensity and shear stress profiles are found for the two configurations, with significantly larger dispersive stresses measured in the aligned wind farm, $\sim 40\% u_*^2$, compared to the staggered wind farm, $\sim 10\% u_*^2$. The friction velocity is 30% greater for the staggered wind farm compared to the aligned farm.

9. Profiles of kinematic heat flux indicate a reduction of surface scalar (heat) flux within wind farms compared to a flat boundary layer without wind turbines, for the studied wind farm density. A greater reduction was measured in the staggered wind farm.

10. The turbulent correlation coefficient and Prandtl number profiles follow similar trends between the two wind farm configurations, with levels near the top tip height compatible to those found near the top of canopies.

11. Compared to a flat boundary layer where shear production is balanced by dissipation, the TKE budget involves a number of significant terms in the wind-farm flows, including shear production, vertical turbulent transport, wake production and pressure transport, which are similar to that of canopy-type flows. The wake production and vertical transport terms are particularly significant, especially for the aligned farm. Buoyancy production is negligible for both wind farms.

12. The thrust coefficient is approximately two to three times greater in the staggered wind farm compared to the aligned wind farm, revealing that wind farms with the same turbines and the same turbine distribution density but different configurations exhibit different aerodynamic loading characteristics due to varying wake interaction causing variation in sheltering of downwind turbines.

13. The added roughness models exhibit a wide range of estimates and do not account for turbine array configuration. The more complex model of Calaf et al. [4] provided the closest estimate for the aligned farm, while that of Frandsen et al. [13] provided the best estimates for the staggered configuration.

This study provides new insights into the effects of wind-farm configuration on turbulent flow and transport of momentum and scalars in wind farms. It also provides detailed data for validating and motivating the development of improved models for the turbulent momentum and heat fluxes, and the turbine-induced forces in numerical models of wind farms (e.g., computational fluid dynamics models such as LES). Measurement strategies presented here provide useful knowledge about the minimally required data that must be gathered, which can prove useful in planning field campaigns where often a limited number of sampling stations are available. Future work will include model validation as well as further investigation and analysis of scalar transport in wind farms. Understanding the effects of wind farms on surface fluxes is important and new studies are currently underway with detailed surface flux information to better understand the sign and distribution of heat flux changes after the installation of a

wind farm. Further investigation of wind farms with varying turbine density and configuration are required to develop models to predict C_T, which is a critical parameter in course-resolution weather and climate models. Characterizing lateral wake interaction is important for predicting power production as well as total turbulence intensity within the developing flow of a wind farm. Work to better characterize the scales of interaction will be important and help fill a critical need for improved models to predict turbulence intensity, which take into account turbine density and wind farm configurations.

Chapter 3

Effect of Large Wind Farms on Surface Scalar Flux[†]

[†] **This chapter was published as Zhang W, CD Markfort and F Porté-Agel. 2013. Experimental study of the impact of large-scale wind farms on land-atmosphere exchanges. *Environmental Research Letters*. 8(1) 015002 doi:10.1088/1748-9326/8/1/015002**

3.1 Abstract

Large-scale wind farms, covering a significant portion of the land and ocean surface, may affect the transport of momentum, heat, mass and moisture between the atmosphere and the land locally and globally. To understand the wind-farm atmosphere interaction, we conducted wind-tunnel experiments to study the surface scalar (heat) flux using model wind farms, consisting of more than ten rows of wind turbines – having a typical streamwise and spanwise spacings of five and four rotor diameters – in a neutral boundary layer with a heated surface. Spatial distribution of the surface heat flux was mapped with an array of surface heat flux sensors far within the quasi-developed regime of the wind-farm flow. Although the overall surface heat flux change produced by the wind farms is found to be small, with a net reduction of 4% for the staggered wind farm and nearly zero change for the aligned wind farm, the highly heterogeneous spatial distribution of the surface heat flux, dependent on wind farm layout, is significant. The difference between the minimum and maximum surface heat flux can be up to 12% and 7% in the aligned and staggered wind farm, respectively. This finding is important for planning intensive agriculture practice and optimizing farm land use strategy regarding wind energy project development. The well-controlled wind-tunnel experiments presented in this study also provides a first comprehensive dataset on turbulent flow and scalar transport in wind farms, which can be further used to develop and validate new parameterizations of surface scalar fluxes in numerical models.

Keywords

Surface heat flux; Turbulence; Wind farm-atmosphere interaction; Wind-tunnel experiment

3.2 Introduction

As global wind power capacity is growing exponentially, it is foreseen that many more large-scale wind farms will be built onshore and offshore. It is of great interest to understand how they may affect the transport of momentum, heat, moisture and trace gases (e.g. CO_2) between the land surface and the atmosphere, and possible subsequent environmental impacts in terms of long-term sustainability of wind power (Baidya Roy [77]). Some of the best wind resources in the U.S., for example, are over farmland, especially in the central plains (Gunturu and Schlosser [78]). In these regions, near-surface momentum, heat and moisture transport can be very important because changes in surface meteorological conditions (e.g., the near-surface wind speed, daily maximum and minimum temperatures, surface sensible and latent heat flux) affected by wind farms, may impact local agricultural practices. In some cases, the impact may be beneficial. For example, a field experimental campaign on wind-turbine wake effects on crops in central Iowa found that the wind turbine cools the near-surface air in the summer, which helps crops to thrive (Crop/Wind-Energy Experiment or CWEX, see Rajewski et al. [79]). However, potential drying and increased irrigation requirement may not be a favorable effect.

Modelling studies of the influence of utility-scale wind farms on regional and global climate have shown that the impacts maybe substantial (Ivanova and Nadyozhina [80], Baidya Roy et al. [81], Keith et al. [23], Baidya Roy and Traiteur [25], Barrie and Kirk-Davidoff [24], Baidya Roy [77], Wang and Prinn [82], Fitch et al. [83] and Zhou et al. [84]). For instance, Baidya Roy [77] found that wind farms significantly affected near-surface air temperature and humidity as well as surface sensible and latent heat fluxes. The signs of the impacts (i.e., increase or decrease), are reported to depend on static stability and total water mixing ratio lapse rates of the atmosphere. Recent high-resolution large-eddy simulations (LES) studies are able to resolve detailed fluid dynamics and heat transport within and over wind farms as well as near the land surface (Calaf et al. [4], Calaf et al. [69], Lu and Porté-Agel [14], Porté-Agel et al. [5], Wu and Porté-Agel [28]). Lu and Porté-Agel [14] reported that the surface momentum and heat fluxes in a very large wind farm underwent substantial reduction of more than 30% and 15% respectively, relative to that of the stable boundary layer flow without wind

turbines. In contrast, Calaf et al. [69] found surface heat flux increased by 10-15% and a reduction of the momentum flux, from their LES study of wind-farm flows subjected to a neutral boundary layer with temperature as a passive scalar. It is not clear what key factors lead to the different results of the surface heat flux change.

So far most studies on near-surface temperature and fluxes altered by large-scale wind farms have been carried out by numerical simulations. In fact, rarely are these studies validated against observational evidence (Baidya Roy and Traiteur 2010). The computational results are dependent on the accuracy of the models employed and the realism of the methods applied to parameterize wind turbines (e.g., Barrie and Kirk-Davidoff [24],, Wang and Prinn [82]). In particular, the validity of representing the impacts of wind turbine arrays on momentum transport by the widely-applied added roughness length models needs further study, evidenced by Markfort et al. [7]. Therefore, new observations in the field and laboratory are in high demand to advance our understanding of turbulent wakes and scalar transport in wind farms and for numerical model development.

There are few laboratory studies or field observations on land-atmospheric scalar or heat transport in wind farms. Though field observation is generally preferred, point-based measurements of heat, water vapour and CO_2 fluxes are very challenging to interpret due to flow non-stationarities as well as turbulence heterogeneity around turbines. Wind-tunnel simulations have proved to be very valuable to study the turbulent wake characteristics and momentum/heat transport in scaled-down wind farms (e.g., Cal et al. [29], Chamorro and Porté-Agel [17], Chamorro et al. [36], Markfort et al.[7]). High spatial and temporal resolution data taken under well-controlled conditions not only provide the full picture of turbulent flow and flux characteristics but contain sufficient details to validate numerical models.

The goal of this study is to acquire direct measurements of the spatial distribution of the surface heat flux altered by large-scale wind farms, as well as the turbulent flow and flux characteristics near the surface in a thermally-controlled wind tunnel. This work will advance our understanding of turbulent transport and surface scalar (heat) flux within a large-scale wind farm, provide comprehensive datasets for validating numerical models and improve planning and interpretation of field observations.

3.3 Facilities, Models and Measurements

Experiments were carried out in the closed-loop thermally-controlled boundary-layer wind tunnel at the Saint Anthony Falls Laboratory, University of Minnesota. The main test section for boundary-layer flow studies has a length of 16 m and a cross-section of 1.7×1.7 m^2. The facility is able to achieve desired thermal stratification conditions by controlling the air and the floor temperature independently in the range of 5 °C to 80 °C $\pm$ 0.25 °C. To generate a deep turbulent boundary layer with the depth (δ) of 0.5 m, a tripping mechanism (40-mm picket fence) was used at the entrance of the test section. Primary characteristics of the simulated turbulent boundary layer with a surface heat source are summarized in Table 3.1. With the freestream wind speed (U_∞) set at 3.2 m s^{-1}, the resulting bulk Richardson number Ri_b is – 0.09 and the Obukhov length L is about 0.4 m. Though the floor was heated to 72 °C, the enhanced buoyancy effect is negligible due to the shear and additional turbulence generated by wakes within the wind farms. It follows that the heat source at the surface does not affect the dynamics of the flow within the wind farms, thus heat is treated as a passive scalar (Markfort et al. [7]).

Table 3.1: Characteristics of the turbulent boundary layer with a surface heat source.

Floor θ_s (°C)	Air θ_0 (°C)	Roughness z_0 (mm)	Friction vel. u_* (m s^{-1})	Re_δ (= $U_\infty \delta/\nu$)	Ri_b	δ/L
72	12	0.08	0.12	1 x 10^5	– 0.09	– 1.25

The model wind farms were composed of miniature model wind turbines, which were employed in previous wind-turbine wake studies (e.g., Chamorro et al. [36], Markfort et al. [7] , Zhang et al. [32], Zhang et al. [34]). The rotor diameter d is 0.128 m and the hub height is 0.104 m, with the bottom tip of the turbine at a height of 0.04 m and the top tip at 0.168 m high. The rotor swept area of the turbines is within the lowest 1/3 of the turbulent boundary layer, ensuring geometric similarity with field-scale wind farms. Two idealized wind farm layouts, perfectly aligned and staggered wind farms were studied, as illustrated in Figure 3.1. In both wind farms, the rotor plane of each wind turbine is perpendicular to the main direction of the flow. The turbines rotate in

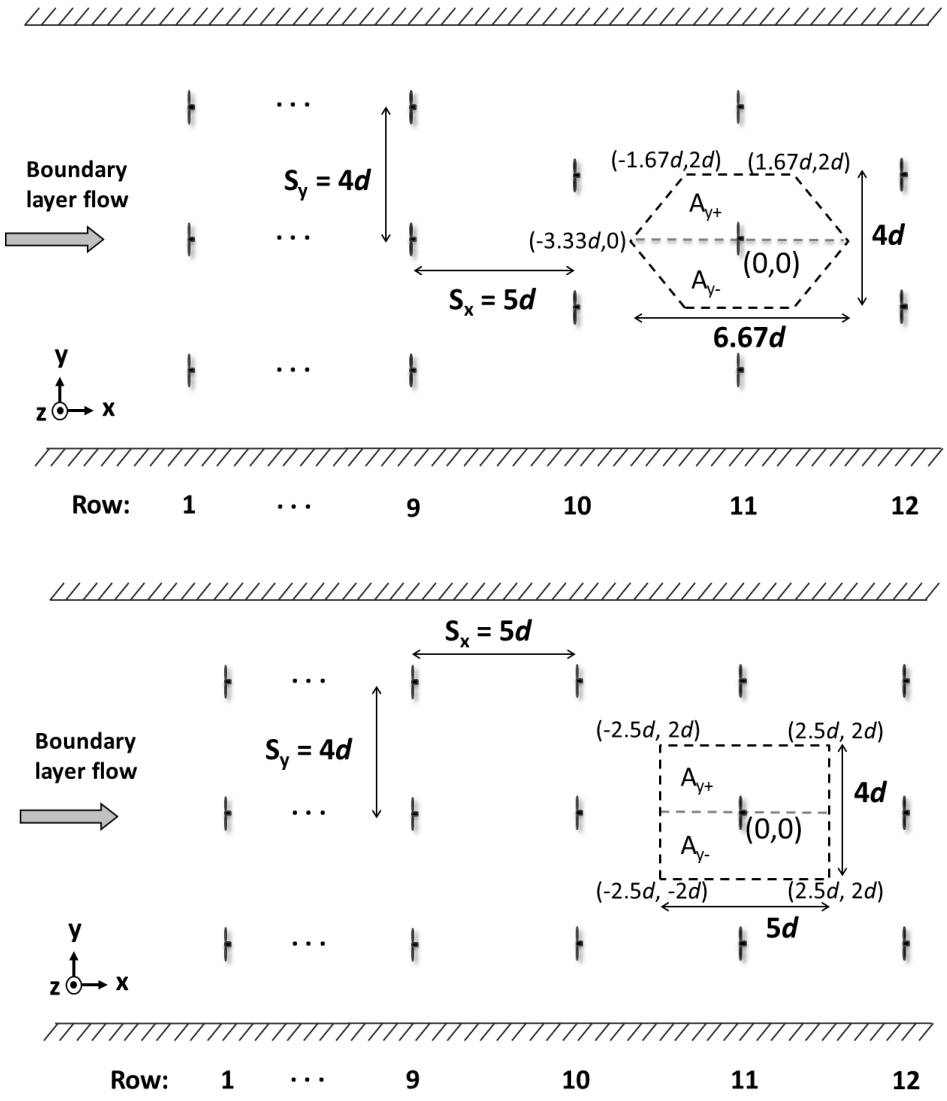

Figure 3.1: Schematic diagram of the tributary area to a single turbine in the staggered (upper) and aligned (bottom) wind farms.

a counter-clockwise manner, inducing the clockwise rotation of the wake when looking downwind. The aligned farm consists of a wind turbine array of 12 rows and 3 columns, with a typical streamwise spacing of $5d$ and the spanwise spacing of $4d$. The staggered wind farm has the same arrangement in the odd-numbered rows as the aligned farm, while two turbines in the even-numbered rows are shifted by $2d$ in the spanwise direction. It is noted that the top-tip height of a turbine or the wind farm height $Z_H(= 1.3d)$ was found to be a key length scale to characterize the turbulent flow and thus being used to normalize the height above the surface [7].

The right-handed Cartesian coordinate system is defined in Figures 3.1 and 3.2. Similar coordinate definition was used in Calaf et al. [69], Markfort et al. [7] and Wu and Porté-Agel [67]. As the spatial distribution and change of surface heat flux in an effective unit area (A) is of particular interest, we set the origin at the center of A, where the target turbine is located. It is important to note that the distributed wind turbine density is the same for both wind farm layouts, with A of $20d^2$ per wind turbine. For the convenience of discussion, A is further divided into specific sub-areas: the near wake region A_{NW} (x/d = [0, 1], y/d = [– 0.22, 0.22]), the downwelling side of the wake A_{y-} (y/d = [– 2, 0]) and the upwelling side of the wake A_{y+} (y/d = [0, 2]). The limit of x/d varies between –3.33 and 3.33 depending on y/d in A_{y-} and A_{y+} for the staggered farm, while it is constant (= [– 2.5, 2.5]) in A_{y-} and A_{y+} for the aligned farm.

Measurements of the surface heat flux were made using flat-plate type heat flux sensors (Captec, Inc.). The thin-foil heat flux sensor consists of a thermoelectric panel laminated between flexible heterogeneous plastic layers. Each heat flux sensor is 0.01 m by 0.01 m, with a thickness of 0.4 mm to minimize flow disturbance caused by mounting them on the surface. A silicone-based heat sink compound was used to ensure good contact between the sensor and the surface. The heat transfer sensitivity of the sensor is 0.6 μV/(W/m^2) and the response time is 0.3 s. Heat flux was calculated by dividing the voltage output, which is proportional to the heat flux through the sensor, by the sensor sensitivity. An array of 19 sensors was mounted to cover the spanwise distance from y/d = [– 2, 2], with an even spacing (Δy) of $0.22d$. Measurements in the streamwise direction were conducted by shifting the entire wind farms multiple times by $\Delta x = 0.5d$ to cover A. Data were recorded every 5 seconds for 20-30 minutes to ensure the convergence of measurements. High-frequency triple-wire (combination of a

x-wire and a cold-wire) anemometer was used to measure vertical profiles of velocity and temperature at selected locations within the wind farm, to understand the vertical momentum and heat transport near the surface. Detailed measurements of the turbulent flow within the same wind farms can be found in Markfort et al. [7].

Once the spatial distribution of heat flux q_s (the surface heat flux at each measured node) is acquired, the overall surface heat flux Q_s is calculated by

$$Q_s = \frac{1}{A} \int q_s dA. \tag{3.1}$$

High-frequency triple-wire (combination of a x-wire and a cold-wire) anemometer was used to measure vertical profiles of velocity and temperature at selected locations within the wind farm, to understand the vertical momentum and heat transport near the surface. Detailed measurements of the turbulent flow within the same wind farms can be found in Markfort et al. [7].

3.4 One-Dimensional Energy Balance Analysis

For a very large wind farm with a length approaching or exceeding the height of the atmospheric boundary layer on flat terrain by a factor of 10 or more, a fully-developed flow regime may ultimately appear and wind-farm flows are expected to display an asymptotic behaviour (Meneveau [15]). It means that horizontally averaged flow quantities can be assumed to vary only as a function of height above the surface. Here we estimate the surface heat flux change induced by such large-scale wind farms from the viewpoint of vertical energy balance. This one-dimensional (1-D) approach will be applied to the wind farm flow to understand the effects of wind farms on surface heat flux, considering that the model wind farm employed in this study allows the flow to reach a quasi-developed state with minimal entrance and side-edge effects at the measurement location.

The change in the internal energy of a system (ΔE) is equal to the sum of the heat added to the system (the balance of various sources of fluxes, ΔQ) and the work (ΔW) done by or on the system. A control volume (C.V.) around a wind turbine is defined for the fully-developed flow regime, as shown in Figure 3.2. The bottom is the ground surface with a fixed temperature $\theta_s = 72^{\circ}C$, and the top is at the thermal boundary layer

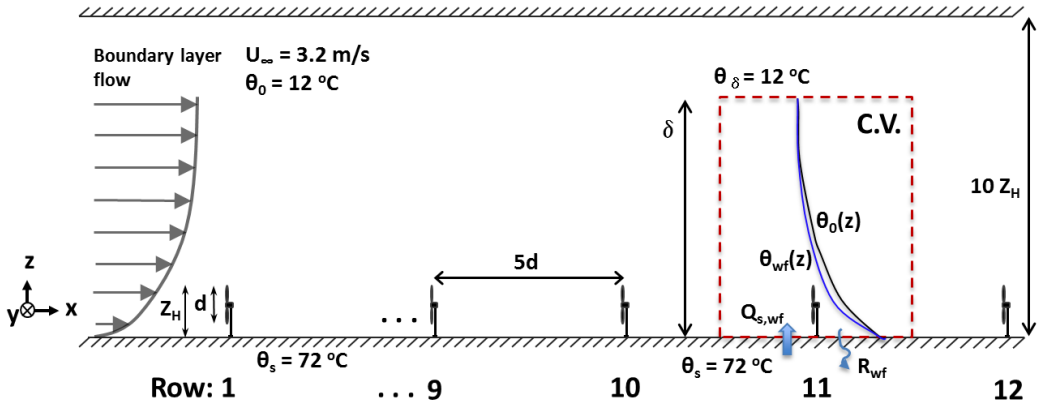

Figure 3.2: Schematic diagram of the vertical energy budget analysis in a control volume around a wind turbine for the fully-developed wind-farm flow regime.

height (δ_θ) with $\theta_\delta = 12°C$. The net heat flux is zero due to the negligible temperature gradient at the top of the control volume. Also, there is no net flux at the upwind and downwind boundaries between wind turbine rows since the flow is at equilibrium. On the surface there is a heat source Q and heat loss from radiation R. Accordingly, the energy budget of the control volume for a unit time is written as follows:

$$\Delta E = \Delta Q + \Delta W. \tag{3.2}$$

in this case ΔW is negligible, and

$$\Delta Q = Q_{s,wf} - R_{wf} - (Q_{s0} - R_0), \tag{3.3}$$

where subscripts "$_0$" and "$_{wf}$" indicate the boundary-layer flow case and the wind farm case, respectively. R_0, R_{wf} are estimated to be less than 0.2% of the internal energy due to the fact that the wind-tunnel floor is a polished aluminum surface. It follows that

$$\Delta Q = Q_{s,wf} - Q_{s0} = \rho C_p \int_0^{\delta_\theta} (\theta_{wf}(z) - \theta_0(z))\, \mathrm{d}z, \tag{3.4}$$

where ρ and C_p are air density and specific heat capacity. This equation indicates that the change in surface heat flux can be approximated by the change in the internal energy of the flow due to the presence of the wind farms.

3.5 Results and Discussion

Spatial distribution of the surface heat flux will be presented for both staggered and aligned wind farms, and representative vertical profiles of turbulent flow and fluxes averaged over several spanwise locations in the quasi-developed flow regime will be shown to aid interpretation of these results. As found by Markfort et al. [7] and Wu and Porté-Agel [67], the lateral turbulent mixing within wind turbine arrays is more efficient in the staggered layout than in the aligned layout. This suggests that spanwise-averaged vertical profiles would better represent the wind-farm flow characteristics for the staggered wind farm than the aligned farm case. Therefore we will focus on the staggered wind farm case by examining both the surface heat flux distribution and vertical profiles of the turbulent flow and fluxes near the surface. Afterwards, we will present and discuss the surface heat flux distribution pattern induced by the aligned farm. Also, it should be noted that the net change in surface heat flux, affected by wind farms, is relative to that of the boundary-layer flow without a wind farm.

3.5.1 Staggered wind-farm case

Spatial distribution of the surface heat flux (q_s) for a unit area in the staggered wind farm, relative to that of the boundary-layer flow without wind turbines (q_{s0}), is shown in Figure 3.3. The surface heat flux is increased by about 24% in the sub-area A_{NW} near the base of the wind turbine due to the locally enhanced turbulent mixing. However, it should be noted that increased surface heat flux is limited to the region adjacent to the wind turbine. Outside this region, there is a relatively uniform distribution of decreased surface heat flux. As we shall see later, the pattern of surface heat flux distribution is associated with multiple wake interaction near the surface in the wind farms. To quantify the net change of the surface heat flux, we summarize the surface heat flux aggregated in specific sub-areas in Table 3.2. The data show an overall surface heat flux reduction of approximate 4% in the staggered wind farm compared to that of the

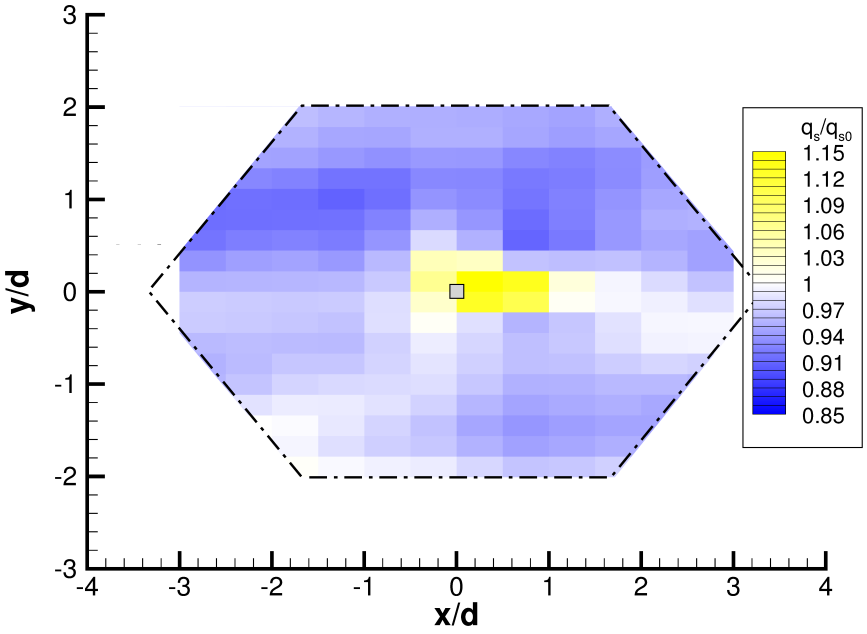

Figure 3.3: Spatial distribution of the mean surface heat flux in an unit area of the staggered wind farm.

boundary-layer flow, with higher values (by 3%) in sub-area A_{y-}, compared with those of A_{y+}. Results of the aligned farm case are also included here and will be discussed in Section 3.5.2.

Figure 3.4(a) shows the spanwise-averaged kinematic heat flux ($\langle Q \rangle_y$) as a function of the height above the surface in the staggered farm case. One can see that the presence of the wind farm strongly affects the turbulent heat flux profile over and through the wind farm. The kinematic heat flux $\langle Q \rangle_y$ displays a higher magnitude, than that in the boundary layer flow without turbines, for $z > Z_H$. However, near the surface $\langle Q \rangle_y$ has a lower magnitude than Q_{s0}. This result is qualitatively consistent with the direct surface heat flux measurements. Calaf et al. [69] obtained near-linear scalar flux profiles, which is different from the complex behavior of the kinematic heat flux observed in measurements here. Their results indicate that the surface heat flux increased by 10-15% in the presence of large-scale wind farms compared to the boundary-layer flow.

Table 3.2: Q_s/Q_{s0} in specific sub-areas of an effective unit area A in the staggered and aligned wind farms.

Wind farm layout	A_{y-} $y/d = [-2, 0]$	A_{y+} $y/d = [0, 2]$	A_{NW} $y/d = [-0.22, 0.22]$, $x/d = (0 - 1]$	Net effect
Staggered	0.972	0.943	1.240	0.962
Aligned	1.033	0.969	1.195	1.0

The change in near-surface air temperature induced by the presence of the wind farms is directly related to the surface heat flux change, and is also an important input of the 1-D energy balance analysis. Figure 3.4(b) shows the comparison of spanwise-averaged temperature profiles with and without the wind farm. Above Z_H, temperature profiles are quite similar for both cases. However, below $0.6Z_H$ the air temperature becomes less in the staggered wind farm than that in the boundary-layer flow. Approaching the surface, the decrease of air temperature in the wind farm becomes larger, about $3°C$ at $z/Z_H = 0.06$. The reduced near-surface air temperature in the presence of the wind farm was also observed from previous field studies, though under statically unstable conditions. Using data collected from a meteorological field campaign at San Gorgonio, Baidya Roy and Taiteur [25] found that the near-surface temperature in the wake downwind of the wind farms was reduced during the day. Furthermore, they related the increased near-surface air temperature gradient to more efficient heat transport from the ground surface to the atmosphere, and subsequently increased surface heat flux (Baidya Roy [77]). However, this reasoning assumes the flux-gradient relationship with a constant effective diffusivity of heat K_H $(= \frac{\overline{w'\theta'}}{\partial\theta/\partial z})$ for the flow near the surface with and without wind farms. In fact, in turbulent wind-farm flows K_H is highly dependent on the flow structure which is hard to know *a priori*. Indeed, as shown by Lu and Porté-Agel [14], the vertical distribution of K_H is quite different in wind farm cases compared to that in the boundary-layer flow. This is also supported by the measured turbulent Prandtl number (Pr_t) profiles (Fig. 17b) in our experiments, discussed in detail by Markfort et al. [7]. Hence, it is problematic to assume a constant K_H near the surface and attribute the enhanced surface heat flux to increased

near-surface temperature gradient.

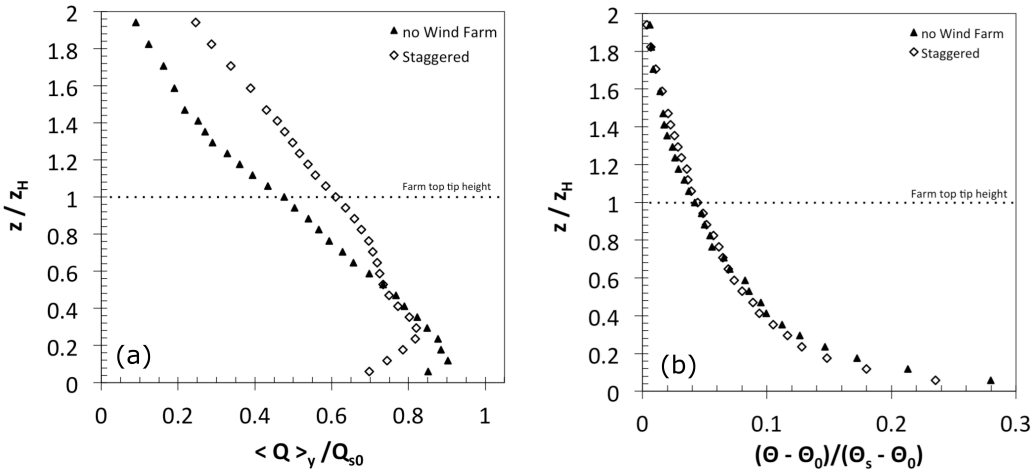

Figure 3.4: Vertical profiles of the spanwise-averaged kinematic heat flux and air temperature in the staggered wind farm, compared to that in the boundary-layer flow.

Instead, if we consider the standard surface-layer scaling which assumes that the surface heat flux Q_s can be expressed as the product of a temperature scale θ_* and a velocity scale u_*, it has been found that the wind-farm induced change in these two scales has an opposite trend. While the increased temperature gradients near the surface lead to an increase in θ_*, the decreased shear stress and reduced velocity result in a reduced u_* compared to the boundary-layer flow (Calaf et al. [69], Lu and Porté-Agel [14], Markfort et al. [7]). Whether the surface heat flux is altered by the presence of the wind farms, and if so, the sign (e.g., increase or decrease) is dependent on the competing effects of the magnitude of increased temperature scale θ_* and reduced velocity scale u_*. Unfortunately we are not able to determine the magnitude of u_* from the current data because there is no evident near-surface logarithmic layer detected within the wind farm.

Using the air temperature profile with the 1-D energy budget was analyzed based on the profiles of air temperature and it was estimated that $Q_{s,wf}/Q_{so}$ is approximately 0.97 for the staggered wind farm case. This result corroborates the overall reduction of the surface heat flux directly measured with surface heat flux sensors. The relationship

(in Eqn. (3.4)) clearly shows that the surface heat flux is reduced if the air temperature affected by the presence of the wind farms is lower than that of the boundary-layer case.

In addition, the turbulent linear correlation coefficient can be used as a measure of the overall efficiency of turbulent transfer mechanism in complex turbulent flows (Roth and Oke [85]). Specifically, $r_{w\theta} = \frac{\overline{w'\theta'}}{\sigma_w \sigma_\theta}$ is an indicator of the overall heat transfer efficiency. A value of unity means the efficiency of heat transfer is optimal. The variation of $r_{w\theta}$ with height in the staggered wind farm case, in Figure 3.5, shows the relative efficiency between the wind-farm and the boundary-layer flows.

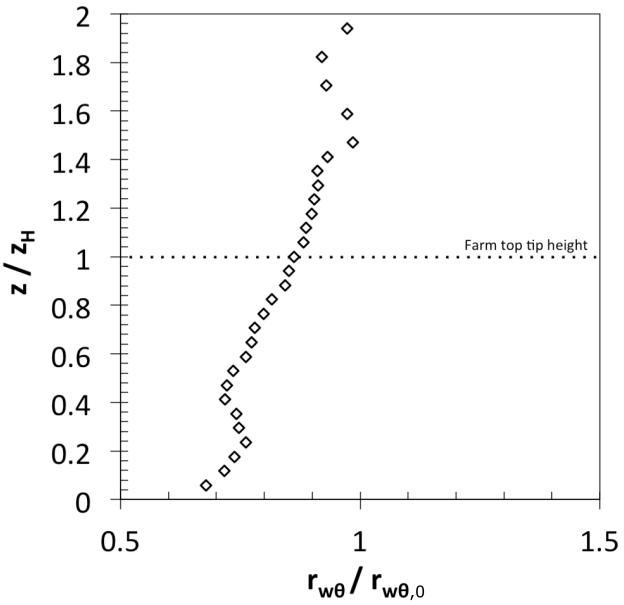

Figure 3.5: Vertical profile of the heat transfer efficiency in the staggered wind farm, compared to that of the boundary-layer flow.

Above Z_H the heat transfer efficiency $r_{w\theta}$ of the wind farm case is comparable to that of the boundary-layer flow. Within the wind farm, however, $r_{w\theta}$ generally decreases with decreasing height above the surface. As approaching the surface, the heat transfer efficiency $r_{w\theta}$ of the staggered wind farm is about 70% of that of the boundary-layer flow. This result indicates that the increased turbulence and heat transport above the wind farm do not necessarily translate into higher surface heat flux at the ground.

3.5.2 Aligned wind-farm case

Wind farm configuration has been found to appreciably affect the momentum and heat transport within and above the wind farm (Markfort et al. [7]). Here we present the surface heat flux distribution of an unit area in a perfectly aligned farm case (Figure 3.6). Similar to the staggered wind farm case, the surface heat flux is increased by about 20% near the base of the wind turbine in the sub-area A_{NW}. Outside this region, the surface heat flux displays an interesting pattern, very different from the relatively uniform distribution of reduced heat flux in the staggered wind farm. The change of the surface heat flux displays a distinct opposite trend on either side of the column of turbines, with increased heat flux in A_{y-} and reduced heat flux in A_{y+}. A similar magnitude of increased and decreased heat flux on the two sides results in nearly a zero net change in the surface heat flux. The difference between the maximum and minimum surface heat flux is about 12% of Q_{s0} in the aligned wind farm and 7% of Q_{s0} (with the minimum being $0.92Q_{s0}$) in the staggered farm. The results indicate that the spatial distribution of surface heat flux is noticeably heterogeneous for both cases, though heat flux displays a relatively uniform distribution in the staggered wind farm.

Multiple-wake interaction and the wake boundary-layer flow interaction are the dominant mechanisms of momentum and heat transport in large-scale wind-farms (see Vermeer et al. [56], Frandsen et al. [13] and Frandsen et al. [27]). The spatial distribution of the surface scalar flux is particularly affected by the complicated wake interactions. The distinct regions of increased versus decreased surface heat flux, with respect to the turbine column in the aligned farm case, are correlated with the wake evolution and wake rotation in the turbine array. Within large-scale wind farms, flow under the effects of multiple-wake interaction can be classified into several regimes (Frandsen et al. [13]): The individual wake behind the first-row of wind turbines (regime I); multiple wakes evolving from a single column of turbines (regime II); wake merging from neighboring turbine columns (regime III); and finally sufficiently mixed wake flow reaching a fully-developed state. According to this division of the wake regimes, it is conjectured that the aligned farm case is subjected to an overlapping coherent wake column – formed primarily from the single column of turbines, i.e. regime III– rotating in a clockwise manner when looking downwind. Subsequently, increased surface heat flux occurs in

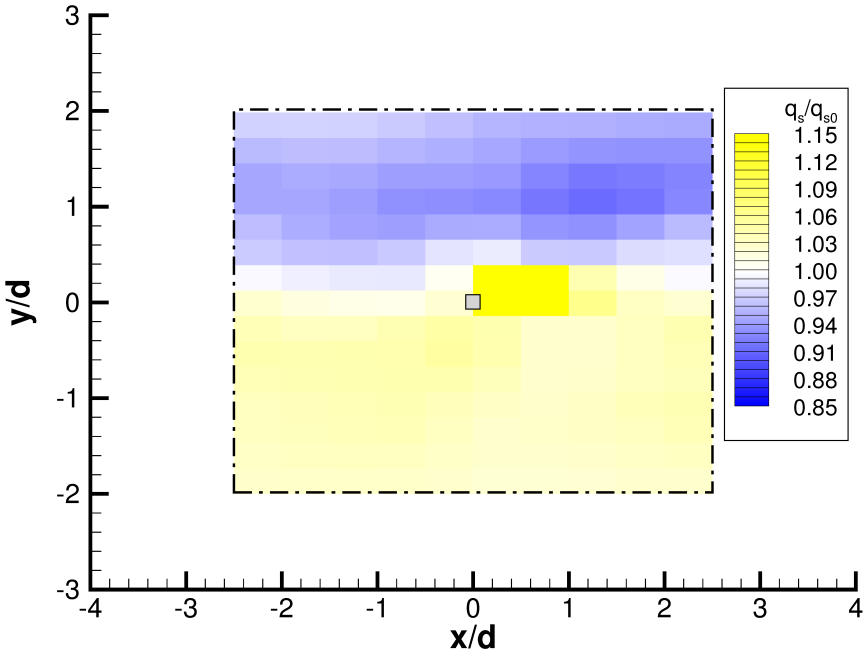

Figure 3.6: Spatial distribution of the mean surface heat flux in a unit area of the aligned wind farm.

A_{y-} as cooler air is brought from above to the surface, while reduced heat flux is observed for the region of A_{y+} as warmer air moves upwards away from the surface. The difference in air temperature profiles, measured on the two sides of the wind-turbine column at $y/d = -1$ and 1 compared to the profile measured at the centerline, $y/d = 0$, show behavior that supports this argument (see Figure 3.8). Compared to what happens in the aligned wind farm, multiple wakes mix much more efficiently in the staggered wind farm, resulting in a relatively uniform distribution of the surface heat flux.

3.6 Summary and Conclusions

Wind-tunnel experiments were conducted to examine the effects of a large-scale wind farm with typical layout on the spatial distribution and net change of the surface heat flux, in a turbulent boundary layer with a surface heat source. For the case of a staggered

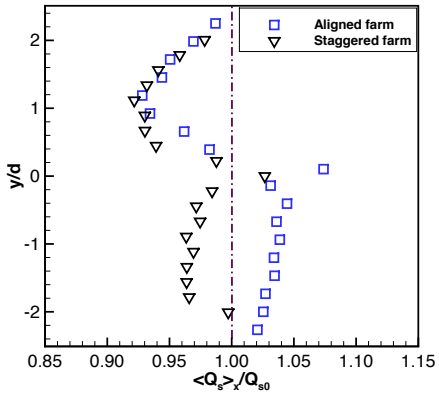

Figure 3.7: Surface heat flux integrated along the streamwise direction, as a function of the spanwise location in the aligned and staggered wind farms.

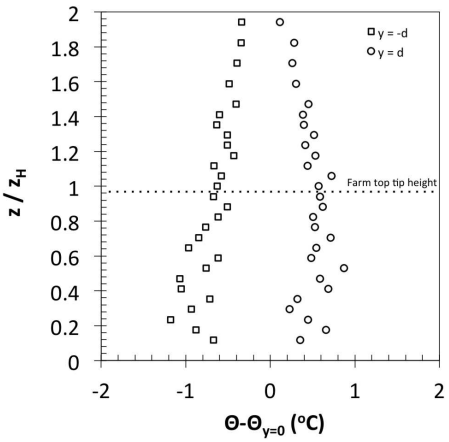

Figure 3.8: Vertical profiles of the difference in mean temperature at $y/d = -1$ and 1 compared to at $y/d = 0$ in the aligned wind farm.

wind farm, except for an increase in the near-wake region of the turbine, the surface heat flux exhibits a relatively uniform distribution and an overall reduction of approximately 4% with respect to the boundary-layer flow without wind turbines. In the aligned farm, two distinctive regions of increased and decreased surface heat flux on either side of turbine columns were identified. The decreased flux on the upwelling side has a similar magnitude as the increased flux on the downwelling side, resulting in a nearly zero net change in the overall surface heat flux. However, the difference between the minimum and maximum surface heat flux is about 12% and 7% in the aligned and staggered wind farm, respectively.

Vertical profiles of near-surface temperature, kinematic heat flux and heat transport efficiency, measured in the quasi-developed flow regime, show evidence supportive of the surface heat flux change in the staggered wind farm. It is found that the turbulent momentum and heat transport near the surface is very different from that above the wind farm; higher turbulence and increased heat flux above does not necessarily translate to higher surface heat flux in a wind farm. In addition, a 1-D energy balance is presented to explain the surface heat flux change in terms of internal energy change in the flow due to the presence of a wind farm.

This work provides the first direct measurements of surface heat flux distribution

in well-controlled conditions. Though the overall surface heat flux change induced by wind farms is small, the highly heterogeneous spatial distribution of the surface heat flux, dependent on the wind farm layouts, is significant. These findings are important, in particular when considering collocation of wind farms with intensive agriculture practice, as the change in surface heat flux due to wind farms may affect irrigation requirement and crop yields. Future experiments are planned to conduct similar measurements with varying wind turbine distribution and configuration under different thermal stratification conditions.

Additionally, attribution of the well-marked surface heat flux distribution to the coherent rotating wake column in the aligned farm suggests that it is essential to simulate the wake rotation effects in numerical models of wind-farm flows in order to reproduce the spatial distribution of the surface heat flux. Without simulating the wake rotation effects, turbulent mixing might be underestimated in the wake, resulting in incorrectly simulated momentum and heat transport near the surface. Parameterization of wind turbines using the actuator line model (ALM) and actuator disk with rotation model (AMD-R) in LES studies by Porté-Agel et al. [5] and Wu and Porté-Agel [28] has demonstrated promising capability to reproduce important turbulent wake features in wind farms, such as the helicoidal tip vortices, enhanced turbulence level near the top-tip height and wake rotation. Further investigation of surface fluxes within large wind farms using our LES framework is planned for different wind-farm layouts and turbine spacing.

Chapter 4

New Canopy-type Model for Wind Farm-Atmosphere Interaction[†]

[†] **This chapter was published as Markfort CD, W Zhang and F Porté-Agel. 2013. A canopy-type model for wind farm-atmosphere interaction. Proceedings of the 2013 International Conference on Aerodynamics of Offshore Wind Energy Systems and Wakes. DTU, Copenhagen, Denmark. Manuscript invited for submission for inclusion in the special issue, "Wind Energy" in Renewable Energy.**

4.1 Abstract

We present a new model for the interactions between large-scale wind farms and the atmospheric boundary layer (ABL) based on similarity to canopy flows. Wind farms capture momentum from the atmospheric boundary layer both at the leading edge and from above. Based on recent findings that turbulent flow in and above wind farms is similar to canopy-type flows, we examine this further with an analytical model that can predict the development length of the wind farm flow as well as vertical momentum absorption. Within the region of flow development, momentum is advected into the wind farm and wake turbulence draws excess momentum in from between turbines. This is characterized by large dispersive fluxes of momentum. Once the flow within the farm is developed, the area-averaged velocity profile exhibits an inflection point, characteristic of canopy-type flows. The inflected velocity profile is associated with the presence of a dominant characteristic turbulence scale, which may be responsible for a significant portion of the vertical momentum flux. Prediction of this scale is useful for determining the amount of available power for harvesting. The new model is tested with results from wind tunnel experiments, which characterize the turbulent flow in and above a model wind farms. The model is useful for representing wind farms in regional scale meteorological and wind resource assessment models, for the optimization of wind farms considering wind turbine spacing and layout, for assessing the impacts of upwind wind farms on nearby wind resources, and the environment.

Keywords Atmospheric boundary-layer (ABL); Wind farm-atmosphere model; Canopy turbulence; Analytical model

4.2 Introduction

The prediction of the mean flow in wind farms is important for determining the mean momentum sink from the atmospheric boundary layer (ABL). This is needed for new parameterizations for the ABL in weather and climate models to account for the increasing presence of wind farms globally. Additionally, optimization of wind farm layouts can be improved with an adequate model for describing how the wind farm harvests wind energy from the ABL. Finally, turbulence in the ABL mediates transport of moisture, pollutants and climate controlling trace gases (e.g. CO_2 and CH_4). Prediction of scalar transport from the surface requires prediction of the surface shear stress and transport efficiency at the ground surface below the wind farm rotor level. For offshore wind farms, the surface shear stress is an important parameter needed to model the surface-layer dynamics in the ocean.

A wind farm can be classified as a type of penetrable roughness, a term first introduced by Brutsaert [86]. Commonly referred to as canopies, this includes forests and built-up urban areas. In such flows the momentum sink is not simply a skin drag as is assumed in surface layer schemes for the ABL, but includes vertically distributed drag due to the turbines as well. Depending on the efficiency of the wind farm at absorbing momentum from the ABL, shear stress may or may not be applied at the ground or water surface. The ABL in regions of tall roughness elements has three characteristic layers: a roughness sublayer (RSL), an inertial layer where the log-law applies and an outer layer. The RSL for a dense canopy is generally about twice the thickness of the layer occupied by the roughness elements ($2Z_H$), the log-layer region where Monin-Obukhov similarity theory (MOST) is applicable, resides between the RSL and the outer layer, or between about $2Z_H$ and about 15% of the total ABL thickness. Generally the ABL thickness is approximately 1000 m, and the height of wind farms is approximately 100 m. Therefore the log-layer would generally exist below 150 m. In the case of a wind farm however, the RSL may be 100 – 200 m deep, based on the above scaling, and therefore it is likely that the log-layer does not consistently form over large wind farms. This may mean that the approach of modeling the wind farm, as surface roughness is not applicable, as the concept of aerodynamic roughness is based on the zero-crossing elevation of the log-law. For mesoscale models, often the first grid level resides in the log-layer of the ABL ($\sim$10

– 100 m) and using the roughness parameterization for the surface is common. However because the wind farm layer intersects this region, it becomes necessary to model the drag of the wind farm within the lowest layers to better represent the effect of the wind farm on the structure of the ABL (e.g. [83]).

Recently the turbulence statistics for fully developed flow in and over a wind-farm were analyzed and it was found that the properties of the flow including the transport efficiencies for momentum and scalars are more similar to those of canopy-type flows than that of a surface layer [7]. However, unlike dense canopies (e.g. a forest), due to the relatively large spacing between wind turbines, the flow exhibits features that are unique to sparse canopies, namely large contributions of dispersive stresses and significant wake production of TKE. Additionally we studied the impact of wind farms on surface heat flux and found a net reduction for a fully developed staggered wind farm [8]. From canopy-type flows we know there are two important characteristic length scales that can be used to characterize the interaction between canopies and the ABL. They include the canopy drag development length scale L_C and a shear length scale L_S ([44] and references therein). Figure 4.1 shows a schematic illustrating both length scales for an idealized wind farm canopy. L_c and L_s are the horizontal and vertical scales related to the absorption of momentum and are important quantities for understanding the overall efficiency of the wind farm. Both of these scales are derived from the dynamic interactions of the mean drag induced by the wind farm on the ABL flow. The vertically distributed drag in the RSL causes an inflected mean velocity profile, leading to the formation of Kelvin-Helmholtz type instability near the top of the wind farm. In order to determine these length scales we need a model for the mean wind profile through the wind farm.

Markfort et al. [7] found that the turbulent flow in wind farms is similar to that of canopy-type flows and the mean velocity across the rotor plane can be modeled using the classic model of Inoue [71]. We examine for the first time whether analytical canopy-type models can represent the turbulent flow within a fully developed wind farm. The assumptions of the models are examined, weaknesses investigated and improvements proposed. In Markfort et al. [7] we used the model from Inoue [71] to determine the thrust coefficient and estimate L_c based on the mean wind profiles. Here we compare

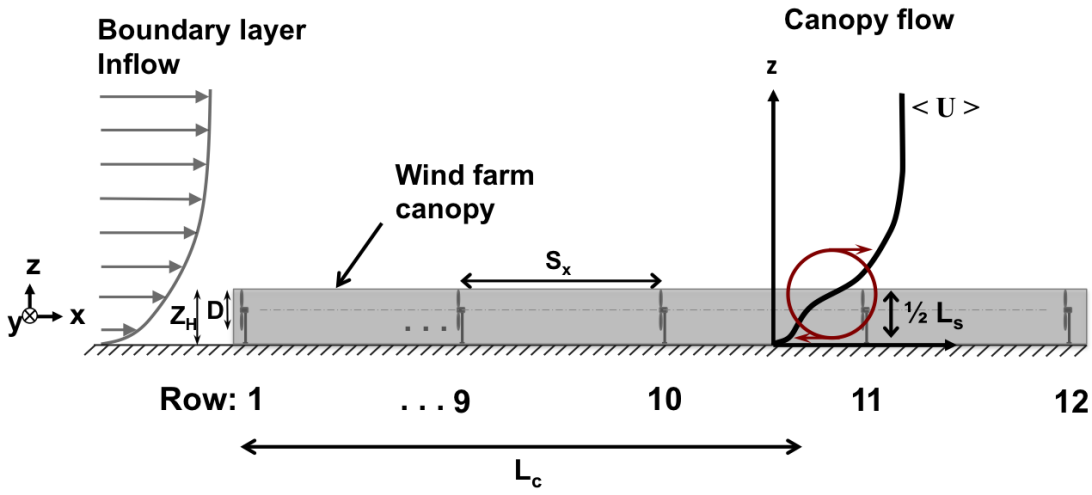

Figure 4.1: Schematic of a developing wind farm canopy-type flow. The distance required for the flow to develop L_c and the shear penetration L_s are directly related to the drag force on the canopy.

those results against results from the spatially averaged, time mean momentum equations often used to represent canopy-type flows. A new model for sparse canopies is considered that can reproduce the effects of the wind farm drag on the flow as well as predict the surface shear stress at the ground or sea surface. Ultimately the goal of this work is to improve parameterization of mean wind and shear stress of wind-farm flow useful in weather, climate and wind farm optimization models.

4.3 Theoretical Background

4.3.1 Formulation of the wind farm canopy model

To avoid having to model the details of individual wakes, the formulation incorporates averaging a unit volume of the flow that, for a uniform canopy, is defined based on the spacing and height of the canopy elements. We also assume neutral stratification of the ABL. Developing field averaged equations for the flow through a wind farm, $u = U + \bar{u}'' + u'$ where $U = \langle \bar{u} \rangle$ is the time and spatially averaged velocity signified by an overbar and angle brackets, respectively, $\bar{u}'' = \bar{u} - U$ is the spatial variation of

the time mean flow around individual turbines, and $u' = u - U - \bar{u}''$ are the turbulent fluctuations. The spatially and temporally averaged momentum conservation equation takes the form:

$$-\frac{\partial \tau(z)}{\partial z} = \frac{1}{\rho}\frac{\partial P}{\partial x} + f_{wf}(z) \tag{4.1}$$

where $\tau(z) = \langle \overline{u'w'} \rangle + \langle \bar{u}''\bar{w}'' \rangle$ is the total wall-normal shear stress, where $\langle \overline{u'w'} \rangle$ is the average kinematic turbulent shear stress,$\langle \bar{u}''\bar{w}'' \rangle$ is the dispersive flux of momentum, ρ is air density, P is mean pressure, and $f_{wf}(z)$ represents the vertically distributed turbine induced force. The dispersive stress is the horizontally unresolved subgrid-scale quantity that arises from horizontal spatial filtering of the momentum equation and represents the contribution to momentum transfer from correlations between spatial variations in the time-averaged flow.

4.3.2 Turbine drag parameterization

A standard parameterization for the turbine-induced force is employed, where

$$F_T = \frac{1}{2}\rho C_T A_T U^2. \tag{4.2}$$

The thrust coefficient is C_T and A_r is the rotor-swept area. The force, per unit mass, distributed over the unit volume occupied by turbines in a wind farm is

$$f_{wf} = \frac{F_T}{Z_H A_f} = \frac{U^2}{L_c}, \tag{4.3}$$

where Z_H is the top-tip height of the wind farm, and $A_f = S_x S_y D^2$ is the unit area of ground per turbine, D is the rotor diameter. S_x and S_y are the x (streamwise) and y (spanwise) spacing between wind turbines in multiples of D. f_{wf} can be simplified to the mean velocity squared divided by L_c. The drag development length scale L_D can be written in terms of the geometry of the wind farm as,

$$L_c = \frac{2 Z_H A_f}{C_T A_r} = \frac{8 Z_H S_x S_y}{\pi C_T}. \tag{4.4}$$

It approximately scales with the distance, from the front edge of the wind farm, required for the spatially averaged, time mean flow to develop within the wind farm. A numerical

study of the ABL transition to urban canopies revealed that the flow development length scales as about $3L_c$, with a form that follows an exponential decay [45].

4.3.3 Reynolds stress parameterization

The Reynolds stresses can be parameterized using the mixing length formulation as,

$$-\left\langle \overline{u'w'} \right\rangle = l_m^2 \left(\frac{\partial U}{\partial z} \right)^2, \tag{4.5}$$

and rearranging allows for determining the mixing length based on measured turbulence profiles as

$$l_m = \left(-\left\langle \overline{u'w'} \right\rangle \right)^{1/2} / \left(\frac{\partial U}{\partial z} \right). \tag{4.6}$$

For a surface layer, $l_m = l_{SL} = \kappa z$, where κ is the von Karman coefficient ($= 0.4$). For dense canopy flows $l_m = l_C = 2\beta^3 L_c$, following [71], where $\beta = u_*/U_{Z_H}$. For sparse canopies where momentum is absorbed by roughness elements as well as the ground, it is likely that a combination of these two mixing lengths are important, with surface layer scaling being important near the ground and canopy scaling more important away from the surface. Coceal and Belcher [45] proposed a model that smoothly varies between these two length scales following a harmonic interpolation function

$$\frac{1}{(l_m)^N} = \frac{1}{(l_{SL})^N} + \frac{1}{(l_C)^N} \tag{4.7}$$

where N can be used to adjust the weights of the contributions. This results in the mixing length being constrained by the smaller of the two length scales depending on height, and it is found that $N = 4$ best fits the measurements in this study. The dispersive stresses contribution is often small and therefore neglected as a first approximation.

4.4 Experiments

4.4.1 Characterization of fully developed wind-farm flow

Measurements of the fully developed wind-farm flow were obtained in a boundary-layer wind tunnel study, reported in Markfort et al. [7]. The experiments considered the development of a neutral boundary layer flow through and over an array of scaled, operating wind turbines. Two layouts were considered to investigate changes in wind direction. Perfectly aligned and perfectly staggered configurations provided insight on how the ABL develops over wind farms. The spacing of the turbines were $S_x = 5D$ and $S_y = 4D$ in both configurations. The diameter of the rotors were $D = 12.8$ cm and the top-tip height of the wind farm was $Z_H = 16.8$ cm. For the staggered case, the even numbered rows were shifted laterally by $y = 2D$. The area of the rotor-swept plane was $A_r = 0.013$ m^2 and the unit area of ground per turbine was $A_f = 0.34$ m^2. Figure 4.2 shows the vertical distribution of rotor area per unit ground area, normalized by A_r/A_f. To characterize the spatially averaged mean flow, profiles were collected downwind of the 12th and 11th rows of turbines at four selected locations for the aligned and staggered wind farms, respectively. The representativeness of the spatially-averaged flow by these profiles was confirmed by simulations of the wind farm using a validated research-level LES code [67].

Figure 4.3 shows the mean velocity profiles for the aligned and staggered wind farm configurations, as well as total stress profiles and contributions of the dispersive stresses. The velocity exhibits an inflected mean wind profile, which is characteristic of canopy-type flows and leads to large-scale instability in the flow. Also unlike dense canopy-flows, the velocity does not go to zero within the canopy layer, but is significant near the surface. The inflection point and height of maximum shear stress occurs at $z \approx 0.9Z_H$. This point defines the top of a canopy flow from a dynamic perspective and provides the best estimate for the drag and shear penetration length scales. The shear stress is reduced with height due to the drag of the wind turbines. Approximately 20% of the maximum shear remains to be absorbed at the ground level. Dispersive stresses were found to be especially significant for the aligned wind farm at 40% of the maximum total stress. The maximum dispersive stress was 10% for the staggered case [7].

Due to the large dispersive stresses and indications that the flow through the aligned

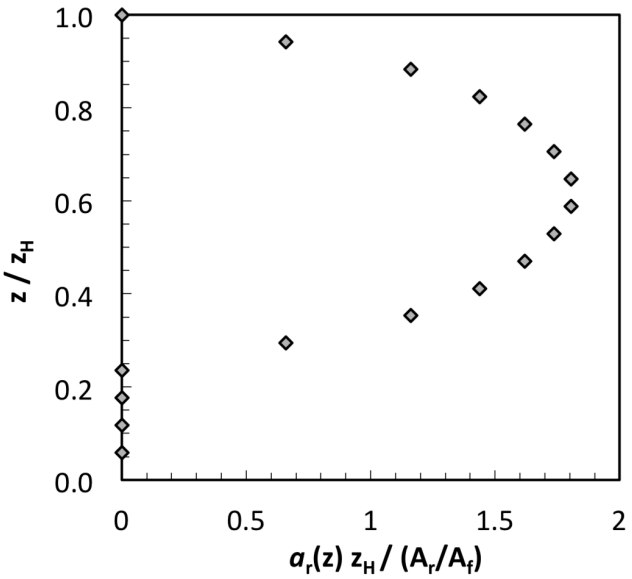

Figure 4.2: Vertical distribution of the normalized local rotor area per unit volume, $a_r(z)$.

wind farm may not be fully developed, based on the estimate of L_c, we will only considering the flow in the staggered wind farm for this analysis. The aligned case may be generally considered a special case, occurring infrequently when the wind is perfectly aligned with the rows of turbines such that the direct upwind turbines wake turbines in adjacent rows. Based on measurements from Barthelmie et al. [19] this may be rare. The flows from non-aligned directions may be considered staggered. In general the wind-farm flow behaves closer to that of the staggered arrangement. As shown in [7], the flow development within a staggered wind farm requires less distance than an aligned wind farm due to more efficient lateral mixing of wakes evidenced by smaller dispersive stresses.

4.4.2 Thrust coefficient

The drag coefficient used in meteorological applications, e.g. flow in canopies, often incorporates the factor of 1/2 into C_D. However, here we use the engineering convention and maintain the factor separate from the estimate of the trust coefficient C_T. To

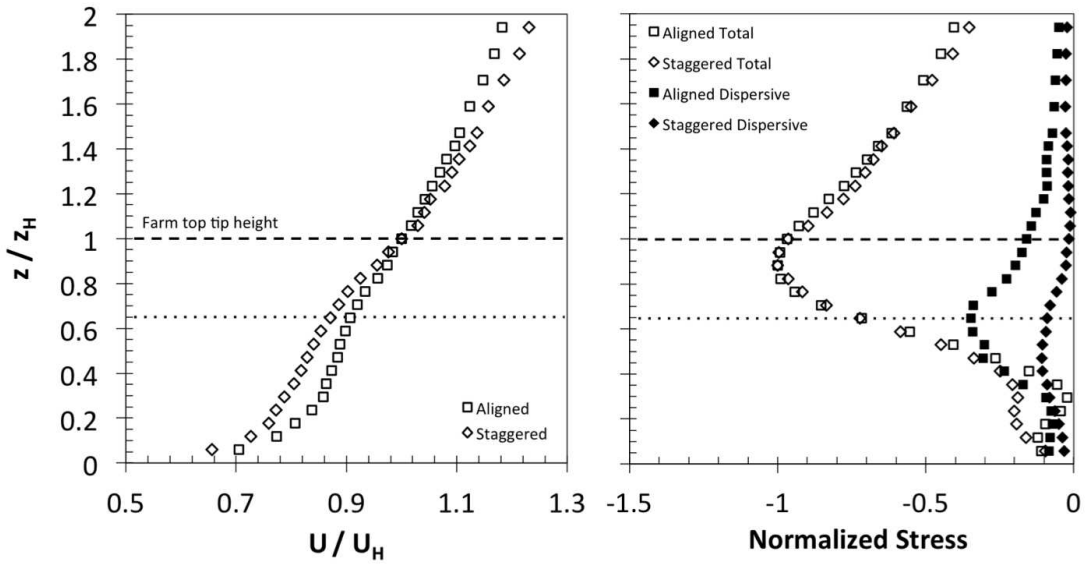

Figure 4.3: (Left) Mean, spanwise averaged velocity profiles measured within an aligned and staggered wind farm. (Right) Total stress and dispersive stress profiles normalized by u_*^2.

estimate C_T from the measured turbulence profiles using Eqn. (4.1), the turbine thrust parameterization defined above in Eqs. (4.3) and (4.4), is employed and rearranged to give

$$C_T = -2\left(\frac{\partial \tau(z)}{\partial z}\right)\left(\frac{8 Z_H S_x S_y}{U^2 \pi}\right). \tag{4.8}$$

Figure 4.4 shows the distribution of C_T measured across the rotor-swept region of the wind farm. The distribution is well represented by a Gaussian function following

$$C_T = a \exp\left[-\frac{\left(\frac{r}{R} - b\right)^2}{2c^2}\right], \tag{4.9}$$

where r/R is the distance form hub height normalized by the rotor radius and the coefficients $a = 1.06$, $b = 0.086$, $c = 0.385$. Calculating the depth averaged value for C_T we determine for the staggered configuration $C_T = 0.49$. This compares well with results based on large-eddy simulation (LES) for flow through a single turbine, modeled

after the turbine used in these experiments, where C_T was determined to be 0.45 (Wu, pers. comm.). Using the experimentally determined value for C_T and the dynamic height of the canopy, we can determine L_c to be approximately 16 m, or $L_c/z_H \approx 100$ for the staggered wind farm. This agrees with the estimate presented in Markfort et al. [7].

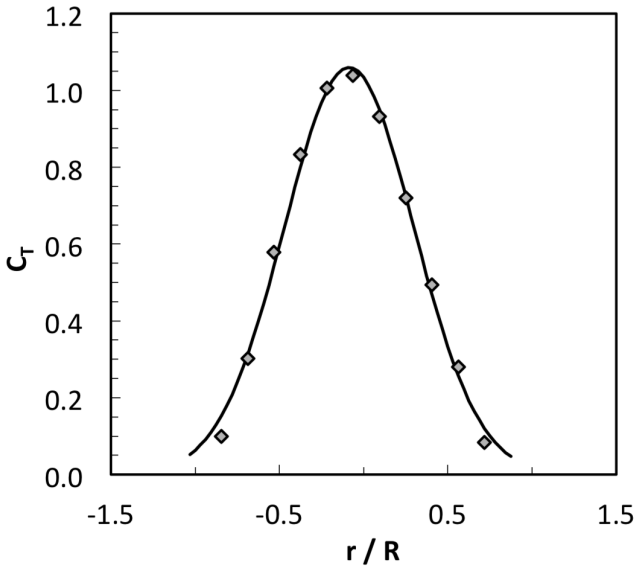

Figure 4.4: Plot of the distribution of the measured thrust coefficient in the fully developed staggered wind farm and a Gaussian fit.

4.4.3 Momentum penetration

The depth of the large scale eddies that carry momentum down into the wind farm from the ABL above is related to the shear instability caused by the inflection point in the mean velocity near the top of the wind farm. The shear instability scale can be approximated as

$$L_s = U_{0.9Z_H} / \left(\frac{\partial U}{\partial z} \right)_{z=0.9Z_H}. \tag{4.10}$$

The measured shear length scale for the experiment is $L_s/Z_H = 3.0$. For plane mixing

layers it can be assumed that the distribution of large-scale vorticity is symmetric about the point of the velocity inflection and penetration is $\approx 1/2L_S$. However due to the presence of the drag elements that cause the shear flow in this case, it is likely that eddies penetrate a fraction less than half of L_S. Another measure of the shear scale may be defined based on the mean velocity above the canopy and deep within the canopy. Here we define the scale of vorticity penetration as

$$\delta_\omega = \frac{U_{z=2Z_H} - U_{z=0.1Z_H}}{\left(\frac{\partial U}{\partial z}\right)_{z=0.9Z_H}}. \tag{4.11}$$

For the fully developed staggered wind farm, $\delta_\omega/Z_H = 1.25$ or about 40% of L_S. From Thom [87], the zero-plane displacement of the log-layer above the canopy can be defined as

$$\frac{d}{Z_H} = 1 - \frac{1}{2}\frac{\delta_\omega}{Z_H}. \tag{4.12}$$

This results in $d/Z_H = 0.37$ for the current experiment and is similar to the value $d/Z_H = 0.38$ determined in Markfort et al. [7] based on the velocity profiles above the wind farm.

4.5 Analytical Canopy Model

4.5.1 Dense canopy model

Inoue [71] developed an analytical model for dense canopies that describes the mean wind profile in a fully developed canopy flow. The model essentially utilizes an assumption of constant mixing length to formulate an exponential decay relationship for $U(z)$ following,

$$U(z) = U_{Z_H} \exp\left[\alpha\left(\frac{z}{Z_H} - 1\right)\right], \tag{4.13}$$

where α is an attenuation coefficient that increases with canopy density ($\alpha = \beta Z_H/l_C$). Results from Markfort et al. [7], compared with results from the previous section, indicate the model performs reasonable well for describing the mean wind across the rotor plane and is useful for determining the momentum absorbed by the wind farm.

One weakness of this model is that it does not faithfully capture the no-slip condition at the surface. Unlike dense canopies for which the model of Inoue was formulated, the mean wind near the surface may be significant in wind farms. The result is that wind farms behave more like sparse canopies where the turbines absorbs significant momentum but a non-negligible amount of momentum may be transferred to the ground as well. The assumptions for the dense canopy model, including the local density, drag coefficient and mixing length are all constant and the momentum is fully absorbed by the canopy, may not hold true when applied to wind farms. To develop a formulation useful for sparse wind-farm canopies, these assumptions must be relaxed to more accurately model the mean wind and shear stress, particularly near the surface.

4.5.2 Sparse canopy model

A sparse canopy is defined as a cluster of roughness elements that are tall enough to absorb significant momentum by form drag, however there remains significant momentum that is transferred to the surface and absorbed through skin friction. Similar flows have been addressed in the context of urban meteorology, as building density tends to vary significantly, leading to a need to depart from the simplified model in Eqn. (4.13). Generally the sparse canopy problem has been addressed using numerical models to solve the momentum conservation equation utilizing similar forms of the quadratic drag and mixing length parameterizations as presented above (e.g. [45]).

The requirement to handle the problem numerically arises from the nonlinear relationship between mean wind speed and the canopy drag force. Alternatively, Wang [88] proposed a linearization of the drag force equation. Here we employ this assumption for the turbine-induced force by relating the force to UU_{Z_H} instead of U^2. Employing the above parameterizations, Eqn. (4.3) and (4.5) are substituted into Eqn. (4.1), and assuming there is a negligible longitudinal pressure gradient results in

$$-\frac{\partial}{\partial z}\left(K\frac{\partial U}{\partial z}\right) = C_L\frac{A_r}{A_f Z_H}U(z)U_{Z_H} \tag{4.14}$$

where $K = \kappa z s u_*$. This allows for an analytical solution with the form

$$U(z) = C_1 I_0(g(z)) + C_2 K_0(g(z)) \tag{4.15}$$

where the coefficients of integration are C_1 and C_2, and I_0 and K_0 are the modified Bessel functions of the first and second kind, respectively, of order 0. I_0 and K_0 depend on

$$g(z) = 2\left(A\frac{z}{Z_H}\right)^{1/2}, \tag{4.16}$$

where

$$\mathrm{A} = C_L\frac{A_r}{A_f}(\kappa\beta s(z))^{-1}. \tag{4.17}$$

Rewriting Eqn. (4.7) as

$$l_m = \kappa z s(z), \tag{4.18}$$

where

$$s(z) = \frac{l_C}{\left[(l_C)^N + (\kappa z)^N\right]^{1/N}} \tag{4.19}$$

provides the distribution of the mixing length, smoothly varying with height. In Eqn. (4.17), A can be interpreted as a dimensionless attenuation coefficient that characterizes the reduction of wind speed within the wind farm. The coefficient determines the shape of the velocity profile integrating the effects of turbine size and spacing, as well as the mixing length and C_T by way of the linearized drag coefficient, C_L.

The two integration coefficients are determined by solving Eqn. (4.15) for the no-slip condition at $z = z_0$ and for a known U_{Z_H}, as

$$C_1 = U(Z_H)[I_0(g(Z_H)) - I_0(g(z_0))K_0(g(Z_H))/K_0(g(z_0))]^{-1}, \tag{4.20}$$

and

$$C_2 = C_1 I_0(g(z_0))/K_0(g(z_0)). \tag{4.21}$$

The linearized drag coefficient, C_L, can be solved by way of solving for A iteratively based on the boundary conditions. Alternatively, based on a number of model runs,

varying the above controlling parameters, Wang [88] found that A could be well characterized based on the shear length scale L_s as expressed in Eqn. (4.10), and ultimately, was well represented with a simple quadratic relationship based on frontal area index, which for the wind farm is simply A_r/A_f. The relationship that best fits the results can be written in terms of the geometry of the wind farm as

$$\mathrm{A} = 4.52\,(A_r/A_f) + 0.62(A_r/A_f)^2. \tag{4.22}$$

In this study we use Eqn. (4.22) to estimate C_L at $z = Z_H$ and then allow A to vary with height following Eqn. (4.17).

Figure 4.5 shows the comparison between the measured mean velocity within the staggered wind farm (from Fig. 4.2) and the prediction of the sparse canopy model. Allowing A to vary vertically produced a result that is closer to the observed velocity profile across the rotor plane than if it is held constant based on Eqn. (4.22).

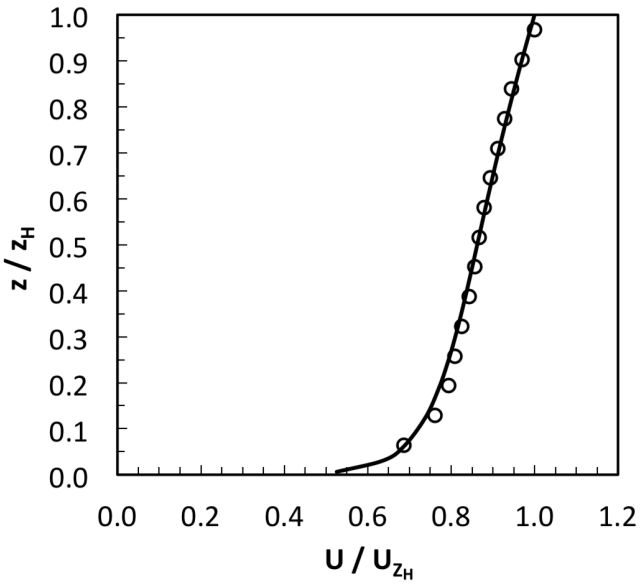

Figure 4.5: Plot comparing the normalized wind profile for the fully developed wind-farm flow in a staggered configuration experiment with the prediction from the sparse canopy model.

This also leads to a better approximation of the velocity gradient at $z/Z_H = 1$ and

therefore a better prediction of L_s. Two key features are captured by the model, first is the exponential attenuation of the velocity with height near the top of the wind farm and across the rotor-swept region, and second is the no-slip condition at the surface.

From Eqn. (4.6) the variation in mixing length is determined based on the measured profiles of mean velocity and shear stress. Using Eqns. (4.5), (4.15) and (4.18), we calculate the effective mixing length and the resulting shear stress based on the model. Figure 4.6 shows the results of the model compared with the data. The mixing length model reproduces the general features of the length scales of the flow with the values near the surface being weighted toward surface layer scaling while the mixing length approaches a constant value of l_C near the top of the wind farm. However, the measurement reveals a different behavior as the maximum measured value occurs near the center of the rotor plane and then decreases up to Z_H. Then the measured mixing length approaches the inertial layer near the top of the wind farm that was identified in [7]. The mixing length model does not capture this behavior but is a good first approximation that is simple to implement, captures the average behavior and results in a reasonable profile for the shear stress. In particular the shear stress profile correctly partitions the amount of momentum absorbed by the wind farm and the shear stress near the surface. The result reveals the remaining stress absorbed by the ground or sea surface. In the present configuration the result is approximately 15 - 20% of the momentum absorbed by the wind farm remains at the surface.

4.6 Summary and Discussion

We have shown that an analytical, sparse canopy model can reasonably represent the mean wind and non-negligible surface shear stress for flow through a wind farm. The model reproduces the no-slip condition at the surface and the surface shear stress by allowing the mixing length to vary with height inside the wind farm. The model can be applied when the details of the flow around individual turbines are not required, and only overall spatially-averaged features of the wind-farm flow are of interest. This model can be solved using basic spreadsheet software, and can be cheaply employed into regional scale atmospheric flow models for weather prediction and wind farm development. Wind turbine spacing is an independent variable in the model and therefore the

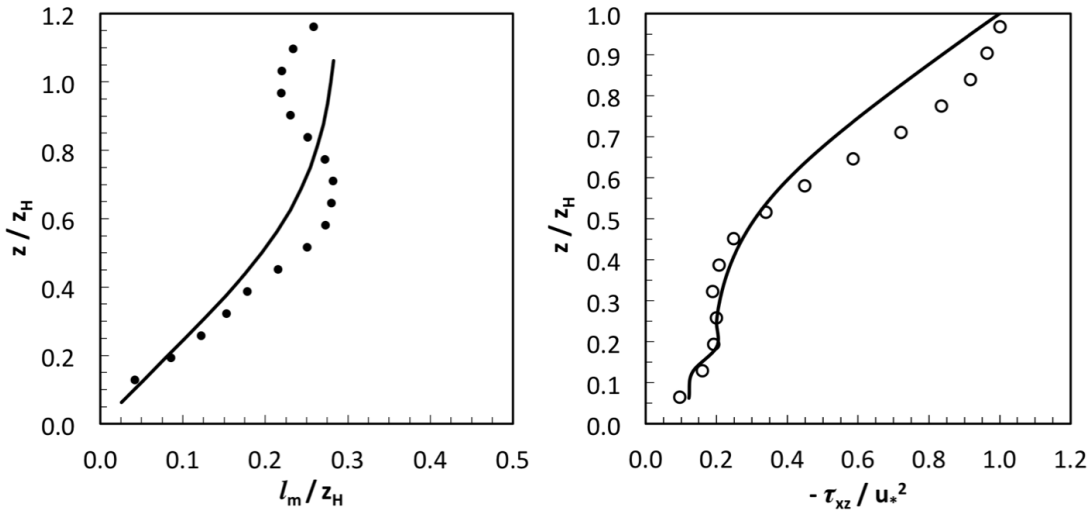

Figure 4.6: Plots comparing measurements with the results of the sparse canopy model for Left: mixing length, and Right: shear stress.

model can be used to optimize the design of wind farm layouts. The optimum turbine spacing can be estimated by minimizing the amount of momentum transferred to the surface. At the same time the shear penetration scale should be kept large to efficiently transfer momentum down from the ABL above the wind farm to the entire rotor-swept region. Given for example the wind farm layout studied here, with the same surface roughness, the turbines could be spaced closer together to capture the remaining momentum currently lost to the surface. For onshore installations, the model could be used to study the effect of changing land cover below the wind turbines to examine how a change in surface roughness may affect the partitioning of momentum between the wind farm and the surface. For offshore wind farms, the surface shear stress is an important boundary condition for sea-surface mixing. If a wind farm absorbs all the momentum, the mixing and temperature structure in the surface mixed layer of the ocean will be dramatically changed compared to before the wind farm was installed. The model should be tested for full-scale wind farms flows, using carefully measured, spatially representative wind profiles and in a validated LES framework. Although the main goals to represent the mean wind and shear stress within a wind farm are achieved

with the current formulation, additional testing at full scale will provide the necessary data to improve the mixing length model and lead to a more robust formulation. Incorporation of dispersive stresses will allow for the consideration of the development region of the flow. Additionally, the mixing length model could be modified to account for atmospheric stability.

Part II

Wake Effects on Biosphere-Atmosphere Interaction

Chapter 5

Canopy Wake Dynamics and Sheltering Effects on Surface Fluxes[†]

[†] **This chapter is accepted for publication as Markfort CD, F Port-Agel and HG Stefan. Canopy wake dynamics and wind sheltering effects on Earth surface fluxes. *Environmental Fluid Mechanics*.**

5.1 Abstract

The atmospheric boundary layer adjustment at the abrupt transition from a canopy (forest) to a flat surface (land or water) is investigated in a wind tunnel experiment. Detailed measurements examining the effect of canopy turbulence on flow separation, reduced surface shear stress and wake recovery are compared to data for the classical case of a solid backward-facing step. Results new provide insights into the interpretation for flux estimation by eddy-covariance and flux gradient methods and for the assessment of surface boundary conditions in turbulence models of the atmospheric boundary layer in complex landscapes and over water bodies affected by canopy wakes. The wind tunnel results indicate that the wake of a forest canopy strongly affects surface momentum flux within a distance of 35 - 100 times the step or canopy height, and mean turbulence quantities require distances of at least 100 times the canopy height to adjust to the new surface. The near-surface mixing length in the wake exhibits characteristic length scales of canopy flows at the canopy edge, of the flow separation in the near wake and adjusts to surface layer scaling in the far wake. Components of the momentum budget are examined individually to determine the impact of the wake. The results demonstrate why a constant flux layer does not form until far downwind in the wake. An empirical model for surface shear stress distribution from a forest to a clearing or lake is proposed.

Keywords

Atmospheric boundary-layer (ABL); Biosphere-atmosphere exchange; Canopy turbulence; Roughness transition; Turbulent transport; Wake turbulence; Wind-tunnel experiment; Backward-facing step (BFS)

5.2 Introduction

Interactions between Earths surface and the atmosphere can be characterized by fluxes of momentum, sensible heat, water vapor and trace gases, (e.g. CO_2 and CH_4). In models of the global atmosphere, which are used, e.g. for weather and global climate projections, these fluxes have to be specified as boundary conditions. Air and water quality depend on the mass fluxes at the air-land and air-water interfaces. Field measurements to quantify climate-controlling trace gas fluxes, as well as air pollutant transport are required inputs for analyses. Modeling and measurement of interfacial fluxes are complicated by heterogeneity of land surface covers and complex terrain; surface fluxes are mediated by turbulence at the air-land or air-water interface of the atmospheric boundary layer (ABL). Significant advective or dispersive fluxes are generated at the interfaces of land and water because the ABL is generally not in equilibrium with the different land or water surfaces e.g. in terms of temperature, moisture content, or trace gas content.

Surface water features are a significant component of the terrestrial landscape, and are often collocated with forests as shown by Lefsky [89] and Lehner and Doll [90]. Forests cover approximately 40% of the terrestrial surface and fragmented canopies, due to natural or anthropogenic causes, dominate significant areas as shown by Laurence [91]. There are an estimated 304 million lakes on Earth, and although lakes only cover about 3% of the Earths land surface with much higher concentrations, upwards of 30% in regions of the boreal zone and in the tropics, they may have a disproportionate effect on land-atmosphere interactions on a global scale including heat, moisture and momentum flux [92, 93, 94, 95]. Surface waters have a significantly lower albedo and larger heat capacity than land and vegetation. Lakes also absorb more solar radiation and store more heat. This causes lakes surface temperatures to often be quite different from the surrounding landscape. Lakes may be a source or sink of sensible heat to the atmosphere, which is often out of phase with the surrounding land. Surface water features are a significant source of moisture to the atmosphere as well. Lake surfaces are aerodynamically much smoother than the surrounding land surface, and because most water bodies are small, having surface areas less than 10 km^2, the atmospheric boundary layer rarely achieves equilibrium over lakes.

Recently small water bodies were identified as potentially significant factors in the global climate system, but large uncertainties still exist as to their contribution. It has become apparent that the terrestrially-derived carbon is only partially delivered by rivers to oceans. The remainder is being washed into lakes, reservoirs and wetlands where it is ultimately off-gassed to the atmosphere as CO_2 or CH_4 [96, 97]. CH_4 has become of increasing concern because emissions from small lakes and wetlands may offset terrestrial carbon uptake by forests [98]. The collocation of the two ecosystems leads to a strong coupling between them that is in part mediated by atmospheric turbulence. The turbulent flow of the lowest part of the ABL over forests is characterized by displacement of the log-layer and Kelvin-Helmholtz type shear layer eddies at the canopy top that dominate biosphere-atmosphere transport (Raupach [99, 68]. The displacement of the mean flow leads to strong wake turbulence downwind of the forest edge, and depending on the extent, height and density of the forest, the flow may separate causing a region of recirculating flow which may be analogous to that downwind of a backward-facing step (BFS). Often the existence of BFS type flow is assumed at the transition to lakes surrounded by a forest canopy or topography (e.g. [100, 101, 102, 103]). Alternatively, earthen berms, windbreaks [104] and even buildings may provide similar sheltering.

In the work of Cassiani et al. [105] and Detto et al. [106], a continuum is proposed between a so-called exit flow (Belcher et al. [48]) and a BFS type flow that depends on the density of the canopy measured as leaf area index (LAI). So far no controlled experiments have been performed to examine whether the turbulent flow behind the canopy is similar to that behind a BFS. Wind sheltering is caused by canopies or embankments that have a variety of lengths, heights and porosities. In previous wind tunnel experiments we have determined that all three factors play a role in the scaling of the separation as well as the shear development length scales.

In a previous study we showed that the flow separation and wake turbulence associated with a canopy strongly affects the transport of momentum, heat, moisture and trace gasses at the air-water interface and therefore also wind-driven processes in lakes (Markfort et al. [11]). The complex flows over lake-covered landscapes was identified recently as one of the greater challenges to ABL processes by Baklanov et al. [107]. Landscapes and lakes are often described using 1-D vertical transport models, which require either modeled or measured representative fluxes at the surface. Specifications of

these fluxes are usually based on models appropriate only for fully developed boundary layers, or field data collected at selected points in the landscape. In either case, effects of the surrounding landscape and wake-induced lateral advection on data interpretation are currently ignored. The impact on interpreting point-based data, collected in the field to determine surface fluxes, is neither fully known nor appreciated. In order to adequately model atmospheric dynamics and fluxes, we must consider heterogeneous landscapes, including canopy transitions.

The main purpose of this study is to investigate the flow separation, turbulence, shear and momentum fluxes in the wake of a canopy and compare the results to the well-known BFS type flow. The two primary goals are (1) to show the significant distance before a new surface layer develops over a much smoother land or water surface downwind of a canopy and (2) to show that wind flow transitions from canopies are fundamentally different from the classical solid BFS which is often used as a proxy in simulation models of the ABL transition in forest clearings or on small lakes and wetlands. In this paper we will investigate the processes leading to the delay of a new surface layer developing downwind of a canopy (BFS), and we will report direct measurements of surface shear stresses that illustrate the actual rate of shear stress development in the wake. Section 5.3 outlines the primary processes and parameters affecting the turbulent flow-field in the wake of a canopy and needed to characterize the two-dimensional ABL evolution. A review of current knowledge gained from solid BFS experiments is also provided. To understand the turbulence characteristics in the wake of a canopy, we use detailed measurements collected in a wind tunnel experiment of flow in the transition from a canopy to a smooth surface clearing (canopy BFS). The measurement methods used are presented in Section 5.4. In Section 5.5 we interpret the new wind tunnel data relative to the flow field downwind of a solid BFS. We illustrate the similarities between the two flows, and highlight key differences. We consider the variation in mixing lengths and turbulence characteristics in the wake flow. Finally we relate measurements of Reynolds stresses in the wake flow field with direct surface stress measurements in the clearing, and determine which terms in the momentum equation are more important for the two flow fields. We focus on the near surface, where most field measurements of fluxes are collected and where the boundary conditions in numerical simulations are imposed, to illustrate how wake turbulence affects the

accuracy of point measurements and calculations of surface fluxes. The results provide a first look at how single-point micrometeorological field data may be interpreted, and how the data from meteorological and eddy-covariance stations placed on a flat landscape (land, lake, wetland or bog) bordered by a forest canopy can be affected. We also provide information on surface shear stress recovery in the landscape downwind from forest canopies, which is an essential boundary condition for the modeling of small lakes. A summary is provided of the main findings and conclusions in Section 5.6.

5.3 Review and Theoretical Background

5.3.1 Review of ABL transition studies

The log-law similarity formulation is known to represent the atmospheric surface layer well, particularly between the roughness sublayer and the outer layer (e.g. Raupach et al. [49]). The zero-plane displacement height, d is included in the log-law to account for the displacement of the log-linear region over complex land cover, including tall and dense roughness elements such as trees. For flows that have no measurable displacement, the surface is considered rough from an aerodynamics point of view due to the lack of a discernible viscous sublayer at the surface, and these surfaces can be characterized solely by an aerodynamic roughness, z_0. For land cover characterized by both roughness and displacement length scales, the roughness elements have a significant vertical component and are densely packed together. These land covers are commonly referred to as canopies and have distinct flow properties (cf. Finnigan [42]). Unlike rough boundary layer flows, which follow the log-law down to the ground surface, the turbulence properties in canopy flows, are more similar to plane mixing-layer type flows [68]. The salient feature of a canopy flow is that the mean velocity profile exhibits an inflection point as the curvature adjusts from the log-layer form above to an exponential form below approximately the top of the canopy [108, 71]. A review of turbulent flows for canopies is provided by Finnigan [42].

ABL models used to represent rough surface flows and canopy flows only apply if the land surface characteristics are statistically homogeneous. In reality, a patchwork of various land cover types often characterizes the terrestrial surface. The evolution of the ABL flow over these surfaces can be quite complex and the method to represent and

interpret the flow depends on the type of land surface (i.e. rough ground or canopy) and the scale being considered. As presented by Brutsaert [109], the scale of horizontal heterogeneity characterizing the land surface, if much larger than the vertical scale of the boundary layer, may be characterized by a single roughness and flux due to the homogenizing properties of the turbulent flow. If the scale of horizontal heterogeneity is greater than 100 times the vertical scale, then the ABL will fully adjust to each surface component and these can be modeled independently with little regard to the interactions between them. On the other hand, surface heterogeneity described by finer intermediate scales must be treated distinctly and the horizontal interactions between them must be considered. If two adjacent land surfaces are characterized by tall, dense roughness elements, which exhibit similar displacement of the log layer, or both surfaces have no displacement height, then a roughness transition will be accompanied by the development of an internal boundary layer (IBL). However, if one surface exhibits a significantly different displacement height relative to the other, then the flow must enter into or exit out of a canopy. This results in additional complexity due to the change in vertical scale at the transition, which must be considered.

The flow transition from a rough surface to a canopy has been studied extensively, and these studies were recently highlighted in a review by Belcher et al. [44]. Fewer studies have focused on the flow exiting a canopy and the subsequent development of a new surface layer downwind. Efforts to characterize this specific flow in field experiments as well as numerical experiments using large-eddy simulations (LES) were reported by Detto et al. [106] and Cassiani et al. [105], respectively. The results indicate that, if the surrounding canopy is dense enough, the ABL may separate leading to a standing rotor, similar to that downwind of a solid BFS. From tower measurements near the canopy edge, Detto et al. [106] identified intermittent rotor formation. Cassiani et al. [105] found that a leaf area index (LAI) greater than four produced a flow with characteristics similar to that of a BFS.

Additional research has been completed to understand the flow dynamics at forest transitions. Ross [110] used an analytical approach to study the flow over heterogeneous canopies. Sanz Rodrigo et al. [111] and Banerjee et al. [112] studied turbulence in the gap of forest clearings for a variety of upwind conditions in a boundary layer wind tunnel, and using analytical methods, respectively. Other studies have considered the entrance

flow problem, e.g. Belcher et al. [48] using a theoretical and linear approach, Morse et al. [113] using wind tunnel experiments, and Dupont and Brunet [114] and Yang et al. [115] using LES. Field studies were conducted by Irvine et al. [116]. Moltchanov et al. [52] investigated the relative importance of dispersive stresses on the flow entering a canopy. Plate [117] presented some of the earliest studies on the disturbance of the ABL flow by shelterbelts or windbreaks and analyzed the recovery of the boundary layer to its pre-disturbance state. Wang and Takle [118] studied the turbulent flow around windbreaks using numerical simulations. Judd et al. [119] and Patton et al. [120] considered the effects of windbreaks on the structure of the ABL using wind tunnel experiments and LES, respectively. New efforts have considered the complexity of the canopy structure using LES with synthetically generated realistic canopy structure [121] and using highly resolved field measurements of canopy structure (Schlegel et al. [122]).

Belcher et al. [48] provided a scaling analysis for the flow in and over inhomogeneous canopies. Important scales that were identified in this study include the entrance length scale, or canopy drag development scale, as well as the shear penetration length scale. Similar processes exist in flows through aquatic vegetation (Siniscalchi et al. [123]). Flows in and over heterogeneous canopies with topography have also been studied (Ross and Baker [124]).

Most micrometeorological flux measurements in the ABL are collected within the roughness sublayer where the log law does not apply. In spatially variable landscapes with a mix of canopies and rough and flat surfaces, wake flows shed from canopies lead to local pressure gradients and advection of momentum that complicates the interpretation of these measurements. The consideration of heterogeneous source distribution for scalars of interest complicates this problem further [125]. A review of the current state of knowledge on non-homogeneous canopy flows was recently provided by Belcher et al. [44].

5.3.2 Momentum transfer in ABL transitions

The momentum budget and its components are key for understanding the extent and effect of a canopy wake on a downwind lake or flat land surface. Due to the abrupt nature of the ABL transitions from a forest to a clearing or a wetland, the sudden absence of the canopy drag force leads to a significant flow acceleration and an adverse

pressure gradient that may cause flow separation (Fig. 5.1). Depending on the length of the canopy, the hypothetical internal boundary layer (IBL) will begin at the upwind end of the canopy or at the shoreline. The downwind shear zone is a region of higher turbulence intensity due to the shear layer and wake growth behind the canopy. Due to the relatively low roughness in a clearing or over a water body, the new equilibrium layer grows slowly.

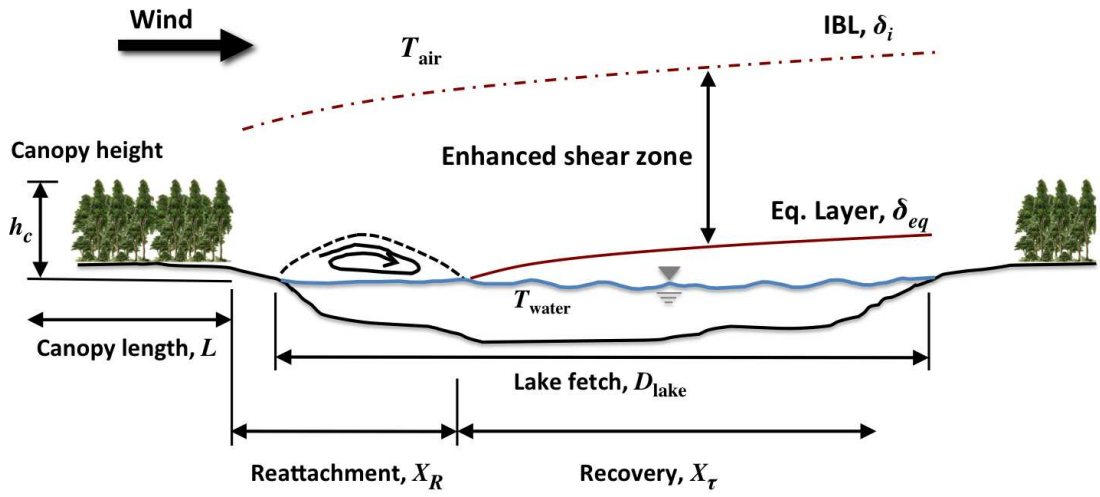

Figure 5.1: Schematic of wake zone and boundary layer growth at a tree canopy to lake transition.

The size of the separation zone downwind of the canopy edge is dependent on the length of the canopy L, its porosity and its height h_c (h, for comparison with solid BFS type flows). Where mean flow reattachment occurs, at a distance X_R, the surface shear stress is by definition zero. Downwind of that location, the shear recovery begins and grows asymptotically over a distance X_τ. Near the surface, the development and growth of an equilibrium sub-layer, which is adjusted to the downwind surface, can be expected. An enhanced turbulent wake zone exists between an internal boundary layer above and the equilibrium layer. It is important to determine the point of mean flow reattachment in order to define the origin of the newly developing surface layer. We may assume that the flow after reattachment is similar to the classic equilibrium sublayer associated with a roughness transition.

The momentum conservation equation employing Reynolds averaging in time for the

flow over, through and in the wake of a canopy step, averaged in the spanwise direction (as signified by the angle brackets below), and written in Cartesian coordinates is as follows:

$$\langle \bar{u} \rangle \partial_x \langle \bar{u} \rangle + \langle \bar{w} \rangle \partial_z \langle \bar{u} \rangle = \\ - \rho^{-1} \partial_x \left\langle \bar{P} \right\rangle - \partial_z \left\langle \overline{u'w'} \right\rangle - \partial_z \left\langle \bar{u}'' \bar{w}'' \right\rangle - \partial_x \left\langle \overline{u'u'} \right\rangle - \partial_x \left\langle \bar{u}'' \bar{u}'' \right\rangle - F_{c,x} \quad (5.1)$$

$$\langle \bar{u} \rangle \partial_x \langle \bar{w} \rangle + \langle \bar{w} \rangle \partial_z \langle \bar{w} \rangle = \\ - \rho^{-1} \partial_z \left\langle \bar{P} \right\rangle - \partial_x \left\langle \overline{w'u'} \right\rangle - \partial_x \left\langle \bar{w}'' \bar{u}'' \right\rangle - \partial_z \left\langle \overline{w'w'} \right\rangle - \partial_z \left\langle \bar{w}'' \bar{w}'' \right\rangle - F_{c,z} \quad (5.2)$$

where the flow varies only in the streamwise and vertical directions. In this formulation we use the meteorological convention, where x, y, z are the Cartesian coordinate directions corresponding to the mean wind, lateral and vertical directions, respectively; the velocity components corresponding to these directions are u, v, and w, respectively, P is the pressure, ρ is the density of air and $F_{c,i}$ is the body force due to the canopy. The drag force on the canopy is parameterized as

$$F_{c,i} = C_D a \eta^{-1} \langle \bar{u}_i \rangle^2 \quad (5.3)$$

where C_D is the bulk drag coefficient, a is the canopy area density (defined as the single sided projected area normal to the mean flow) of canopy elements divided by the unit volume of air around elements. The porosity is represented as $\eta = 1 - \lambda_p$, where $\lambda_p = \sum A_p / A_t$ is the plan area density calculated as the sum of the plan area of canopy elements A_p divided by the total canopy area A_t and represents the volume fraction occupied by canopy elements for a uniform canopy. The subscript i may be x or z, associated with Eqs. (5.1) or Eqn (5.2), respectively. The canopy force is primarily acting in the x-direction. The overbar signifies time averaging, while the prime and double prime are used to signify fluctuations about the mean in time and space, respectively. The spatially varying terms are dispersive fluxes. For more information regarding these potentially important terms, see Finnigan [42] and Belcher et al. [44].

The drag development length scale that arises from the drag force, Eqn. (5.3), assuming $\eta \approx 1$, is

$$L_c = (C_D a)^{-1}. \tag{5.4}$$

It scales as the distance the flow must traverse the homogeneous canopy to reach a balance between vertically advected and turbulent momentum flux [48]. For tree canopies, a is based on a combination of leaf area and woody area, and can be used to determine a vertically integrated plant area density or plant area index (PAI) from the ground level, $z = 0$ to the top of the canopy, $z = h$. PAI may be approximated by the leaf area index (LAI), often without significant error, which is available from remote sensing. The LAI is calculated as

$$LAI = \int_0^h a(z)dz, \tag{5.5}$$

Another important length scale that can be determined based on the dynamics of the flow is the shear length scale

$$L_s = \frac{\bar{u}_h}{(d\bar{u}/dz)_{z=h}}, \tag{5.6}$$

which is related to the size of Kelvin-Helmholtz type eddies that form in the shear layer at the top of the canopy. The shear at the canopy top leads to enhanced turbulence and more efficient transport as compared to a wall-bounded surface layer [68]. Raupach et al. [68] related the shear length scale to the longitudinal spacing of coherent Kelvin-Helmholtz type eddies (Λ_x), which can be detected using single and two point correlation analysis of the turbulence velocity signal near the canopy top. They found a proportionality relationship between the two scales with the form $\Lambda_x = mL_s$. The constant m is approximately 8.1 for dense canopies. A number of studies have found the linear relationship begins to break down for relatively sparse canopies with L_s/h greater than approximately 0.6, which corresponds to a LAI of less than about 4, see Novak et al. [126] and Bailey and Stoll [127].

Above the roughness sublayer, the flow characteristics are similar to an inertial sublayer of a classical rough-wall boundary layer, where eddy size scales approximately with height. The roughness sublayer extends up from approximately $2h$ to $3h$. In

the inertial layer wind velocity follows the log-law with a zero level displacement d to account for the drag of the canopy [128]. Developed flow over a canopy can be modeled using Monin-Obukhov similarity theory, which for thermally isotropic or neutral flows can be expressed by the log-law as

$$\bar{u}(z) = \frac{u_*}{\kappa} \ln\left(\frac{z-d}{z_0}\right) \tag{5.7}$$

where u_* is the friction velocity, κ is the von Karman constant ($= 0.4$), d is the zero-plane displacement and z_0 is the aerodynamic roughness of the canopy.

5.3.3 Overview of a solid BFS experiment

In this study we will discuss differences between the canopy BFS and the classical solid BFS. The log-law models the incoming flow over a BFS. The turbulent mixing length in the attached surface layer on top of a BFS scales with height above the surface, while the flow over a canopy is more similar to a mixing layer type flow [68]. The length scales of importance for the canopy flow are L_c and L_s as discussed earlier. This difference in the approach flow of a canopy BFS and a solid BFS may have a significant effect on the flow transitioning to the new surface layer downwind of the step.

A number of wind tunnel experiments have previously been performed for a solid backward-facing step (BFS) type flows. A review of existing work on BFS flows was provided by Eaton and Johnston [129]. Many of these experiments were designed to test various turbulence models used in computational fluid dynamics (CFD) simulations. One of the challenges is to correctly model separated flows and to forecast the point where the mean flow reattaches to the downwind surface. A high-Reynolds number flow experiment over a solid BFS was conducted by Driver and Seegmiller [130] in the wind tunnel at NASA Ames Research Center. The mean velocities and turbulence statistics were measured in detail using laser Doppler velocimetry (LDV), and surface shear stress was measured downwind of the separation zone using Laser Interferometry and the Preston tube technique. A no-slip boundary layer was developed over a smooth wall before the flow reached the BFS. The Reynolds number based on the step height, $h = 1.27$ cm, was $\mathrm{Re_h} = 3.7 \times 10^4$ and the boundary layer thickness at the step edge reached 1.9 cm. The expansion ratio based on the height of the step h and the total

height of the wind tunnel section $H_{wt} = 11.43$ cm, was $ER = H_{wt}/(H_{wt} - h) = 1.125$. The expansion ratio was kept small to minimize the freestream pressure gradient due to the sudden expansion at the edge of the step. The momentum thickness based Reynolds number, $\mathrm{Re}_\theta = 5{,}000$ ensured a fully turbulent boundary layer. Two cases were considered in this experiment, one with the top wall (opposite the step) parallel to the bottom wall, and the other with the top wall deflected up at 6 degrees to determine the effect of an increased pressure gradient. Only results from the parallel case will be presented here. The final data from the experiment was provided to the community for CFD validation via NASAs National Program for Applications-Oriented Research in CFD, Alliance CFD Verification and Validation effort. Details of the experiments can be found in the paper by Driver and Seegmiller [130]. Results from the experiment with a solid BFS will be compared with our experimental results for the canopy BFS. Included in Table 5.1 are the characteristics of the solid BFS used in the NASA Ames wind tunnel experiments by Driver and Seegmiller [130].

5.4 Boundary Layer Wind Tunnel Experiments

5.4.1 Experimental setup

Canopy BFS experiments were conducted in the large-scale, thermally-stratified boundary layer wind tunnel in the St. Anthony Falls Laboratory at the University of Minnesota. Atmospheric conditions measured in the field are typically non-stationary including variable wind direction and often slow wind speeds. In the wind tunnel we can simulate stationary flows that are fully adjusted to the surface conditions. This allows for investigation of flow details that are difficult to capture in the field, especially for example, the mean flow topology. In particular, it is possible to determine the existence and extent of flow separation. The wind tunnel has a 16 m long test section with a cross-sectional area of 1.7×1.7 m^2 and has a 6.6:1 area contraction ratio at the test section entrance. The tunnel was operated in closed loop and the boundary layer was tripped by an 8 cm tall picket fence at the entrance of the test section. The test section floor was made of smooth aluminum plates whose temperature can be controlled. This allows a thermally stratified (neutral, stable or unstable) boundary layer flow to be developed. Temperatures between 5°C to 80°C of both the floor and the air are achievable within

± 0.25°C. In these experiments, the test section floor and air were controlled by an automated heating/cooling system at 30°C to simulate a neutral boundary layer. Upwind of the canopy section, a 5 mm diameter chain roughness with a streamwise spacing of 10 cm was placed on the floor of the tunnel across the width of the test section. This ensured that a turbulent boundary layer was developed as the flow transitioned over the canopy. The freestream wind velocity was controlled at $U_0 = 2$ m s^{-1}. Further details of the wind tunnel have been described by Carper and Porté-Agel [54].

The model canopy consisted of a uniform staggered array of 6.3 mm diameter wooden cylinders, with 25.4 mm spacing, inserted into a 7 mm thick, rigid baseboard. The void ratio or porosity of this array was $\eta = 0.95$. The uniform canopy height h was 10 cm. Modular panel sections were constructed that could easily be inserted into the wind tunnel to achieve variations in canopy length and porosity. The canopy spanned the entire width of the test section, and after a number of preliminary tests to check the longitudinal flow development, we determined experimentally based on mean and turbulent characteristics that a canopy length of 2.5 m ensured a developed flow over the canopy before the transition to a smooth flat surface. The length is supported by theoretical analysis by Belcher et al. [48], numerical simulation results by Coceal and Belcher [45] and Dupont and Brunet [114] and experimental evidence from Morse et al. [113]. In [45] it was found that the development length for the flow entering canopies is $x_A = c_A L_c ln(K)$, where $c_A \approx 3$ and $K = hU_B(h)/L_c u_*$ with $U_B(h)$ as the inflow boundary layer velocity at the level of the canopy height. In our case $x_A/L_c = 6.6$ which is similar to that found in the studies by Dupont and Brunet [114] and Morse et al [113]. The canopy in this study is approximately 3.8 times longer than required based on the above theory, providing adequate confidence that the flow is fully developed.

The experimental canopy in the wind tunnel has a vertically uniform foliage density. The canopy geometry is similar to that in studies of Yue et al. [131] and of Rominger and Nepf [132]. However many forest canopies exhibit non-uniformity in the foliage density distribution. Nevertheless, similar flow characteristics inside and above field and idealized laboratory canopies have been found in a number of studies (Finnigan [42]). The flow in the wind tunnel canopy is fully turbulent, with canopy element Reynolds number, $Re_d = d_{rod} u_*/\nu = 160$. The coherent structure dynamics of the canopy flow have been studied by Novak et al. [126] as well as others, who found that

the dynamics in natural canopies with inherent heterogeneity are similar to idealized laboratory canopies. Characteristics of the model canopy are summarized in Table 5.1. Potentially significant differences exist between the canopy BFS and the solid BFS wind tunnel experiments, beyond obvious differences in porosity. Specially the ratio of boundary layer thickness to step height δ/h are different. Therefore we do not intend to make direct quantitative comparisons between the solid BFS and the canopy BFS; instead we illustrate the significant topological differences in the two flow fields. In particular we will consider the differences in the separation of the boundary layer due to the differences in longitudinal pressure gradients at the step and canopy edges. We will investigate the differences in flow structure over the solid step and the canopy to see how these may contribute to the evolution of and the level of turbulence in the wake. We will also see how the differences in momentum deficit over the canopy step and the solid step may contribute to the significantly longer distance required for the surface shear stress to recover downwind of the canopy.

The roof of the boundary layer wind tunnel was adjustable, allowing for studies of zero pressure gradient boundary layers. Over the canopy a minimal pressure gradient was maintained, as will be evaluated later. The angle of the roof was not changed over the downwind smooth surface. The overall blockage effect of the canopy was small due to the large test section size. The solid blockage by the canopy was estimated based on the ratio of the total projected frontal area of the canopy to the wind tunnel cross-sectional area. The expansion ratio based on the total canopy height was $ER = 1.062$, which was smaller than for the BFS case. For blockage that covers a significant area of floor surface it is useful to describe the blockage effect in terms of dynamic quantities. The Association of German Engineers (VDI [133]) has developed guidance for wind tunnel testing, limiting blockage to less than 5% of the wind tunnel cross section. A dimensionless parameter to describe blockage can be written as $P^* = \left(\frac{\partial P}{\partial x}\delta\right) / \left(\frac{\rho}{2}U_\delta^2\right)$. In our wind tunnel experiment, the value for P^* over the canopy was 1.2%.

5.4.2 Instrumentation

Measurements of the flow field and surface shear stress were made to characterize the distribution of wake flow characteristics and fluxes using a combination of particle image

Table 5.1: Characteristics of the wind tunnel experiments.

	h (cm)	H_{wt}/h	ER	δ/h	L/h	a (m^{-1})	Re_h
Solid BFS	1.27	9	1.125	1.5	80	∞	3.7×10^4
Canopy BFS	10	17	1.062	6	25	1.0	1.5×10^5

H_{wt} = wind tunnel test section height, h = canopy (step) height, ER = expansion ratio, = boundary layer thickness, L = streamwise length of the canopy or step, a = canopy area density, Re_h = Reynolds number of wind tunnel experiment based on canopy or step height and mean flow velocity

velocimetry (PIV), cross wire (×-wire) probes and pressure based measurements including Pitot and Preston tubes (Fig. 5.2). The Pitot tube was used for calibration of the ×-wire sensor as well as for recording the freestream wind speed. High-resolution PIV (TSI, Inc.) was used to measure two velocity components in 2-D vertical streamwise (x-z) planes along the centerline of the test section and centered between two rows of canopy elements (cylinders). A 190 mJ dual-head Nd:YAG laser (Quantel-USA) was used as the light source. The laser beam was focused and transformed into a light sheet ($\sim$ 1.5 mm thick) using cylindrical and spherical lenses. Two PowerView Plus 4MP 12-bit CCD cameras (2,048 × 2,048 pixels) fitted with 10^5 mm lenses and operating in frame-straddle mode were mounted to capture particle images. The seeding particles were composed of olive oil, which was atomized using compressed air to generate 1 μm droplets which were released via a vent in the test section floor downwind of the trip. The seed was allowed to fully homogenize within the tunnel prior to measurements. Calibration of the particle images was achieved by imaging a target with a regular grid placed in line with the light sheet. The total size of the field of view (FoV) was approximately 14 cm × 14 cm. The scale factor was then determined based on the known grid spacing. The PIV images were processed using a recursive Nyquist cross-correlation procedure analysis, starting with 64 × 64 pixel interrogation windows and ending with 32 × 32 pixel interrogation windows with a 50% interrogation window overlap. A FFT convolution and a Gaussian peak finding algorithm augmented the analysis. Using these settings provided approximately 10 particle image pairs per interrogation window, which

results in an expected uncertainty in finding the peak displacement of 0.1 pixels [134]. With particle image displacements of 8 to 10 pixels, this corresponds to an error smaller than 2% per velocity vector. Pixel locking errors were avoided by slightly defocussing the particle images. Vector fields were post-processed to check their quality and vectors deemed in error were backfilled based on accepted methods reported by Raffel et al. [135]. Vectors deemed erroneous accounted for less than 2% of vectors in any field and were replaced by vectors interpolated using a Gaussian scheme from valid neighboring vectors. Final instantaneous vector fields were recorded with 127×127 vectors with a spacing of 1.1 mm, which corresponds with the smallest scales for this turbulent flow. In order to have sufficient data to converge the flow statistics for second order turbulence and covariance components, 3,000 instantaneous vector fields were acquired for each FoV. The mean velocity measured with PIV agreed with Pitot tube profiles, and multiple wind speeds were considered to determine that the results presented here are Reynolds-number independent.

Seven PIV windows or FoV were measured (Fig. 5.2). To characterize the fully developed flow within the canopy, a FoV was centered at $x/h = -5$ starting just above the top of the baseboard. No canopy elements were removed and only a gap approximately 1.4 cm ($\sim$ 12 vectors) wide was viewable at the center of the window. An additional FoV was measured above the canopy to characterize the turbulent flow in the canopy and the boundary layer above. Similarly another stacked FoV pair was centered at $x/h = -0.2$. Three subsequent FoV were captured at the downwind edge to $x/h = 4$, which was determined to be beyond the downwind extent of the separation region. The canopy was painted flat black to minimize reflections and a fluorescent paint was used along with an optical filter, mounted on the camera, to ensure good data quality near surfaces.

Hot-wire anemometry (HWA) was employed to characterize the boundary layer above the canopy and the wake adjustment downwind. A standard cross-wire ($\times$-wire) type sensor was used to measure high temporal resolution profiles of streamwise and wall normal instantaneous velocities. The probe consisted of two 5 μm platinum-coated tungsten wires, which are copper-plated and soldered to the prong ends and etched, yielding an active length-to-diameter ratio of about 200. The signals were acquired using a 10-channel A.A. Labs Systems (Ramat-Gan, Israel) Constant Temperature Anemometer

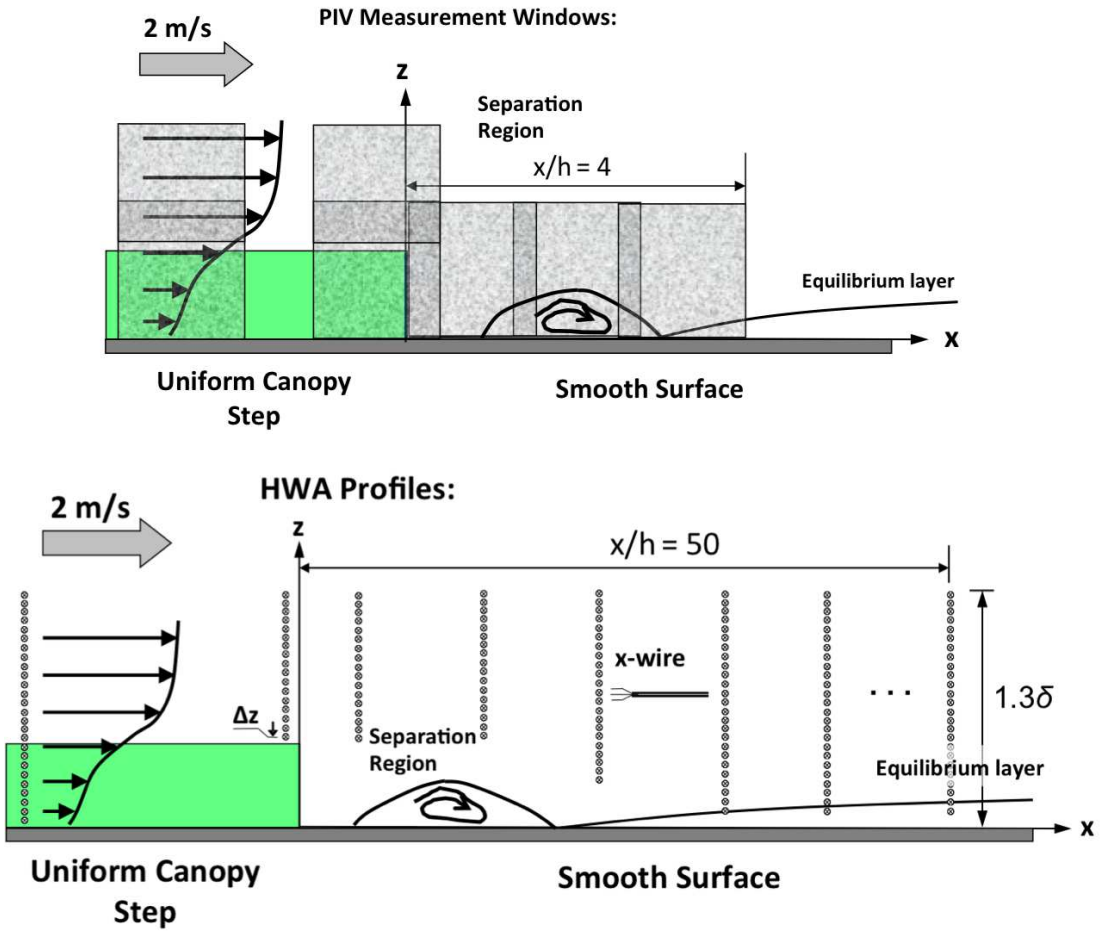

Figure 5.2: Schematic of measurement locations for the canopy BFS experiments. Top: PIV measurement windows upwind of the canopy edge ($x = -5h$), at the canopy edge and downwind to beyond the mean flow reattachment location (seven fields of view); Bottom: $\times$-wire profiles measured outside the highly unsteady separation region from $x = -5h$ to $x = 50h$ and up to $z = 8h$ (16 profiles, exact profile positions not shown, profile locations listed in text). Note: figures are not drawn to scale.

(CTA) system on an AN-1003 board, which was connected to a National Instruments (Austin, TX) 16 channel 24-bit PXI data acquisition system (NI 4472), and custom LabView programs. Data were streamed to a quad core desktop commuter hard drive for later transfer and data processing. The overheat ratio was set to 1.5. The signal was sampled at 20 kHz, low-pass filtered at a frequency of 2 kHz and digitized with a 12 bit A/D converter. Each position was sampled for 90 s providing a total number of 1.8×10^5 instantaneous data points per channel for each measurement position. Calibration was performed in a homemade standalone jet calibrator fitted with a heating/cooling unit to allow for a range of temperatures to be achieved. The calibration was conducted against a Pitot tube and a fine-wire thermocouple with a constant temperature held at the same temperature as the wind tunnel test section, 30 ± 0.25°C, to avoid bias errors due to thermal drift of the voltage signal. Five velocities and seven inclination angles were collected and a cubic-spline lookup table method was used to determine instantaneous velocities from the two voltage records. Calibration was performed before and after the experiments to verify the calibration throughout the experiment. More details on the calibration procedure can be found in Bruun [58] and Tropea et al. [59]. Measurement uncertainty for mean velocities was within 1%, while turbulence statistics were accurate within approximately 3% to 5% depending on the turbulence levels in the flow and distance to the wall or to the canopy model (cf. [136, 137]).

The sensor was mounted on a traversing system (Velmex, Inc) with a high-resolution stepper motor allowing for accurate vertical positioning and was controlled with a custom LabView program. Additionally, due to the conductive nature of the aluminum test section floor, an electric circuit was set up to signal contact of the conductive sensor holder with the floor to allow for accurate origin placement. Profiles were collected with a normalized vertical spacing of $\Delta z/h = 0.05$ up to $z/h = 0.4$, then $\Delta z/h = 0.1$ up to $z/h = 3$, followed by $\Delta z/h = 0.5$ up to $z/h = 8$. Locations within the canopy and in the separation region were not included due to errors associated with an intrusive measurement method in recirculating flows. The vertical profiles were collected at distances of $x/h = -5, -2, 0, 2, \cdots 12, 16, 20, 25, 30, 40, 50$ (Fig. 5.2). Additionally a profile was collected over the rough upwind surface to characterize the boundary layer development upwind of the canopy. Another profile was collected with the canopy and roughness removed to characterize the smooth downwind surface. Comparisons with Pitot tube

measurements revealed good agreement between the mean profiles. Second-order finite differencing was used to calculate spatial derivatives presented in the analysis. Finally surface shear stress was measured using a Preston tube following the procedure of Patel [138]. The Preston tube method tends to perform poorly in regions of strong pressure gradients and near flow separation. Therefore, only the far wake region is represented in our dataset for the canopy step.

5.4.3 Developed flow over the canopy and over the smooth floor

In this section we present the upwind and downwind boundary conditions that framed the transition from the canopy to the flat smooth surface in the wind tunnel experiments. Figure 5.3 shows profiles of normalized mean velocity, streamwise normal and wall-normal Reynolds stresses in and above the canopy at a distance $x = -5h$ upwind of the canopy edge. The turbulence stresses are normalized by the friction velocity, defined as $u_* = \left(-\langle\overline{u'w'}\rangle_{z=h}\right)^{1/2}$. Measurements were taken in multiple spanwise planes to determine the significance of dispersive stresses, it was found that they are minimal and can be neglected, but we note that dispersive fluxes will be increasingly important for sparser canopies (cf. Poggi et al. [51]). The measured profiles compare well with previous canopy flow studies, exhibiting characteristics of dense canopy flows, including an inflected mean velocity profile, and turbulence and shear stress profiles that diminish exponentially within the canopy (cf. Finnigan [42]).

Determination of the canopy drag development length scale L_c requires knowledge of the canopy area density and canopy element drag coefficient. The canopy area density is equal to the frontal area of canopy elements divided by the unit volume surrounding each element. In the wind tunnel experiment $a = \lambda_f h = 10\ \mathrm{m}^{-1}$, where $\lambda_f = A_f/A_t$ is the roughness density. The drag coefficient can be calculated based on the flow for the fully developed region at $x/h = 5$. Rearranging relevant terms of the momentum equation,

$$C_D(z) = -\left(\frac{\partial\langle\overline{u'w'}\rangle}{\partial z} - \frac{1}{\rho}\frac{\partial\langle\overline{P}\rangle}{\partial x}\right)\left(a\langle\bar{u}\rangle^2\right)^{-1}. \tag{5.8}$$

The parameterization for form drag utilizes the standard meteorological convention and does not include the factor of 1/2, commonly used in an engineering context. To

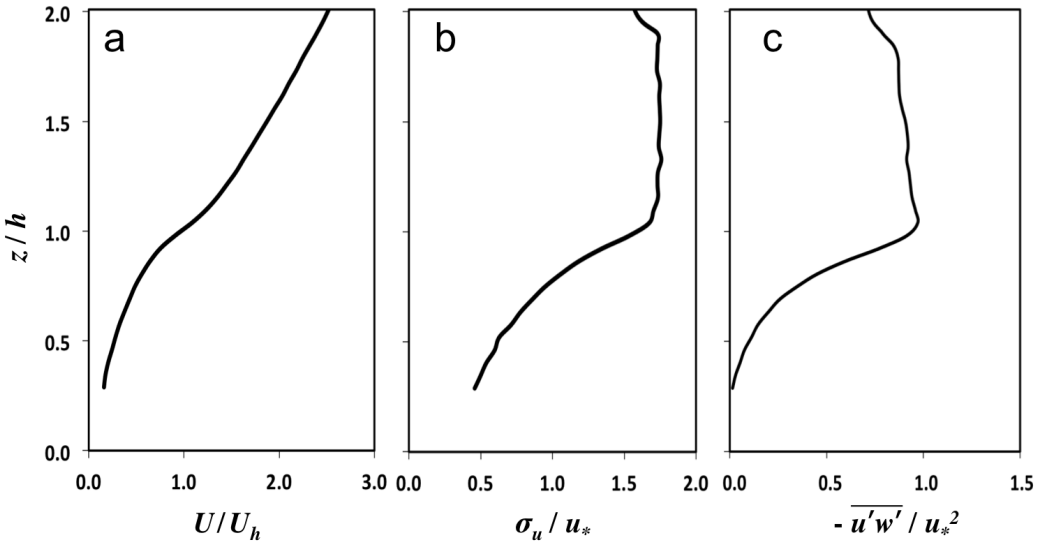

Figure 5.3: Profiles for the developed flow in and above the model canopy from PIV. a) mean velocity normalized by the mean velocity at the top of the canopy U_h, b) Root-mean-square velocity perturbations normalized by u_*, c) Reynolds shear stress normalized by u_*^2.

estimate the influence of the longitudinal pressure gradient, we considered the balance with with the slope of the shear stress over the canopy

$$\frac{\partial \left\langle \overline{u'w'} \right\rangle}{\partial z} - \frac{1}{\rho} \frac{\partial \left\langle \overline{P} \right\rangle}{\partial x}. \tag{5.9}$$

Based on the shear stress profile presented in Fig. 5.3c, for z/h between 1 and 1.9, the kinematic pressure gradient is 0.04 m s^{-2}. Using this result and measurements of the stress divergence and local mean velocity, a vertical distribution of C_D was determined. The drag coefficient varied between 0.6 to 1.6 from the top of the canopy down to approximately $z/h = 0.2$. The variation is related to sheltering by upstream canopy elements and the variation of Reynolds number with height (cf. [139, 140]). The average C_D through the canopy was approximately 1.2 and the value at the height of the centroid of the applied drag force was 1.0. If we take $C_D = 1.0$, then L_c is entirely described by the geometry of the canopy as $L_c = \lambda_f h^{-1}$. Using this value we could determined that L_c was approximately 0.1 m or equal to the canopy height. This is consistent with dense forest canopies commonly found in the field (cf. Belcher et al. [44]). The model

scale LAI could be easily calculated as LAI = ah and was equal to 1.0. However, one could consider L_c with canopy height in a dynamic scaling to relate the model scale to the field scale. For a field scale canopy with a mean height of 20 m, and an $L_c/h = 1$, if we assume a nominal drag coefficient of 0.2 as commonly found in field experiments (Kaimal and Finnigan [50]), the equivalent canopy area density for the field case would be 0.25 m^{-1}. The equivalent LAI ≈ 5, which is comparable with the field study of Detto et al. [106] and the LES runs #2 (LAI = 4) and #3 (LAI = 6) by Cassiani et al. [105].

Based on Eqn. (5.6), the shear layer scale is $L_s = 0.33h$. Raupach et al. [68] reported that the signature of Kelvin-Helmholtz type coherent vortices could be detected near the top of canopy flows. Using single and two-point correlation statistics the streamwise spacing of these vortices can be determined. It was found that there exists a linear relationship between the shear length scale L_s and the vortex spacing Λ_x. In this study it was determined that the proportionality constant $m = \Lambda_x/L_s \approx 9$. This is slightly larger than $m = 8.1$ found by Raupach et al. [68], but within the range found in other studies, e.g. Bailey and Stoll [127]. The zero-plane displacement height was determined as the level at which the mean drag acts [141, 87]

$$d = \frac{\int_0^h z F_c(z) dz}{\int_0^h F_c(z) dz}. \tag{5.10}$$

The displacement height was found to be 0.07 m or $d/h = 0.7$. By fitting the measured velocity profile above the canopy to Eqn. (5.7), the aerodynamic roughness was determined to be z_{01}=12 mm or $z_0/h = 0.12$. This value matches the theoretical model from Raupach [49], which estimates that a canopy of the density studied here results in the maximum effective roughness relative to the canopy height.Canopy aerodynamic characteristics are summarized in Table 5.2.

To characterize the fully developed boundary layer flow over the smooth surface downwind of the canopy step, we removed the canopy and the roughness chains, and measured the fully-developed velocity profile over the wind tunnel floor. Figure 5.4 shows the mean velocity normalized by the freestream velocity U_0 plotted on Cartesian scales against the canopy height. Also shown is a semi-logarithmic plot of the velocity profile normalized by the viscous scale. Because the surface is aerodynamically

Table 5.2: Model canopy characteristics.

	LAI_{exp}	LAI_{field}	u_*/U_h	d/h	z_0/h	C_D	L/L_c	L_c/h	L_s/h
Canopy BFS	1.0	5.0	0.38	0.7	0.12	1.0	25	1	0.33

LAI = plant area index, h = canopy (step) height, d = zero plane displacement, z_0 = aerodynamic roughness, C_D = effective canopy element drag coefficient , L = streamwise length of the canopy or step, L_c = drag development length scale, L_s = shear length scale

smooth, the effective roughness depends on Reynolds number. The momentum thickness Reynolds number, $\mathrm{Re} = \mathrm{U}_0\theta/\nu = 5,040$. The data fall on the universal law of the wall boundary layer

$$u^+ = \frac{1}{\kappa}\ln z^+ + A \tag{5.11}$$

where $z^+ = zu_*/\nu$ and ν is the kinematic viscosity, $\kappa = 0.4$, and $A = 5$ (Fig. 5.4b). The effective roughness length for the surface can be estimated by the Classer fit method of the data in the inertial sublayer. We determined $z_{02} = 0.15\nu/u_*$ and estimated the effective roughness to be $z_{02} = 0.03$ mm. The surface shear stress, and therefore the surface roughness, grows with mean wind speed over the smooth surface. Although the surface is solid and smooth (aluminum plates), and not water as in lakes, a similar behavior is expected over water, at least qualitatively.

Longitudinal energy spectra of streamwise and vertical velocity components measured at $z = 0.1$ m or $z/h = 1$ of the incoming flow upwind of the canopy are shown in Figure 5.5. The spectra were calculated by taking the fast Fourier transform (FFT) of the time series of the velocity fluctuations (u' and w', 2^{16} samples) utilizing a square window of 2^{12} points. Using Taylors hypothesis and standard surface layer scaling, the analysis shows the classical production subrange and inertial subrange for the surface layer turbulence, identified as regions that follow power law scaling with -1 and -5/3 slope, respectively. These regions intersect at $kz = 1$ as is expected in the atmospheric boundary layer [142]. However, unlike in the full-scale field boundary layer, there is only approximately one decade corresponding to production and one and a half decades in

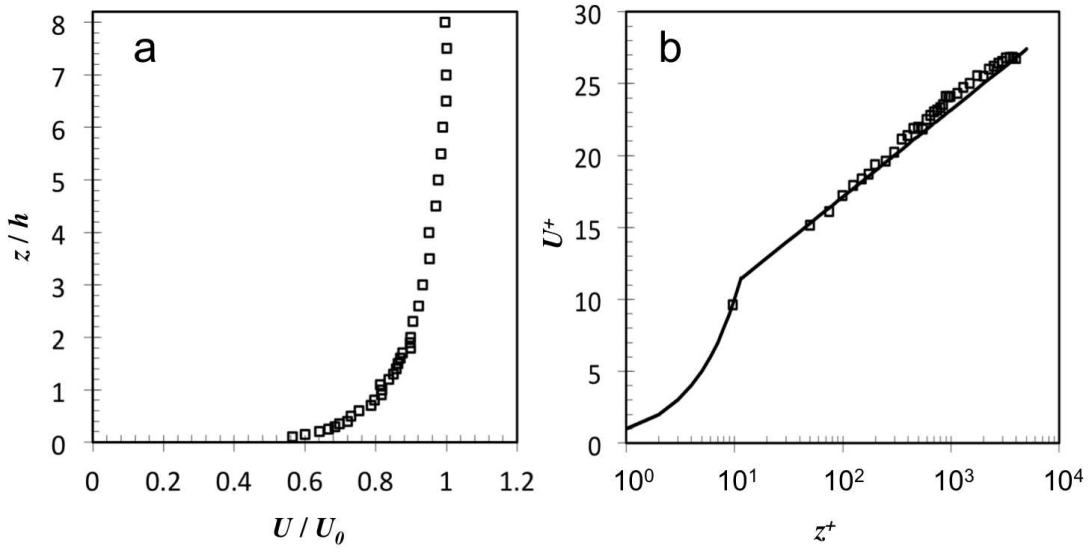

Figure 5.4: Boundary layer velocity profile at an infinite distance downwind of the canopy BFS. a) vertical profile of the normalized mean velocity, b) the mean velocity plotted in wall units along with the law-of-the-wall for the viscous and inertial sublayers.

the inertial subrange. In the inertial range, both $E_u(k)$ and $3E_w(k)/4$ collapse, indicating isotropic behavior. The transition from the inertial to viscous subrange occurs at a scale of approximately 5 mm ($\Delta = \pi/\kappa$), which is larger than the resolution of the PIV measurements. The normalized energy spectra for the developed flow over the canopy measured at $z/h = 1.5$ and $x/h = 5$ are plotted based on canopy scaling parameters, appropriate for roughness sublayer turbulence, and show good agreement with previous experiments (e.g. Kaimal and Finnigan [50]). In particular a clear region corresponding to the production subrange with a spectral slope of one, a peak at relatively low frequency, and an inertial range with slope of -2/3 are clearly shown. Similar results were shown in the wind tunnel experiments of Novak et al. [126].

5.5 Results

Next we report the key turbulent flow features observed and/or measured in the wind tunnel in the transition (wake) from the canopy BFS to the downwind smooth surface. We interpret these results compared to the dominant features reported for the

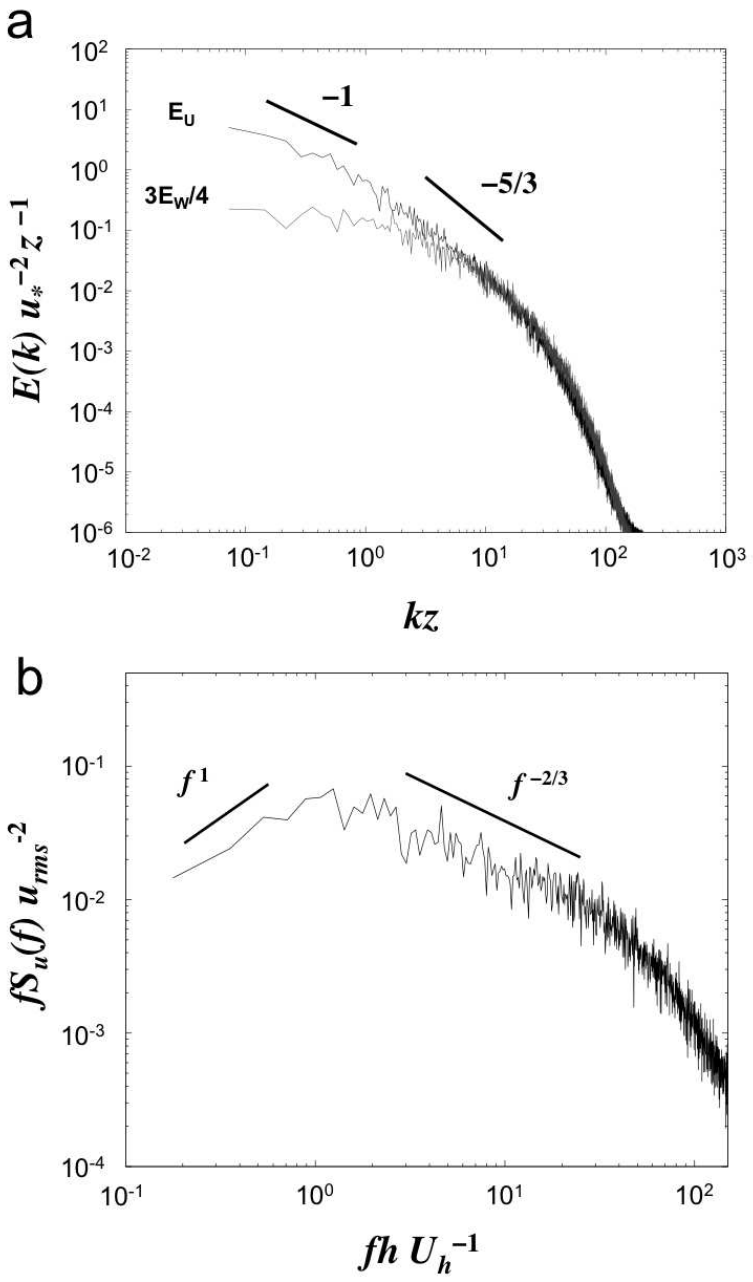

Figure 5.5: a) Longitudinal energy spectra of streamwise and vertical velocity components measured by an ×-wire probe, in the velocity profile upwind of the canopy entrance at $z = 0.1$ m ($z/h = 1$), normalized based on surface layer scales, b) the velocity spectra for the streamwise velocity component in the fully developed flow over the canopy at $x/h = 5$ and $z/h = 1.5$, normalized based on canopy flow scales.

solid backward facing step (BFS) by Driver and Seegmiller [130] and illustrate the differences between the canopy BFS with a porosity $\eta = 0.95$ and the solid BFS with $\eta = 0$. Because there are differences between the two experiments, especially the ratio of boundary layer thickness to step height δ/h, we do not intend to make direct quantitative comparisons between the two BFSs; instead we illustrate and interpret the significant topological differences in the two flow fields. We review the solid BFS first as it serves as a reference. Specific analyses presented in the following sections include:

Section 5.5.1: We present the mean velocity and turbulence statistics in a two – dimensional plane along the centerline of the flow. The streamlines illustrate the differences in flow topology. We can also see the effect of a much larger effective roughness and mixing-layer type instability over the canopy propagating into the wake.

Section 5.5.2: We present mean flow profiles, integral characteristics of the boundary layer in the transition (wake), and an analysis of the velocity deficit. These show clearly that a new surface layer cannot be detected for long distances downwind of the transitions. There are significant differences in the integral properties of the flow over the canopy BFS versus the solid BFS, larger distances are required for momentum to recover downwind of a canopy BFS. We also see that the velocity deficit in the canopy wake follows a power-law decay similar to a plane wake and is height-invariant, which is in contrast to the solid BFS.

Section 5.5.3: We present the momentum budgets in the longitudinal and vertical directions for the two BFS flows. We discuss the significance of each term of the momentum equation at various locations in the wake flow. Significant contributions of the advection, stress divergent and pressure terms for long distances downwind of the canopy are demonstrated; this supports the long recovery distances observed in the mean and turbulence flow statistics.

Section 5.5.4: We present an analysis for the mixing length characteristics in the flow field. We see clearly the wide range of length scales, which need to be captured in models of wake flows involving flow separation.

Section 5.5.5: We present the direct measurements of surface shear stresses, which are important for parameterizing heat, moisture and mass fluxes at the land-atmosphere interface, and for modeling of transport processes in small lakes and wetlands. We then demonstrate the challenges of determining surface fluxes due to the non-equilibrium state of the flow in the wake region. This is important for point-based field measurements, e.g. surface fluxes of CO_2 and CH_4, especially for surface layer parameterizations used in models of the ABL.

5.5.1 Measurements of the turbulent statistics

Solid BFS turbulence

The transition of the mean wind flow over a solid BFS is characterized by the separation of the flow at the step edge, a separation eddy, and then mean flow reattachment and downwind boundary layer redevelopment. The key length scale is the reattachment length which depends on the incoming boundary layer flow, particularly its Reynolds number, mean pressure gradient, and level of inflow turbulence [129].

Figure 5.6 shows the 2-D normalized mean velocity field and corresponding streamlines for the flow over a solid BFS. The inflow has a relatively thin turbulent boundary layer, which separates at the edge of the step, and reattaches downstream. A significant region of low momentum flow exists downwind of the step. The streamlines identify the separation region. Note that the secondary reverse eddy at the bottom corner of the step was not captured by these LDV measurements. Based on oil film interferometry, the location of mean flow reattachment was found to occur at $x/h = 6.2$. This is in good agreement with the separation streamline based on the velocity data.

Figure 5.7 shows the turbulence intensity and Reynolds stresses in the wake flow downwind of the solid BFS. Due to the smoothness of the wall on top of the step, the incoming turbulence is quite low, and most of the turbulence is generated downwind by the shear layer that forms between the overlying flow and the separation region. This also leads to intense Reynolds shear stresses in the flow. The turbulence intensity and shear stress are observed to persist far downstream of the location of mean flow reattachment, i.e. beyond $x/h = 30$. More details can be found in Driver and Seegmiller

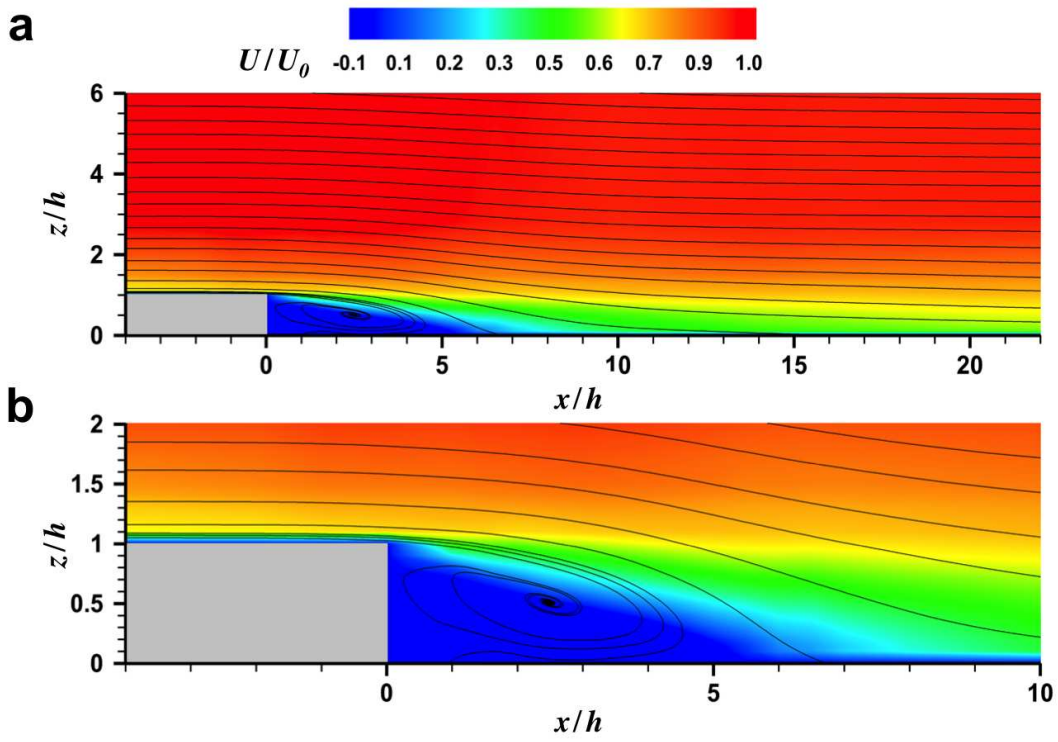

Figure 5.6: Flow over a solid BFS. Contours of normalized mean streamwise velocity and streamlines result from LDV profile measurements. The velocity measurements are normalized by the freestream velocity, U_0. a) Full dataset, and b) zoomed to details of separation region just downwind of the canopy edge. A grey box illustrates the location of the solid step. Data from Driver and Seegmiller (1985).

[130]. These results highlight the salient characteristics of solid BFS type flows. Next we will examine how the flow field and turbulence structure of wind blowing over a canopy impacts the wake of a canopy BFS.

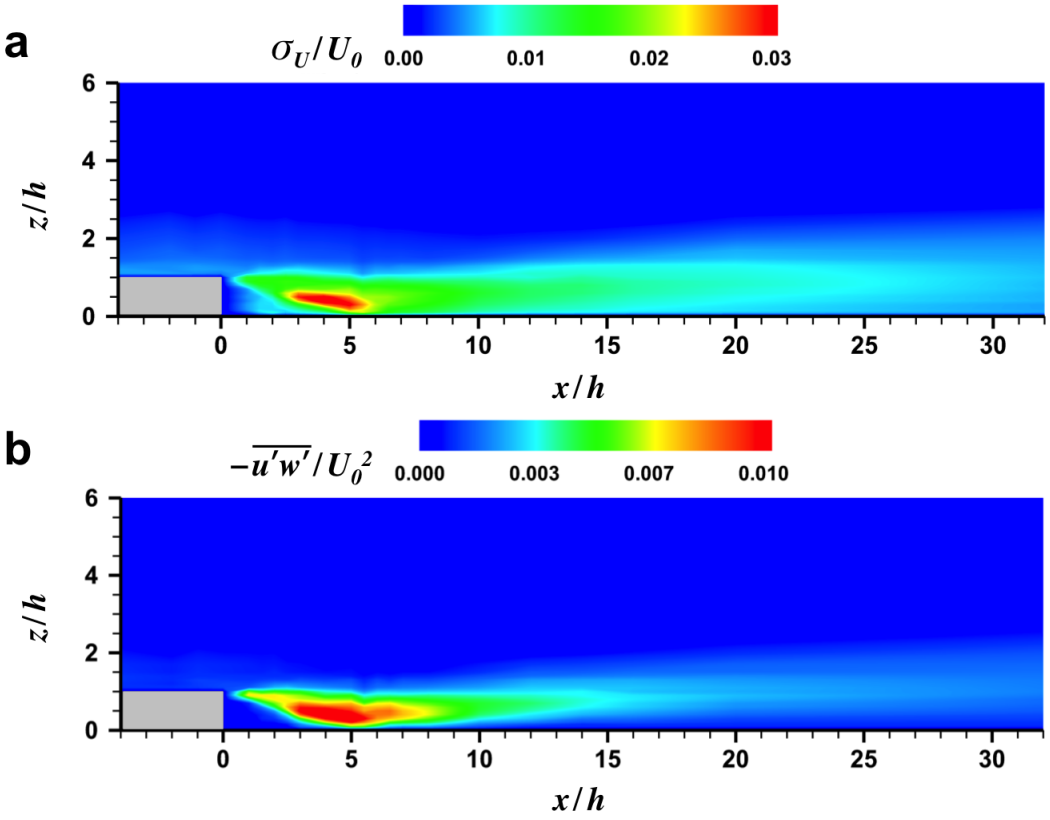

Figure 5.7: Solid BFS turbulent flow fields. Turbulence fields from LDV profile measurements for: a) turbulence intensity, b) and Reynolds stress distribution. A grey box illustrates the location of the solid step. Data from Driver and Seegmiller (1985).

Canopy BFS turbulence

Unlike the turbulent flow over the smooth surface of a solid BFS, the flow over a canopy exhibits a flow structure that is similar to a plane mixing layer. This results in a thicker boundary layer and higher turbulence intensity and shear stress over the canopy, and leads to distinctly different flow properties in the wake of a canopy BFS compared to a solid BFS. However, the mean flow over and through a canopy BFS displays some

similarities to the BFS type flow as well. Figure 5.8 shows the high-speed flow over the canopy measured in the wind tunnel. In the lee of the canopy, a separation zone can be identified. The mean flow reattaches further downwind, and a new boundary layer begins to redevelop. Some flow propagates within the canopy and leaks out downstream of the edge. Upwind of the canopy edge, exit effects are detected. In particular, although higher order turbulence statistics do not appear to vary, the mean velocity and streamlines show indications of subsidence and acceleration downwind of approximately $x/h = -4$. This is in contrast to the flow over a solid BFS, where the sharp corner causes an immediate separation of the flow (as seen in Fig. 5.6). In the case of the canopy BFS, the leakage flow leads to a unique situation where the longitudinal pressure gradient increases gradually from the edge until a critical value is reached when the flow can no longer remain attached to the wall. The primary cause of flow separation is the loss of mean kinetic energy due to increasing pressure in the flow direction until forward flow is no longer possible against an increasing adverse pressure gradient. At this location the flow separates from the wall (e.g. Castillo et al. [143]). An additional length scale, i.e. the distance to where the flow separates X_s, emerges in addition to the standard BFS reattachment length scale X_R. In this wind tunnel experiment $X_s = 1h$ and $X_R = 2.5h$.

Compared to a surface layer type flow, the flow over a canopy is more turbulent due to the coherent Kelvin-Helmholtz type instability that forms over the canopy. The high turbulence and shear levels near the top of the canopy are maintained beyond the downwind edge of the canopy (Fig. 5.9), and as they are advected downwind they take on topological characteristics similar to an advected plume. The high turbulence and shear levels are observed far downwind of the canopy, well beyond $x/h = 50$. It is not clear how much of this is due to the differences between a rough or smooth wall versus the particular effect of the large turbulent eddies in the flow over a canopy. According to Raupach et al. [68] and Finnigan [42], the correlation coefficient or momentum flux relative to the absolute amount of turbulence in the flow over canopies is approximately $r_{uw} = (\overline{u'w'})/\sigma_u\sigma_w = 0.5$ compared to 0.3 for surface layers. Therefore the efficiency of momentum flux is about 1.7 times higher over canopies and may contribute to the shorter distance to reattachment.

The enhanced turbulence in the wake would be expected to have a significant effect

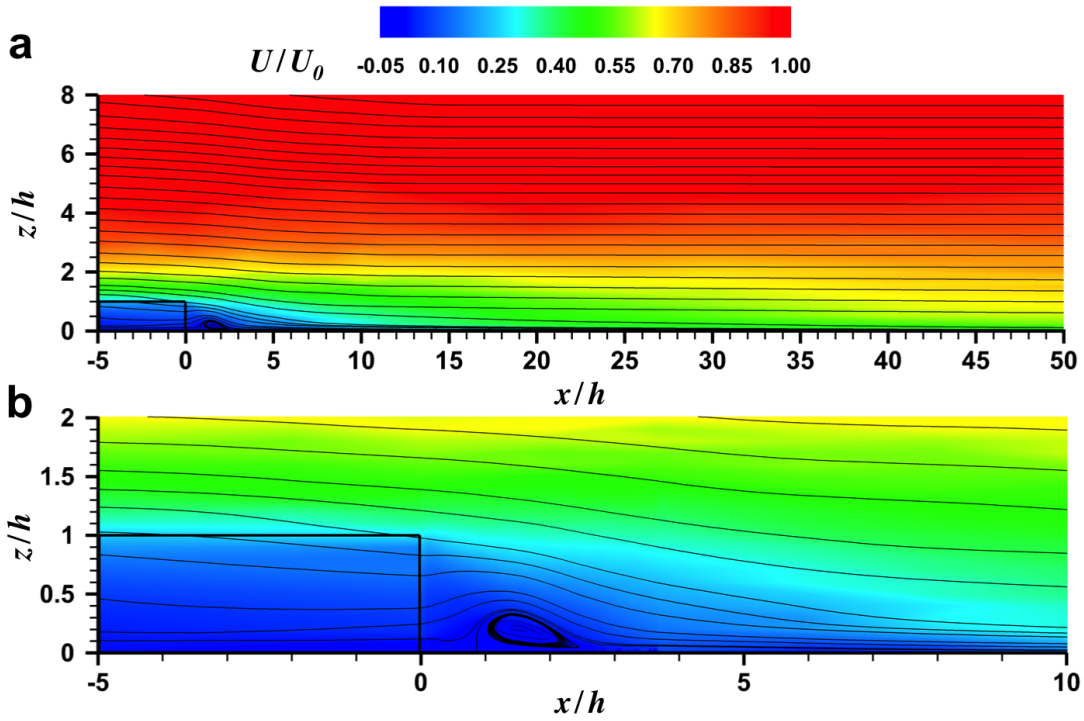

Figure 5.8: Canopy BFS flow fields. Contours of normalized mean streamwise velocity and streamlines result of ensemble averaged PIV velocity measurements over and downwind of the canopy edge combined with ×-wire profiles. The velocity measurements are normalized by the freestream velocity, U_0. a) Full dataset and, b) zoomed to details of separation region just downwind of the canopy edge. A thick black line outlines the top and lee-edge of the canopy.

on the flux of scalars, such as heat, moisture and trace gases. Vogel and Eaton [144] report that the heat fluxes downwind of a solid BFS are decreased at the lee edge of the step in the separated flow and substantially enhanced near the location of flow reattachment. The enhanced heat flux then asymptotically decreases in the far wake toward equilibrium with the downwind surface.

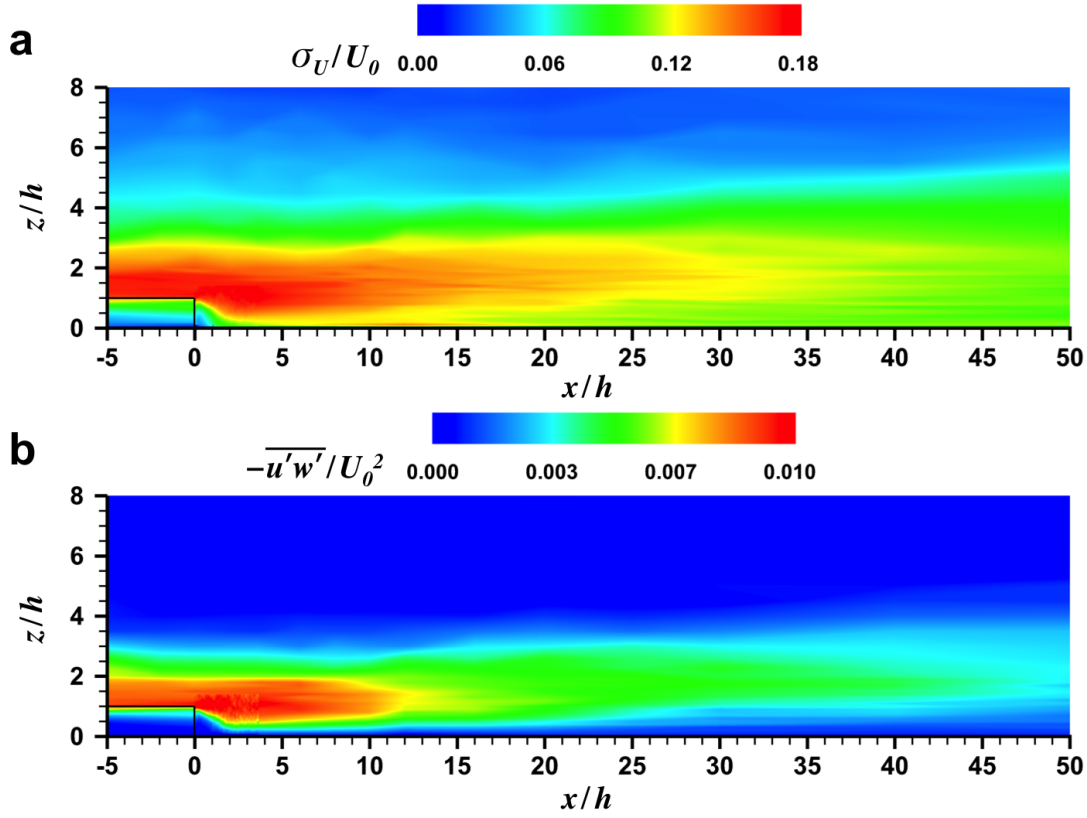

Figure 5.9: Canopy BFS turbulence fields. a) Turbulence intensity and b) Reynolds shear stress distribution in the x-z plane from combined fields of ensemble averaged PIV and ×-wire measurements. A black line outlines the top and lee-edge of the canopy.

It would be useful to find an effective step height that could be used to relate the distance to reattachment X_R for a canopy BFS to the X_R for a solid BFS. As a first approach we considered an effective step height, set equal to the displacement height, $d = 0.7h$. If we take an effective height $h^* = \gamma h$, where $\gamma = d/h$, we get $X_R = 3.57h^*$. This is much less than $X_R/h \approx 6$ found for a solid BFS. The displacement height is

therefore not a useful effective step height.

Alternatively, if the flow over the canopy is similar to a plane mixing layer, it would be reasonable that beyond the canopy edge, the mixing layer would evolve, expanding at a rate here assumed to be $d\delta_{\mathrm{ML}}/dx \approx 0.2$, (Dziomba and Fiedler [145]). Applied to a solid BFS, the distance to reattachment would be predicted to be $X_R/h \approx 5$. This is a shorter than the observed result $X_R/h \approx 6.2$. However, for the canopy the mixing layer model is more appropriate because the high-speed flow above the canopy and a low-speed leakage flow within the canopy are very similar to the classic mixing layer case. At the edge of the canopy, the canopy drag goes to zero and the turbulence is allowed to evolve unimpeded and the mixing layer grows until it is fully interacting with the wall. The flow then becomes a complex combination of the evolving mixing layer and the development of a surface layer flow. In our example of the canopy BFS flow, the shear layer scale is $L_s = 0.33h$. Finnigan [42] noted that a better estimate of the size of the coherent eddies at the top of the canopy is the vorticity thickness, $\delta_\omega = \Delta U/(dU/dz)_h$. The penetration of mixing layer vorticity can be estimated to be approximately $\delta_\omega/2$. At $x/h = -5$, the vorticity penetration is $\delta_\omega/2 \approx 0.44h$. At the canopy edge, $x/h = 0$, the flow has already began to adjust, and the vorticity penetration is $\delta_\omega/2 \approx 0.52h$. Based on a linear expansion rate estimated for the mixing layer flow at the canopy edge, $d\delta_{\mathrm{ML}}/dx \approx 0.195$, distance to reattachment is estimated to be at $X_R/h \approx (1 - 0.52)/0.195 = 2.46$ (cf. Lesieur [146]). This is in reasonable agreement with our measurements and may lead to an appropriate method for determining the reattachment length scale. This work would need to be extended to other canopy configurations to investigate the possibility for predicting X_R based on δ_ω. It is noted that δ_ω needs to be less than h for this method to be applicable, and therefore is only appropriate for dense canopies.

In addition to the mixing layer type turbulence at the canopy top, a significant momentum deficit in the wake of the canopy is another cause for the high turbulence as the flow moves toward adjustment with the new surface. A fully adjusted surface layer downwind was not observed in our measurements. The mean velocity profile is significantly different from the law-of-the-wall (see Fig. 5.10), and the Reynolds stress profile at $x = 50h$ peaks at approximately $z/h = 2$ (see Fig. 5.18). A fully adjusted surface layer would exhibit the peak Reynolds stress very near the surface at $z^+ \sim 30$ or

nearly $z/h = 0.1$. It is therefore clear that the flow requires very long distances to adjust to the new surface downwind of the canopy BFS. It is noteworthy that long recovery distances were also found for a solid BFS and other separating boundary layer flows at albeit lower Reynolds numbers by Bradshaw and Wong [147]. As will be explored later, the long transition affects the interpretation of point-based turbulence and flux measurements collected in the field, and causes the breakdown of common surface layer parameterizations in ABL models.

5.5.2 Development of mean flow properties

Figure 5.10 shows selected mean velocity profiles in the transition from the fully developed flow over the solid BFS and over and in the canopy BFS to the fully adjusted smooth boundary layer profile. The velocity profile approximating $x/h = \infty$ is measured on top of the step for the solid BFS case and corrected for elevation; for the canopy BFS case it is taken as the fully developed profile over the smooth wind tunnel floor, measured when the canopy was removed. It is evident that even at a distance $x/h = 50$ downwind of the canopy, the mean velocity profile is far from fully adjusted in both the solid and the canopy BFS experiments. The lowest measured velocity was at $z/h = 0.1$. If a new equilibrium layer has begun to develop near the surface (theoretically starting at $x = X_R$) it did not reach $z/h = 0.1$ before the last profile at $x/h = 50$.

By interpreting the mean velocity profiles in the context of roughness transition theory, some unique features can be identified (e.g. Garratt [148, 149]). Well above the canopy level, the velocity profiles exhibit classic rough to smooth transition characteristics, as the flow accelerates downwind of the canopy. The velocity data reflect the effects of the very rough upwind canopy up to and beyond $x/h = 50$. The internal boundary layer height has only grown to approximately $z/h = 2$ at $x/h = 50$. This corresponds to a distance $x/\delta \approx 10$. Based on the classic roughness transition model by Elliott [39], for $M = \ln(z_{01}/z_{02}) = 5.99$, $\delta_{IBL}/h = 4.2$ at $x/h = 50$. This value is twice as large as the experimental value. The model result is significantly in error because the power law formulation may not adequately represent a boundary layer transitioning from a rough to smooth surface [150, 151].

Displacement thickness δ^* and momentum thicknesses θ provide integral characteristics of the boundary layer transition. The ratio H of these measures $H = \delta^*/\theta$

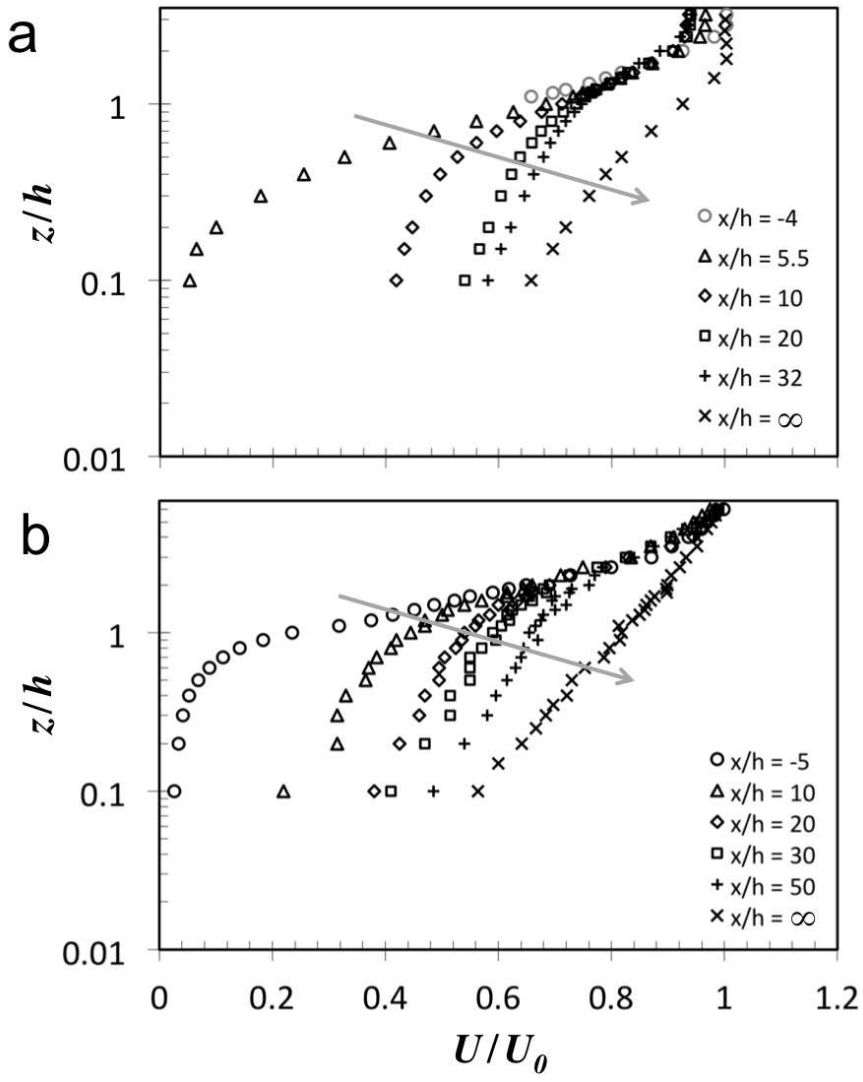

Figure 5.10: Selected normalized mean velocity profiles in the transition from: a) the solid BFS and b) canopy BFS to a fully developed smooth turbulent boundary layer. Arrows indicate increasing downwind distance.

defines the von Karman type shape factor (not to be confused with H_{wt}, the wind tunnel height). Figure 5.11 shows the displacement and momentum thickness distributions over and downwind of the canopy BFS as well as the shape factor. The value of H for a developed turbulent boundary layer is between 1.3 and 1.4 [152, 153]. A critical value of H at which point the flow becomes unstable and separates from the surface, has been determined to be approximately 2.76 ± 0.23 by Castillo et al. [143]. The plot of H in Figure 5.11 supports the observation of separated flow downwind of the canopy. The critical value of H is reached between $x/h = 0$ and 4, and based on the high-resolution PIV measurements; the flow reattaches at $x/h = 2.5$. The three integral values asymptotically approach the values of the fully developed downwind boundary layer. At $x/h = 50$ the shape factor is 1.3, which is within the range expected for a developed turbulent boundary layer. The reader is referred to Figure 9 in Driver and Seegmiller [130] for a similar plot for the solid BFS flow. The biggest difference is that the displacement and momentum thicknesses over the canopy BFS are large compared to the solid BFS. H is also larger over the canopy (nearly 3) compared to the developed surface layer value of 1.3 for the solid BFS.

Figure 5.12 shows the velocity deficit distribution downwind of the separated flow region. The velocity deficit is approximated as the difference between the reference velocity U_{ref}, taken as the approximate fully developed downwind velocity at the elevation of interest, and the velocity $U(x/h, z/h)$ at some position in the wake. In the far wake region, the velocity deficit is well represented by a power law. The distribution of velocity deficit is shown for two heights ($z/h = 0.5$ and 1.0) for both the solid BFS and the canopy BFS. The solid BFS exhibits variable wake recovery rates with height, while the velocity deficit recovery for the canopy BFS is nearly height independent. The recovery is more rapid in the far wake of the canopy BFS and follows a power law with an exponent similar to that of a plane wake, i.e. close to -0.5. In the near wake region, the velocity deficit does not follow a power law, but it is noteworthy that the adjustment occurs more rapidly in the near wake region of the solid BFS compared to the canopy BFS.

The rate of velocity deficit recovery provides an indication of the distance required for the boundary layer to develop. The findings for the flow development behind the canopy BFS indicate that the boundary layer develops to approximately the 90% level

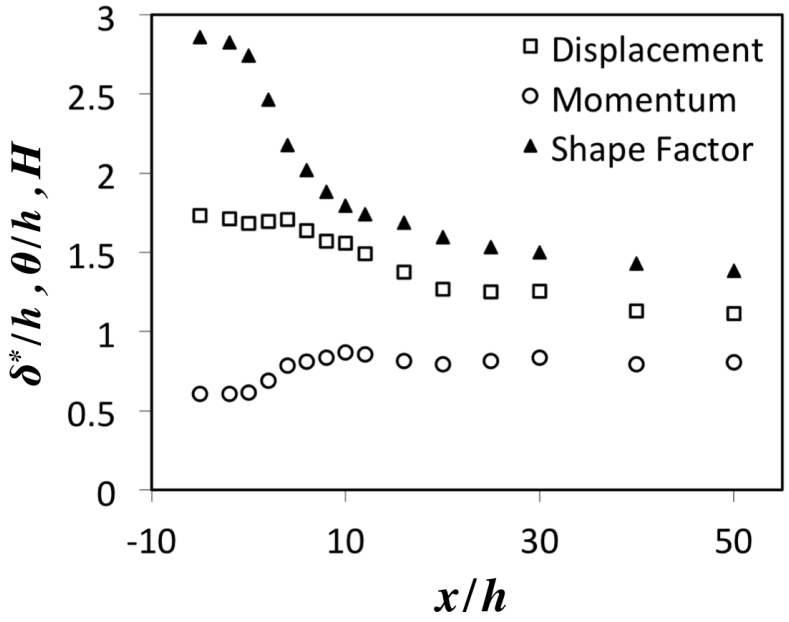

Figure 5.11: Variation of displacement thickness, momentum thickness, and shape factor for the canopy BFS.

just beyond $x/h = 100$. These results, in particular showing the very long recovery distance, are similar to the findings of Bradshaw and Wong [147].

5.5.3 Momentum budget in the wake region

Next we examine the relative contribution of each of the terms in the momentum equations (Eqs. (5.1) and (5.2)) in the wake of the solid BFS and the canopy BFS. The evaluations are focused near the surface, at a relatively low elevation of $z/h = 0.2$. The reason for this is that a height of $z = 2$ m is often the height at which meteorological data are collected in the field over low vegetation and water bodies (see Aubinet et al. [154] and various references therein for similar ecosystems), and increasingly high resolution ABL simulations use this low elevation as the first grid level. Generally the height of trees in forests is on the order of 10 m. Hence a relative height of $z/h = 0.2$ makes sense from an order of magnitude point of view. Additionally, $z/h = 0.2$ was the lowest elevation at which vertical gradients in the wind tunnel measurements could be evaluated. This height $z/h = 0.2$ also coincides with the center of the separation zone

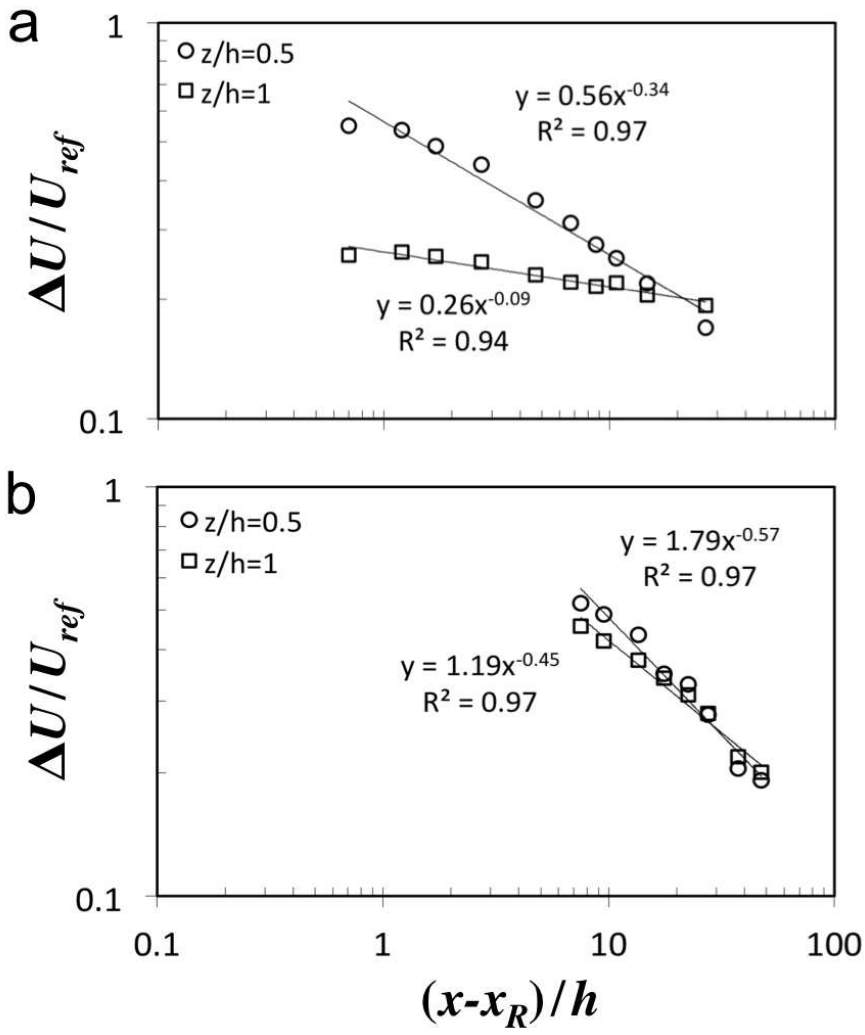

Figure 5.12: Velocity deficit distribution normalized by the reference velocity in the wake of a) the solid BFS and b) the canopy BFS at half the step or canopy height $z/h = 0.5$ and at the height of the step or canopy $z/h = 1$. The horizontal distance X_R is the distance from the step to the location of reattachment.

where we expect to see the largest range of scales to be present in the wake flow.

In this analysis the pressure term has been calculated as the residual of the balance of the other directly measured terms. The terms are normalized using the characteristic upwind friction velocity over the solid BFS and the canopy BFS, respectively, and the height of the step, h/u_*^2. In the evolution of the terms for the solid BFS (Fig. 5.13) and for the canopy BFS (Fig. 5.14) we see that all terms may be important at various positions within the wake. Downwind of the relatively dense wind tunnel canopy, the dispersive stresses were negligible. This may only be the case if the canopy edge has a uniform structure (i.e. $a(y, z)$ is constant), as is the case in this experiment, and is relatively dense. Canopies with gaps along the edge, or relatively sparse canopies may exhibit significant lateral variability in the mean wind. This will lead to significant dispersive stresses. Dispersive stresses have been found to be important at the entrance of even uniform dense canopies [52]. They may also be significant just upwind and near the edge of the canopy.

Downwind of a solid BFS, and for the momentum balance in the x-direction, the shear divergence, advection and pressure terms are all important throughout the transition. The shear and pressure terms are dominate. In the z-direction, the vertical normal stress divergence term is balanced by the pressure term. The effects of mean flow separation are found to diminish in the far wake beyond approximately $x/h = 15$ to 20.

The evolution of the momentum budget components downwind of the canopy BFS is shown in Figure 5.14. Similar patterns exist for the canopy BFS and the solid BFS. In Figure 5.14, and for the x-direction momentum components, the shear, advection and pressure terms are all dominant throughout the transition. The z-direction momentum components in Figure 5.13 and Figure 5.14 show similar behavior and magnitudes. The vertical normal stress term and pressure term are balanced in the near wake and the vertical advection term becomes important after reattachment. The effects of the canopy wake are evident in the x-direction terms even at $x/h = 20$ as shear divergence and advective flux terms remain significant. On the other hand, the effects of separation have dissipated before approximately $x/h = 15$ for the z-direction terms. This is coincident with decreased effects of subsidence with distance in the wake. It is clear for both the solid BFS and the canopy BFS that the pressure term is important in the wake flow

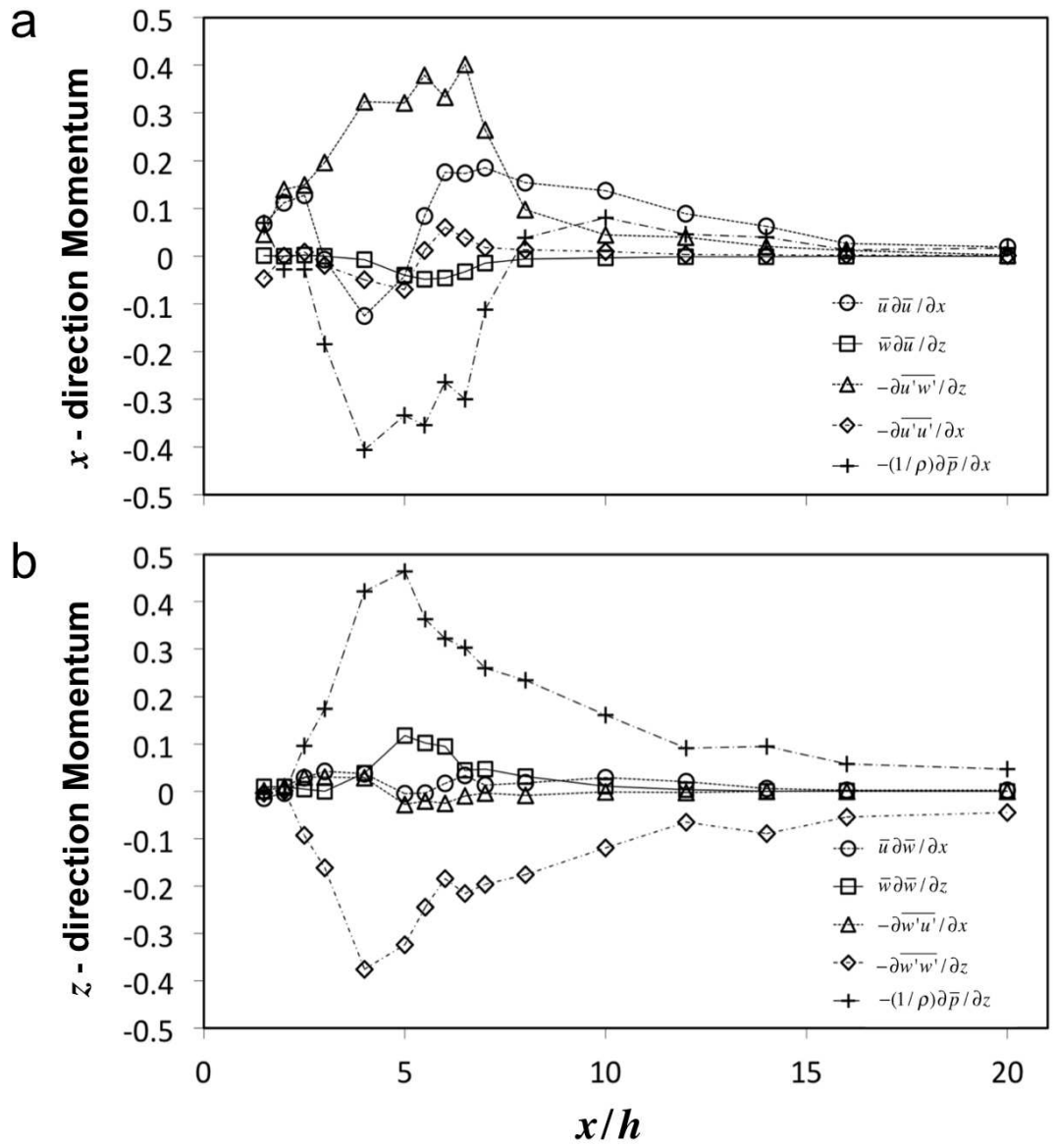

Figure 5.13: Solid BFS: a) Distribution of the terms in the momentum equation for a) the x-direction and b) z-direction at $z/h = 0.2$. Terms are normalized by h/u_*^2, where h is the canopy height and u_* is the friction velocity at the top of the solid BFS.

and must be included in any model describing the flow (cf. Belcher et al. [44]). In a developed boundary layer, over a flat surface, a constant flux region is present near the surface, in contrast the above data show that the vertical gradient of the Reynolds stress is not zero downwind of a canopy BFS nor a solid BFS. Therefore, the common practice to collect turbulent flux measurements at some height above the surface and equating the measured flux to that at the surface is not appropriate in flows affected by wake turbulence. Measurements must be collected at multiple heights near the surface to establish the flux gradient and need to be extrapolated to the surface to determine the correct surface flux. In Section 5.5.5 we show this only applies well below the elevation of maximum Reynolds stress in the wake. It is also clear from Fig. 5.14 that advective fluxes are important and must be accounted for long distances from the canopy edge.

5.5.4 Mixing length characteristics in the canopy wake

Prediction of a complex turbulent flow like the separated flow behind a solid BFS or a canopy BFS requires use of CFD. Many terms in the momentum equation are important for modeling the wake flow behind a canopy BFS or a solid BFS. To solve the momentum equation, a closure model is required for the Reynolds stress term. Combining the eddy-viscosity hypothesis (Boussinesq [155]) with Prandtl's [156] mixing length theory provides a common turbulence model to compute the Reynolds stresses as a function of the mean velocity gradients. The model can be written as $-\left\langle \overline{u'w'} \right\rangle = K_m(dU/dz)$, where, according to mixing length theory, the eddy viscosity K_m is parameterized as $K_m = l_{\text{eff}}^2 \left|\partial U/\partial z\right|$. The effective mixing length l_{eff} can therefore be determined from experimental data as $l_{\text{eff}} = \sqrt{-\left\langle \overline{u'w'} \right\rangle / (\partial U/\partial z)^2}$. The effective mixing length scale can also be used to identify different regions in the flow,based on the dominant scales present.

In the surface layer the effective mixing length is $l_{\text{SL}} = \kappa z$ and in a mixing layer $l_{\text{ML}} = 1/2 L_s$ where L_s is the length scale of characteristic eddies above the canopy. In the canopy layer, Inoue [71] proposed that the effective mixing length takes the form $l_{\text{CL}} = 2(u_*/U_h)^3 L_c$. For dense canopies with vertically uniform foliage density distribution, as in this wind tunnel experiment, l_{CL} is expected to be constant. For the canopy BFS experiment $l_{\text{CL}}/h = 0.11$, which is smaller than an estimate of l_{ML}. The extent of the separation zone X_R is also be expected to appear as an apparent scale.

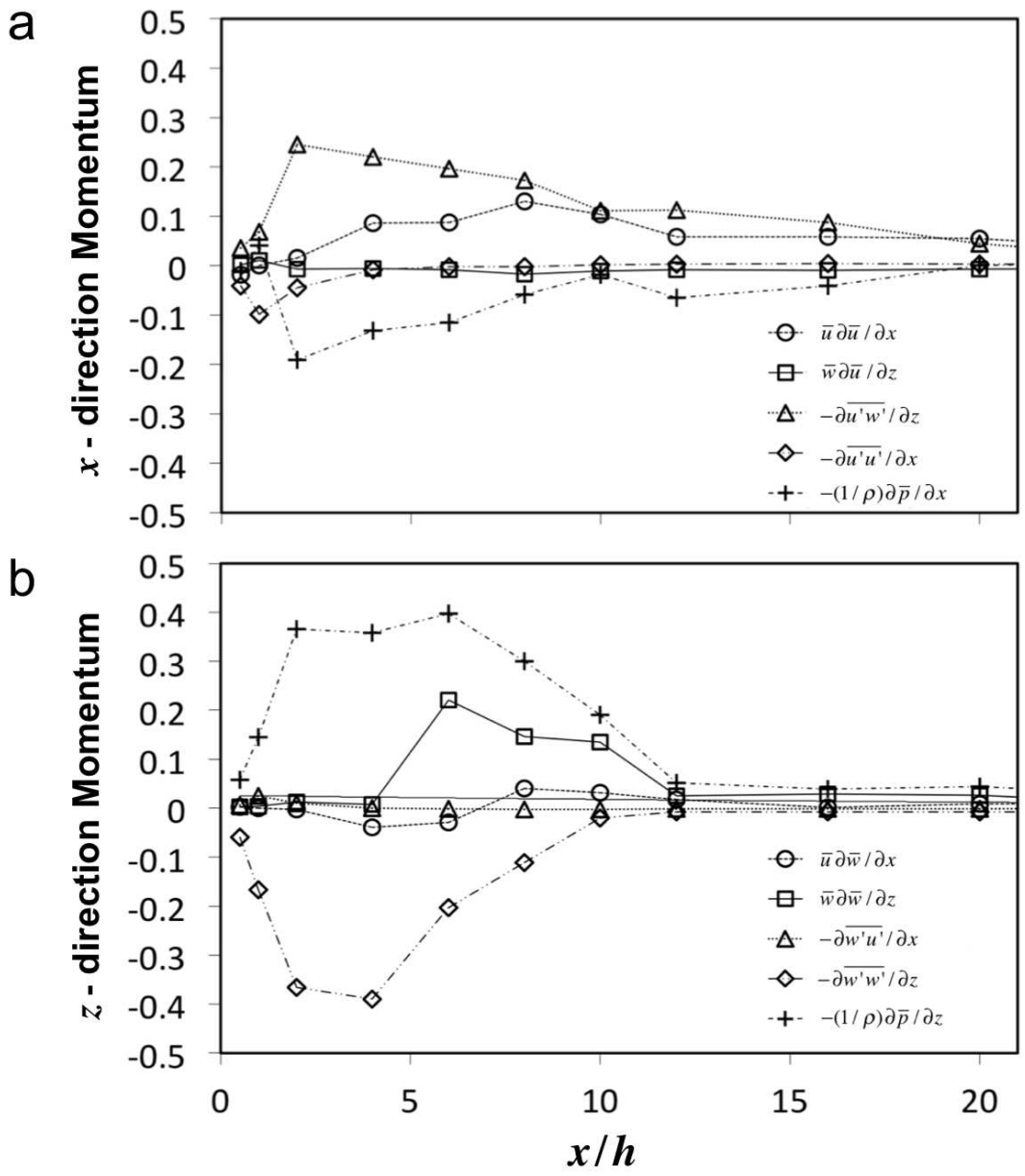

Figure 5.14: Canopy BFS: a) Distribution of the terms in the momentum equation for the x-direction and b) z-direction (b) at $z/h = 0.2$. Terms are normalized by h/u_*^2, where h is the canopy height and u_* is the friction velocity at the top of the canopy.

The separation bubble consists of a standing eddy, in this case, with a size $l_{\mathrm{SB}} \approx 0.4h$; the subsequent mixing length for the separation bubble is approximately, $l_{\mathrm{SB}} \approx L_{\mathrm{SB}}/2$. In Figure 5.15 we see the evolution of the effective mixing length l_{eff} downwind of the canopy BFS. Again we chose a height of $z/h = 0.2$ for reasons highlighted in Section 5.5.3 and also because l_{eff} exhibits the largest range in the wake, near the downwind surface. This also coincides with the lowest elevation in the flow for which the velocity gradient can be calculated in this experiment. At the canopy edge, $x/h = 0$, the scale is approximately the same as the canopy length scale, l_{CL}. In the separation region, the scale is similar to that associate with the separation bubble, l_{SB}. This also coincides with the height of the measurement. After about $x/h = 10$ the mixing length is approximately the value for a wall-bounded surface layer flow, l_{SL}. The mixing length smoothly transitions between the scales associated with these flow types.

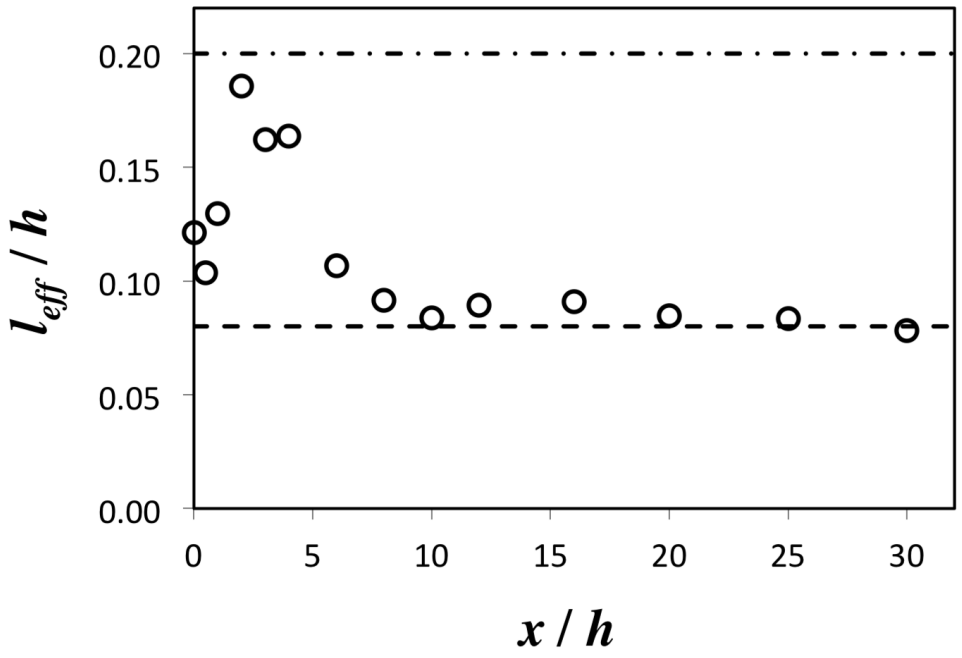

Figure 5.15: Distribution of the effective mixing length l_{eff} in the wake of the canopy BFS at $z/h = 0.2$. The dashed line is the surface layer scale over the downwind surface, and the dash-dotted line is the scale for the separation bubble.

5.5.5 Shear stress recovery

Direct surface shear stress measurements

The evolution of the turbulent flow in the wake of the canopy BFS is connected to the surface shear stress recovery. The development of the surface shear stress is a crucial boundary condition for determining surface fluxes of momentum, heat, moisture and other scalar quantities across the surface of a forest clearing, wetland, or small lake in the wake of a canopy BFS. Measurements of the surface shear stress with a Preston tube were made downwind of the edge of the solid BFS and the canopy BFS. The mean surface shear stress is zero where the boundary layer reattaches at X_R and then approaches the final downwind equilibrium stress $\tau_{s\ \mathrm{ref}}$ exponentially. The exponential form was found to match the solid BFS data of Bradshaw and Wong [147] well (Ottesen Hansen [102]). The relative surface shear stress distribution followed an exponential function between the location of flow reattachment and $x - X_R = 5h$. We found similar results for this region based on the data from Driver and Seegmiller [130]. In Figure 5.16 we see that the surface shear stress downwind of the point of mean flow reattachment ($x = X_R$) recovers much more quickly in the wake of the solid BFS case than for the canopy BFS. The exponential function fits the solid BFS data well between the location of flow reattachment and $x - X_R \approx 10h$, however the fit is poorer further downwind, in the far wake. A power law form fits the solid BFS data for the entire recovery, while an exponential function gives a better fit for entire stress recovery in the wake of the canopy BFS.

The exponential function takes the form,

$$\frac{\tau_s}{\tau_{s\ \mathrm{ref}}} = 1 - \exp\left[-\frac{x^*}{\lambda}\right] \tag{5.12}$$

where τ_s is the surface shear stress at $x^* = x - X_R$, $\tau_{s\ \mathrm{ref}}$ is the surface shear stress after equilibrium, and λ is a characteristic length scale of the shear stress recovery. λ most likely depends on canopy height, canopy porosity, momentum thickness over the canopy, roughness of the downwind surface and atmospheric stability. However, canopy height h, was proposed by Ottesen Hansen [102], and likely works well in the near wake. The experimental result is $\lambda \approx 5h$ for the solid BFS (fitting Eqn. (5.12) only to the near wake region) and $\lambda = 15h$ for the canopy BFS (fitting Eqn. (5.12) to

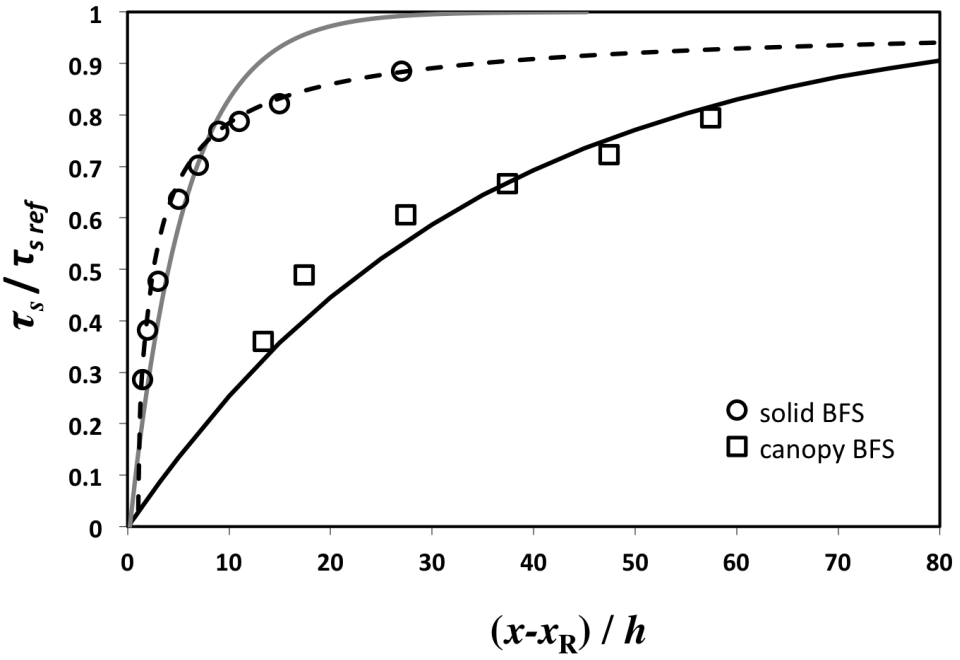

Figure 5.16: Surface shear stress distribution (measured with Preston tube); with an exponential fit following Eqn. (5.12), behind a solid BFS (grey solid line, $R^2 = 0.85$), (Driver and Seegmiller, 1985) and a canopy BFS (black solid line, $R^2 = 0.95$); Also plotted is a power law fit for the solid BFS (black dashed line, $R^2 = 0.99$). The zero-crossing corresponds to the reattachment of the flow at $x = X_R$.

the entire dataset). The power law best fit to the entire dataset for the solid BFS is $\tau_s(x^*)/\tau_{s\ \mathrm{ref}} = 0.9(x^*/h)^{-0.62}$.

The directly measured surface shear stress approaches 90 percent of $\tau_{s\ \mathrm{ref}}$ at downwind distances of $X_\tau = x^* \approx 35h$ and $X_\tau = x^* \approx 100h$ for the solid BFS and canopy BFS, respectively. The recovery distance is nearly three times longer for the canopy BFS than for the solid BFS. The most likely cause for this dissimilarity is the large difference in boundary layer thickness of the BFS. Over the smooth wall the boundary layer is much thinner than over the canopy. The momentum thickness over the canopy is also about three times that of the solid BFS ($\theta_{\mathrm{Canopy}}/\theta_{\mathrm{Wall}} = 0.6h/0.19h$). It is likely that the upwind momentum thickness needs to be included in a function for λ. Our experimental data need to be extended beyond the two cases considered here to develop a parameterization for λ.

To develop a robust relationship for the characteristic length scale λ in Eqn. (5.12), experiments varying several parameters need to be conducted. Assuming that λ is principally a function of h and θ_{Canopy}, the expected approximate range of λ in the wake of a forest canopy can be conjectured: The smooth wall on top of the solid BFS causes the momentum thickness above the step to be near a minimum, while based on Raupach [99], the canopy density selected for our wind tunnel experiment likely causes the largest relative momentum thickness for canopy flows. It is therefore likely that the range from $\lambda \approx 5h$, for the solid BFS to$\lambda \approx 15h$, for the canopy BFS gives a reasonable first approximation of the minimum and maximum recovery length scales to be expected downwind of a solid or porous BFS. An additional factor that may increase the distance required for full shear stress recovery downwind of a canopy would be a stably stratified atmosphere. Sufficient surface cooling may prevent eddies from transporting momentum down from the above shear layer and limit the development of surface shear stress. Similarly, the recovery length downwind of a canopy may be decreased by a convective atmosphere or increased roughness downwind of the BFS. The shear stress recovery seen in Figure 5.16 can be taken as the approximate range to be expected in the field.

Shear stress measurements based on log-law fits to mean velocity profiles in the wake of canopies in other wind tunnel experiments, and shear stresses measured in the field over the ice cover of a lake revealed that 90% shear stress recovery depended on canopy

height and porosity and occurred between $X_\tau + X_R = 40h$ to $60h$ (Markfort et al. [11]). Our new wind tunnel results reveal a wider range from approximately $35h$ to $80h$ for shear stress recovery; the previous estimates fall within this new range.

Challenges for measuring surface shear stress in the flow

The kinematic turbulent shear stress measured in the constant flux layer of the ABL is often used as a surrogate for surface shear stress at the ground. Based on estimates using empirical relationships for roughness transitions, it is often assumed that beyond about 200 m downwind of a transition, one can expect to be within a new equilibrated surface layer below approximately 2 m from the ground, where the constant flux layer assumption holds. However, as shown above in Figure 5.14 the gradient in vertical momentum flux is not zero for long distances downwind of a canopy at $z/h = 0.2$, and a new adjusted surface layer may not form for at least $100h$ downwind of the canopy. Canopies are generally on the order of 10 m tall, meaning that at 2 m above the ground, the wake from an upwind canopy may persist for 1,000 m over smooth terrain.

We have made measurements of the kinematic (Reynolds) shear stress in the wake of a canopy BFS at $z/h = 0.2$. We present them in Figure 5.17 relative to a reference value $\overline{u'w'}_{\text{ref}}$ at $x/h = \infty$ and $z/h = 0.2$. The transect of the Reynolds shear stress plotted in Figure 5.17 has a trend that is very different from surface shear stress measured directly at the surface with a Preston tube and shown in Figure 5.16. As the wind moves over the edge of the step or exits the canopy, the Reynolds shear stress just behind the step is small, due to the low speed and low turbulence of the flow exiting the canopy. In the wake region, the shear stress increases rapidly in the shearing flow and peaks near the location of flow reattachment of the mean flow. Between about $x/h = 30$ to 50 the shear stress then decays asymptotically toward an adjusted final value. The data in Figure 5.16 and 5.17 highlight the challenge for interpreting turbulence measurements collected at a single point, since the surface shear stress inferred from the Reynolds stress measurements taken at a distance $x/h < 30$ from the canopy edge and at $z/h = 0.2$ would significantly overpredict the surface shear stress. The predicted relative shear stress would even have the incorrect trend, indicating increased shear, when in fact the surface shear stress is decreased. For distances $30 < x/h < 50$, the measurements overpredict the developed shear stress by 20 to 30 percent. Because a new surface

layer has not fully developed by $x/h = 50$, it is likely that the apparent adjustment to the reference shear stress, exhibited at $x/h = 50$, is due to the relaxation of the wake turbulence rather than due to the development of a new wall bounded shear layer.

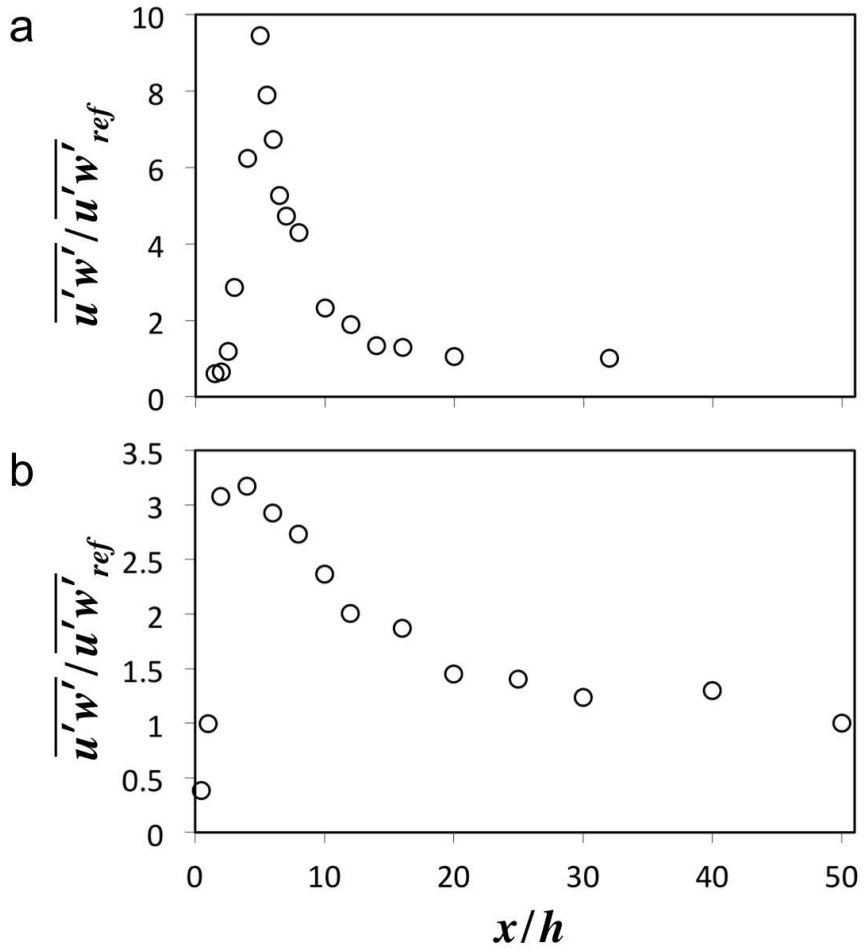

Figure 5.17: Reynolds stress distribution, measured at $z/h = 0.2$ downwind of a) the solid BFS and b) the canopy BFS.

Figure 5.18 shows selected profiles of the Reynolds stress illustrating the evolution in the wake of the canopy. Shear stress estimates based on measurements collected at a single point in the flow would greatly over estimate the surface shear stress due to the enhanced turbulence in the wake. The magnitude of overestimation depends on the elevation of the measurement relative to the canopy height and distance downwind of the

canopy. The vertical variation in shear stress near the surface, below about $z/h = 0.5$, can be well approximated by a linear fit. Generally the profiles trend to values lower than the reference shear stress at the surface far downstream from the point of reattachment. In Figure 5.18 the reference is taken as the stress measured at the smooth surface at $x/h = \infty$ for the fully developed profile. The surface approximations follow a trend that is similar to that of the directly measured surface shear stress (Fig. 5.16). However due to scatter in the data, they are not in perfect agreement.

A reasonable projection of the surface shear stress may be obtained by extrapolation to the surface of the vertical trend between two or more measurement points below $z/h = 0.5$ and well beyond the point of mean flow reattachment. Downwind of approximately $x/h = 30$, extrapolation of covariance measurements to the surface provides a more robust estimate of the surface shear stress. Upwind of this region, the stress gradient is large and small data scatter may lead to significant error in the surface shear stress estimated from turbulence measurements at small elevations above the smooth wall at $0 < z/h < 0.5$.

5.6 Summary and Conclusions

Wind tunnel experiments were conducted to investigate the turbulent flow and momentum fluxes in the wake of an abrupt canopy to clearing transition. This work provides the first detailed measurements of the turbulence and surface shear stress distribution in the wake of a canopy BFS. Results were compared to the solid BFS type flow, which is often used as a surrogate in field studies and models of wind sheltering for clearings, wetlands and small lakes surrounded by forest. The turbulence field is shown to be significantly different in the wake of a canopy BFS compared to a smooth, solid BFS, and both are much different from a simple transition in roughness due primarily to displacement of the ABL upwind of the transition. The mean flow topology, including the separation and velocity deficit distribution, as well as the turbulence characteristics in the near and far wake of the canopy and solid BFS, show substantial differences. The turbulent wake flow behind a dense canopy needs a longer distance to recover but reattaches earlier than the solid BFS wake flow. The surface shear stress recovery downwind of the transition, obtained by direct measurements, was substantially different from that

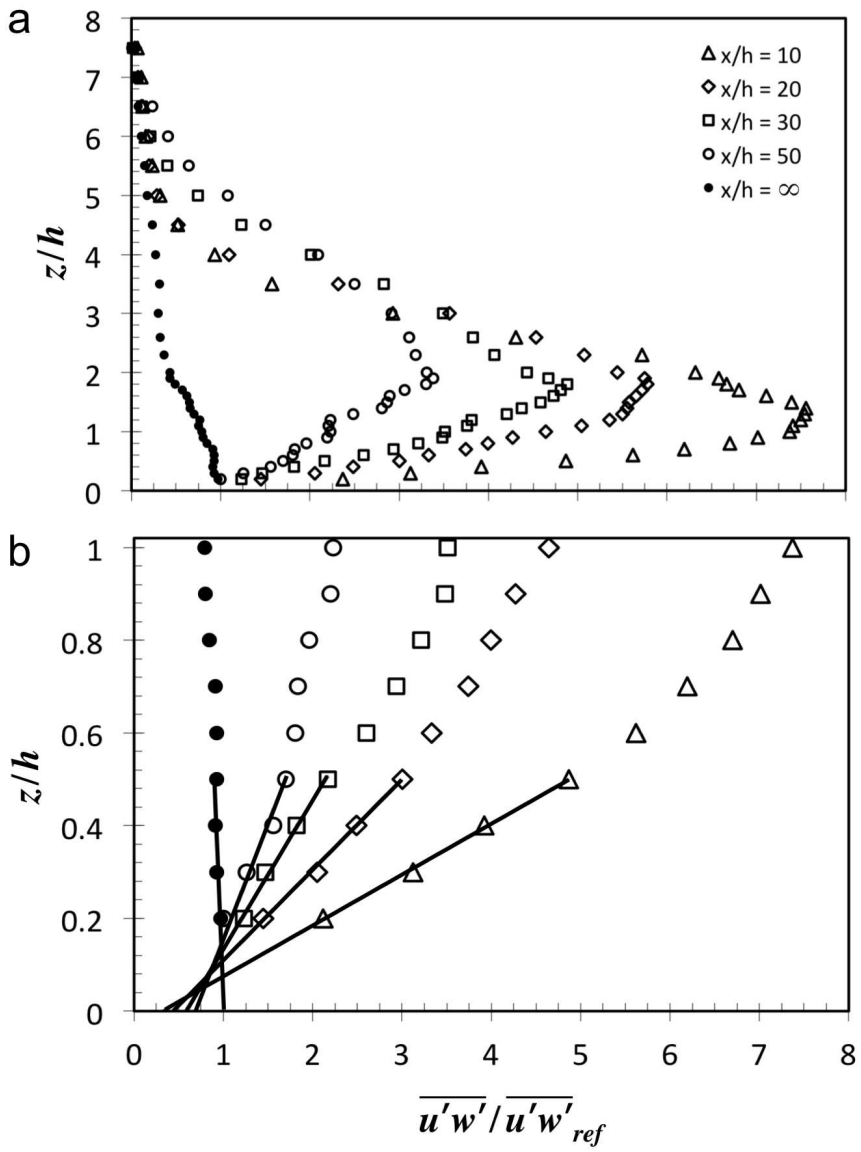

Figure 5.18: Reynolds stress profiles at selected distances downwind of the canopy BFS. a) Full vertical profiles up to the top of the boundary layer, b) profiles up to $x/h = 1$. Linear regression for each profile below $z/h = 0.5$.

of measurements of turbulent fluxes near the surface due to the absence of a developing surface layer in the wake. The surface shear stress recovery followed an exponential function, which may be parameterized, based on canopy characteristics.

We found similarities and differences in terms of the overall flow properties between a solid BFS and canopy BFS. The wake flow was found to have three distinct and important length scales that depend on the porosity and height of the canopy: a separation scale X_S, a reattachment scale X_R and a shear recovery scale X_τ. Both flows exhibited a separation bubble. The mean flow separated a short distance downwind of the canopy edge, not exactly at the edge as is the case for the solid BFS. Reattachment occurred at $2.5h$ downwind of the dense canopy BFS and about twice that distance for the solid BFS. The turbulent ABL will always separate at the downwind edge of a solid BFS, whereas separation is not guaranteed downwind of a canopy BFS. If separation occurs, it is not likely to occur from the top of the canopy. Linear growth of the vorticity scale of the mixing layer downwind of the canopy was found to reasonably predict X_R. Direct measurements showed that surface shear stress recovered at downwind distances between 35 to 100 times the step or canopy height, respectively. The range can be attributed mainly to differences in the momentum thickness over the canopy and solid step. The mean flow and turbulence statistics required more than 100 times the canopy height to adjust to the new surface after leaving the canopy. A momentum budget analysis revealed that each term is significant at various positions in the wake flow. In particular the advection, stress divergence and pressure terms are significant in the wake. Analysis of the mixing length near the surface exhibits a wide range of scales depending on the region of the flow.

The absence of a developing surface layer at the lowest measurement height of $z/h = 0.1$ at a distance of 50 times the canopy height, i.e. long after reattachment, and corresponding, e.g. to a fetch of 1 km for a 20 m tall canopy, presents a challenge for micrometeorological flux measurements. Interpretations of measurements obtained by bulk transport and gradient-based flux methods may be subjected to strong wake effects. A measurable logarithmic layer may not form over forest clearings and small lakes within distances on the order of a kilometer downwind from forest edges. Turbulent fluxes measured within the canopy wake are overwhelmed by wake turbulence and do not represent transport at the land or water surface. The constant flux layer

assumption becomes erroneous in the wake region, and therefore the surface flux cannot be accurately determined by standard eddy covariance measurements. Similarly, surface fluxes evaluated in ABL models using standard wall model formulations, which are only appropriate for homogeneous landscapes, will lead to substantial errors in wake-affected regions.

It is already know from additional wind tunnel measurements, not presented here, that parameters, such as the length and porosity of the canopy, affect the wake structure and the distance required for the flow to fully redevelop. Additionally, the effects of the ratio of canopy height to boundary-layer thickness as well as the aerodynamic roughness of the downwind surface also require further study. Another important parameter in need of investigation is the thermal stability of the ABL, especially over lakes where buoyancy effects are significant. How thermal stratification affects the wake turbulence and flow recovery needs to be investigated. As already indicated, scalar transport and heat budget terms are also affected by wake turbulence and in need of quantification.

Chapter 6

Wind Sheltering of a Lake by a Tree Canopy or Bluff Topography[†]

[†] **This chapter was published as Markfort CD, ALS Perez, JW Thill, DA Jaster, F Porté-Agel and H. G. Stefan. 2010. Wind sheltering of a lake by a tree canopy or bluff topography. *Water Resources Research*. 46, W03530. doi:10.1029/2009WR007759**

6.1 Abstract

A model is developed to quantify the wind sheltering of a lake by a tree canopy or a bluff. The experiment-based model predicts the wind-sheltering coefficient a priori, without calibration, and is useful for one-dimensional (1-D) lake hydrodynamic and water quality modeling. The model is derived from velocity measurements in a boundary layer wind tunnel, by investigating mean velocity profiles and surface shear stress development downwind of two canopies and a bluff. The wind tunnel experiments are validated with field measurements over an ice-covered lake. Both wind tunnel and field experiments show that reduced surface shear stress extends approximately 50 canopy heights downwind from the transition. The reduction in total shear force on the water surface is parameterized by a wind-sheltering coefficient that is related to the reduction of wind-affected lake area. While all measurements are made on solid surfaces, the wind-sheltering coefficient is shown to be applicable to the lake surface. Although several canopy characteristics, such as its height, aerodynamic roughness, and its porosity affect the transition of velocity profiles and surface shear stress onto a lake, a relationship based on canopy height alone provides a sufficiently realistic estimate of the wind-sheltering coefficient. The results compare well with wind-sheltering coefficients estimated by calibration of lake water temperature profile simulations for eight lakes.

Keywords

Atmospheric boundary-layer (ABL); Canopy; Lakes; Modeling; Simulation; Surface mixed layer; Water quality; Wind mixing; Wind sheltering

6.2 Introduction

Wind stress and heat flux are arguably the most important causes of large-scale circulation as well as turbulence in small to medium lakes. They strongly affect water quality and ecological processes, and are therefore included in dynamic lake water quality and ecosystem models. Textbooks on limnology (e.g., Hutchinson [157]), the Encyclopedia of Inland Waters (Rueda and Vidal [158]; Monismith and MacIntyre [159]), and reviews of lake hydrodynamics (e.g., Fischer et al. [160]; Wüest and Lorke [161]) all include information on how wind stress causes mixing in lakes. Wind stress on the lake surface induces lake currents, surface and internal waves, and turbulence, all of which can be determining processes for the vertical mixing, the ecology and the geochemistry of a lake, especially in the surface mixed layer (SML) and the benthic boundary layer. Forced convection induced by wind stress on the water surface, and free thermal convection induced by heat loss from the water to the atmosphere are the main processes that generate SML turbulence and control the transport of momentum, heat, and mass (e.g., dissolved oxygen, CO_2, CH_4 and water vapor) across the air-water interface and within the SML. Yet despite numerous studies, wind stress, especially on small lake surfaces, is still not well understood or easy to quantify (Wüest and Lorke [161]).

In deterministic models of lake water quality, algorithms for internal mixing, and rates of surface gas transfer and evaporative heat exchange at the air-water interface are linked to wind stress on the lake surface. However, the reduction of wind velocity over a lake (wind sheltering) by a tree canopy or a bluff can rarely be included, a priori. Wind sheltering is usually considered a posteriori by applying a "wind-sheltering coefficient" to calibrate simulated against observed lake properties, e.g., temperature profiles.

To understand and simulate the wind-driven processes in a lake, wind velocity, and shear stress on the water surface must be resolved for the entire lake surface area. Wind sheltering can significantly reduce the area of wind access, especially on small lakes, as is illustrated in Figure 6.1 by the reflection of visible light on surface waves in Holland Lake (15 ha surface area). Of the Earths total number of lakes (and other standing water bodies) 99.9% are small having areas less than 10 km^2. These lakes account for 54% of the cumulative global lake surface area (Downing et al. [92]). For the majority of the Earths lentic surface water bodies, wind sheltering is therefore important.

Figure 6.1: Aerial image of light reflection by surface waves of a lake. Wind is blowing from the land onto the lake, from the right to the left. The image is the result of the wind sheltering effect of trees on the wavefield on the surface of the lake. A wind-sheltered zone is clearly visible (source is USGS).

Specifying wind shear on a small lake downwind of a canopy of trees (forest), crops (agricultural fields), buildings (urban areas), or a bluff is difficult because the atmospheric boundary layer (ABL), over the lake, is undergoing a change as the velocity profile is adjusting from a specific land cover to a relatively smooth water surface. In the transition, wind speed and wind shear stress on a lake surface are reduced compared to observations at a weather station in flat and open terrain. Airport wind data are commonly available, and it would be useful to know how to adjust the measured wind speeds to account for wind sheltering of a nearby lake.

The objective of this study is to evaluate, by laboratory and field measurements, the along-wind evolution of the surface shear stress as wind blows from a rough and tall canopy (e.g., forest) or a bluff onto a relatively smooth lake surface. Velocity measurements in boundary layer wind tunnel simulations of a canopy to lake transition, as well as field measurements over a lake surface downwind from a tree canopy will be obtained and analyzed to determine the along-wind transect of the surface shear stress on the lake surface. A relationship between normalized surface shear stress and distance

from the canopy will be used to determine the extent of wind sheltering for a given canopy. From these results a model will be developed to predict the wind-sheltering coefficient. The predicted wind-sheltering coefficient will be compared to the wind-sheltering coefficient determined from one dimensional (1-D) lake hydrodynamic/water quality model simulations for eight lakes.

6.3 Background

Wind shear stress (drag) on a lake surface is an important boundary condition for lake hydrodynamic and water quality models. Information is currently lacking on the distribution of surface shear stress, especially on smaller lake surfaces where sheltering is important. Since momentum and mechanical energy fluxes across the air-water interface scale as the wind speed squared and cubed, respectively, even small spatial variations in surface wind speed can be expected to produce comparatively large spatial variations in wind-driven currents, turbulence, and resulting mass transport in a lake (e.g., Melville [162]).

Many investigators have confirmed that surface area and fetch are the most important parameters controlling momentum and energy transfer at a lake surface and the resulting epilimnion or SML thickness (Davies-Colley [163]; Gorham and Boyce [164]; Condie and Webster [165]; Boehrer and Schultze [166]). Mass (e.g., dissolved oxygen, CO_2, CH_4 and water vapor) transfer across the air-water interface is also known to depend strongly on wind speed over a lake (Wanninkhof et al. [167]; Wanninkhof et al. [168]; Wanninkhof et al. [169]), but determining where the reference wind speed should be measured is still subject to assumptions. As a result, gas exchange coefficients for lakes, as a function of wind speed, still have a component of uncertainty.

Wind sheltering of a lake is characterized by atmospheric flows, ranging from the ABL adjustment in response to a surface roughness transition, e.g., from low vegetation on flat terrain, to transition from irregular terrain, e.g., between hills or mountains onto a lake surface. Downwind of a roughness transition, the wind velocity profile can be characterized by two layers. The properties of the upper layer depend only on the surface conditions upwind of the transition while the lower portion of the profile is affected by the new surface condition. This lower region is termed the internal boundary

layer (IBL), which grows deeper downwind from the transition (e.g., Oke [170]; Stull [60]; Garratt [149]). In the lowest approximately 10% of the IBL, referred to as the equilibrium sublayer, the flow is fully adjusted to the new surface with no influence from the upwind surface.

Still the IBL paradigm may be unsuitable for wind sheltering of lakes because many lakes are found in landscapes characterized by tall plant canopies, e.g. trees, where the flow downwind is more complicated than a simple roughness transition because it also involves a flow separation or wake and a possible recirculation downwind of the transition (Cassiani et al. [105]; Flesch and Wilson [171]; Wilson and Flesch [172]). The wake region is characterized by the interaction between a lower layer of relatively low velocity wind (or momentum deficit caused by drag induced by the tree canopy), and a region of higher velocity wind flowing above the canopy. At the trailing edge of the canopy, and over the lake surface, the interaction of these two layers of contrasting velocity produces a blending shear layer and downward flux of momentum (Fig. 6.2). The wake effect is accentuated by increasing canopy density or when a lake is surrounded by elevated terrain (i.e., bluff). In that case the wind field resembles a backward-facing step (BFS) type of circulation, or coherent rotor-like vortices and wake separation (Cassiani et al. 2008).

The ABL transition between canopies and clearings has been investigated numerically by Liu et al. [173], Patton et al. [120], Wilson and Flesch [172], Yang et al. [115], and Cassiani et al. [105] and experimentally by Chen et al. [174], Irvine et al. [116], and Detto et al. [106] among others. Our attention is focused on lakes in flat terrain where the canopy is the dominant cause of wind sheltering. Although a number of studies have been carried out to characterize the ABL downwind of roughness transitions and canopies, the resulting downwind surface shear stress development continues to resist complete theoretical treatment because all the terms in the time-averaged mean momentum balance remain significant.

For lake modeling, wind speeds measured at local weather stations, e.g., at an airport several kilometers from a lake, are commonly used. The lack of on-lake wind observations as well as the wind sheltering by canopies and bluffs necessitate that 1-D numerical lake hydrodynamic/water quality models are calibrated for wind speed by a wind-sheltering coefficient, (Ford and Stefan [100]; Hondzo and Stefan [175]). The wind-sheltering

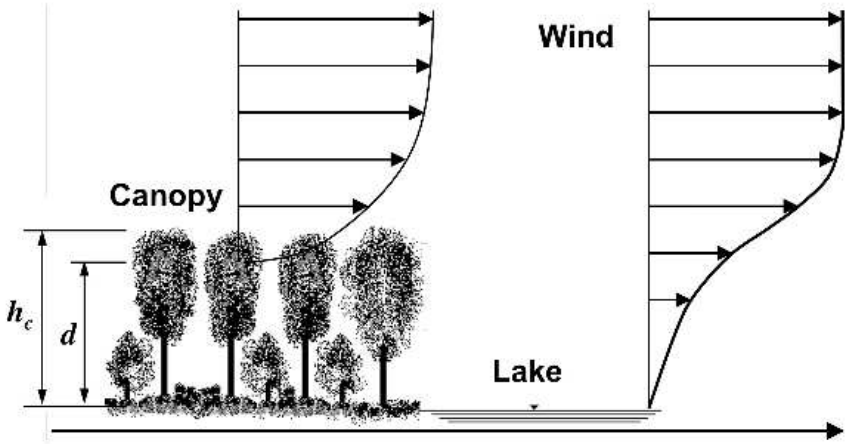

Figure 6.2: Schematic of wind blowing over a tree canopy at the edge of a lake and the associated wind-field transition in the atmospheric boundary layer downwind over the lake. (Also appropriate for flow over a bluff to lake transition.) Here h_c, canopy height; d, displacement height.

coefficient minimizes the mean residual between simulated model results and observed lake water quality or circulation data (e.g., temperature profiles). This remains the only method for determining the value of W_{str}.

6.4 Momentum Transfer at a Lake Surface

The transport of momentum across the air-water interface of a lake generally occurs from the atmosphere to the water, whereas heat or mass (e.g., dissolved oxygen, CO_2, CH_4, and water vapor) transfer can occur in either direction. As the wind blows over the water surface, the water surface generates a drag on the wind, slowing the wind nearest the surface. Practical estimates of the shear stress on a lake surface can be obtained from

$$\tau = C_D \rho_a U_z^2, \tag{6.1}$$

where C_D is a drag coefficient, ρ_a is the density of air, and U_z is the time averaged wind velocity at some specified height z above the water surface. The wind velocity profile for a fully developed wind field follows the log-law based on the von Karman mixing

length similarity theory given by

$$U = \frac{u_*}{\kappa} \ln\left(\frac{z}{z_0}\right), \tag{6.2}$$

where the von Karman constant $\kappa = 0.4$, u_* is the shear (friction) velocity defined as $u_* = \sqrt{\tau/\rho_a}$, z is height, and z_0 is the aerodynamic surface roughness. This similarity form of the velocity profile is only appropriate for neutral atmospheric conditions and may be adjusted for the effects of buoyancy and density stratification using the Businger-Dyer relationships (cf. Stull [60]; Garratt [149]).

The empirical dimensionless drag coefficient C_D is a function of wave roughness, which is a rather complicated function of both wind speed and the state of wave development or wave age (Vickers and Mahrt [176]; Wüest and Lorke [161]). The wave age is simply the ratio of wave phase speed to either the wind velocity or roughly 30 times the shear (friction) velocity. By this association of C_D with wave age and mean velocity, a relationship between C_D and U_{10} (mean wind speed measured at 10 m height) is established (Fig. 6.3). For the surface of a lake, the drag coefficient is given by a variation of Charnock's law (Charnock [177]; Wüest and Lorke [161]):

$$C_{D,10} = \left[\kappa^{-1} \ln\left(\frac{10g}{C_{D,10}U_{z=10}^2}\right) + 11.3\right]^{-2}, \tag{6.3}$$

where g is the gravitational acceleration, U_{10} and $C_{D,10}$ are the mean velocity and surface drag coefficient, respectively, taken at a height of 10 m. Equation (6.3) is implicit in $C_{D,10}$, but converges within a few iterations and has been shown to be valid for wind speeds greater than about 5 m s^{-1}.

For small lakes, wind speed is generally low (commonly $U_{10} < 5$ m s^{-1}) because of wind sheltering, giving the greatest variability to the drag coefficient. Because of sheltering and limited fetch, wave fields on lakes are often immature. In addition to spatial wind speed variability, these interactions are the primary complications in determining momentum transfer from the atmosphere into the lake surface boundary layer. For lesser wind speeds, i.e., $U_{10} < 4$m s^{-1} the values of observed drag coefficients are yet to be adequately described by any physical model. Wüest and Lorke [161] suggest

the following empirical relationship for a wind speed measured at a height of 10 m:

$$C_{D,10} = 0.0044 U_{10}^{-1.15}. \tag{6.4}$$

Using Equations (6.1) – (6.4), the wind shear stress can be determined on a water surface. It should be noted that Charnock's law assumes a well-developed wave field with a wave phase speed similar to the mean wind speed. For less developed wave fields, the frequency of wave formation and destruction is much greater, and requires a larger input of momentum for a given wind speed resulting in a higher drag coefficient than is predicted. Therefore, the values of shear stress plotted in Figure 6.3 should be taken as the lower bound on the expected shear stress that would be observed on the lake water surface.

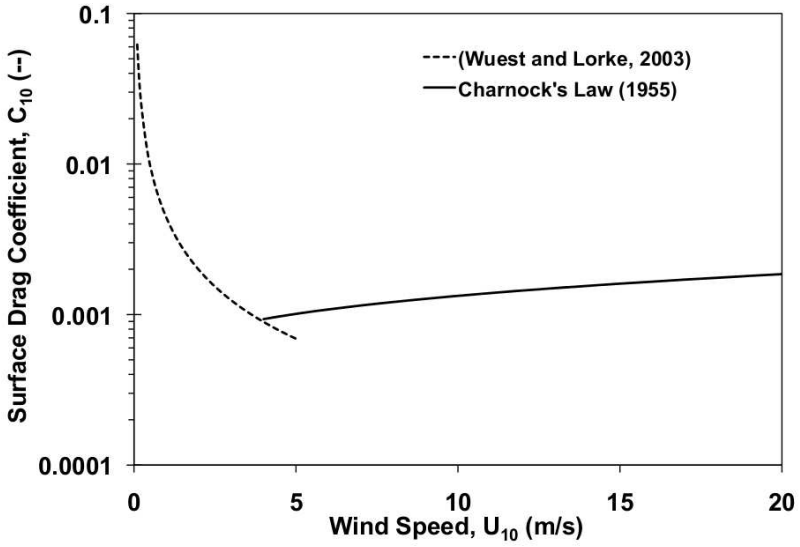

Figure 6.3: Wind-drag coefficient C_D on a water surface as a function of wind speed U_{10} measured at standard 10 m height above the water surface (Equations (6.3) and (6.4).

6.5 Methods of Experimental Investigation

Experiments designed to investigate the development of the wind field and surface shear stress over a lake, downwind from a canopy and a bluff were conducted both in the

Boundary Layer Wind Tunnel at the University of Minnesotas Saint Anthony Falls Laboratory (SAFL), and over the ice-covered Round Lake near Andover, Minnesota (latitude, 45°14′24″N; longitude, 93°21′22″W).

6.5.1 Wind tunnel experiments

Three wind tunnel experiments were conducted, to study the evolution of the mean velocity and surface shear stress downwind of the transition from a vegetation canopy (i.e., trees) and a bluff to a lake surface, for two porous canopies and a solid BFS. The experiments were conducted in the main test section of the SAFL wind tunnel, which is 1.7 m wide, 1.8 m high, and approximately 16 m long (Fig. 6.4). In this study, the tunnel was operated in closed circuit and the average free-stream wind velocity was between 10 to 15 m s^{-1}. The experiments were run for neutral conditions at air temperatures between 27°C and 28°C. The turbulent boundary layer was developed with assistance from a tripping mechanism (8 cm picket fence) located at the exit of the wind tunnel contraction where the boundary layer test section begins ensuring a deep turbulent boundary layer formed before flow adjusted to the canopy or step. Additional details of the wind tunnel characteristics are provided by Farell and Iyengar [178] and Carper and Porté-Agel [54].

The first experimental set-up was considered to be an approximate representation of a canopy of sparse trees or other thin vegetation that ends at the shore of a lake. In this experiment, several layers of wire mesh placed over the wind tunnel floor simulated the canopy. The floor of the wind tunnel by contrast is a smooth surface. The porosity of the wire mesh was 98.0%. The model canopy had a height of 5 cm, covered the total width of the wind tunnel, and extended over a length of $48h_c$ (where h_c is the canopy height) in the flow direction. The wire mesh represents a porous canopy step that ends at $x = 0$.

The Reynolds number, based on canopy (or step) height, is given by

$$\mathrm{Re} = \frac{U_r h_c}{\nu}, \tag{6.5}$$

where U_r and ν are the reference velocity (measured at the downwind edge of the canopy, x = 0, and at six canopy heights, $z = 6h_c$), and kinematic viscosity of air, respectively,

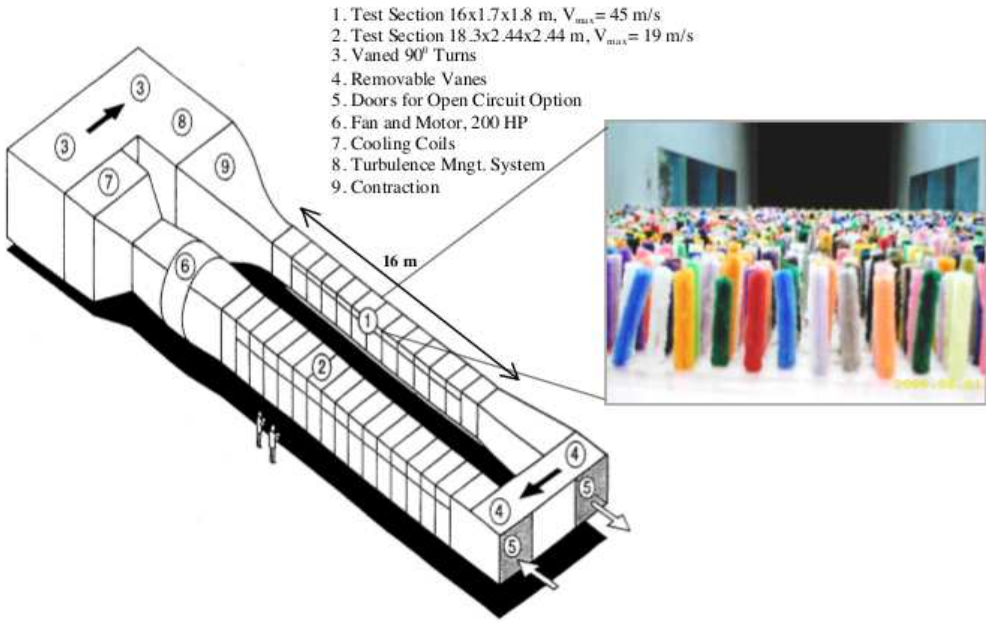

Figure 6.4: St. Anthony Falls Laboratory Boundary Layer Wind Tunnel (schematic). The inset photograph shows wind tunnel main test section (1) (view upwind) with canopy made of flexible tufted wire (canopy height $h_c = 7.5$ cm, canopy width is 1.8 m, and canopy porosity is 78%).

was 4×10^4. The reference velocity is nearly the free-stream velocity and is used solely for comparison of different canopies.

Table 6.1: Summary of variables for the three wind tunnel experiments

	Wire Mesh	Tufted Wire	Solid Step
Canopy Characteristics			
Canopy porosity (%)	98	78	0
Height of canopy h_c (cm)	5	7.5	5.1
Displacement height d (cm)	2.3	6.6	5.1
Relative displacement d/h_c	0.46	0.88	1
Roughness of canopy z_{0c} (mm)	13	5	0.04
Roughness of downwind surface z_{0s} (mm)	0.01	0.01	0.01
Velocities and Shear Stresses			
Reference wind velocity U_r^a (m/s)	13.09	9.46	8.95
Canopy shear velocity u_{*c} (m/s)	1.73	1.00	0.48
Shear stress at canopy top τ_c (N/m^2)	3.86	1.29	0.30
Canopy (step) height Reynolds number	4×10^4	5×10^4	3×10^4

U_r is the velocity measured at the end of the canopy ($x = 0$) at a height $z = 6h_c$ above the wind tunnel floor (h_c is height of the canopy).

Measurements of the time-averaged wind velocity at different positions in the boundary layer were made with a Pitot tube connected to a precision differential manometer (10 torr Baratron differential pressure transducer). The manometer has an accuracy of ±0.0005 mmHg, and has a self-calibration option. The outer diameter of the Pitot tube was 3 mm, and it was mounted on a traversing system designed to allow precise vertical positioning above the wind tunnel floor at the centerline of the test section. The Pitot tube does not require calibration and the accepted lower operation limit is a pressure difference corresponding to a velocity of 0.4 - 0.5 m s^{-1}. Vertical profiles of wind velocity were measured over the wire mesh near the transition ($x = 0$) and also at seven positions downwind of the transition (x/h_c = 4.0, 8.0, 12.0, 22.0, 36.0, 55.2 and 108).

The second experiment represented a homogeneous stand of trees. The model canopy was created from flexible tufted wire (i.e., pipe cleaners). The tufted wires were inserted

into a 2.5 cm thick foam board, which was placed on the wind tunnel floor (Fig. 6.4). The canopy had a height of 7.5 cm and porosity of 78%. It covered the total width of the wind tunnel and extended over a length of $53h_c$ in the flow direction. Foam board, of the same thickness but without a canopy, was installed on the wind tunnel floor downwind from the canopy and represented a relatively smooth surface.

The Reynolds number, based on canopy height, was 5×10^4. Wind velocity profiles were measured with the Pitot tube, as in the first experiment, at the edge of the canopy ($x = 0$) and at nine positions downwind of the canopy (x/h_c = 2.7, 5.3, 8.0, 14.7, 26.7, 43.3, 54.3, 79.2 and 89.1).

The third experiment considered flow over a solid BFS representing a bluff or rows of buildings on the upwind side of a lake. The step was created from styrofoam boards and had a height of approximately 5.0 cm. It covered the total width of the wind tunnel and extended over a length of $80h_c$ in the flow direction with an upstream smooth ramp to direct the flow and minimize separation. The wind tunnel floor downwind from the BFS was similarly covered with Styrofoam having the same smooth surface roughness. The Reynolds number, based on step height, was 3×10^4. Wind velocity profiles were measured at the end of the canopy ($x = 0$) and at nine positions downwind (x/h_c = 4.0, 8.0, 12.0, 22.0, 40.0, 55.2, 81.4, 118.8 and 133.6).

The roughness of the wind tunnel floor was determined from the measured velocity profiles. To characterize the upwind surface, a velocity profile was measured at the end of the canopy or BFS ($x = 0$) and within the quasi-fully developed surface layer above the canopies. Characteristics for all three experiments are summarized in Table 6.1. The blocking ratio of the canopy on the flow in the wind tunnel test sections was less than 4%, and the ceiling of the wind tunnel was inclined to minimize any longitudinal pressure gradient, which prevented acceleration of the mean flow over the canopy. Further details of the experiments are given in reports by Jaster et al. [179] and Perez et al. [180].

The surface shear stress was calculated for each velocity profile from Equation (6.2), and is a function of the position relative to the windward shoreline. After significant distance downwind of the canopy, shear stress increased asymptotically to a constant value. The calculated shear stress was therefore normalized to the farthest downwind value.

6.5.2 Field study

An investigation of the ABL transition from land to a lake at field scale was conducted at Round Lake. Round Lake is, as its name implies, is nearly round with a diameter of approximately 1 km. It is set in a landscape having very flat topography with trees along much of the shoreline. The upwind surrounding area topographically varies by no more than 3 m within approximately 2 km from the lake perimeter (Fig. 6.5). This provides nearly an ideal case to isolate and study the affects of flow over a canopy transition to a small lake.

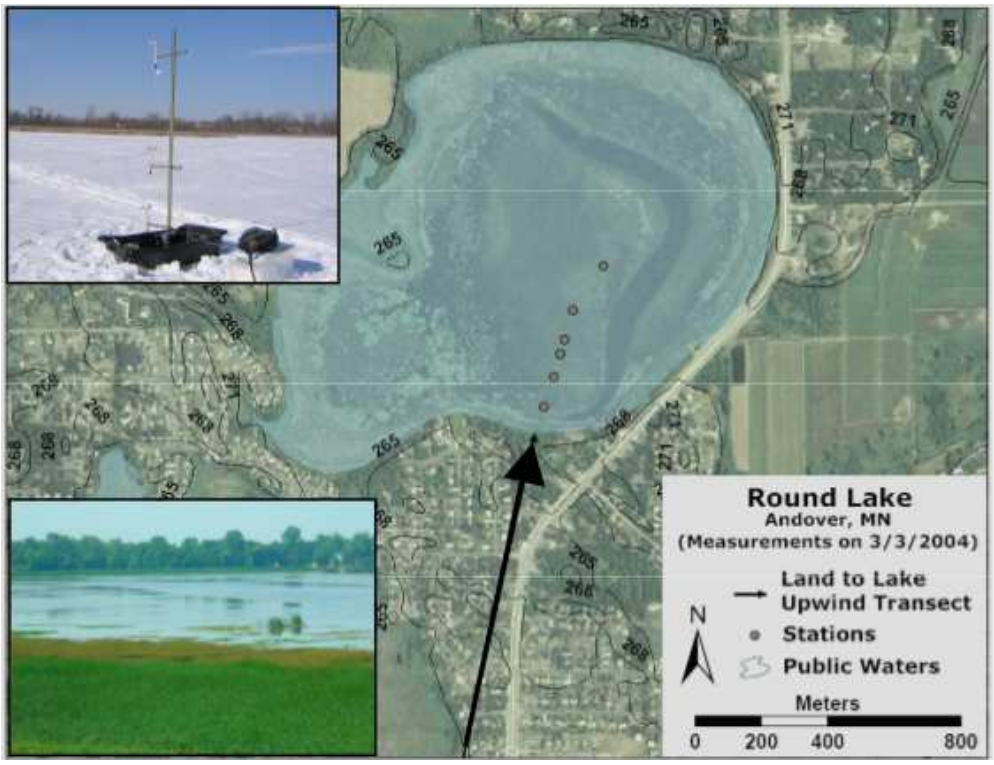

Figure 6.5: Aerial photograph of Round Lake and surrounding area in 2006. Topographic elevations range from 265 to 268 m above mean sea level. Primary wind direction and measurement stations for experiment on 3 March 2004 are identified. Top inset photo shows view of mobile station on 3 March 2004, and bottom inset photo shows view of the south shore and canopy structure in July 2008.

Vertical wind velocity profiles were measured over the lake in the winter in order to take advantage of the solid ice surface on the lake, which was approximately flat

and level. It also made the measurements independent of lake water level, although the roughness of the ice and snow cover is somewhat different from that of the water surface. The data presented here were collected in February and March of 2004.

The objective of the field experiment was to obtain vertical profiles of wind speed at various locations over the lake surface to determine how wind profiles vary downwind of the canopy edge. Three measurement stations were established on the lake with a vertical array of wind speed sensors. Station 1 was installed near the center of the lake as a reference. Station 2 was installed in different fixed locations on different days, except on 28 February 2004 when station 2 was used in two locations, denoted as 2a and 2b. Station 3 was mounted on a sled that was periodically moved to different locations on the lake. The different positions were denoted as $M1$, $M2$, $M3$, etc, with the prefix, "M" denoting that the station was mobile (Fig. 6.5).

At each station three Met One model 014-A cup anemometers were mounted at various heights on each of the 2.5 m high vertical masts. The heights of the anemometers above the top of the ice/snow cover during each period of measurement are listed in Table 6.2. In general, the lowest sensor was mounted at a height of 0.3-0.6 m, the middle sensor at a height of 0.8-1.5 m, and the highest sensor at a height of 2.3-2.5 m. A Wind Sentry wind direction sensor (manufactured by R.M. Young) was attached to two of the masts at a height of 1.7 to 1.85 m. In all cases, the wind speed and direction were measured at 10-second intervals.

The wind speed data measured with the cup anemometers were processed using a 12 min moving-window average. The 12 min average wind speeds were plotted as a function of $\ln(z)$ to obtain a linear plot, the slope and intercept of which are related to the shear (friction) velocity and the aerodynamic roughness length, respectively, using Equation (6.2). This relationship is only appropriate for near neutral conditions and the low measurement heights imply that the stability correction should be small in this case. To evaluate the appropriateness of the linearized log-law fit to the wind speed profile data, a linear correlation coefficient R^2 was computed at every 12 min interval.

Ultimately, the wind shear stress is a function of fetch; that is, the distance the wind has blown over the water surface from the canopy edge. The fetch was determined from GPS coordinates of each measurement station plotted on a georeferenced map of the lake, and was measured from the tree line to each station in 30° increments around

Table 6.2: Instrument heights in the field experiments on Round Lake

Instrument	28 February 2004	3 March 2004
	Station 1	
014A-1	0.54	0.35
014A-2	1.10	0.77
014A-3	2.30	2.41
Wind Vane	1.80	1.82
	Station 2	
014A-1	0.43	0.32
014A-2	1.22	1.51
014A-3	2.30	2.45
Wind Vane	1.70	–
	Mobile Station	
014A-1	0.43	0.59
014A-2	1.14	1.24
014A-3	2.32	2.49
Wind Vane	–	1.85

Note: Instruments are anemometer and wind vane. Height is in meters.

the lake perimeter. Therefore, as the wind direction changed, the fetch changed as a function of direction. Further details of the field experiments are reported by Thill [181].

6.6 Results and Discussion

6.6.1 Wind tunnel results

Examples of plots of the velocity profiles measured in the wind tunnel downwind from the canopy are shown in Figure 6.6. The data have been normalized by canopy height h_c and for vertical distance and reference velocity, U_r (measured at $x = 0$ and $z = 6h_c$). The reference velocity represents the free stream velocity, minimizing the effect of the canopy or the wind tunnel ceiling.

Aerodynamic characterization of the wind tunnel floor without a canopy

The shear (friction) velocity is obtained from the slope of the straight-line fit to the data on a semi-logarithmic plot, and z_0 by extrapolating the straight line to the height $z = z_0$ where $U = 0$ (Fig. 6.7). The wind velocity profile without a canopy is a fully developed turbulent velocity profile as shown by the linearity of the semi-logarithmic plot. The data in this plot can be fit to Equation (6.2). From this data the absolute roughness of the wind tunnel floor was determined to be approximately 1×10^{-5} m (0.01 mm). This value of z_0 is consistent with previous data collected in the same wind tunnel (Carper and Porté-Agel [54]). In our experiments the wind tunnel floor represents the water surface of the lake, which will have a different roughness, but the relative roughness between the canopy and downwind surface is within a comparable order of magnitude. To illustrate this, we compare our wind tunnel experiments to previously reported values of surface roughness provided for a range of land covers (Table 6.3). The relative roughness for the tufted wire canopy experiment (0.005 / 0.00001 = 500) is comparable to values from Table 6.3 for a transition from trees to ice (0.4 / 0.0008 = 500).

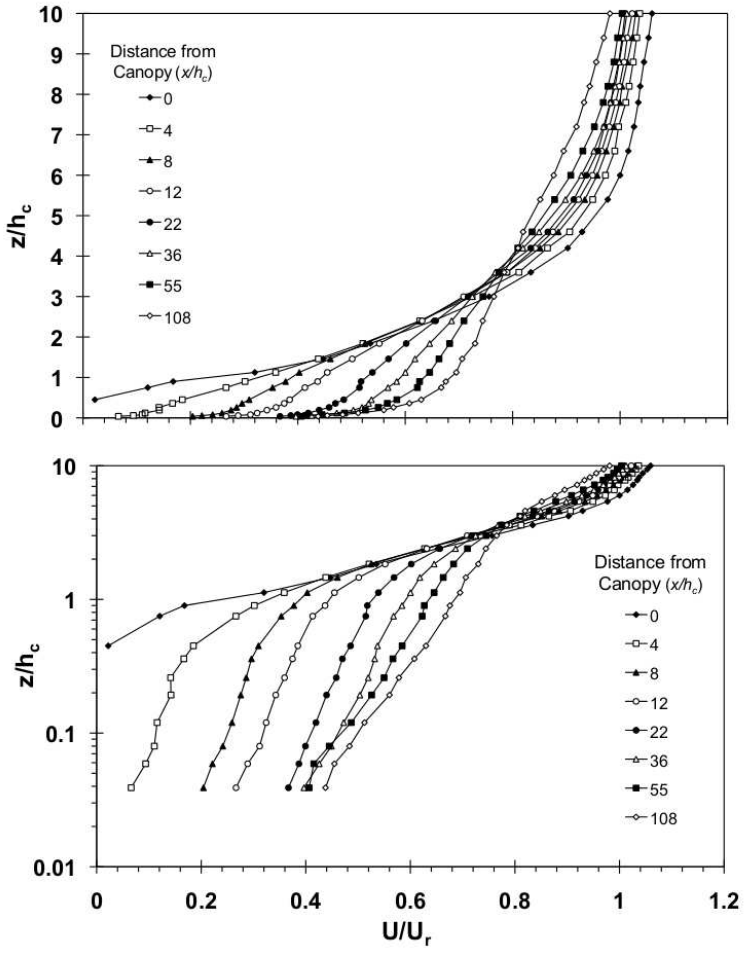

Figure 6.6: Normalized velocity profiles measured in the wind tunnel, downwind from the wire mesh canopy, plotted on (top) arithmetic scale and (bottom) semi-log scale. Vertical distances are from wind tunnel floor and normalized by canopy height ($h_c = 5.0$ cm). Horizontal velocities U are normalized to reference velocity U_r measured at the edge of the canopy ($x = 0$) and at six canopy heights above the wind tunnel floor ($z = 6h_c$).

Table 6.3: Common aerodynamic roughness, canopy height, and zero-plane displacement for different surfaces

Surface	z_0 (m)	h_c (m)	d/h_c
Open water	$10 \times 10^{-5} - 0.1$	–	–
Ice	1×10^{-3}	–	–
Snow	$10 \times 10^{-4} - 0.5$	–	–
Bare soil	0.001 – 0.01	–	–
Turf grass	0.0012 – 0.023	0.015 – 0.1	–
Prairie grass	0.04 – 0.20	0.25 – 1.0	–
Agricultural fields	0.005 – 0.12	0.18 – 1.4	–
Woodland trees	0.4 – 0.9	8 –15	0.6 – 0.75
Coniferous forest	0.28 – 3.9	10 – 27	0.61 – 0.92
Tropical forest	2.2 – 4.8	32 – 35	0.85

Here z_0, aerodynamic roughness; h_c, canopy height; d, displacement. Adapted from Table 2.2 of Oke [170] and Table A6 of Garratt [149].

Aerodynamic characterization of the experimental canopies

The aerodynamic characterization of the canopy is essential information to understand how the model canopies compare to the field scale. Because the top of the canopy is not a solid wall, the wind penetrates some distance into the canopy. A description of this process is given by Finnigan [42], Stull [60] and Garratt [149]. The turbulent velocity profile above a canopy can be fit to the modified log-law equation:

$$U = \frac{u_{*c}}{\kappa} \ln\left(\frac{z-d}{z_{0,c}}\right), \tag{6.6}$$

where the subscript c defines variables associated with the canopy. Equation (6.6) is equivalent to Equation (6.2) with the inclusion of displacement height d. The three aerodynamic parameters (u_{*c}, $z_{0,c}$ and d) were estimated by imposing a semi-log plot of a velocity profile measured over the canopy. Velocity profiles measured at the edge ($x = 0$) of the canopy (Fig. 6.7) were used to determine all three parameters. The displacement height d for the canopies was determined using an iterative process outlined by Stull [60].

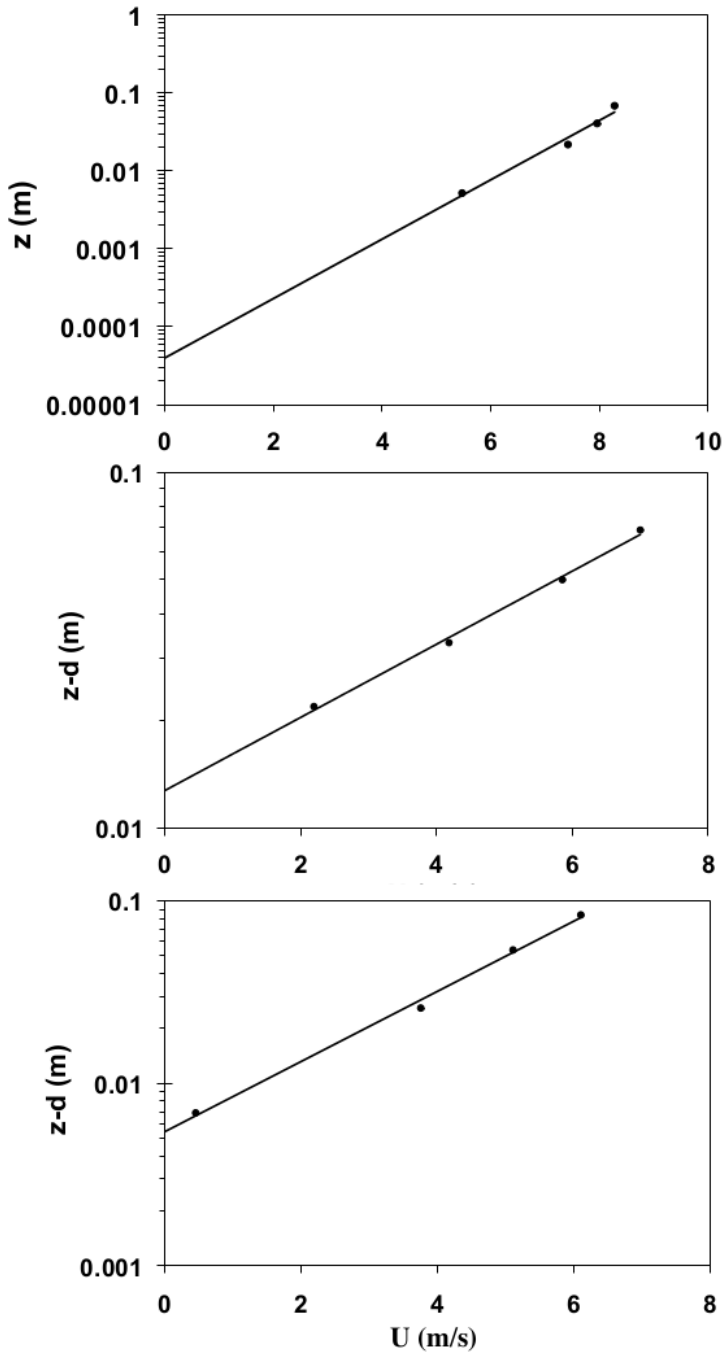

Figure 6.7: Determination of canopy roughness z_0 based on the method given by Stull (1988) for the (top) foam board, (middle) wire mesh canopy, and (bottom) tufted wire canopy.

The relative displacement height for the wire mesh, $d/h_c = 0.46$ indicates a penetration to more than half the canopy height, and for the tufted wire (pipe cleaner) canopy, $d/h_c = 0.88$ indicates penetration to 12% of the canopy height, and for a solid backward facing step, $d/h_c = 1$ indicates no penetration. As an estimate, $d = 2/3h_c$ is often used for real vegetation canopies consisting of trees or other plants when direct measurement is not feasible (Oke [170].

Once the displacement height was determined, the canopy roughness could be obtained by extrapolation of the linear fitted plot of U vs. $\ln(z - d)$ to a zero velocity (Fig. 6.7). The canopy roughness was determined to be approximately 0.013 m for the wire mesh 0.005 m for the pipe cleaner, and 0.00004 m for the solid step. The canopy shear (friction) velocity, at $x = 0$, was computed using Equation (6.6); it is proportional to the slope of the line in Figure 6.7. Results from the analysis of the canopy data for the three experiments are summarized in Table 6.1. There was a wide variation in roughness between the three canopies in the wind tunnel. The wire mesh canopy was over 1000 times rougher than the wind tunnel floor, while the pipe cleaner canopy was 500 times rougher, and the solid step was the same roughness as the wind tunnel floor.

Structure of the wind velocity field in the transition from canopy to smooth surface

A separated flow region was detected downstream of the pipe cleaner canopy and the backward facing step (BFS), but not behind the wire mesh canopy. The distance to reattachment was about six to eight times the displacement height of the canopy. This is consistent with results for a BFS from Jovic and Driver [182], Le et al. [183], Aider et al. [184], and for canopies (Cassiani et al. [105]). After a distance $x/h_c = 25$, development of the new IBL was identified. It was characterized by rising shear stresses with distance from the canopy. Between $x/h_c = 8$ and $x/h_c = 25$ shear stress on the lake surface is increasing, depending on canopy roughness and porosity.

Three distinct layers were identified in the measured velocity profiles downwind from the point of reattachment: (1) the IBL in response to the shear on the wind tunnel floor, (2) an outer layer far above the canopy, and (3) a mixing/blending layer between layers (1) and (2). With sufficient distance downwind from the canopy, the mixing layer disappears and a single boundary layer with a log-law velocity profile forms. These

results match the description provided by Walker and Nickling [185] for flow behind dunes and simulated results by Cassiani et al. [105].

Velocity deficit and surface shear stress deficit

The velocity profiles above and downwind from the canopy are affected by the physical characteristics of the canopy such as the shape of the canopy elements and the porosity of the canopy. In particular, the aerodynamic roughness and the displacement height, which characterize the velocity profile above the canopy, are affected.

All wind velocity profiles over the model lake surface show a velocity deficit relative to the wind velocity profile without a canopy (Fig. 6.8), and the roughest canopy has a much larger velocity deficit than the smoothest canopy. A direct comparison of velocity profiles at the end of the canopy ($x = 0$), and downwind ($x/h_c = 90$) illustrates that even at a relatively large distance, there is still a measurable velocity deficit for both of the canopies. Far downwind from the solid backward-facing step, ($x/h_c = 90$), the velocity profile had transitioned closer to that of the reference profile without a canopy. It is clear that the behavior of the velocity profile for the BFS is distinctly different from those for the two porous and rough canopies that require a distance longer than $x/h_c = 100$ to overcome the canopy effect entirely.

The results of the wind tunnel experiments indicate that downwind of the canopy, in the transition from the land to the lake surface, the shear velocity (stress) is greatly reduced. When normalized with reference shear (friction) velocity U_{*r}, far downwind, the sheltering extends over a downwind distance of approximately 40 to 60 times the canopy height (Fig. 6.9). Specifically the experiments show the shear stress on the surface downwind from the canopy was unaffected by wind sheltering after $x/h_c = 100$, and the effect was less than 10% after $x/h_c = 60$ for all cases. This compares with the theoretical form that surface shear stress is related to sheltering element height by $\tau \sim (h/x)$, developed by Counihan et al. [186] for an array of roughness elements and verified by Bradley and Mulhearn [187]. Similar to the result found in the field by Bradley and Mulhern our results for surface shear stress were found to adjust at a slower rate than given by the model of Counihan et al. [186].

These results lead to the conclusion that surface shear stresses recover from the wind sheltering effect much faster than velocity profiles downstream from the canopy. This

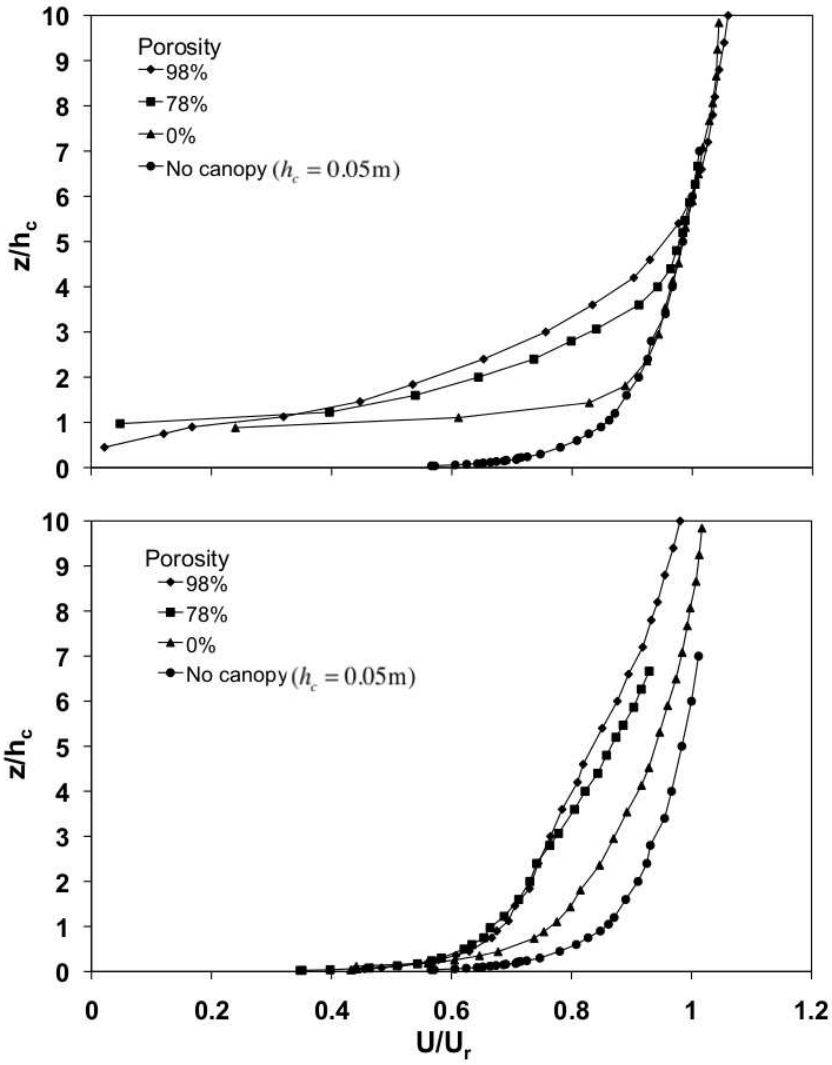

Figure 6.8: Normalized wind velocity profiles in the wind tunnel for three canopies (0%, 78%, and 98% porosity) at the end of the canopy (top) at $x = 0$ and (bottom) at $x = 90h_c$ downwind from the end of the canopy. A reference velocity profile for without a canopy is plotted and normalized with the height of the solid backward-facing step.

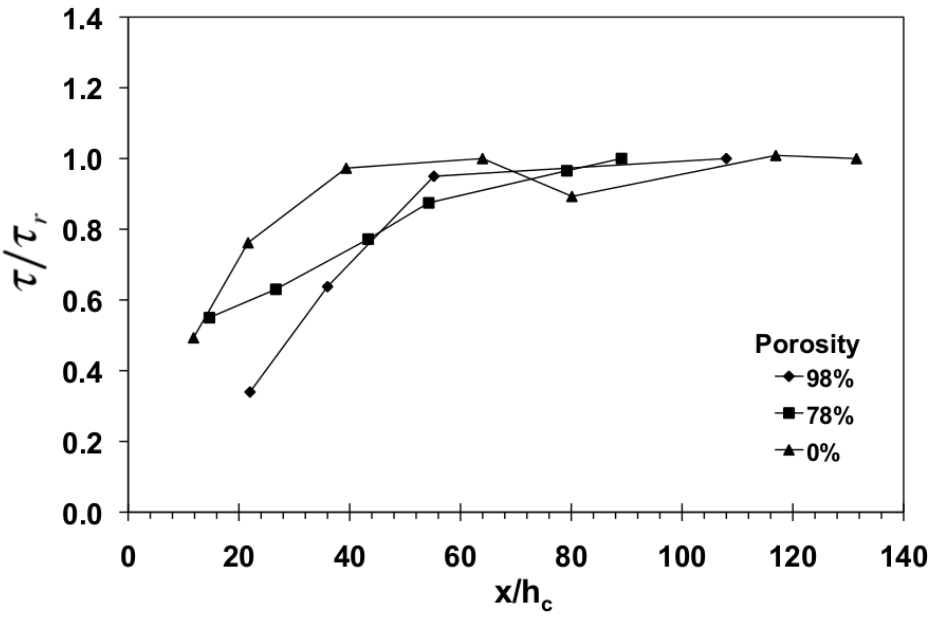

Figure 6.9: Normalized and time-averaged shear stress τ/τ_r as a function of normalized distance (x/h_c) downwind of three canopies in the wind tunnel.

agrees with previous results for roughness transitions (e.g. Bradley [188]).

6.6.2 Field study results

The results from the field study of shear (friction) velocity, calculated as discussed in the previous section, show station locations and mean wind direction (Fig. 6.10). Since the mean wind speed was not constant during the field experiments, shear (friction) velocities had to be normalized to account for the non-stationary wind field. All measurements were referenced to a time-variable baseline velocity to make meaningful comparisons. This was accomplished by dividing each value of u_* by the corresponding value of u_* measured at station 1. These normalized values of u_* from each station were averaged for the entire duration of the measurement. The variation in normalized u_* throughout the sampling period is indicated by error bars, which represent one standard deviation about the mean. Sampling periods ranged from a minimum of just over an hour, for the mobile stations, to about five hours for the fixed stations.

The surface shear stress or shear (friction) velocity on a lake surface is a function of distance from the canopy. Therefore normalized shear (friction) velocities were plotted against distance. Like the shear (friction) velocity data, the multiple fetch values are averaged over the total sampling period for each station, and represented as a single point with error bars indicating one standard deviation about the mean.

The roughness coefficient on the lake ice/snow cover was determined to be in the range from 0.0005 to 0.004 m for the various station locations. The measurements confirm that the aerodynamic roughness of ice and snow on Round Lake is similar to that of open water, previously reported (Table 6.3).

The data show that surface shear stress on the lake varies the most over the first 500 m downwind of the transition from the canopy along the shore onto the lake, and the shear stress at the transition point from the canopy to the lake surface extends to approximately zero. The canopy surrounding the lake was estimated in the field to be approximately 10 m high. The length of reduced shear stress therefore is found to be approximately $50h_c$ (Fig. 6.11). This matches the results of the wind tunnel study and those by Bradley and Mulhearn [187].

Unlike a water surface, which deforms as the wind blows over it, a lake covered by ice with or without snow on it has properties analogous to a rigid flat plate. To

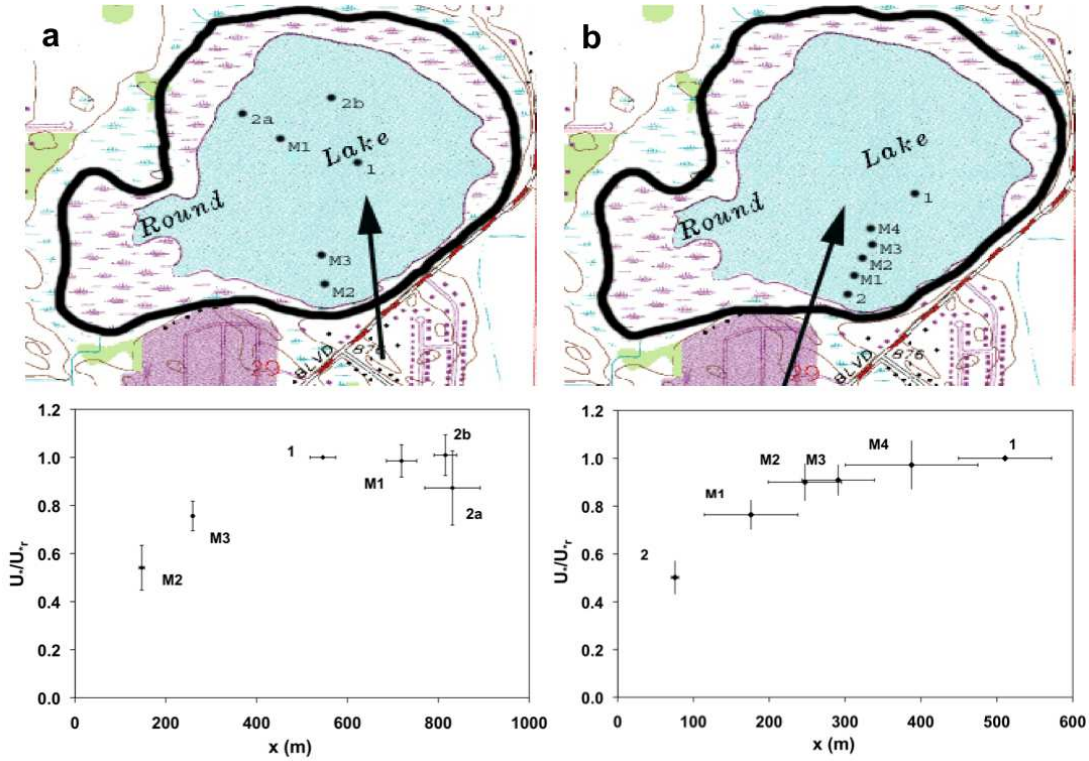

Figure 6.10: Measurement station locations for wind speed measurements on (a) 28 February 2004 and (b) 3 March 2004, where "M" identifies mobile stations and the arrow indicates mean wind direction during the measurement period. The bottom plots show normalized and time-averaged shear velocity u_*/U_{*r} as a function of distance from the tree line. Error bars indicate one standard deviation of measurements.

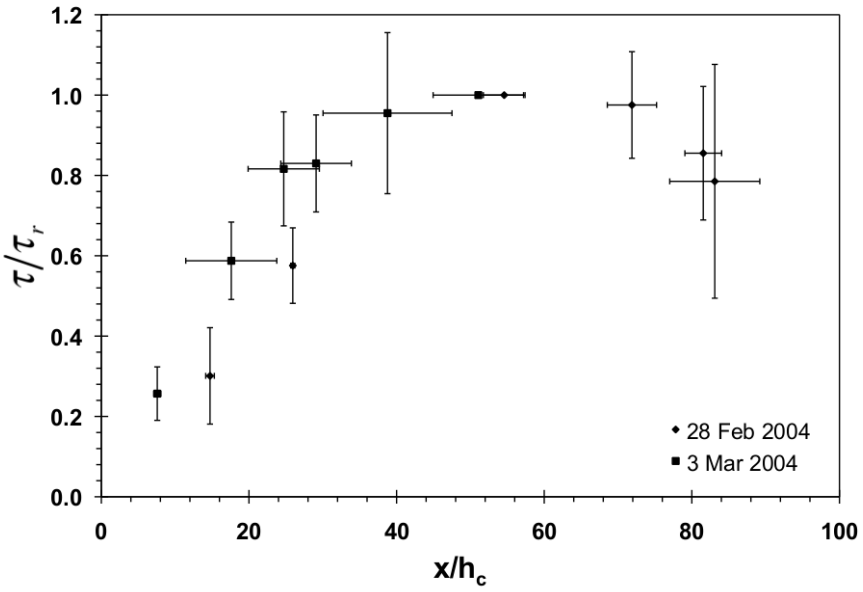

Figure 6.11: Normalized and time-averaged shear stress τ/τ_r as a function of normalized distance x/h_c from shoreline trees at Round Lake, Andover, MN.

determine whether the shear stress results from the data collected over the ice can be extended to open water conditions, shear stress on a flat plate for a distance of 1,000 m, based on inversion of the friction law technique shown by Schlichting and Gersten [152], and for open water were plotted as a function of wind speed (Fig. 6.12). Shear stress at distance $x = 1,000$ m is considered in this example to ensure that the turbulent boundary layer is fully developed and is comparable to the field scale. This is also the size of the lake in this experiment. The shear stress development over open water is calculated from Equations (6.1) – (6.3). The result shows that the shear stress over a flat surface or ice-covered lake is comparable in magnitude to that on open water for a distance of 1,000 m. In general, data collected over the ice are representative of open water conditions, although minor differences at small wind velocities (i.e., $U_{10} < 10$ m s^{-1}) are evident. Although wind speeds were not measured at a height of 10 m, it is safe to infer from the maximum wind velocity of 5 m s^{-1} measured at a height of 2.3 m that wind velocities at 10 m were less than the 10 m s^{-1} threshold.

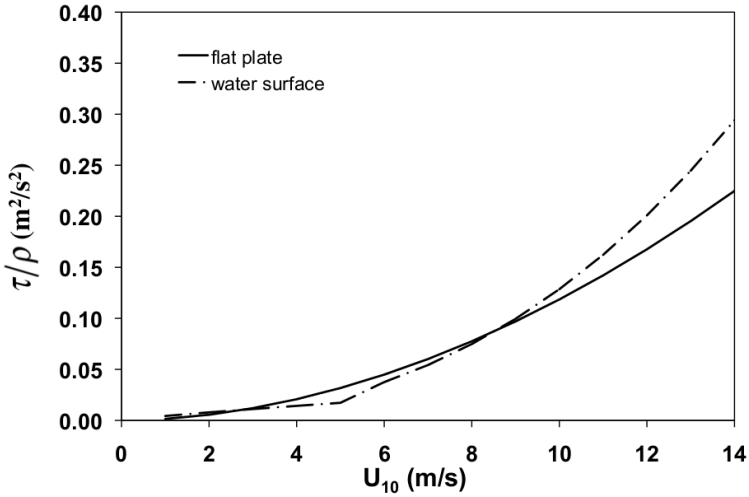

Figure 6.12: Plot of surface shear stress τ as a function of wind speed U over a flat plate (i.e., ice cover) at $x = 1000$ m and over a water surface (Equation (6.1) with Equations (6.3) and (6.4) for drag coefficients).

6.6.3 Application to lake modeling

The theory for internal boundary layer (IBL) development from a rough to a smooth surface suggests that a new equilibrium layer develops over the new surface without influence from the upwind surface. The experiments confirm this, and the extent of lake sheltering, in terms of a surface shear stress development downwind from a canopy, can be roughly related to canopy height. In terms of surface shear stress, wind sheltering is shown to extend over a length of approximately $40h_c$ to $60h_c$. Therefore, a lake with a diameter less then 40 to 60 times the adjacent canopy height (e.g., 10 to 15 m for mature forests and relatively dense tree lined shores) has a sheltered length of approximately 400 to 900 m. Such a lake will experience wind velocities and shear stresses significantly smaller than those measured e.g., at a nearby airport or unsheltered station on or near a lake. The characteristic "shear deficit length" x_τ of $40h_c$ to $60h_c$ differs substantially from the reattachment length for the flow over a step, which is commonly given as $5h_c$ to $7h_c$ (Aider et al. [184]).

A simple geometrically based relationship to estimate the wind-sheltering coefficient for relatively round lakes based on the area of wind access can be derived using this shear

deficit length with independent variables, lake size and canopy height. The area of a lake where surface shear stress is not significantly reduced by wind sheltering approximates the area of wind access,

$$A_{\text{wind access}} = \frac{D^2}{2}\cos^{-1}\left(\frac{x_\tau}{D}\right) - \frac{1}{2}x_\tau\sqrt{D^2 - x_\tau^2}, \tag{6.7}$$

where D is the equivalent circular diameter of the lake, based on lake surface area, A_{lake}. The wind-sheltering coefficient is then defined as the ratio of the area of wind access, Equation (6.7), to the total lake surface area:

$$W_{str} = \frac{A_{\text{wind access}}}{A_{\text{lake}}} = \frac{2}{\pi}\cos^{-1}\left(\frac{x_\tau}{D}\right) - \left(\frac{2x_\tau}{\pi D^2}\right)\sqrt{D^2 - x_\tau^2}. \tag{6.8}$$

When the canopy height shrinks to zero, x_τ also diminishes, and the area of wind access, as to be expected, approaches the total lake surface area. Similarly a very large lake affectively has no wind sheltering, and the wind-sheltering coefficient equals 1.0.

A range of predictions by Equation (6.8) for $x_\tau/h_c = 40$, 50 and 60 are plotted along with calibration results from lake temperature model simulations (Fig. 6.13). The new model for *a priori* estimation of the wind-sheltering coefficient is validated by comparison with calibrated wind-sheltering coefficient values W_{str}^{+} from eight lakes of different sizes. The model-calibrated wind-sheltering coefficients are from Hondzo and Stefan [175] using wind data from nearby airports. The only data not previously recorded for these lakes were the average canopy heights surrounding the lakes. Topographic maps, satellite photos and field observations were used to estimate an appropriate canopy height for each of the lakes. Canopy heights ranged from 5 m for sparse shoreline trees and agricultural crops to 15 m for dense old growth forests with topographic relief.

Determining an average canopy height is not trivial. One has to consider a number of factors such as the canopy coverage along the shore, and the dominant direction of winds during the growing season. One should consider the tallest, most continuous canopy closest to the lake, because the influence of canopies further from the lake is decreased with distance and shorter canopies along the lake might be sheltered by nearby larger ones. For example, if agricultural fields surround a lake, but a dense line (wind-break type) of trees border the shoreline, the canopy height should be considered as the wind-break height. Lake shape also affects the overall lake sheltering. Although a

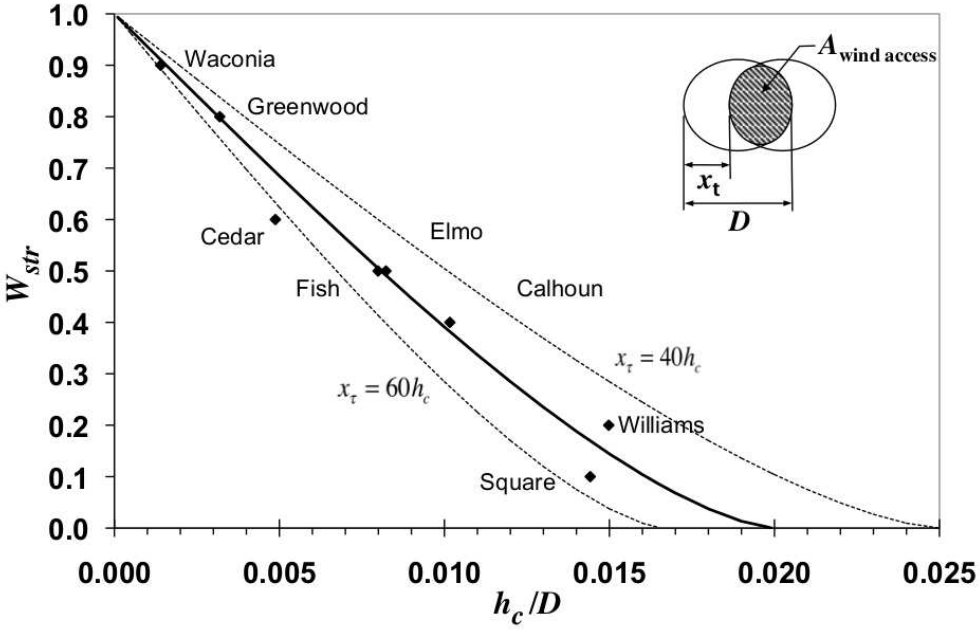

Figure 6.13: Wind-sheltering coefficient, W_{str}, as a function of canopy height, h_c, to lake diameter, D, ratio. The solid line gives the prediction by the wind-sheltered area model on the basis of wind tunnel and field experiments (Equation (6.8)). Symbols are wind-sheltering coefficients from Hondzo and Stefan (1993) obtained by calibration of a one-dimensional water temperature stratification model for eight lakes of different sizes.

number of the lakes in Table 6.4 were not round and had variable canopy characteristics, considering an effectively round lake and constant canopy height for the wind sheltering estimate by Equation (6.8) gave good results. The new wind-sheltering model shows good agreement with the 1-D model calibrated wind-sheltering coefficients and can be used to estimate wind-sheltering coefficients a priori.

Table 6.4: Summary of wind-sheltering coefficients predicted by the wind-sheltered area model for eight lakes compared to wind-sheltering coefficients obtained by calibration of a 1-D water temperature stratification model

Lake	Surface Area (km^2)	Circular Diameter (km)	Calibrated Year	W_{str}^+	Near Lake Land Cover	h_c (m)	W_{str}
Thrush	0.07	0.30	1986	0.01	forest with relief	15	0.00
Williams	0.35	0.67	1984	0.2	forest/agricultural field	10	0.15
Square	0.85	1.04	1985	0.1	old-growth forest	15	0.17
Fish	1.16	1.22	1987	0.5	agricultural field/shoreline trees	10	0.49
Elmo	1.23	1.25	1988	0.5	agricultural field/shoreline trees	10	0.51
Calhoun	1.71	1.48	1971	0.4	suburban forest	15	0.38
Cedar	3.3	2.05	1984	0.6	agricultural field/shoreline trees	10	0.69
Greenwood	7.7	3.13	1986	0.8	forest/wetland	10	0.80
Waconia	10.0	3.57	1985	0.9	sparse shoreline trees	5	0.91

W_{str}, wind-sheltering coefficient given by Equation (6.8); W_{str}^+, calibrated wind-sheltering coefficients (Hondzo and Stefan, 1993). Some characteristics of the eight lakes are also given.

On the basis on the data set used to validate the new wind-sheltering model, it seems reasonable to expect that a well-defined (wind-break type) tree line along the lakeshore will produce an effect similar to a wide forest canopy in terms of downwind surface shear stress development. This can be seen in Figure 6.13 and Table 6.4 for Fish, Elmo and Cedar lakes, which have a belt of trees along their shorelines. It would seem more important that the tree line be continuous and relatively dense. However, we did not investigate canopies of limited width in a rigorous way and it would be premature to draw conclusions on a threshold density or width.

Although this model was developed for nearly round lakes, the same geometric principle relating the shear deficit length and lake size is believed to apply to lakes of arbitrary shape. It is also important to note that the woody canopy elements along with foliage appear to be an important contributor to the sheltering effect. The field results, for a mostly deciduous canopy, show that even during the winter when there are no leaves, sheltering still occurs. This supports the importance of considering the roughness density or frontal area index as opposed to leaf area index when characterizing the canopy density as pointed out by Raupach [99].

While practical for 1-D lake models, the wind-sheltering coefficient discussed above neglects details of non-uniform wind speed distributions over lakes that are important for three-dimensional lake models (e.g., Wang and Hutter [189]; Wang et al. [189]; Wang [190]; Rueda et al. [191]). Our results for surface shear stress development downwind of a canopy or a bluff may be useful as input to these modeling applications.

6.7 Conclusions

Wind stress distribution on a lake surface is an important boundary condition for simulating lake circulation and water quality. However, the effect of vegetation canopies, buildings, and topography surrounding a lake on the distribution of surface shear stress on the lake is poorly understood. In this paper, the transition of the ABL wind field from a rough canopy or a bluff to a smooth surface and the associated surface shear stress (shear velocity) development have been explored experimentally.

Experiments were conducted in a boundary layer wind tunnel to determine the extent of wind sheltering by a bluff or vegetation (tree) canopies of varying height,

roughness and porosity. Wind velocity profiles downwind from the canopies or bluff were measured, and shear stress distributions were derived from the measurements. Results of field experiments, conducted on the ice-covered Round Lake, validate the wind tunnel results. In both the wind tunnel and the field, a reduced surface shear stress over a distance of 40 to 60 times the canopy height was observed. These findings provide the basis for a simple but sufficiently accurate model to estimate wind-sheltering coefficients that can be used in numerical 1-D hydrodynamic/water quality models of stratified lakes. The new wind-sheltering model predicts *a priori* an area-based wind-sheltering coefficient based on canopy height and lake size alone. Wind-sheltering coefficients predicted by the model were validated against those obtained by calibration of simulated lake temperature profiles for measurements in eight stratified lakes over a period of several years, and the a priori model results compare well to the a posteriori determined values (Fig. 6.13). The results show that small lakes ($A_{\text{lake}} < 1$ km^2) will experience substantial sheltering if surrounded by a continuous canopy or a bluff greater than 10 m high.

Another outcome of the study is the recognition that lake modelers should use wind velocity data collected near or on a lake cautiously. It is important to consider land cover near lakes when measuring wind speed on a lake for the purpose of lake processes simulation. It is likely that the wind data collected near or on a lake are not representative of the spatial distribution of wind over the lake surface. A better understanding of how wind-sheltering impacts wind patterns on lakes, and how it affects the interpretation of measurements at a single point is required. The results from wind tunnel and field experiments provide useful information about how wind sheltering of a lake diminishes downwind of a canopy or a bluff. Wind direction is also important in interpreting wind data collected on or near a lake, especially for lakes of irregular shape or with heterogeneous land cover and topography. The model presented in this paper provides a tool to estimate the wind-sheltering coefficient of a (small) lake, which previously could not be determined without in situ measurements.

Chapter 7

Wind Sheltering Effects on Methane Flux from Wetlands[†]

[†] **This chapter was published as Godwin CM, PJ McNamara and CD Markfort. 2013. Evening methane emission pulses from a boreal wetland correspond to convective mixing in hollows. *J. Geophysical Research: Biogeosciences.* 118, 1-12. doi:10.1002/jgrg.20082.**

7.1 Abstract

Spatial and temporal heterogeneity of methane flux from boreal wetlands makes prediction and up-scaling challenging, both within and among wetland systems. Drivers of methane production and emissions are also highly variable, making empirical model development difficult and leading to uncertainty in methane emissions estimates from wetlands. Previous studies have examined this problem using point-scale (static chamber method) and ecosystem-scale (flux tower methods) measurements, but few studies have investigated whether different processes are observed at these scales. We analyzed methane emissions from a boreal fen, measured by both techniques, using data from the Boreal Ecosystem-Atmosphere Study. We sought to identify driving processes associated with methane emissions at two scales and explain diurnal patterns in emissions measured by the tower. The mean methane emission rates from flux chambers were greater than the daytime, daily mean rates measured by the tower, but the nighttime, daily mean emissions from the tower were often an order of magnitude greater than emissions recorded during the daytime. Thus, daytime measurements from either the tower or chambers would lead to a biased estimate of total methane emissions from the wetland. We found that the timing of nighttime emission events was coincident with the cooling and convective mixing within hollows, which occurred regularly during the growing season. We propose that diurnal thermal stratification in shallow pools traps methane by limiting turbulent transport. This methane stored during daytime heating is later released during evening cooling due to convective turbulent mixing.

Keywords
Methane emissions; Boreal fen; Flux measurements; Diurnal methane pulse; Thermal stratification

7.2 Introduction

Methane emissions from natural wetlands are estimated to range from 100 – 231 Tg per year, which makes wetlands the largest natural source of methane (Solomon et al. [192]). Boreal wetlands are a major source of methane (CH_4) emissions (Mikaloff-Fletcher et al. [193], Harriss et al. [194]) and are expected to have a net warming effect on global climate (Frolking et al. [195]). Although total wetland area has been constrained for North America and Eurasia (Bridgham et al. [196]), substantial uncertainty exists in the total emissions from these wetlands (Mikaloff-Fletcher et al. [197]; Olivier et al. [198]; Wuebbles and Hayhoe [199]). Much of this uncertainty is due to the substantial variation in emission rates among wetlands Bubier and Moore [200]; Moore and Knowles [201]; Saarnio et al. [202]) and the difficulty of predicting emission rates from habitat classification and remote-sensing data (Christensen et al. [203]; Potter et al. [204]). Estimates from a single wetland are affected by spatial (Alm et al. [205]; Dinsmore et al. [206]) and temporal (Dinsmore et al. [207]; Mikkela et al. [208]; Windsor et al. [209]) variability. Locally, emission rates are often correlated with environmental parameters including soil temperature (Hargreaves et al. [210]; Høj et al. [211]; Wille et al. [212]), water table position [Bubier [213]; Heikkinen et al. [214]; Huttunen et al. [215]), soil moisture content (Granberg et al. [216]; Rhew et al. [217]), vegetation coverage (Bartlett et al. [218]; Joabsson and Christensen [219]), and interactions among several of these variables (Christensen et al. [220]; Nakano et al. [221]; Rask et al. [222]). Integrating flux rates across spatially variable landscapes improves emission estimates (Christensen et al. [223]; Dalva et al. [224]; Flessa et al. [225]; Huttunen et al. [215]), but this method of up-scaling requires fine-scale spatial models of parameters that drive CH_4 emission.

Emissions of CH_4 from wetlands are commonly measured using the flux chamber method (Moore and Roulet [226]). In this method, a small area of wetland soil (typically < 1 m^2) is covered with an airtight chamber, and the flux is calculated from the change in headspace CH_4 concentration over time (Levy et al. [227]). These short-term measurements have high certainty for the area covered by the chamber, but many chambers are needed to describe spatial variability within a wetland. Data from manually operated chambers often have poor temporal resolution due to the amount of

time required to sample the chambers and measure the headspace gas concentration. As a result, few studies using chambers attempt to characterize temporal dynamics at time-scales shorter than weeks (Mikkelä et al. [208]; Waddington et al. [228]; Whalen and Reeburgh [229]). Furthermore, chamber sampling may have artifacts due to collar installation, differential heating (Denmead [230]), headspace pressure, and lack of turbulence within the headspace (Moore and Roulet [226]; Pihlatie et al. [231]).

Whereas the chamber method yields measurements that are spatially and temporally restricted, tower-based flux measurements integrate the flux over much larger spatial scales (Fan et al. [232]; Riutta et al. [233]) and have superior temporal resolution (Laurila et al. [234]). In both the flux gradient tower method and the eddy-covariance tower method, the footprint of the flux tower is proportional to the tower height, atmospheric boundary layer conditions (Hargreaves et al. [210]), and surrounding topography (Vesala et al. [235]). These tower-based micrometeorological methods have the advantage of larger measurement area than chambers, which means that the tower measurements integrate across greater spatial variability. However, because tower measurements are sensitive to micrometeorological conditions, their effective footprint is variable depending upon wind direction, atmospheric stratification, and turbulence levels.

Efforts to integrate CH_4 flux from plant-scale chamber measurements to wetland-scale tower-based measurements have shown reasonably good correspondence between the two methods. Alm et al. [205] measured CH_4 flux from a bog using both chambers and a tower and found that the tower measurements were within the range of flux measured by chambers in different microhabitats. Others have shown correspondence between flux tower measurements and area-weighted estimates from chamber measurements based upon habitat classifications (Schrier-Uijl et al. [236]), microtopography (Clement et al. [237]) and plant communities (Riutta et al. [233]). Forbrich et al. [238] showed that separate predictive models for three habitat classifications produced better correspondence with the tower than a single model for an entire wetland. However, a similar area-weighted model by Hendriks et al. [239] overestimated the flux measured by a tower. Although these studies have shown encouraging results, there remains a critical need to reconcile chamber-based measurements with flux tower measurements, particularly with regard to driving forces at disparate scales including temporal dynamics in emissions that occur over timescales that are not readily resolved by the chamber

method.

We used an existing dataset of chamber and tower measurements (previously not analyzed) from the Boreal Ecosystem-Atmosphere Study (Bubier et al. [240]; Crill and Varner [241]; Sellers et al. [242]) to compare chamber-based measurements of CH_4 emissions to tower-based measurements for a single wetland. We sought to address three questions using this dataset: (1) How do measurements of CH_4 flux differ between the chamber and tower measurement techniques? (2) Which drivers of CH_4 flux are important at these two measurement scales? and (3) Are episodic events in flux rate apparent when using the tower method?

7.3 Methods

7.3.1 Description of the field site

The Boreal Ecosystem-Atmosphere Study (BOREAS) was an international collaborative project conducted from 1990 until 2000, with the purpose of quantifying the exchange of greenhouse gases between the boreal ecosystem and the atmosphere (Sellers et al. [242]). Substantial effort was made to measure the exchange of carbon dioxide (CO_2) and CH_4 at nested spatial scales using multiple methods. Previous publications provide detailed descriptions of the methods, data, and findings associated with the project (Bellisario et al. [243]; Bubier et al. [244]; Lafleur et al. [245]; Sellers et al. [242]). During the 1996 field season, BOREAS investigators conducted intensive sampling of CH_4 and CO_2 flux from a minerotrophic fen using static chambers and tower-based methods. The fen (tower fen) is located in the Northern Study Area (NSA), near Thompson, Manitoba, Canada and is characterized by hummock-hollow microtopography (Lafleur et al. [245]). The fen is approximately 50 ha in area and is surrounded by boreal forest. Lafleur et al. [245] describe the hydrology, plant composition, and climate of the fen.

7.3.2 Static chamber measurements

Methane emissions were measured using the static chamber method (Bubier [240]; Bubier et al. [244]; Moore and Roulet [226]) from June to October 1996. Opaque chambers

(0.053 m^2) were used to collect samples of headspace gas from permanent collars embedded in the peat. Twelve chambers were sampled along spurs off of a boardwalk leading to the flux tower. The chambers were sampled during the day (P. Crill, personal communication, 2011) by collecting five samples of headspace gas at 2-4 minute intervals and measuring the CH_4 concentration by gas chromatography (Bubier et al. [240]). The CH_4 flux from the chambers was calculated from the regression of CH_4 concentration in the chamber versus time. Uncertainty in the CH_4 flux measurements was estimated at less than 1%, with a minimum detectable flux of 0.07 nmoles CH_4 m^{-2} s^{-1} (Bubier et al. [240]). Chambers were sampled at approximately 7-day intervals for a total of 20 sampling dates. Data were excluded when ebullition was observed while manipulating the chambers (Bubier et al. [240]). Flux measurements were obtained from a minimum of six chambers on each date, with at least 10 chambers on 14 of the sampling dates. The CH_4 flux data from the chambers were included in a regional analysis by Bubier et al. [246].

7.3.3 Tower flux measurements

The tower-based CH_4 flux measurements from the BOREAS NSA fen tower have not been published previously. Methane flux was measured over the fen surface from May to November 1996 using the flux gradient technique from wind speeds recorded at heights of 2.5, 4.0, and 6.0 m (McCaughey et al. [247]). Half-hourly averaged concentration gradients of CH_4 were calculated from measurements every 6 min using a gas chromatograph with a flame ionization detector at heights of 3.59 m and 6.65 m (Crill and Varner [241]). The gas chromatograph had an analytical precision of 0.2%.

The CH_4 flux was measured using the flux gradient approach (Eqn. (7.1)) where F_s is the mole flux density (nmoles m^{-2} s^{-1}) following Monin-Oboukhov similarity theory (Oke [170]).

$$F_s = -K_s \frac{\Delta c}{\Delta z} \tag{7.1}$$

$K_s = kzu_*/\Phi_s$ is the eddy diffusivity (m^2 s^{-1}), c is the amount of CH_4 (nmoles m^{-3}), Δz is the distance between the two measurement heights z_1 and z_2 (m), $u_* = \kappa(\Delta u/\Delta \mathrm{lnz})\Phi_m^{-1}$ is the friction velocity (m s^{-1}), determined from the slope of the wind

profile. κ is the von Karman constant (= 0.4), and u_* and K_s are corrected for atmospheric stability by Φ_m and Φ_s following Businger et al. [248]. u_* and K_s were determined using momentum flux and heat flux measured based on log-law similarity in an adjusted surface layer.

7.3.4 Quality control for tower data

In general, micrometeorological techniques are limited to ideal sites where the flow is fully adjusted to the surface and where Monin-Obukov similarity theory holds (Kaimal and Finnigan [50]). Forest or short shrub cover surrounds the fen, which is rougher than the fen surface. Transitions from an upwind rough forested surface to a relatively smooth fen leads to a change in drag on the flow resulting in the flow accelerating at the transition and adjustment to the new surface. The flow equilibrates to the fen surface and adjusts vertically with downwind fetch from the transition. The resulting internal boundary layer grows downwind. The thickness of the equilibrium layer is about 30% of the fetch distance over surfaces like that of a sedge fen (Raabe [249]). Additionally, at the transition between the fen and the forest, the flow may be displaced from the ground surface by approximately the height of the forest h, often resulting in a separation and wake region to form downwind of a transition, and a long fetch is required ($\sim 100h$) for the flow to equilibrate (Markfort et al. [11]). The forest on the eastern boundary of the fen is about 150 m from the tower. Currently there are no methods available to account for the effect the wake behind the forest canopy over a fen to determine fluxes during times when wind blows from directions without adequate fetch. Therefore, due to relatively short fetch length downwind of the forest, fluxes cannot be determined downwind of the forest canopy using the flux gradient method.

There are two main lobes of the fen with a sufficiently long fetch, each greater than 400 m (Fig. 7.1). The narrowest lobe extends to the southeast while a broad region extends to the north and northwest of the tower. The longer fetch of these lobes allows for use of the flux gradient approach to measure CH_4 fluxes. Tower data were excluded when the wind direction was not parallel to the axes of the suitable fetches of the fen. Data were accepted for wind blowing from the following sectors: ESE ($115° - 145°$), W ($245° - 297°$), and NNW ($315° - 340°$) (Fig. 7.1). A total of 6,725 half hour average CH_4 measurements were collected; however, 70% were eliminated based on wind direction.

Figure 7.1: Layout of the BOREAS NSA fen site, after Lafleur et al. (1997). Sectors identifying acceptable wind directions and approximate source area represented in tower-based flux measurement. Image copy-right GeoEye, obtained through Google Earth (www.google.com).

Data were also excluded when the friction velocity (u_*) was less than 0.1 m s^{-1} or the atmospheric stability was not near neutral (Ri > 0.2). These criteria ensured that the boundary layer flow over the surface of the fen was fully turbulent, and the flow was shear dominated and fully interacting with the surface. The choice of a threshold u_* and Ri can be rather arbitrary. In practice, the lowest threshold for u_* has been found to vary from 0.1 to 0.5 m s^{-1}, but this is highly dependent upon site characteristics (Aubinet et al. [154]; Laurila et al. [234]). The friction velocity u_* was tested for the site-specific flux data to determine the threshold of dependence (Fig. 7.2). No clear u_* dependence was found, except possibly near zero, so a conservative value ($u_* = 0.1$) was chosen to minimize artifacts due to limited shear. The Ri threshold is set to the established critical value (0.25) where turbulence may not fully interact with the surface due to negative buoyancy (Baker and Griffis [250]). Only 22% of collected data met these strict criteria, therefore no attempt was made to quantify a seasonal CH_4 budget. This resulted in a semi-continuous record of CH_4 flux. Most of the data excluded from analysis from the tower were during nighttime and periods of weak winds. Data from the tower were separated into daytime measurements between 08:00 and 17:00 hours (n = 625) and nighttime measurements between 17:00 and 08:00 hours (n = 869). Seasonal, monthly, and diurnal mean flux rates were computed as the mean of multiple flux measurements during a specific time period. These averages are not equivalent to fluxes integrated over time (e.g. monthly flux) or budgets, both of which require more complete continuous records of flux.

An advantage of the flux gradient approach is that it is not sensitive to many of the limitations of the eddy covariance method, namely sensor alignment and flow deflection. Both methods are based on the assumption of stationary and homogeneous flow and require a long fetch to limit advection effects. Therefore, for long-term measurements of trace gas flux, the flux gradient approach may not be better or worse than the more commonly employed eddy covariance method. Pattey et al. [251] present a modern technique for measuring CH_4 with a tunable diode laser in conjunction with the eddy covariance method. In their study they found that eddy covariance and flux gradient methods show good correspondence. An important limitation of the flux gradient technique is that significant gradients in the scalar quantity must be measured to accurately

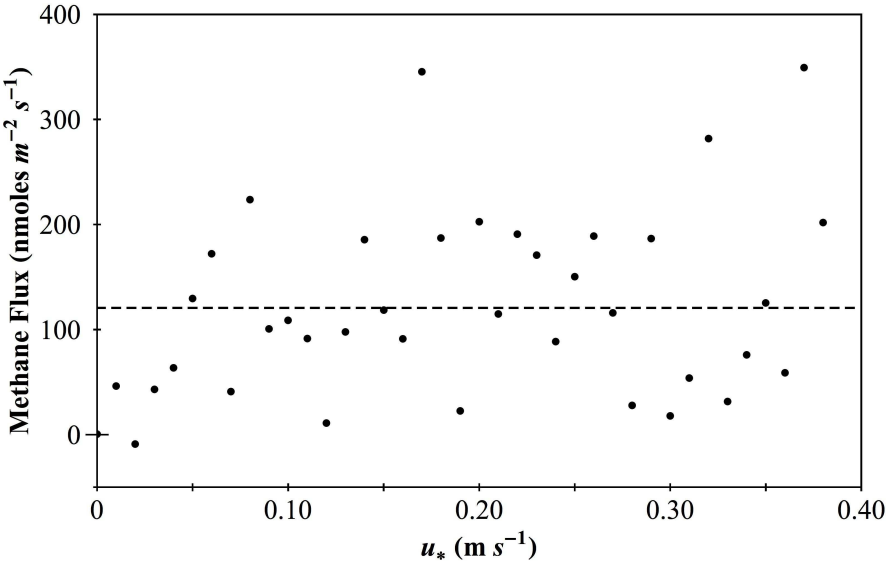

Figure 7.2: Dependence of methane flux on friction velocity (u_*). Data points are mean flux, binned by levels of u_*, the mean methane flux is shown as a dashed line.

resolve fluxes; however, this may not be the case over forests, and under highly convective conditions in the atmosphere. The measurements presented here do not consider fluxes over the forest but over short vegetation covering the fen. The flux gradient technique was developed for such a case. The effect of convection in the atmosphere does contribute to small gradients during the day; however, since our focus is on capturing the large pulses during the evening transition when the atmospheric stability is nearly neutral and turbulence is shear derived, the accuracy of the measured gradient in CH_4 is optimal. The footprint of the flux tower is limited by the selected wind sectors to ensure that the flux measurements are derived from the fen. Additionally, due to the criteria excluding data from times when the atmosphere is stable or during weak-wind conditions, the extent of the footprint is not expected to vary significantly.

7.3.5 Auxiliary data and analyses

Various other environmental, meteorological, and ecological data were measured in the fen and were available in the BOREAS dataset. Additional data included air temperature, water table height, and soil temperature profiles adjacent to the flux tower at

30 min intervals over the sampling period. Temperature measurements in the hollows were partitioned into three depths representing overlying water or pools (1, 5, and 10 cm) and six depths representing the underlying peat (25, 50, 75, 100, 150, and 200 cm). We performed this classification using the diurnal variability in temperature, which was much greater near the surface (1-10 cm) than below 25 cm. This result indicates that the peat-water interface was 10 to 25 cm below the surface. We represent the strength of thermal stratification as the temperature gradient between 1 and 5 cm depth in the water ($\Delta T/\Delta z$). We performed Spearmans rank correlation analyses for both the chambers and tower to determine if commonly measured parameters explain variability in CH_4 flux. For each chamber sampling date, the chamber data describe only spatial variance but the tower data describe both temporal and spatial variance. Because the spatial and temporal components of the tower data cannot be distinguished, we chose to compare the chambers and tower without using statistical hypothesis tests about the means.

7.4 Results

7.4.1 Spatial and temporal variability in chamber flux measurements

The 12 chamber locations produced mean seasonal fluxes between 22.4 and 318 nmoles CH_4 m^{-2} s^{-1} (range of measurements 1 – 1,389 nmoles m^{-2} s^{-1}). Although chambers differed in their seasonal mean flux, each chamber showed substantial temporal variability. The majority of the chambers showed a seasonal pattern of CH_4 flux, reaching a maximum during August (Fig. 7.3). The mean of chamber flux measurements taken in each 24 h span was positively correlated with daily water table level (Spearmans $r^2 = 0.42$, n = 9), whereas no correlation was observed between methane flux and daily mean air temperature ($r^2 < 0.01$, n = 20), minimum air temperature ($r^2 = 0.05$, n = 20), or peat temperature at 20 cm ($r^2 < 0.01$, n = 20).

7.4.2 Comparison of daytime chamber and tower flux data

Due to equipment failures and prevailing wind patterns, only 10 sampling dates had at least one daytime CH_4 flux measurement from both the chambers and the tower.

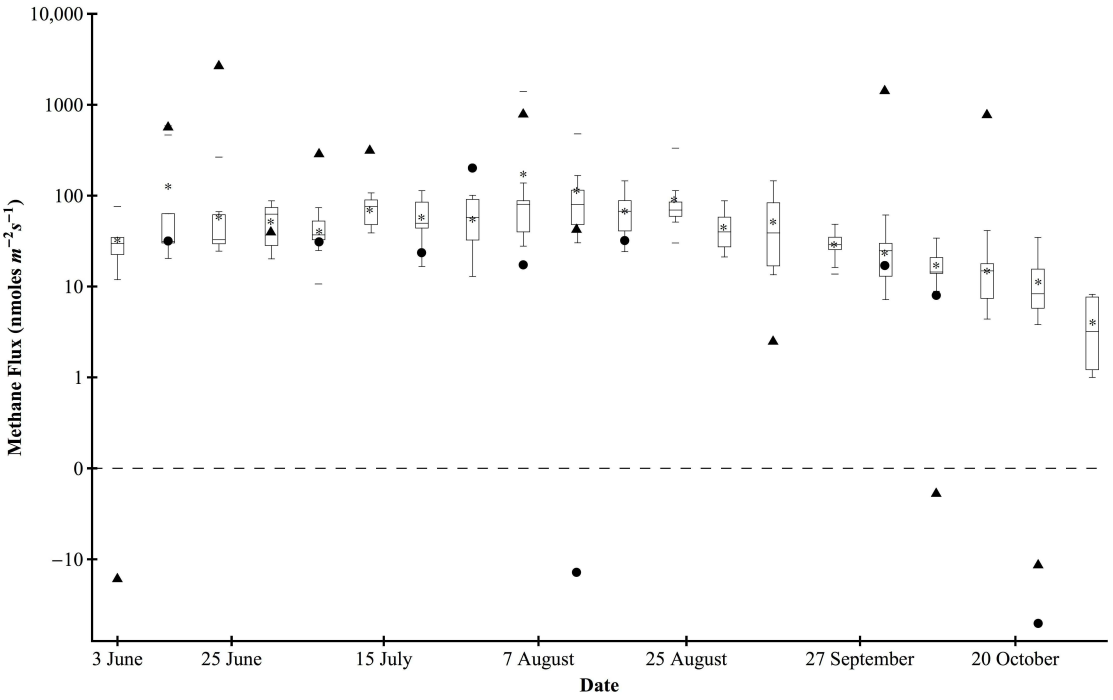

Figure 7.3: Seasonal trend in methane emission from the fen as measured by the chambers and the flux tower. The chamber data are displayed as boxplots for each date, with the centerline representing the median flux, the edges of the box representing the 25% and 75% quantiles, and the whiskers representing the maximum and minimum values. The mean chamber flux is denoted as a star and outliers greater than 1.5 times the interquartile range are denoted by horizontal dashes. Mean tower measurements during the daytime (08:00 - 17:00) are represented by circles and mean measurements during the following nighttime period are represented by triangles. For each measurement date, at least six chamber measurements were included (n = 10). The number of half-hour mean measurement represented in each point, for the daytime tower flux, was n = 7, 3, 6, 6, 3, 7, 1, 1, 4, and 1, respectively. The number of half-hour mean measurement represented in each point, for the nighttime tower flux, was n = 5, 11, 11, 3, 9, 3, 2, 9, 3, 1, 11, 1, and 26, respectively.

Mean flux measurements from chambers exceeded the mean of flux measurements from the tower during the daytime for all dates except 22 July (Fig 7.3), but the minimum chamber flux was less than the mean of flux measurements from the tower on six of the dates. On dates where the tower recorded a positive flux of CH_4 to the atmosphere, the mean of flux measurements from the chambers was 28 – 420% higher than the mean of flux measurements from the tower recorded during the daytime. Across sampling dates, the mean of daytime tower measurements was weakly correlated with the mean chamber measurements (Spearmans $r^2 = 0.15$, n = 10).

7.4.3 Temporal variability in tower flux measurements

Similar to the chamber measurements, the daytime (08:00 - 17:00) tower measurements show a strong seasonal pattern. Daytime flux measurements from the fen were mostly negative during the spring, but flux became positive and reached a plateau during the growing season from early June until early October (Fig. 7.4a). The means of daytime flux measurements in each month were the following: -90 nmoles CH_4 m^{-2} s^{-1} in May, 19 nmoles CH_4 m^{-2} s^{-1} in June, 27 nmoles CH_4 m^{-2} s^{-1} in July, 12 nmoles CH_4 m^{-2} s^{-1} in August, 9.5 nmoles CH_4 m^{-2} s^{-1} in September, and -8.5 nmoles CH_4 m^{-2} s^{-1} in October. The nighttime emissions from the fen showed a different seasonal pattern than the daytime measurements with consistently positive flux (Fig. 7.4b). The means of nighttime flux measurements in each month were the following: 298 nmoles CH_4 m^{-2} s^{-1} in May, 322 nmoles CH_4 m^{-2} s^{-1} in June, 891 nmoles CH_4 m^{-2} s^{-1} in July, 597 nmoles CH_4 m^{-2} s^{-1} in August, 93 nmoles CH_4 m^{-2} s^{-1} in September, and 28.7 nmoles CH_4 m^{-2} s^{-1} in October. The maximum emission rate of 24,008 nmoles CH_4 m^{-2} s^{-1} occurred on 1 July at 21:38. The micrometeorological data indicated near-neutral atmospheric stability ($Ri \approx 0$) and a high gradient of CH_4 near the surface (0.84 ppm m^{-1}). Across the entire season, the mean of nighttime flux measurements was 325 nmoles CH_4 m^{-2} s^{-1} (n = 869, standard error = 42), compared to 53 nmoles CH_4 m^{-2} s^{-1} (n = 625, standard error = 10) for daytime flux. The mean of nighttime emission rates was often an order of magnitude greater than the mean of positive daytime emission rates on the same date (n = 50, mean 11-fold, max 138-fold). These elevated nighttime emissions were highest during July (mean ± standard error, 24 ± 10-fold, n = 15) and August (17 ± 10-fold, n=6) and lower during June (4.5 ± 1.7-fold, n=16),

September (1.5 ± 0.57-fold, n=8), and October (1.1 ± 0.45-fold, n=4).

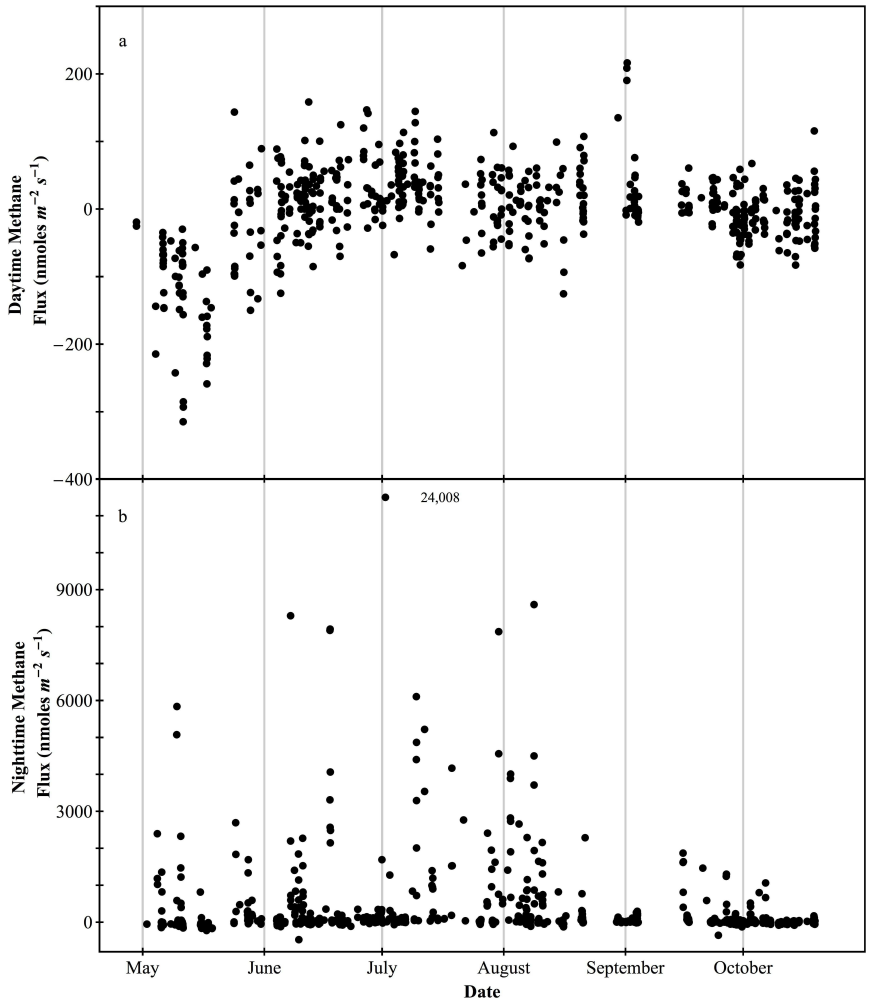

Figure 7.4: (a) Seasonal pattern of daytime (08:00-17:00 CST) and (b) nighttime methane fluxes during the growing season.

Daily mean CH_4 flux measurements from the tower were weakly correlated with other measured variables (including temperature in hummocks or hollows, wind direction, water table height, photosynthetic activity, and solar radiation) during the entire measurement period and within each month (Appendix Table A1 (in Godwin et al. [12]), all $r^2 < 0.50$). Daily mean flux rates during daytime were weakly correlated with air temperature and peat temperature at 10 cm over the measurement period ($r^2 = 0.25 - 0.28$).

Daily mean flux rates during the nighttime were weakly correlated with nighttime maximum air temperature ($r^2 = 0.23$), peat temperature at 10 cm ($r^2 = 0.16 - 0.17$), daily mean moisture flux ($r^2 = 0.24$), and CO_2 flux ($r^2 = 0.21$) from the fen. Methane flux was poorly explained by all measured variables at half-hour intervals throughout the measurement period and within each month (Appendix Table A2 (in Godwin et al. [12])). The strongest predictors of flux rates averaged at half-hour intervals were air temperature ($r^2 = 0.15$, n = 1,455), and peat temperature at 10 cm ($r^2 = 0.21 - 22$, n = 1,455). Daytime flux rates averaged half-hourly showed weak correlation with air temperature ($r^2 = 0.15$, n = 610) and peat temperature at 10 cm ($r^2 = 0.22$, n = 610). Nighttime flux rates averaged at half-hour intervals over the measurement period were weakly correlated with peat temperature at 10 cm ($r^2 = 0.23 - 0.25$, n = 845). Overall, explanatory power of any of these known drivers of flux was low ($r^2 < 0.25$).

Two periods are apparent in the semi-continuous flux record. During the first period (early morning until early afternoon), fluxes are nearly zero. During the second period (15:00 and 24:00), the largest fluxes of CH_4 occur. Unfortunately around 23:00 to 01:00, the shear stress and wind speed are unacceptably low, so we cannot identify the end of the event (Fig. 7.5a). Evidence that high flux continues after the wind decreases can be seen in the comparison between the flux time series and the ambient CH_4 concentration measured at the two heights (Fig. 7.5b). Although the flux time series is discontinuous due to the stringent quality control restrictions, and it cannot be shown that high flux rates occur every day, ambient concentrations were measured continuously and suggested high nighttime methane emissions. Unlike the flux measurements from the tower, concentrations are less sensitive to wind speed, wind direction, or atmospheric stability.

The thermal gradient ($\Delta T/\Delta z$) in the hollows (between 1 and 5 cm) showed a strong diurnal pattern (Fig. 7.5c). The surface of the standing water in the hollows was heated during the day due to solar input and cooled at night. Throughout the measurement record, cooling of the water in the hollows was found to be consistently coincident with the peaks in CH_4 concentration and flux measured by the tower (Fig. 7.5). Although data on the spatial coverage of hollows are not available for the fen, Lafleur et al. [245] indicate that the fen is characterized by hummock-hollow structure. On dates when thermal stratification of hollows was absent (e.g. 6-7 July), the nighttime

emission events were not observed (Fig. 7.5). Periods without thermal stratification (n = 17 days) were observed from June through October and were characterized by low irradiance, cooler air temperatures, some precipitation, and low ambient methane concentrations (supplemental material (in Godwin et al. [12])).

7.5 Discussion

7.5.1 Comparison of tower and chamber measurements

The discrepancy between the chamber measurements and daytime flux tower measurements is likely attributable to spatial heterogeneity in CH_4 emission, which has been observed within other wetlands (Alm et al. [205]; Bubier et al. [246]; Dinsmore et al. [206]). Variation in topography (Waddington and Roulet, 1996], plant distribution (Moosavi and Crill [252]; Riutta et al. [233]), soil moisture or water table position (Bellisario et al. [243]) and oxygen availability in the soil (Askaer et al. [253]) lead to patchiness in emissions within a wetland. Given this heterogeneity, a small number of chambers located adjacent to the flux tower is likely inadequate to characterize the flux across the footprint area of the tower and therefore the entire ecosystem. Wetlands with more homogeneous structure would be expected to have similar flux estimates as measured by the chambers and tower.

In a heterogeneous wetland, chamber-based estimates may be biased due to chamber locations and up-scaling the flux measurements across the area of representative habitat. The BOREAS fen has a moisture gradient and the tower was located in a wetter area near the edge of the fen (Lafleur et al. [245]), both of which suggest that the chamber locations are likely to have higher flux rates than other areas within the footprint of the tower. Due to quality control criteria, the comparisons in Figure 7.3 include only a few half-hourly tower measurements. A more continuous record of flux might provide a more robust comparison with the chambers and would allow integration of a daily flux. However, since the flux estimates were based upon 30 min averages of measurements recorded every 6 minutes, these estimates are sufficiently supported for comparison with the chambers that were sampled once each day over approximately 30 min. Sampling artifacts from the chambers (such as heating or ebullition) are typically small in magnitude (Denmead [230]; Moore and Roulet [226]), but may be sufficient

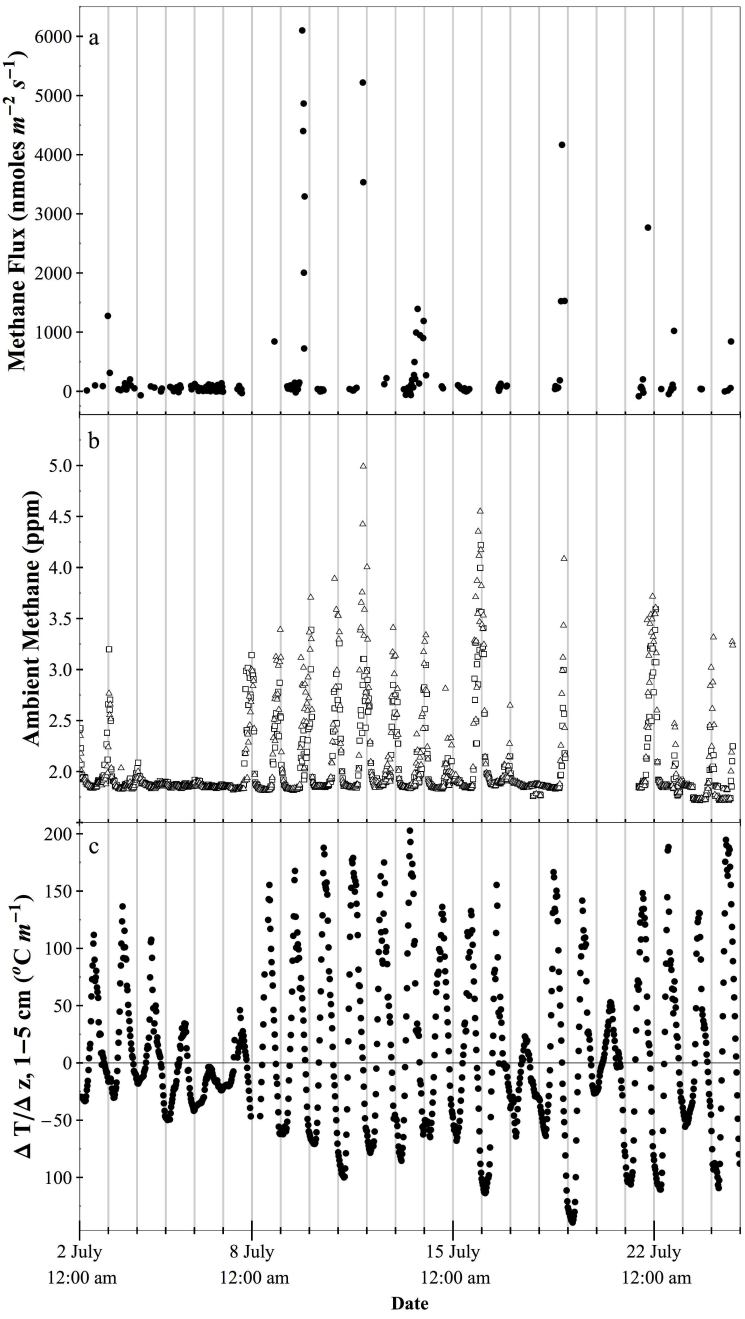

Figure 7.5: (a) Semi-continuous time series of methane flux as measured by the tower during the dates 2-25 July. (b) Ambient methane concentrations measured at 3.59 m (open triangles) and 6.65 m (open squares). (c) Thermal gradient ($\Delta T/\Delta z$) in the upper 5 cm of a hollow.

to account for a portion of the difference in daytime CH_4 flux observed between the chambers and the tower.

7.5.2 Temporal patterns in flux

The nighttime emissions measured by the flux tower were greater than the daytime emissions. This phenomenon has been observed in other studies utilizing chamber sampling and soil gradient methods, although the amplitude of the nighttime or evening increases were small (nighttime magnitude $< 150\%$ of daytime) (Nakano et al. [221]; Whiting and Chanton [254]) compared to those presented here. Yavitt et al. [255] used chambers to document increased nighttime emissions from a sedge meadow during the summer (magnitude 200%), but this pattern was absent at the same sites during the spring and reversed in the fall. Similarly, Whalen and Reeburgh [229] recorded elevated nighttime and evening emissions at two tundra sites using chambers (magnitude and 150 - 200%), but the diurnal pattern was absent or reversed at other sites. In contrast, the elevated nighttime emission rates presented here were observed throughout the growing season. Mikkelä et al. [208] documented elevated nighttime emissions in a boreal mire using chambers, but this difference was not consistently observed in lower areas of the wetland. Nighttime emission rates in drier communities were elevated (2 to 20-fold) relative to daytime, but this pattern was absent or reversed in more moist communities, including standing pools. The authors proposed that the elevated nighttime emissions were attributable to decreased methanotrophy due to lower temperatures at night or to the delayed release of substrates by plants. Although we are unable to determine if drier areas such as hummocks contributed to elevated CH_4 fluxes in our analysis, there is strong evidence that drier regions of the wetland have lower CH_4 flux (Bellisario [243]; Moosavi and Crill [252]), suggesting that the substantial nighttime emission events were not localized to drier regions.

Nighttime emissions peaks of comparable magnitudes have not been found in other studies utilizing the flux tower method (Harazono et al. [256]; Zona et al. [257]). Previous studies using tower-based measurements show no evidence of diurnal patterns in CH_4 emissions in wetlands lacking appreciable surface water (Forbrich et al. [238]; Rinne et al. [258]; Shurpali et al. [259]). Elevated daytime CH_4 emissions have been described in a wet tundra meadow adjacent to a lake (Fan et al. [232]) and from a

managed peat meadow where the pattern corresponded to peaks in CO_2 uptake and latent heat flux (Hendriks et al. [239]). Higher flux rates in daytime compared to nighttime were recorded by eddy correlation measurements from the BOREAS southern study area fen (Suyker et al. [260]), which included inundated hollows during the growing season (Suyker et al. [261]). Jackowicz-Korczyski et al. [262] found little diurnal variation in CH_4 flux from a Swedish mire, but did document elevated nighttime emissions from areas of the wetland adjacent to a lake (magnitude $< 150\%$). Kroon et al. [263] documented a consistent diurnal pattern in CH_4 flux from a peatland with a substantial area of surface water in ditches. Emission rates were elevated (magnitude $< 130\%$) during the afternoon and early evening, closely matching the diurnal pattern in soil temperature. In comparison to all other published studies of CH_4 flux over daily timescales, the BOREAS fen shows a distinct diurnal pattern with the majority of the flux from the ecosystem occurring during the night. It remains possible that nighttime emission events occur in other wetlands, but have been missed due to a lack of nighttime sampling. Also, wind velocity and shear stress were often reduced at night relative to daytime, which prevented reliable tower-based measurements. This shortcoming of the flux tower approach resulted in exclusion of the majority of nighttime measurements in the BOREAS dataset, but the acceptable data show that the nighttime pulses are regular.

Despite the consistency and large magnitude of the nighttime peaks observed in the BOREAS fen, the flux was poorly correlated with commonly associated variables including peat temperature (Bartlett et al. [218]; Bubier et al. [213]; Heikkinen et al. [214]), water table height (Alm et al. [205]; Bellisario et al. [243]; Hendriks et al. [239]), and net ecosystem exchange (Christensen et al. [264]). The strength of the correlations for the fen dataset showed little improvement when performed separately by month or by daytime and nighttime. This lack of strong dependence upon any single driver might be explained by significant spatial heterogeneity within the tower footprint, or a less-studied driver.

The flux rates observed by the tower during the nighttime were higher and had a greater range than previously published measurements from flux towers (Table 7.1). However, previous studies using the chamber method in northern wetlands have reported mean fluxes greater than 250 nmoles CH_4 m^{-2} s^{-1} (Harriss et al. [194]; Moosavi and

Crill [252]; van Huissteden et al. [265]; Vourlitis et al. [266]) and maximum rates greater than 1000 nmoles CH_4 m^{-2} s^{-1} (Harriss et al. [194]; Moosavi and Crill [252]; Roulet et al. [267]). The chamber measurements of CH_4 flux from the BOREAS NSA fen were high relative to many northern wetlands and indicate substantial capacity for CH_4 production within the fen. Methane production from the fen may be supported by comparatively high net carbon uptake documented during the 1996 growing season (Bubier et al. [268]) and increased precipitation (Bubier et al. [246]).

Table 7.1: Summary of methane flux measurements in northern wetlands using eddy covariance and flux gradient methods

Location	Sampling Period	Range of Flux (nmoles $m^{-2}s^{-1}$)	Mean Flux (nmoles $m^{-2}s^{-1}$)	Source
Mire, Sweden	2 years	0 to 346	107 (midseason)	[262]
Mire, Finland	Discontinuous	<0 to 75	10.8 (annual)	[210]
Fen, Finland	1 year	-35 to 173	24.9 (annual)	[258]
Peatland, Scotland	2 years	–	118 (annual)	[269]
Peatland, MN, USA	Discontinuous	87 to 195	–	[270]
Tundra floodplain, Russia	Growing season	4.1 to 25	13.5 (seasonal)	[271]
Bog, Finland	Growing season	0 to 87	5.3 to 37 (seasonal)	[205]
Managed fen, Netherlands	3 years	<0 to 113	23 (annual)	[263]
Peatland, MN, USA	Growing season	0 to 121	11.5 to 14.4 (annual)	[237, 259]
Fen, Finland	2 Growing seasons	-0.5 to 409	15.0 to 16.4 (seasonal)	[233]
Peatlands, Netherlands	3 years	–	0 to 69 (annual)	[239]
Mire, Finland	Growing season	0 to 142	13.4	[238]
Fen, SK, Canada	Growing season	0 to 337	140	[260]
Fen, MB, Canada	Growing season (nighttime)	-474 to 24,008	325	This study
Fen, MB, Canada	Growing season (daytime)	-442 to 2,999	53	This study

7.5.3 Possible mechanisms for nighttime emission events

The nighttime methane pulses could be the result of several driving forces. In this section we evaluate a number of documented mechanisms by using the available data and by comparing the magnitudes of pulses observed elsewhere to those presented in this paper. First, we propose a novel mechanism whereby CH_4 produced during the daytime is trapped in thermally stratified hollows and is released as pulses during evening cooling and convective mixing of the water. The magnitude and timing of nighttime methane emission pulses in our data set could be readily explained by this mechanism alone, as detailed below. The second group of mechanisms involves the role of vascular plants. Methane emission is commonly augmented by transport through vascular tissues and by the substrates that are exuded by plants. Vascular plants may also inhibit methane emission by transporting oxygen into the peat. Finally, effects of diurnal temperature fluctuations on the production and consumption of CH_4 are discussed. A schematic of the different flux pathways is presented in Figure 7.6.

Stratification in Hollows

The periodic nighttime CH_4 emission events observed in the tower dataset were not explained by hourly regressions against forcing variables (temperature in hummocks or hollows, wind direction, water table height, photosynthetic activity, and solar radiation, see Appendix Tables A1 and A2 (in Godwin et al. [12])). However, the episodic evening emission events and increased CH_4 concentrations just above the fen showed coincident timing with thermal destratification and convective cooling within the upper 10 cm of hollows (Fig. 7.5). Stratification within wetland pools and hollows has been documented previously (Van der Molen and Wijmstra [272]). Methane produced beneath the hollows may be effectively trapped by thermal stratification, accumulating within the lower (cooler) layers of water or at the peat-water interface. Under thermal stratification, emission of CH_4 occurs primarily through molecular diffusion. Molecular diffusion is substantially slower than turbulent diffusion and is likely the dominant transport process in the pools (Fischer et al. [160]). Ebullition has also been found to occur in stratified water bodies and wetlands, but could not be detected in this study. The strength of the thermal gradient should not affect the size of the emission event,

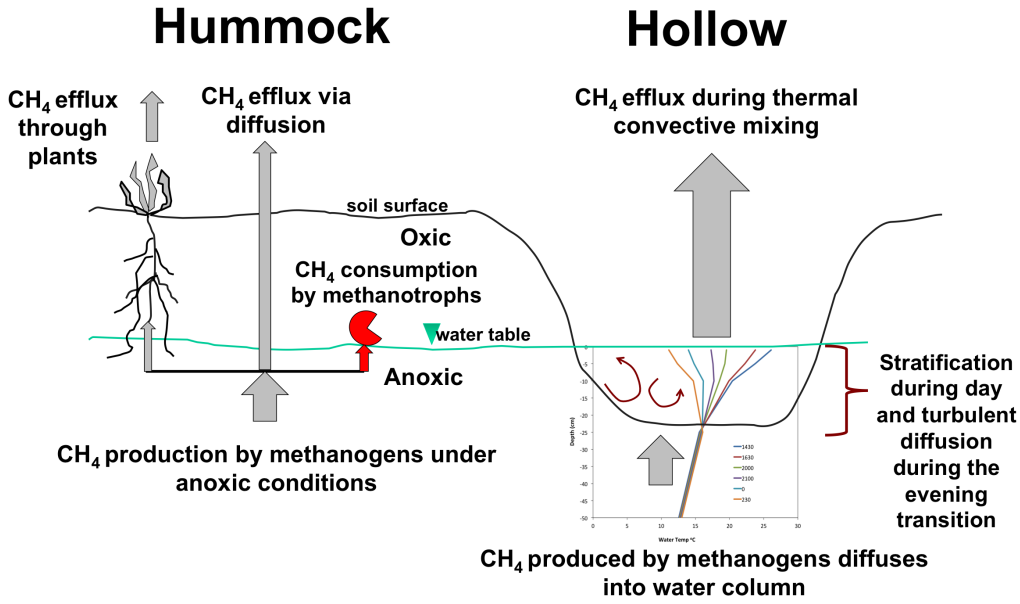

Figure 7.6: Schematic showing the pathways for methane flux from the soil to the atmosphere. The proposed mechanism of stratification controlled flux through hollow pools is highlighted, and the relative magnitude of the flux is indicated by the width of the arrow. Temperature profiles, taken from the data (1 July 1996) were overlaid on the hollow to illustrate the diurnal temperature structure within the wetland.

and thus $\Delta T/\Delta z$ was not used as a predictive variable for regressions. Although it is not possible with a discontinuous record of half-hourly flux measurements, this mechanism could be evaluated by comparing the rate of destratification with the onset of emission events in a dataset with finer temporal resolution (e.g. eddy covariance).

Although the solubility of CH_4 in water is low at the temperatures recorded in the hollows (Duan and Mao [273]), this mechanism is capable of producing emission events of the same magnitude as those observed by the tower. For instance, we assume that if hollows covered 30% of the fen surface at a mean depth of 20 cm, the cooler layer of water near the peat could store the equivalent of 45 mmoles m^{-2} across the area of the fen. If this stored methane were to be released over a 6 h time period with a linear rise and fall, the equivalent peak emission rate would be 2,074 nmoles CH_4 m^{-2} s^{-1}. This rate represents a hypothetical maximum storage capacity for the defined hollows, and only one percent of the measurements from the tower exceeded this emission rate. Thus the storage capacity within pools can account for the released methane during the evening transition, and the feasible emission rates via this mechanism are within the observed rates in this study.

Other studies have documented diurnal accumulation of dissolved CH_4 due to thermal stratification in shallow aquatic systems (Crill et al. [274]; Ford et al. [275]). Hollows have been shown to act as hotspots for CH_4 production and emission in wetlands (Alm et al. [205]; Bubier et al. [276]; Clement et al. [237]; Waddington and Roulet [277]). In addition to destratification releasing trapped CH_4, cooling at the surface dramatically increases the flux of gas to the atmosphere (MacIntyre et al. [278]). Studies in stratified lakes show that the flux attributable to cooling (buoyancy flux) at night exceeds the flux that may be attributed to wind-driven flux (MacIntyre et al. [279]). The effect of destratification and heat flux on gas emissions from wetland hollows has not been identified previously, but these physical processes may impact the flux of CH_4 from wetlands with standing water.

Studies have identified terrestrial freshwater bodies as major contributors of CH_4 to the atmosphere (Bastviken et al. [98]; Roulet et al. [280]). Convective mixing has been identified as a control of CH_4 and CO_2 release, especially from small water bodies (Eugster et al. [281]; Read et al. [282]). Recent work on the abundance and distribution of lakes has revealed that the majority of water bodies are smaller than 0.01

km^2 (Downing et al. [92]; McDonald et al. [93]). Although the role of convective mixing in gas flux has been described at a range of spatial scales from small lakes (Read et al. [282]) to the ocean (Rutgersson et al. [283]), convective mixing of inundated wetlands could represent a substantial and previously unrecognized component of methane flux.

CH_4 transport through plants

Diurnal patterns in CH_4 emission from wetlands have been attributed to diffusion of CH_4 through aerenchymatous tissues and stomatal conductance (Joabsson et al. [284]). In many wetland plant species, these tissues transport atmospheric oxygen to roots and stems in anoxic sediments, but may also be an important pathway for CH_4 flux as well (Hargreaves et al. [210]; Morrissey et al. [285]). However, unlike the elevated nighttime CH_4 emissions observed in the BOREAS fen, aerenchymatous transport of CH_4 produces diurnal patterns in which flux is highest during the period of peak photosynthetic activity (Lloyd et al. [286]; Mikkelä et al. [208]; Thomas et al. [287]), though this correlation may be weak (Askaer et al. [288]). Although aerenchymatous transport of CH_4 may have occurred in the fen, the timing and magnitude of this mechanism are inconsistent with the nighttime emission events observed here.

Control by plant exudates and oxygen

Oxygen transport through aerenchymatous tissue may lead to diurnal fluctuations in the rate of methanotrophy. However, unlike the diurnal patterns observed in CH_4 transport, decreased transport of oxygen at night due to stomatal closure would serve to decrease CH_4 oxidation, leading to increased emission rates. Studies have documented decreased soil oxygen content at night (Lloyd et al. [286]; Thomas et al. [287]) and seasonal patterns in CH_4 oxidation (King [289]; Roslev and King [290]), but it is not clear that plant-mediated cycles in oxygen availability within the soil could affect emission rates over diurnal timescales. Plants play another important role in CH_4 dynamics by supplying carbon substrates for methanogenesis. This coupling is evidenced by vegetation clipping studies (Waddington et al. [277]; Whiting and Chanton [254]). Isotope analysis and assays of methanogenesis and methanotrophy performed in the BOREAS NSA fen in 1993 indicated that the carbon in CH_4 was recently sequestered and oxidation within

the soil did not control CH_4 emission rates (Bellisario et al. [243]). Since the availability of oxygen is closely coupled to the water table depth (Granberg et al. [216]), it is hypothesized that CH_4 oxidation most likely occurred in the hummocks rather than the hollows. Diurnal fluctuations in methanogenesis may also be attributed to a time lag between CO_2 fixation by plants and the release and consumption of substrate by soil microbes (Waddington et al. [228]; Whiting and Chanton [254]). Although the diurnal pattern of CO_2 flux from the BOREAS fen during the 1994 growing season indicated peak photosynthetic activity around noon (Lafleur et al. [245]) and a similar pattern was documented in 1996 (McCaughey et al. [247]), it is not clear if the timing and magnitude of documented lag effects are consistent with the nighttime emission events described here.

Control by peat temperature

While CH_4 emission peaks commonly occur during daytime (Long et al. [291]), peak emissions have been observed during nighttime when the water table was 0 - 40 cm below the surface (Mikkelä et al. [208]). These authors suggested that diurnal temperature fluctuations caused methanotrophic activity to decline during nighttime. Under favorable conditions, methanotrophs can consume CH_4 at rates greater than 3,500 nmoles CH_4 m^{-2} s^{-1} (Gupta et al. [292]; Popp et al. [293]), although these rates are extreme and might not be representative of the complexity found in a wetland. Granberg et al. [216] demonstrated that water table depth controls the effect of temperature on net CH_4 emission (production - oxidation) from wetland soils. Increasing temperature above the water table leads to higher rates of methanotrophy and decreased net flux, whereas warmer temperatures at and below the water table lead to higher rates of methanogenesis and increased net flux.

While these studies demonstrate that it is feasible for methanotrophs to consume CH_4 at a rate similar to that of nighttime emission events, the magnitude of diurnal temperature changes is not sufficient to explain the magnitude of the emission events. The parameter Q10 is the proportional increase in the rate of methanogenesis or methanotrophy attributed to a 10°C increase in temperature and is used to describe the sensitivity of methanogenesis to temperature (Whalen [294]). Estimates of the Q10 for methanogenesis in wetlands range from < 1 to 35 (Whalen [294]) and the Q10 for methanotrophy

is approximately 2 (Segers [295]; Whalen [294]). During the measurement period, the maximum diurnal temperature range of peat beneath the hummocks was 26.4°C at 1 cm, 15.5°C at 10 cm, 12.1°C at 25 cm, and less than 1.4°C below 50 cm. In the hollows, the maximum diurnal temperature change was 27.6°C at 1 cm, 21.7°C at 5 cm, 12.7°C at 10 cm, 3.0°C at 25 cm and less than 1.4°C below 50 cm. The temperature maxima in the shallow peat (1- 10 cm) typically occurred during daytime, but the maxima in deeper layers occurred later, between 18:00 and 24:00. The effect of diurnal temperature fluctuation on methanogenesis is clearly insufficient to explain the large nighttime emission events measured by the tower. Similarly, the temperature fluctuations in the shallow peat indicate a maximum change of 550% in the rate of methanotrophy. Although diurnal patterns in methanotrophy due to temperature may occur, the potential rates do not appear sufficient to explain the nighttime emission events during the warmest months. Furthermore, the lack of consistent correlation between flux and peat temperature in hummocks and hollows at daily or half-hourly timescales suggests that the nighttime peaks in emission are likely not the result of temperature fluctuations.

7.6 Summary

This study compared previously unpublished flux tower measurements of CH_4 flux with chamber measurements from the BOREAS NSA fen. The spatial extent of the chambers was much smaller than the footprint of the flux tower, which might explain the apparent discrepancy between the chamber data and the daytime measurements by the tower. Additionally, regular nighttime CH_4 emission events were found that were not previously detected using chambers. The substantial nighttime CH_4 emissions observed from the fen exceed the magnitude of diurnal fluctuations observed in other studies using flux tower methods. We attribute these emission events to short-term storage of CH_4 in thermally stratified hollows and subsequent release through destratification and buoyancy flux. The flux rates derived from the chambers are compatible with the estimates of CH_4 production required to produce these emission events. Other previously identified (or classical) drivers could not explain the magnitude of CH_4 emissions observed in the fen. The large emission events are unlikely to be captured using discrete samples from chambers, but nevertheless may represent a substantial portion of the daily flux from

the ecosystem. The results of this study illustrate that relatively short-term physical controls can have a significant influence on ecosystem-atmosphere exchange and must be captured in measurement strategies. However, biogeochemical processes leading to methane production must coincide with surface water thermal stratification for this phenomenon to be present. Future work should determine what physical conditions must be present for such dynamics to exist, and if indicators can be identified to help modelers include these processes in biogeochemical models.

Chapter 8

Conclusion and Discussion

The objective of this study was to investigate the effects of wake turbulence on the structure of the atmospheric boundary layer (ABL) and surface fluxes in wake-affected landscapes. Boundary layer separation and wake flows near the earth's surface, due to abrupt transitions from forests to clearings or lakes and due to wakes generated by wind turbines affect land-atmosphere coupling, including turbulent transport and surface fluxes. Detailed conclusions addressing each of the research questions posed in Sec. 1.1 are provided at the end of each chapter. Overall this work has identified the significance of wakes on the structure of the ABL and land-atmosphere exchanges. New models to account for ABL wakes have been proposed, specifically for large wind farms and for wind-sheltered lakes or clearings. The challenges of making measurements to quantify biosphere-atmosphere exchanges of methane were demonstrated for a wind-sheltered wetland. A new abiotic mechanism was show to control the episodic release of methane, due to the diurnal heating and cooling effects on turbulent transport within and over the wetland. Because methane production is very heterogeneously distributed and its transport can be controlled by abiotic and biotic factors, which can change rapidly, it is difficult to accurately quantify the spatially integrated flux from an ecosystem. This research demonstrates the need for a fully integrated, interdisciplinary approach.

8.1 Major Research Findings

The research presented in Part I provides a new understanding of how wind farms affect the structure of the ABL and surface fluxes (Markfort et al. [7] and Zhang et al. [8]). In particular, the spatially averaged, time mean flow within large turbine arrays is similar to that of spare canopies. The distance required for the development of the flow can be characterized based on the average drag characteristics of the wind farm. Within this region, momentum is advected through the wind farm and drawn laterally into the turbines as the wakes develop. Additionally, the flow exhibits the inflected mean velocity profile observed in canopy flows. The result is a shear penetration length-scale, which is on the order of the height of the wind farm, and is responsible for a significant portion of the entrainment of momentum from the ABL above.

Direct measurements of surface heat flux in wind tunnel experiments reveal a significant effect of wind farm installation, which depends on wind farm layout. For the staggered configuration, the change in heat flux, compared to the boundary layer without wind turbines, was relatively homogeneous due to efficient lateral mixing of the wakes. The net change was an overall reduction of approximately 4%. For the aligned wind turbine configuration, the net change in heat flux, was marginal. However, due to wake rotation, the net change of heat flux on either side of the turbine rows was significant. The heat flux increased by about 4% on the downwelling side, while it decreased approximately the same amount on the upwelling side. This could have significant implications for the energy budget of landscapes, particularly agricultural lands, where water use is carefully managed. Associated changes in trace gas flux to and from crops could affect crop health and yields. For offshore wind farms, the change in heat flux along with reduced surface shear stress could affect mixing in the ocean surface mixed layer .

A new analytical model was proposed for wind farms that takes advantage of their similarity to sparse canopies (Markfort et al. [9]). The new model has advantages over the current added roughness models as the new model remains faithful to the structure of the flow, representing the momentum extracted within the rotor layer above the ground surface. With knowledge of the turbine thrust characteristics, wind farm layout and turbine heights, the model is capable of predicting the mean velocity profile and

shear stress partitioning between the turbines and the land or sea surface.

The research presented in Part II provides new information on how abrupt forest canopy edges and escarpment topography effects the ABL. Turbulence and surface flux measurements have been obtained that provide new insights into the near-surface transport of momentum, heat and scalars (Markfort et al. [10]). In particular, the flow in the wake of a canopy is significantly different from the classic flow over a solid backward-facing step. Unlike a solid step, leakage flow though the canopy effectively delays flow separation to some distance downwind of the canopy edge. If the canopy is adequately dense, the flow will separate leading to a standing rotor eddy, with reattachment at some distance downwind. Downwind of reattachment, the wake turbulence decays and a new wall bounded flow develops. Surface shear stress increases from zero at reattachment until it equilibrated with the new surface downwind. The length scale associated with surface shear stress recovery is key for characterizing the extent of wind sheltering.

A new model describing the effects of wind-sheltering for land-atmosphere interaction and in particular for lakes and wetlands was developed (Markfort et al. [11] and Markfort et al. [10]. The new model for wind sheltering of lakes is based on the size of the lake and the height of the surrounding canopy. The model is designed to correct the standard 1-D bulk drag and Monin-Obukhov similarity theory models for the effects of sheltering. The model was validated against a calibrated lake hydrodynamic model and found to perform well. It was found that the model faithfully predicts the effect of wind sheltering for medium size lakes and larger. However as lakes become smaller, with a mean fetch of less than $\sim$ 1 km, the sensitivity of the model to the simplifying assumptions, i.e. of the lake having a circular shape and that the canopy can be represented by a single characteristic height, causes the model to breakdown. A new field study was recently conducted at a small lake to investigate these factors further and to develop a new generation wind sheltering model that will be appropriate for small lakes and wetlands.

An analysis of ecosystem-atmosphere flux data, collected at a boreal wetland, revealed the effects of wind sheltering on fluxes of methane. In particular, due to wind sheltering, the water-filled hollow on the wetland, which are only $\approx$ 20 cm deep, stratified daily and thereby trapped methane below the water surface. During evening transition,

the pools convectively cooled causing the methane to be released in large pulses. Previous studies have not documented this phenomenon due to limitations in the measurement methods used. For example, flux chambers are capped during the measurement, limiting outgoing long-wave radiation and preventing convective cooling of the pools. Also the flux gradient method is not applicable when the ABL is stably stratified, as is often the case during the night. However, with careful analysis to ensure the data were well controlled to only include measurements with adequate fetch and during conditions with adequate turbulence production, the beginning of the pulse events could be accurately detected.

8.2 Discussion

The research presented in this thesis demonstrates that simple parameterizations can be used with analytical tools to accurately represent the flow of momentum flux in wind farms. A new model was developed and validation against data collected in controlled wind tunnel experiments. The model should also be tested at the field scale, and should be extended to take into account thermal stability as well. One key attribute of the model is that it can predict the surface fluxes at the ground or sea surface. The model can be useful for representing wind farms in regional scale models and for wind farm design optimization. It can also be useful for assessing environmental impacts, e.g. by providing a boundary condition for determining changes in scalar fluxes, e.g. over agricultural landscapes, and for surface layer modeling of the ocean and large lakes covered by wind farms.

This research shows that for many landscapes, the standard similarity theory does not adequately represent transport at the earth's surface, due primarily to the generation of wakes that cause the "constant-flux" layer assumption to fail. However, with knowledge of the characteristic distances over which wake flows dominate downwind of abrupt transitions, this work shows that it is possible to develop simple parameterizations that can be used to correct for the effects of wakes. Canopy transitions are likely the most important contributor of wake turbulence in the ABL. This study only considered fully developed canopy flows transitioning to fields or lakes under neutrally

stratified conditions. However, the effect of canopy length, porosity and the stratification of the atmosphere needs to be investigated further to expand the usefulness of the models. Due to wind sheltering, there is currently no robust method for determine surface fluxes in models or measurements for wake-affected regions. This also impacts our ability to close budgets for energy and trace gases, such as water vapor, carbon dioxide and methane. With new advances in parameterizations for ABL processes and surface fluxes that can account for wakes, this challenge will be addressed.

This research has the potential to significantly improve our understanding and ability to model the effects of complex terrain on the ABL, relevant for regional-scale weather, climate and hydrologic models, as well as ecosystem models (e.g. lake water quality models). It is also useful for the design, analysis and interpretation of micrometeorological and surface flux measurements. Understanding how canopy heterogeneity in the landscape and atmospheric stability affect the evolution of the flow in the near wake ($\sim$ O(100 m)) and over longer distances ($\sim$ O(1 km)) is important: (i) for improving ABL models, (ii) for analyzing and interpreting flux measurements at the biosphere-atmosphere interface, and (iii) for parameterizing surface fluxes of momentum, heat and trace gases in regional-scale models. Wakes generated by complex landscapes also affect the available wind power. Enhanced turbulence due to abrupt transitions from canopies to clearings may adversely impact wind energy production.

The complexity of the ABL and its interactions with biospheric processes and engineered systems occur at a wide range of length and time scales. The nonlinear interactions of and between abiotic and biotic processes makes it challenging to develop accurate models without taking advantage of a multi-method approach, including the used of lab, field and theoretical techniques. This thesis has demonstrated that using an integrated research methodology and interdisciplinary approach is key to working toward solving important environmental challenges.

References

[1] A. S. Monin and A. M. Obukhov. Basic laws of turbulent mixing in the atmosphere near the ground. *Tr Akad Auk, SSSR Geophiz Inst*, 24(151):1963–1987, 1954.

[2] R. Avissar and T. Schmidt. An evaluation of the scale at which ground-surface heat flux patchiness affects the convective boundary layer using large-eddy simulations. *J. Atmos. Sci.*, 55:2666–2689, 1998.

[3] C. B. Hasager, L Rasmussen, A Peña, L E Jensen, and P-E Réthoré. Wind farm wake: The horns rev photo case. *Energies*, 6:696–716, doi:10.3390/en6020696, 2013.

[4] M. Calaf, C. Meneveau, and J. Meyers. Large eddy simulation study of fully developed wind-turbine array boundary layers. *Phys. Fluids*, 22, doi:10.1063/1.3291077, 2010.

[5] F. Porté-Agel, H. Lu, Y.-T. Wu, and R. J. Conzemius. Large-eddy simulation of atmospheric boundary layer flow through wind turbines and wind farms. *J. Wind Eng. Ind. Aerodyn.*, 99(4):154–168, 2011.

[6] S. Baidya Roy. Mesoscale vegetation-atmosphere feedbacks in Amazonia. *J. Geophys. Res.*, 114:D20111, doi:10.1029/2009JD012001, 2009.

[7] C. D. Markfort, W. Zhang, and F. Porté-Agel. Turbulent flow and scalar transport through and over aligned and staggered wind farms. *Journal of Turbulence*, page doi:10.1080/14685248.2012.709635, 2012.

[8] W. Zhang, C. D. Markfort, and F. Porté-Agel. Experimental study of the impact of large-scale wind farms on land–atmosphere exchanges. *Environ. Res. Lett.*, 8:1–8, doi:10.1088/1748–9326/8/1/015002, 2013.

[9] C. D. Markfort, W. Zhang, and F. Porté-Agel. A canopy-type model for wind farm-atmosphere interaction. In *Proceedings of the 2013 International Conference on Aerodynamics of Offshore Wind Energy Systems and Wakes*, pages 1–12. DTU, Copenhagen, Denmark, 2013.

[10] C. D. Markfort, F. Porté-Agel, and H G Stefan. Canopy wake dynamics and wind sheltering effects on earth surface fluxes. *Environmental Fluid Mechanics*, accepted.

[11] C. D. Markfort, A. L. S. Perez, J. W. Thill, D. A. Jaster, F. Porté-Agel, and H. G. Stefan. Wind sheltering of a lake by a tree canopy or bluff topography. *Water Resour. Res.*, 46:W03530, doi:10.1029/2009WR007759, 2010.

[12] C. M. Godwin, P. J. McNamara, and C. D. Markfort. Evening methane emission pulses from a boreal wetland correspond to convective mixing in hollows. *J. Geophys. Res.-Biogeosciences*, 118:1–12, doi: 10.1002/jgrg.20082, 2013.

[13] S. Frandsen, R. Barthelmie, S. Pryor, O. Rathmann, S. Larsen, J. Højstrup, and M. Thøgersen. Analytical modelling of wind speed deficit in large offshore wind farms. *Wind Energy*, 9:39–53, 2006.

[14] H. Lu and F. Porté-Agel. Large-eddy simulation of a very large wind farm in a stable atmospheric boundary layer. *Physics of Fluids*, 23, doi:10.1063/1.3589857, 2011.

[15] C. Meneveau. The top-down model of wind farm boundary layers and its applications. *Journal of Turbulence*, page doi:10.1080/14685248.2012.663092, 2012.

[16] J. Meyers and C. Meneveau. Optimal turbine spacing in fully developed wind farm boundary layers. *Wind Energy*, 14 doi:10.1002/we469, 2011.

[17] L. P. Chamorro and F. Porté-Agel. Turbulent flow inside and above a wind farm: A wind-tunnel study. *Energies*, 4:1916–1936, 2011.

[18] M. Mechali, L. Jensen, R. Barthelmie, S. Frandsen, and P.E. Rethore. Wake effects at Horns Rev and their influence on energy production. *European Wind Energy Conference and Exhibition. Athens, 2006*, 2006.

[19] R. J. Barthelmie, K. Hansen, S. T. Frandsen, O. Rathmann, J. G. Schepers, W. Schlez, J. Phillips, K. Rados, A. Zervos, E. S. Politis, and P. K. Chaviaropoulos. Modelling and measuring flow and wind turbine wakes in large wind farms offshore. *Wind Energy*, 12:431–444, 2009.

[20] R. J. Barthelmie, S. T. Frandsen, P. E. Rethore, and L. Jensen. Analysis of atmospheric impacts on the development of wind turbine wakes at the Nysted wind farm. In *European Offshore Wind Conference 2007, Berlin 4.-6.12.2007*, 2007.

[21] A. Crespo, J. Hernandez, and S. Frandsen. Survey of modelling methods for wind turbine wakes and wind farms. *Wind Energy*, 2:1–24, 1999.

[22] P. E. J. Vermeulen and P. J. H. Builtjes. Turbulence measurements in simulated wind turbine clusters. *Report 82-03003, TNO Division of Technology for Society*, 1982.

[23] D. Keith, D. J. D. Denkenberger, D. Lenschow, S. Malyshev, S. Pacala, and P. Rasch. The influence of large-scale wind-power on global climate. *PNAS*, 101(46):16115–16120, 2004.

[24] D. Barrie and D.B. Kirk-Davidoff. Weather response to a large wind turbine array. *Atmos. Chem. Phys.*, 10:769–775, 2010.

[25] S. Baidya Roy and J. J. Traiteur. Impacts of wind farms on surface air temperatures. *PNAS*, 107:17899–17904, doi:10.1073/pnas.1000493107, 2010.

[26] S. Frandsen. On the wind speed reduction in the center of large clusters of wind turbines. *J. Wind Eng. Ind. Aerodyn.*, 39:251–265, 1992.

[27] S. T. Frandsen, H. E. Jorgensen, R. Barthelmie, O. Rathmann, J. Badger, K. Hansen, S. Ott, P.-E. Rethore, S. E. Larsen, and L. E. Jensen. The making of a second-generation wind farm efficiency model complex. *Wind Energy*, 12:445–458, 2009.

[28] Y. T. Wu and F. Porté-Agel. Large-eddy simulation of wind-turbine wakes: Evaluation of turbine parametrisations. *Boundary-Layer Meteorol*, 138(3):345–366, 2011.

[29] R. B. Cal, J. Lebrón, L. Castillo, H. S. Kang, and C. Meneveau. Experimental study of the horizontally averaged flow structure in a model wind-turbine array boundary layer. *Journal of Renewable and Sustainable Energy*, 2, doi:10.1063/1.3289735, 2010.

[30] G.P. Corten, P. Schaak, and T. Hegberg. Velocity profiles measured above a scaled wind farm. Technical report, ECN-RX–04-123, European Wind Energy Conference, London, UK 22–25, Nov. 2004, 2004.

[31] L. P. Chamorro and F. Porté-Agel. A wind-tunnel investigation of wind-turbine wakes: Boundary-layer turbulence effects. *Boundary-Layer Meteorol.*, 132(1):129–149, April 2009.

[32] W. Zhang, C. D. Markfort, and F. Porté-Agel. Near-wake flow structure downwind of a wind turbine in a turbulent boundary layer. *Exp. Fluids*, 52:1219–1235, 2012.

[33] L. P. Chamorro and F. Porté-Agel. Thermal stability and boundary-layer effects on wind-turbine wakes: A wind-tunnel study. *Boundary-Layer Meteorol*, 136:515–533, 2010.

[34] W. Zhang, C. D. Markfort, and F. Porté-Agel. Wind-turbine wakes in a convective boundary layer: a wind-tunnel study. *Boundary-Layer Meteorol*, 146(2), 2013.

[35] P. E. Hancock and F. Pascheke. Wind tunnel simulations of wind turbine wake interactions in neutral and stratified wind flow. *10th EMS Annual Meeting, 10th European Conference on Applications of Meteorology (ECAM) Abstracts, held Sept. 13-17, 2010 in Zurich, Switzerland*, 2010.

[36] L. P. Chamorro, R.E.A. Arndt, and F. Sotiropoulos. Turbulent flow properties around a staggered wind farm. *Boundary-Layer Meteorol.*, doi: 10.1007/s10546-011-9649-6, 2011.

[37] H. Lettau. Note on aerodynamic roughness-parameter estimation on the basis of roughness-element description. *J. Appl. Meteor.*, 8:828–832, 1969.

[38] S. Dupont and Y. Brunet. Coherent sturctures in canopy edge flow: a large-eddy simulation study. *Journal of Fluid Mechanics*, 630:93–128, 2009.

[39] W. P. Elliott. The growth of the atmospheric internal boundary layer. *Trans. Amer. Geophys. Union.*, 39:1048–1054, 1958.

[40] D. H. Wood. Internal boundary layer growth following a step change in surface roughness. *Boundary-Layer Meteorol.*, 22:241–244, 1982.

[41] H. A. Panofsky and J. A. Dutton. *Atmospheric Turbulence – Models and Methods for Engineering Applications.* John Wiley and Sons, New York, 397pp., 1984.

[42] J. Finnigan. Turbulence in plant canopies. *Annu. Rev. Fluid Mech.*, 32:519–571, 2000.

[43] M. Ghisalberti. Obstructed shear flows: similarities across systems and scales. *J. Fluid Mech.*, 641:51–61, 2009.

[44] S. E. Belcher, I. N. Harman, and J. J. Finnigan. The wind in the willows: Flows in forest canopies in complex terrain. *Ann. Rev. Fluid Mech.*, 44:479–504, 2012.

[45] O. Coceal and S. E. Belcher. A canopy model of mean winds through urban areas. *Quart J Roy Meteorol Soc*, 130:1349–1372, 2004.

[46] H. Cheng and I.P. Castro. Near wall flow over urban-like roughness. *Boundary-Layer Meteorol*, 104:229–259, 2002.

[47] O. Coceal, T.G. Thomas, I.P. Castro, and S.E. Belcher. Mean flow and turbulence statistics over groups of urban-like cubical obstacles. *Boundary-Layer Meteorol.*, 121:491–519, 2006.

[48] S. E. Belcher, N. Jerram, and J. C. R. Hunt. Adjustment of a turbulent boundary layer to a canopy of roughness elements. *J Fluid Mech*, 488:369–398, 2003.

[49] M. R. Raupach, R. A. Antonia, and S. Rajagopalan. Rough-wall turbulent boundary layers. *Appl. Mech. Rev.*, 44(1):1–25, 1991.

[50] J.C. Kaimal and J.J. Finnigan. *Atmospheric Boundary Layer Flows: Their Structure and Measurement*. Oxford Univ. Press, U.S., 1994.

[51] D. Poggi, G.G. Katul, and J.D. Albertson. A note on the contribution of dispersive fluxes to momentum transfer within canopies. *Boundary-Layer Meteorology*, 111:615—621, 2004.

[52] S. Moltchanov, Y. Bohbot-Raviv, and U. Shavit. Dispersive stresses at the canopy upstream edge. *Boundary-Layer Meteorology*, 139:333–351, 2011.

[53] Y. Ohya and T. Uchida. Laboratory and numerical studies of the convective boundary layer capped by a strong inversion. *Boundary-Layer Meteorol*, 112:223–240, 2004.

[54] M. A. Carper and F. Porté-Agel. Subfilter-scale fluxes over a surface roughness transition. Part I: Measured fluxes and energy transfer rates. *Boundary-Layer Meteorol.*, 126:157–179, 2008.

[55] L. P. Chamorro and F. Porté-Agel. Velocity and surface shear stress distributions behind a rough-to-smooth surface transition: A simple new model. *Boundary Layer Meteorol.*, 130:29–41, January 2009.

[56] L. J. Vermeer, J. N. Sørensen, and A. Crespo. Wind turbine wake aerodynamics. *Prog. Aerospace Sci.*, 39:467–510, 2003.

[57] D. Spera. *Wind Turbine Technology: Fundamental concepts of wind turbine engineering*. ASME Press: New York, 1994.

[58] H. H. Bruun. *Hotwire anemometry, Principles and Signal Analysis*. Oxford Univ. Press, U.K., 1995, 507 pp.

[59] C. Tropea, J.F. Foss, and A. Yarin. *Handbook of Experimental Fluid Mechanics*. Springer, Berlin, 1757pp., 2007.

[60] R. B. Stull. *An introduction to Boundary-Layer Meteorology*. Kluwer Academic Publishers, 670 pp., 1988.

[61] D. Medici and P. H. Alfredsson. Measurements on a wind turbine wake: 3d effects and bluff body vortex shedding. *Wind Energy.*, 9:219–236, 2006.

[62] A. Rosen and Y. Sheinman. The power fluctuations of a wind turbine. *J Wind Eng Ind Aerodyn*, 59:51–68, 1996.

[63] K. Thomsen and P. Sørensen. Fatigue loads for wind turbines operating in wakes. *J. Wind Eng. Ind. Aerodyn.*, 80:121–136, 1999.

[64] S. Frandsen and M. Thogersen. Integrated fatigue loading for wind turbines in wind farms by combining ambient turbulence and wakes. *J Wind Engineering*, 23(6):327–340, 1999.

[65] T. Burton, D. Sharpe, N. Jenkins, and E. Bossanyi. *Wind Energy Handbook*. John Wiley and Sons, West Sussex, 2001.

[66] H. Hu, Z. Yang, and P. Sarkar. Dynamic wind loads and wake characteristics of a wind turbine model in an atmospheric boundary layer wind. *Experiments in Fluids*, pages doi:10.1007/s00348–011–1253–5, 2012.

[67] Y. T. Wu and F. Porté-Agel. Simulation of turbulent flow inside and above wind farms: Model validation and layout effects. *Boundary-Layer Meteorol*, 146(2):181–205, 2013.

[68] M. R. Raupach, J. J. Finnigan, and Y. Brunet. Coherent eddies and turbulence in vegetation canopies: The mixing-layer analogy. *Boundary-Layer Meteorology*, 78:351–382, 1996.

[69] M. Calaf, M. B. Parlange, and C. Meneveau. Large eddy simulation study of scalar transport in fully developed wind-turbine array boundary layers. *Phys. Fluids*, 23, doi:10.1063/1.3663376, 2011.

[70] M. R. Raupach and R. H. Shaw. Averaging procedures for flow within vegetation canopies. *Boundary-Layer Meteorology*, 22:79–90, 1982.

[71] E. Inoue. On the turbulent structure of airflow within crop canopies. *J. Meteor. Soc. Japan*, 41:317–326, 1963.

[72] C. Yi. Momentum transfer within canopies. *J of Appl Meteor and Climat*, 47:262–275, 2006.

[73] H. M. Nepf. Drag, turbulence, and diffusion in flow through emergent vegetation. *Water Resour Res*, 35(2):479–489, 1999.

[74] C. Dunn, F. Lopez, and M. Garcia. Mean flow and turbulence in a laboratory channel with simulated vegetation. Technical report, Hydraulic Eng. Ser. 51, U. of Ill. At Urban-Champagne, Urbana, 1996.

[75] D. Poggi, A. Porporato, L. Ridolfi, J. Albertson, and G. Katul. The effect of vegetation density on canopy sub-layer turbulence. *Boundary-Layer Meteorology*, 111:565–587, 2004.

[76] H. Nepf, M. Ghisalberti, B. White, and E. Murphy. Retention time and dispersion associated with submerged aquatic canopies. *Water Resour. Res.*, 43:doi:10.1029/2006WR005362, 2007.

[77] S. Baidya Roy. Simulating impacts of wind farms on local hydrometeorology. *J. Wind Eng. Ind. Aerodyn.*, 99:491–498, 2011.

[78] U. B. Gunturu and C. A. Schlosser. Characterization of wind power resource in the united states. *Atmos. Chem. Phys.*, 12:9687–9702, 2012.

[79] D. A. Rajewski, E. S. Takle, J. K. Lundquist, S. P. Oncley, J. H. Prueger, T. W. Horst, M. E. Rhodes, R. Pfeiffer, J. L. Hatfield, K. K. Spoth, and R. K. Doorenbos. Crop wind energy experiment (CWEX): Observations of surface-layer, boundary layer, and mesoscale interactions with a wind farm. *Bull. Am. Meteorol. Soc.*, 94:655–672, 2013.

[80] L. A. Ivanova and E. D. Nadyozhina. Numerical simulation of wind farm influence on wind flow. *Wind Energy*, 24:257–269, 2000.

[81] S. Baidya Roy, S. W. Pacala, and R. L. Walko. Can large wind farms affect local meteorology? *J. Geophys. Res.*, 109:1–6, 2004.

[82] C. Wang and R. G. Prinn. Potential climatic impacts and reliability of large-scale offshore wind farms. *Environ. Res. Lett.*, 6:025101, 2011.

[83] A. C. Fitch, J. B. Olson, J. K. Lundquist, J. Dudhia, A. K. Gupta, J. Michalakes, and I. Barstad. Local and mesoscale impacts of wind farms as parameterized in a mesoscale nwp model. *Mon. Weather Rev.*, 140:3017–3038, 2012.

[84] L M Zhou, Y H Tian, S. Baidya Roy, C Thorncroft, L F Bosart, and Y L Hu. Impacts of wind farms on land surface temperature. *Nature Clim. Change*, 2:539–543, 2012.

[85] M Roth and T. R. Oke. Relative efficiencies of turbulent transfer of heat, mass and momentum over a patchy urban surface. *J. Atmos. Sci.*, 52:1863–1874, 1995.

[86] W. Brutsaert. *Evaporation into the atmosphere: Theory, history and applications.* Springer, 316 pp., 1982.

[87] A. S. Thom. Momentum absorption by vegetation. *Q. J. R. Meteorol. Soc.*, 97:414–428, 1971.

[88] W. Wang. An analytical model for mean wind profiles in sparse canopies. *Boundary Layer Meteorol.*, 142:383–399, 2012.

[89] M A Lefsky. A global forest canopy height map from the moderate resolution imaging spectroradiometer and the geoscience laser altimeter system. *Geophys. Res. Lett.*, 37:L15401, 2010.

[90] B Lehner and P Doll. Development and validation of a global database of lakes, reservoirs and wetlands. *J. Hydrol.*, 296:1–22, 2004.

[91] Laurence W. Forest-climate interactions in fragmented tropical landscapes. *Phil. Trans. R. Soc. Lond.*, 359:345–352, 2004.

[92] J. A. Downing, Y. T. Prairie, J. J. Cole, C. M. Duarte, L. J. Tranvik, R. G. Striegl, W. H. McDowell, P. Kortelainen, N. F. Caraco, J. M. Melack, and J. J.

Middelburg. The global abundance and size distribution of lakes, ponds, and impoundments. *Limnol. Oceanogr.*, 51(5):2388–2397, doi: 10.4319/lo.2006.51.5.2388, 2006.

[93] C P McDonald, J A Rover, E G Stets, and R G Striegle. The regional abundance and size distribution of lakes and reservoirs in the united states and implications for estimates of global lake extent. *Limnol. Oceanogr.*, 57(2):597–606, 2012.

[94] W R Rouse, C J Oswald, J. Binyamin, and et al. The role of northern lakes in a regional energy balance. *J. Hydrometeorology*, 6:291–305, 2005.

[95] C Spence, W R Rouse, D Worth, and C Oswald. Energy budget processes of a small northern lake. *J. Hydrometeorology*, 4:694–701, 2003.

[96] J J Cole, Y T Prairie, N F Caraco, and et al. Plumbing the global carbon cycle: Integrating inland waters into the terrestrial carbon budget. *Ecosystems*, 10:171–184, 2007.

[97] L J Tranvik, J A Downing, J B Cotner, S A Loiselle, R G Striegl, T J Ballatore, P Dillon, K Finlay, K Fortino, L B Knoll, P L Kortelainen, T Kuster, S Larsen, I Laurion, D M Leech, S L McCallister, D M McKnight, J M Melack, E Overholt, J A Porter, Y Prairie, W H Renwick, F Roland, B S Sherman, D W Schindler, S Sobek, A Tremblay, M J Vanni, A M Verschoor, E van Wachenfeldt, and G A Weyhenmeyer. Lakes and reservoirs as regulators of carbon cycling and climate. *Limnol. Oceanogr.*, 54:2298–2314, 2009.

[98] D Bastviken, L J Tranvik, J A Downing, P M Crill, and A Enrich-Prast. Freshwater methane emissions offset the continental carbon sink. *Science*, 331:50, 2011.

[99] M. R. Raupach. Simplified expression for vegetation roughness length and zero-plane displacement as function of canopy height and area index. *Boundary-Layer Meteorol.*, 71:211–216, doi:10.1007/ BF00709229, 1994.

[100] D. E. Ford and H. G. Stefan. Thermal predictions using an integral energy model. *J. Hydraul. Div. Am. Soc. Civ. Eng.*, 106(1):39–55, 1980.

[101] A Huber, G N Ivey, G Wake, and C E Oldham. Near-surface wind-induced mixing in a mine lake. *J. Hydraul. Engr.*, 134(10):1464–1472, 2008.

[102] N E Ottesen Hansen. *Developments in Water Science*, volume 11, chapter Effects of Boundary layers on mixing in small Lakes, pages 341–356. Elsevier, Oxford, U. K., 1979.

[103] S Rubbert and J Kongeter. Measurements and three-dimensional simulations of flow in a shallow reservoir subject to small-scale wind field inhomogeneities induced by sheltering. *Aquatic Sciences*, 67:104–121, 2005.

[104] M. R. Hipsey and M Sivapalan. Parameterizing the effect of a wind shelter on evaporation from small water bodies. *Water Resour. Res.*, 39(12):1339, doi:10.1029/2002WR001784, 2003.

[105] M. Cassiani, G. G. Katul, and J. D. Albertson. The effects of canopy leaf area index on airflow across forest edges: Large-eddy simulation and analytical results. *Boundary-Layer Meteorol.*, 126:433–460, doi:10.1007/s10546–007–9242–1, 2008.

[106] M. Detto, G. G. Katul, M. B. Siqueira, J.-Y. Juang, and P. Stoy. The structure of turbulence near a tall forest edge: The backward-facing step flow analogy revisited. *Ecol. Appl.*, 18(6):1420–1435, doi:10.1890/ 06–0920.1, 2008.

[107] A A Baklanov, B Grisogono, R Bornstein, and et al. The nature, theory, and modeling of atmospheric planetary boundary layers. *Bull. Am. Meteorol. Soc.*, 92(2):123–128, 2011.

[108] I N Harman and J. J. Finnigan. A simple unified theory for flow in the canopy and roughness sublayer. *Boundary-Layer Meteorol.*, 123:339–363, 2007.

[109] W. Brutsaert. Land-surface water vapor and sensible heat flux: Spatial variability, homogeneity, and measurement scales. *Water Resour Res*, 34:2433–2442, 1998.

[110] A N Ross. Flow within and above a canopy of variable density. *Q. J. R. Meteorol. Soc.*, 138:1259–1272, 2012.

[111] J Sanz Rodrigo, J van Beeck, and G Dezsö-Veidinger. Wind tunnel simulation of the wind conditions inside bidimensional forest clear-cuts: application to wind turbine siting. *J. Wind Eng. Ind. Aerodyn.*, 95:609–634, 2007.

[112] T Banerjee, G Katul, S Fontan, D. Poggi, and M Kumar. Mean flow near edges and within cavities situated inside dense canopies. *Boundary-Layer Meteorol.*, 2013, doi:10.1007/s10546-013-9826-x.

[113] A P Morse, B A Gardiner, and B J Marshall. Mechanisms controlling turbulence development across a forest edge. *Boundary-Layer Meteorol.*, 103:227–251, 2002.

[114] S. Dupont and Y. Brunet. Edge flow and canopy structure: a large-eddy simulation study. *Boundary-Layer Meteorol.*, 126:51–71, 2008.

[115] B. Yang, M. R. Raupach, R. H. Shaw, K. T. Paw U, and A. Morse. Large-eddy simulation of turbulent flow across a forest edge. Part I: Flow statistics. *Boundary-Layer Meteorol.*, 120:377–412, doi:10.1007/ s10546–006–9057–5, 2006.

[116] M. R. Irvine, B. A. Gardiner, and M. K. Hill. The evolution of turbulence across a forest edge. *Boundary-Layer Meteorol.*, 84:467–496, doi:10.1023/A:1000453031036, 1997.

[117] E. Plate. The aerodynamics of shelter belts. *Agric. Meteorol.*, 8:203–222, 1971.

[118] H Wang and E S Takle. Boundary-layer flow and turbulence near porous obstacles. *Boundary-Layer Meteorol.*, 74:73–88, 1995.

[119] M J Judd, M. R. Raupach, and J. J. Finnigan. A wind tunnel study of turbulent flow around single and multiple wind breaks. part 1: Velocity fields. *Boundary-Layer Meteorol.*, 80:127–165, 1996.

[120] E. G. Patton, R. H. Shaw, M. J. Judd, and M. R. Raupach. Large-eddy simulation of windbreak flow. *Boundary-Layer Meteorol.*, 87:275–306, doi: 10.1023/A:1000945626163, 1998.

[121] G Bohrer, G G Katul, R L Walko, and R Avissar. Exploring the effects of microscale structural heterogeneity of forest canopies using large-eddy simulations. *Boundary-Layer Meteorol.*, 132:351–382, 2009.

[122] F Schlegel, J Stiller, A Bienert, H G Maas, R Queck, and C Bernhofer. Large-eddy simulation of inhomogeneous canopy flows using high resolution terrestrial laser scanning data. *Boundary-Layer Meteorol.*, 142:223–243, 2012.

[123] F Siniscalchi, V I Nikora, and J Aberle. Plant patch hydrodynamics in streams: mean flow, turbulence and drag forces. *Water Resour. Res.*, 48:W01513, doi:10.1029/2011WR011050, 2012.

[124] A N Ross and T P Baker. Flow over partially forested ridges. *Boundary-Layer Meteorol.*, 146:375–392, 2013.

[125] X. Lee. Air motion within and above forest vegetation in non-ideal conditions. *Forest Ecol. and Mngt.*, 135:3–18, 2000.

[126] M D Novak, J S Warland, A L Orchansky, R Ketler, and S Green. Wind tunnel and field measurements of turbulent flow in forests, part I: uniformly thinned stands. *Boundary-Layer Meteorol.*, 95:457–495, 2000.

[127] B N Bailey and R. Stoll. Turbulence in sparse, organized vegetative canopies: a large-eddy simulation study. *Boundary-Layer Meteorol.*, 2013, doi: 10.1007/s10546-012-9796-4.

[128] W Paeschke. Experimentelle untersuchungen zum rauhigkeits- und stabilitätsproblem in der bodennahen luftschicht. *Beiträge z. Phys. D. freien Atmosf*, 24:163–189, 1937.

[129] J Eaton and J Johnston. A review of research on subsonic turbulent flow reattachment. *AIAA J.*, 19:1093–1100, 1981.

[130] D. M. Driver and H. L. Seegmiller. Features of a reattaching turbulent shear layer in divergent channel flow. *AIAA J.*, 23(2):163–171, 1985.

[131] W Yue, M B Parlange, C Meneveau, W Zhu, R van Hout, and J Katz. Large-eddy simulation of plant canopies using plant-scale representation. *Boundary-Layer Meteorol.*, 124:183–203, 2007.

[132] J T Rominger and H M Hepf. Flow adjustment and interior flow associated with a rectangular porous obstruction. *J. Fluid Mech.*, 680:636–659, 2011.

[133] VDI. *Environmental meteorology – Physical modelling of flow and dispersion processes in the atmospheric boundary layer – Application of wind tunnels*. Series 3783 Part 12. Beuth Verlag, 2000.

[134] J Westerweel. Fundamentals of digital particle image velocimetry. *Meas. Sci. Technol.*, 8:1379–1392, 1997.

[135] M. Raffel, C. E. Willert, S. T. Wereley, and J. Kompenhans. *Particle Image Velocimetry: A Practical Guide*. Springer, 2nd edition, 2007.

[136] N. Hutchins, T. B. Nickels, I. Marusic, and M. S. Chong. Hot-wire spatial resolution issues in wall-bounded turbulence. *J. Fluid Mech.*, 635:103–136, 2009.

[137] F. E Jorgensen. The computer-controlled constant temperature ameometer: aspectes of the set-up, probe calibration, data acquisition, and data collection turbulence. *Meas. Sci. Technol.*, 12:1378–1387, 1996.

[138] V. C. Patel. Calibration of the preston tube and limitations on its use in pressure gradients. *J. Fluid Mech.*, 23:185–208, 1965.

[139] D. Poggi, G G Katul, and J D Albertson. Momentum transfer and turbulent kinetic energy budget within a dense model canopy. *Boundary-Layer Meteorol.*, 111:589–614, 2004.

[140] M. R. Raupach and A. S. Thom. Turbulence in and above plant canopies. *Annu. Rev. Fluid Mech.*, 13(97–129), 1981.

[141] P S Jackson. On the displacement height in the logarithmic velocity profile. *J. Fluid Mech.*, 111:15–25, 1981.

[142] G G Katul, C R Chu, M. B. Parlange, J. D. Albertson, and T A Ortenburger. Low-wave-number spectral characteristics of velocity and temperature in the atmospheric surface-layer. *J. Geophys. Res.-Atmos.*, 100:14243–14255, 1995.

[143] L Castillo, X Wang, and W K George. Separation criterion for turbulent boundary layers via similarity analysis. *J. Fluid Mech.*, 126:297–304, 2004.

[144] J C Vogel and J K Eaton. Combined heat-transfer and fluid dynamic measurements downstream of a backward-facing step. *J of Heat Transfer-Transactions of the ASME*, 107:922–929, 1985.

[145] B Dziomba and H E Fiedler. Effect of initial conditions on two-dimensional free shear layers. *J. Fluid Mech.*, 152:419–442, 1985.

[146] M. Lesieur. *Turbulence in fluids*. Springer, New York, 558 pp, 4th edition, 2008.

[147] P Bradshaw and F Y F Wong. The reattachment and relaxation of a turbulent shear layer. *J. Fluid Mech.*, 51(1):113–135, 1972.

[148] J. R. Garratt. The internal boundary layer: A review. *Boundary-Layer Meteorol.*, 50:171–203, 1990.

[149] J. R. Garratt. *The atmospheric boundary layer*. Cambridge University Press, New York, 1992, 316 pp.

[150] R. A. Antonia and R. E. Luxton. The response of a turbulent boundary layer to a step change in surface roughness. *J. Fluid Mech.*, 53:737–757, 1972.

[151] J L Walmsley. Internal boundary-layer height formulae – a comparison with atmospheric data. *Boundary-Layer Meteorol.*, 47:251–262, 1989.

[152] H. Schlichting and K. Gersten. *Boundary Layer Theory*. Springer, New York, 799 pp., 8th edition, 2000.

[153] F M White. *Viscous fluid flow*. McGraw, New York, 629 pp, 2006.

[154] M Aubinet, T Vesala, and D Papale. *Eddy Covariance: A practical guide to measurement and data analysis*. Springer, New York, 438 pp., 2012.

[155] J. Boussinesq. Théorie de l'écoulement tourbillant. *Acad. Sci. Inst. Fr., Paris*, 23:46–50, 1877.

[156] L Prandtl. Über die ausgebildete turbulenz. *Z. Angew. Math. Mech*, 5:136, 1925.

[157] G. E. Hutchinson. *Geography, Physics and Chemistry, vol. 1.* John Wiley and Sons, New York, 1015 pp., 1957.

[158] F. J. Rueda and J. Vidal. *Encyclopedia of Inland Waters*, chapter Currents in the upper mixed layer and in unstratified water bodies, pages 568–582. Elsevier, Oxford, U. K., 2009.

[159] S. G. Monismith and S. MacIntyre. *Encyclopedia of Inland Waters*, chapter The surface mixed layer in lakes and reservoirs, pages 568–582. Elsevier, Oxford, U. K., 2009.

[160] H. B. Fischer, E. J. List, R. C. Y. Koh, J. Imberger, and N. H. Brooks. *Mixing in Inland and Coastal Waters*. Academic Press, San Diego, Calif, 483 pp, 1979.

[161] A. Wüest and A. Lorke. Small-scale hydrodynamics in lakes. *Annu. Rev. Fluid Mech.*, 35:373–412, doi:10.1146/annurev.fluid. 35.101101.161220, 2003.

[162] W. K. Melville. The role of surface-wave breaking in air!sea interaction. *Annu. Rev. Fluid Mech.*, 28:279–321, doi:10.1146/annurev.fl.28.010196.001431, 1996.

[163] R. J. Davies-Colley. Mixing depths in New Zealand lakes. *N. Z. J. Mar. Freshwater Res.*, 22:517–527, 1988.

[164] E. Gorham and F. M. Boyce. Influence of lake surface area and depth upon thermal stratification and the depth of the summer thermocline. *J. Great Lakes Res.*, 15(2):233–245, 1989.

[165] S. A. Condie and I. T. Webster. Estimating stratification in shallow water bodies from mean meteorological conditions. *J. Hydraul. Eng.*, 127(4):286–292, doi:10.1061/(ASCE)0733–9429(2001)127:4(286), 2001.

[166] B. Boehrer and M. Schultze. Stratification of lakes. *Rev. Geophys.*, 46:RG2005, doi:10.1029/2006RG000210, 2008.

[167] R. Wanninkhof, J. Ledwell, and W. S. Broecker. Gas exchange wind speed relation measured with sulfur hexafluoride on a lake. *Science*, 227:1224–1226, doi:10.1126/science.227.4691.1224, 1985.

[168] R. Wanninkhof, J. Ledwell, and J. Crusius. *Air Water Mass Transfer: Selected Papers From the Second International Symposium on Gas Transfer at Water Surfaces*, chapter Gas transfer velocities on lakes measured with sulfur hexafluoride. ASCE, Reston, Va, 1990.

[169] R. Wanninkhof, W. E. Asher, D. T. Ho, C. Sweeney, and W. R. McGillis. Advances in quantifying air!sea gas exchange and environmental forcing. *Annu. Rev. Mater. Sci.*, 1:213–244, doi:10.1146/annurev. marine.010908.163742, 2009.

[170] T. R. Oke. *Boundary Layer Climates*. Routledge-Taylor and Francis, New York, 435 pp, 2nd edition, 1987.

[171] T. K. Flesch and J. D. Wilson. Wind and remnant tree sway in forest cutblocks. i. measured winds in experimental cutblocks. *Agric. and For. Meteorol.*, 93:229–242, doi:10.1016/S0168–1923(98)00112–9, 1999.

[172] Wilson J. D. and T. K. Flesch. Wind and remnant tree sway in forest cutblocks. iii. a windflow model to diagnose spatial variation. *Agric. Meteorol.*, 93:259–282, doi:10.1016/S0168–1923(98)00121–X, 1999.

[173] J. Liu, J. M. Chen, T. A. Black, and M. D. Novak. $E - \epsilon$ modelling of turbulent air flow downwind of a model forest edge. *Boundary-Layer Meteorol.*, 77:21–44, doi:10.1007/BF00121857, 1996.

[174] J. M. Chen, T. A. Clack, M. D. Novak, and R. S. Adams. *Wind and Trees*, chapter A wind tunnel study of turbulent airflow in forest clear cuts. Cambridge University Press, New York, 1995.

[175] M. Hondzo and H. G. Stefan. Lake water temperature simulation model. *J. Hydraul. Eng.*, 119(11):1251–1273, doi:10.1061/(ASCE)0733–9429(1993)119:11(1251), 1993.

[176] D. Vickers and L. Mahrt. Fetch limited drag coefficients. *Boundary-Layer Meteorol.*, 85:53–79, doi:10.1023/A:1000472623187, 1997.

[177] H. Charnock. Wind stress on a water surface. *Q. J. R. Meteorol. Soc.*, 350:639–640, doi:10.1002/qj.49708135027, 1955.

[178] C. Farell and A. K. S. Iyengar. Experiments on the wind tunnel simulation of atmospheric boundary layers. *J. Wind Eng. Ind. Aerodyn.*, 79:11–35, doi:10.1016/S0167–6105(98)00117–2, 1999.

[179] D. A. Jaster, A. L. S. Perez, F. Porté-Agel, and H. G. Stefan. Wind velocity profiles and shear stresses on a lake downwind from a canopy: Interpretation of three experiments in a wind tunnel. Rep. 493, St. Anthony Falls Laboratory, Univ. of Minn., Minneapolis, 2007.

[180] A. L. S. Perez, D. A. Jaster, F. Porté-Agel, and H. G. Stefan. Wind velocity profile and shear stresses downwind from a canopy: Experiments in a wind tunnel. Rep. 492, St. Anthony Falls Laboratory, Univ. of Minn., Minneapolis, 2007.

[181] J. W. Thill. Wind velocity measurements on two small ice covered lakes: A compilation of data with some results and discussion. Rep. 527, St. Anthony Falls Laboratory, Univ. of Minn., Minneapolis, 2009.

[182] S. Jovic and M. Driver. Backward-facing step measurements at low reynolds number, $\mathrm{Re}_h = 5000$. NASA Tech. Memo. TM-108807, 1994.

[183] H. Le, P. Moin, and J. Kim. Direct numerical simulation of turbulent flow over a backward-facing step. *J. Fluid Mech.*, 330:349–374, doi:10.1017/S0022112096003941, 1997.

[184] J. L. Aider, A. Danet, and M. Lesieur. Large-eddy simulation applied to study the influence of upstream conditions on the time dependent and averaged characteristics of a backward-facing step flow. *J. Turbul.*, 8(51):1–30, 2007.

[185] I. J. Walker and W. G. Nickling. Simulation and measurement of surface shear stress over isolated and closely spaced transverse dunes in a wind tunnel. *Earth Surf. Processes Landforms*, 28:1111–1124, doi:10.1002/esp.520, 2003.

[186] J. Counihan, J. C. R. Hunt, and P. S. Jackson. Wakes behind two-dimensional surface obstacles in turbulent boundary layers. *J. Fluid Mech.*, 64(3):529–563, doi:10.1017/S0022112074002539, 1974.

[187] E. F. Bradley and P. J. Mulhearn. Development of velocity and shear stress distributions in the wake of a porous shelter fence. *J. Wind Eng. Ind. Aerodyn.*, 15:145–156, doi:10.1016/0167–6105(83)90185–X, 1983.

[188] E. F. Bradley. A micrometeorological study of the velocity profiles and surface drag in the region modified by a change in surface roughness. *Q. J. R. Meteorol. Soc.*, 94:361–379, doi:10.1002/qj.49709440111, 1968.

[189] Y. Wang, K. Hutter, and E. Bäuerle. Three-dimensional wind-induced baroclinic circulation in rectangular basins. *Adv. Water Resour.*, 24:11–27, doi:10.1016/S0309–1708(00)00034–8, 2001.

[190] Wang Y. Importance of subgrid!scale parameterization in numerical simulations of lake circulation. *Adv. Water Resour.*, 26:277–294, doi:10.1016/S0309–1708(02)00166–5, 2003.

[191] F. Rueda, J. Vidal, and G. Schladow. Modeling the effect of size reduction on the stratification of a large wind!driven lake using an uncertainty-based approach. *Water Resour. Res.*, 45:W03411, doi:10.1029/2008WR006988, 2009.

[192] S. Solomon, D. Qin, M. Manning, M. Marquis, K. Averyt, M. M. B. Tignor, H. L. Miller, and Z. Chen. *Climate Change 2007 - The Physical Science Basis, Contribution of Working Group I to the Fourth Assessment Report of the IPCC.* Cambridge, 2007.

[193] S. E. Mikaloff-Fletcher, P. P. Tans, L. M. Bruhwiler, J. B. Miller, and M. Heimann. CH_4 sources estimated from atmospheric observations of CH_4 and its C-13/C-12 isotopic ratios: 2. Inverse modeling of CH_4 fluxes from geographical regions. *Global Biogeochemical Cycles*, 18(4):15, 2004.

[194] R. C. Harriss, E. Gorham, D. I. Sebacher, K. B. Bartlett, and P. A. Flebbe. Methane flux from northern peatlands. *Nature*, 315(6021):652–654, 1985.

[195] S. Frolking, N. Roulet, and J. Fuglestvedt. How northern peatlands influence the earths radiative budget: Sustained methane emission versus sustained carbon sequestration. *J. Geophys. Res*, 111(G01008):G01008, 2006.

[196] S. D. Bridgham, J. P. Megonigal, J. K. Keller, N. B. Bliss, and C. Trettin. The carbon balance of north american wetlands. *Wetlands*, 26(4):889–916, 2006.

[197] S. E. Mikaloff-Fletcher, P. P. Tans, L. M. Bruhwiler, J. B. Miller, and M. Heimann. CH_4 sources estimated from atmospheric observations of CH_4 and its C-13/C-12 isotopic ratios: 1. Inverse modeling of source processes. *Global Biogeochemical Cycles*, 18(4):17, 2004.

[198] JGJ Olivier, JA Van Aardenne, F Dentener, L Ganzeveld, and J Peters. *Non-CO_2 Greenhouse Gases (NCGG-4)*, chapter "Recent trends in global greenhouse gas emissions: regional trends and spatial distribution of key sources", pages 325–330. edited by A. van Amstel (Millpress, Rotterdam, Netherlands).

[199] D. J. Wuebbles and K. Hayhoe. Atmospheric methane and global change. *Earth-Science Reviews*, 57(3-4):177–210, 2002.

[200] J. L. Bubier and T. R. Moore. An ecological perspective on methane emissions from northern wetlands. *Trends in Ecology and Evolution*, 9(12):460–464, 1994.

[201] T. R. Moore and R. Knowles. Methane emissions from fen, bog and swamp peatlands in quebec. *Biogeochemistry*, 11(1):45–61, 1990.

[202] S. Saarnio, M. Morero, N. J. Shurpali, E. S. Tuittila, M. Makila, and J. Alm. Annual CO_2 and CH_4 fluxes of pristine boreal mires as a background for the lifecycle analyses of peat energy. *Boreal Environment Research*, 12(2):101–113, 2007. Saarnio, Sanna Morero, Micaela Shurpali, Narasinha J. Tuittila, Eeva-Stiina Makila, Markku Alm, Jukka.

[203] T. R. Christensen, I. C. Prentice, J. Kaplan, A. Haxeltine, and S. Sitch. Methane flux from northern wetlands and tundra - An ecosystem source modelling approach. *Tellus Series B-Chemical and Physical Meteorology*, 48(5):652–661, 1996.

[204] C. Potter, S. Klooster, S. Hiatt, M. Fladeland, V. Genovese, and P. Gross. Wetlands in the united states: Satellite-derived estimation based on ecosystem carbon. *Earth Interactions*, 10, 2006.

[205] J. Alm, L. Schulman, J. Walden, H. Nykänen, P. J. Martikainen, and J. Silvola. Carbon balance of a boreal bog during a year with an exceptionally dry summer. *Ecology*, 80(1):161–174, 1999.

[206] K. J. Dinsmore, U. M. Skiba, M. F. Billett, R. M. Rees, and J. Drewer. Spatial and temporal variability in CH_4 and N_2O fluxes from a scottish ombrotrophic peatland: Implications for modelling and up-scaling. *Soil Biology and Biochemistry*, 41(6):1315–1323, 2009.

[207] K. J. Dinsmore, M. F. Billett, and T. R. Moore. Transfer of carbon dioxide and methane through the soil-water-atmosphere system at mer bleue peatland, canada. *Hydrological Processes*, 23(2):330–341, 2009.

[208] C. Mikkela, I. Sundh, B.H. Svensson, and M. Nilsson. Diurnal variation in methane emission in relation to the water table, soil temperature, climate and vegetation cover in a swedish acid mire. *Biogeochemistry*, 28(2):93–114, 1995.

[209] J. Windsor, T. R. Moore, and N. T. Roulet. Episodic fluxes of methane from sub-arctic fens. *Canadian Journal of Soil Science*, 72(4):441–452, 1992.

[210] KJ Hargreaves, D. Fowler, CER Pitcairn, and M. Aurela. Annual methane emission from finnish mires estimated from eddy covariance campaign measurements. *Theoretical and Applied Climatology*, 70(1):203–213, 2001.

[211] L. Hj, R. A. Olsen, and V. L. Torsvik. Archaeal communities in high arctic wetlands at spitsbergen, norway (78 degrees N) as characterized by 16S rrna gene fingerprinting. *Fems Microbiology Ecology*, 53(1):89–101, 2005.

[212] C. Wille, L. Kutzbach, T. Sachs, D. Wagner, and E. M. Pfeiffer. Methane emission from siberian arctic polygonal tundra: eddy covariance measurements and modeling. *Global Change Biology*, 14(6):1395–1408, 2008. Wille, Christian Kutzbach, Lars Sachs, Torsten Wagner, Dirk Pfeiffer, Eva-Maria.

[213] J. L. Bubier. The relationship of vegetation to methane emission and hydrochemical gradient in northern peatlands. *Journal of Ecology*, 83(3):403–420, 1995.

[214] J. E. P. Heikkinen, V. Elsakov, and P. J. Martikainen. Carbon dioxide and methane dynamics and annual carbon balance in tundra wetland in ne europe, russia. *Global Biogeochemical Cycles*, 16(4), 2002.

[215] J. T. Huttunen, H. Nykanen, J. Turunen, and P. J. Martikainen. Methane emissions from natural peatlands in the northern boreal zone in finland, fennoscandia. *Atmospheric Environment*, 37(1):147–151, 2003.

[216] G. Granberg, C. Mikkela, I. Sundh, B. H. Svensson, and M. Nilsson. Sources of spatial variation in methane emission from mires in northern sweden: A mechanistic approach in statistical modeling. *Global Biogeochemical Cycles*, 11(2):135–150, 1997.

[217] R. C. Rhew, Y. A. Teh, and T. Abel. Methyl halide and methane fluxes in the northern alaskan coastal tundra. *Journal of Geophysical Research-Biogeosciences*, 112(G2):G02009, 2007.

[218] K. B. Bartlett, P. M. Crill, R. L. Sass, R. C. Harriss, and N. B. Dise. Methane emissions from tundra environments in the yukon-kuskokwim delta, alaska. *J. Geophys. Res.*, 97(D15):16,645–16,660, doi:10.1029/ 91JD00610, 1992.

[219] A. Joabsson and T. R. Christensen. Methane emissions from wetlands and their relationship with vascular plants: an arctic example. *Global Change Biology*, 7(8):919–932, 2001.

[220] T. R. Christensen, S. Jonasson, T. V. Callaghan, and M. Havstrom. Spatial variation in high-latitude methane flux along a transect across siberian and european tundra environments. *Journal of Geophysical Research-Atmospheres*, 100(D10):21035–21045, 1995.

[221] T. Nakano, S. Kuniyoshi, and M. Fukuda. Temporal variation in methane emission from tundra wetlands in a permafrost area, northeastern siberia. *Atmospheric Environment*, 34(8):1205–1213, 2000.

[222] H. Rask, J. Schoenau, and D. Anderson. Factors influencing methane flux from a boreal forest wetland in saskatchewan, canada. *Soil Biology and Biochemistry*, 34(4):435–443, 2002.

[223] T. R. Christensen, T. Johansson, M. Olsrud, L. Strom, A. Lindroth, M. Mastepanov, N. Malmer, T. Friborg, P. Crill, and T. V. Callaghan. A catchment-scale carbon and greenhouse gas budget of a subarctic landscape. *Philosophical Transactions of the Royal Society a-Mathematical Physical and Engineering Sciences*, 365(1856):1643–1656, 2007.

[224] M. Dalva, T. R. Moore, P. Arp, and T. A. Clair. Methane and soil and plant community respiration from wetlands, kejimkujik national park, nova scotia: Measurements, predictions, and climatic change. *Journal of Geophysical Research-Atmospheres*, 106(D3):2955–2962, 2001.

[225] H. Flessa, A. Rodionov, G. Guggenberger, H. Fuchs, P. Magdon, O. Shibistova, G. Zrazhevskaya, N. Mikheyeva, O. A. Kasansky, and C. Blodau. Landscape controls of CH_4 fluxes in a catchment of the forest tundra ecotone in northern siberia. *Global Change Biology*, 14(9):2040–2056, 2008.

[226] T. R. Moore and N. T. Roulet. A comparison of dynamic and static chambers for methane emission measurements from sub-arctic fens. *Atmosphere-Ocean*, 29(1):102–109, 1991.

[227] P. E. Levy, A. Gray, S. R. Leeson, J. Gaiawyn, M. P. C. Kelly, M. D. A. Cooper, K. J. Dinsmore, S. K. Jones, and L. J. Sheppard. Quantification of uncertainty in trace gas fluxes measured by the static chamber method. *European Journal of Soil Science*, 62(6):811–821, 2011.

[228] JM Waddington and NT Roulet. Atmosphere-wetland carbon exchanges: Scale dependency of CO_2 and CH_4 exchange on the developmental topography of a peatland. *Global Biogeochemical Cycles*, 10(2):233–245, 1996.

[229] S. C. Whalen and W. S. Reeburgh. A methane flux time series for tundra environments. *Global Biogeochem. Cycles*, 2(4):399–409, 1988.

[230] OT Denmead. Approaches to measuring fluxes of methane and nitrous oxide between landscapes and the atmosphere. *Plant and Soil*, 309(1):5–24, 2008.

[231] M K Pihlatie. Comparison of static chambers to measure CH_4 emissions from soils. *Agricultural and Forest Meteorology*, 171172:124136, doi:10.1016/j.agrformet.2012.11.008, 2013.

[232] S. M. Fan, S. C. Wofsy, P. S. Bakwin, D. J. Jacob, S. M. Anderson, P. L. Kebabian, J. B. McManus, C. E. Kolb, and D. R. Fitzjarrald. Micrometeorological measurements of CH_4 and CO_2 exchange between the atmosphere and subarctic tundra. *J. Geophys. Res.*, 97(D15):16627–16643, 1992.

[233] T. Riutta, J. Laine, M. Aurela, J. Rinne, T. Vesala, T. Laurila, S. Haapanala, M. Pihlatie, and E. S. Tuittila. Spatial variation in plant community functions regulates carbon gas dynamics in a boreal fen ecosystem. *Tellus Series B-Chemical and Physical Meteorology*, 59(5):838–852, 2007.

[234] T. Laurila, M. Aurela, and J. P. Tuovinen. *Eddy Covariance Measurements Over Wetlands*. Springer, 2012.

[235] T. Vesala, N. Kljun, U. Rannik, J. Rinne, A. Sogachev, T. Markkanen, K. Sabelfeld, T. Foken, and M. Y. Leclerc. Flux and concentration footprint modelling: State of the art. *Environmental Pollution*, 152(3):653–666, 2008.

[236] AP Schrier-Uijl, PS Kroon, A. Hensen, PA Leffelaar, F. Berendse, and EM Veenendaal. Comparison of chamber and eddy covariance-based CO_2 and CH_4 emission estimates in a heterogeneous grass ecosystem on peat. *Agricultural and Forest Meteorology*, 150(6):825–831, 2010.

[237] RJ Clement, SB Verma, and ES Verry. Relating chamber measurements to eddy correlation measurements of methane flux. *Journal of Geophysical Research*, 100:21–21, 1995.

[238] I. Forbrich, L. Kutzbach, C. Wille, T. Becker, J. B. Wu, and M. Wilmking. Cross-evaluation of measurements of peatland methane emissions on microform and ecosystem scales using high-resolution landcover classification and source weight modelling. *Agricultural and Forest Meteorology*, 151(7):864–874, 2011.

[239] DMD Hendriks, J. Van Huissteden, and AJ Dolman. Multi-technique assessment of spatial and temporal variability of methane fluxes in a peat meadow. *Agricultural and Forest Meteorology*, 150(6):757–774, 2010.

[240] J.L. Bubier, P.M. Crill, R.K. Varner, and T.R. Moore. BOREAS TGB-01/TGB-03 CH_4 chamber flux data: NSA fen, 1998.

[241] P.M. Crill and R.K. Varner. BOREAS TGB-01 CH_4 concentration and flux data from NSA tower sites, 1998.

[242] P. J. Sellers, F. G. Hall, R. D. Kelly, A. Black, D. Baldocchi, J. Berry, M. Ryan, K. J. Ranson, P. M. Crill, D. P. Lettenmaier, H. Margolis, J. Cihlar, J. Newcomer, D. Fitzjarrald, P. G. Jarvis, S. T. Gower, D. Halliwell, D. Williams, B. Goodison, D. E. Wickland, and F. E. Guertin. Boreas in 1997: Experiment overview, scientific results, and future directions. *Journal of Geophysical Research-Atmospheres*, 102(D24):28731–28769, 1997.

[243] L. M. Bellisario, J. L. Bubier, T. R. Moore, and J. P. Chanton. Controls on ch_4 emissions from a northern peatland. *Global Biogeochemical Cycles*, 13(1):81–91, 1999.

[244] J. L. Bubier, T. R. Moore, L. Bellisario, N. T. Comer, and P. M. Crill. Ecological controls on methane emissions from a northern peatland complex in the zone of discontinuous permafrost, manitoba, canada. *Global Biogeochemical Cycles*, 9(4):455–470, 1995.

[245] Peter M. Lafleur, J. Harry McCaughey, David W. Joiner, Paul A. Bartlett, and Dennis E. Jelinski. Seasonal trends in energy, water, and carbon dioxide fluxes at a northern boreal wetland. *J. Geophys. Res.*, 102(D24):29,00929,020, doi:10.1029/96JD03326, 1997.

[246] J. Bubier, T. Moore, K. Savage, and P. Crill. A comparison of methane flux in a boreal landscape between a dry and a wet year. *Global Biogeochemical Cycles*, 19(1), 2005.

[247] J. H. McCaughey, P.M. Lafleur, and D. Jelinski. Boreas tf-10 nsa-fen tower flux and meteorological data, 1999.

[248] J. A. Businger, J. C. Wynagaard, Y. Izumi, and E. F. Bradley. Flux-profile relationships in the atmospheric surface layer. *J. Atmos. Sci.*, 28:181–189, 1971.

[249] A. Raabe. Die hhe der internen grenzschicht. *Z. Meteor*, 41:251–261, 1991.

[250] J. M. Baker and T. J. Griffis. Examining strategies to improve the carbon balance of corn/soybean agriculture using eddy covariance and mass balance techniques. *Agric. and For. Meteorol.*, 128:163–177, doi:10.1016/j.agrformet.2004.11.005, 2005.

[251] E. Pattey, I.B. Strachan, R.L. Desjardins, G.C. Edwards, D. Dow, and J.I. MacPherson. Application of a tunable diode laser to the measurement of CH_4 and N_2O fluxes from field to landscape scale using several micrometeorological techniques. *Agricultural and Forest Meteorology*, 136:222–236, 2006.

[252] S. C. Moosavi and P. M. Crill. Controls on CH_4 and CO_2 emissions along two moisture gradients in the canadian boreal zone. *Journal of Geophysical Research-Atmospheres*, 102(D24):29261–29277, 1997.

[253] L. Askaer, B. Elberling, R. N. Glud, M. Kühl, F. R. Lauritsen, and H. R. Joensen. Soil heterogeneity effects on O2 distribution and CH_4 emissions from wetlands: In situ and mesocosm studies with planar O_2 optodes and membrane inlet mass spectrometry. *Soil Biol. Biochem.*, 42:2254–2265, doi:10.1016/j.soilbio.2010.08.026, 2010.

[254] Gary J. Whiting and Jeffrey P. Chanton. Plant-dependent CH_4 emission in a subarctic canadian fen. *Global Biogeochem. Cycles*, 6(3):225–231, 1992.

[255] J. B. Yavitt, G. E. Lang, and A. J. Sexstone. Methane fluxes in wetland and forest soils, beaver ponds, and low-order streams of a temperate forest ecosystem. *Journal of Geophysical Research-Atmospheres*, 95(D13):22463–22474, 1990.

[256] Y. Harazono, M. Mano, A. Miyata, M. Yoshimoto, R. C. Zulueta, G. L. Vourlitis, H. Kwon, and W. C. Oechel. Temporal and spatial differences of methane flux at arctic tundra in alaska. *Mem. Natl. Inst. Polar Res*, 59:79–95, 2006.

[257] D. Zona, W. C. Oechel, J. Kochendorfer, K. T. Paw U, A. N. Salyuk, P. C. Olivas, S. F. Oberbauer, and D. A. Lipson. Methane fluxes during the initiation of a large-scale water table manipulation experiment in the alaskan arctic tundra. *Global Biogeochem. Cycles*, 23, 2009.

[258] J. Rinne, T. Riutta, M. Pihlatie, M. Aurela, S. Haapanala, J. P. Tuovinen, E. S. Tuittila, and T. Vesala. Annual cycle of methane emission from a boreal fen measured by the eddy covariance technique. *Tellus Series B-Chemical and Physical Meteorology*, 59(3):449–457, 2007.

[259] N. J. Shurpali, S. B. Verma, R. J. Clement, and D. P. Billesbach. Seasonal distribution of methane flux in a minnesota peatland measured by eddy-correlation. *Journal of Geophysical Research-Atmospheres*, 98(D11):20649–20655, 1993.

[260] A. E. Suyker, S. B. Verma, R. J. Clement, and D. P. Billesbach. Methane flux in a boreal fen: Season-long measurement by eddy correlation. *Journal of Geophysical Research-Atmospheres*, 101(D22):28637–28647, 1996.

[261] Andrew E. Suyker, Shashi B. Verma, and Timothy J. Arkebauer. Season-long measurement of carbon dioxide exchange in a boreal fen. *Journal of Geophysical Research: Atmospheres*, 102(D24):29021–29028, 1997.

[262] M. Jackowicz-Korczynski, T.R. Christensen, K. Backstrand, P. Crill, T. Friborg, M. Mastepanov, and L. Strom. Annual cycle of methane emission from a subarctic peatland. *Journal of Geophysical Research*, 115(G2):G02009, 2010.

[263] PS Kroon, AP Schrier Uijl, A. Hensen, EM Veenendaal, and HJJ Jonker. Annual balances of CH_4 and N_2O from a managed fen meadow using eddy covariance flux measurements. *European Journal of Soil Science*, 61(5):773–784, 2010.

[264] T. R. Christensen, T. Friborg, M. Sommerkorn, J. Kaplan, L. Illeris, H. Soegaard, C. Nordstroem, and S. Jonasson. Trace gas exchange in a high-arctic valley 1. variations in CO_2 and CH_4 flux between tundra vegetation types. *Global Biogeochemical Cycles*, 14(3):701–713, 2000.

[265] J. van Huissteden, T. C. Maximov, and A. J. Dolman. High methane flux from an arctic floodplain (indigirka lowlands, eastern siberia). *Journal of Geophysical Research*, 110(G2), 2005. van Huissteden, J. Maximov, T. C. Dolman, A. J.

[266] G. L. Vourlitis, W. C. Oechel, S. J. Hastings, and M. A. Jenkins. The effect of soil-moisture and thaw depth on CH_4 flux from wet coastal tundra ecosystems on the north slope of alaska. *Chemosphere*, 26(1-4):329–337, 1993.

[267] N. T. Roulet, A. Jano, C. A. Kelly, L. F. Klinger, T. R. Moore, R. Protz, J. A. Ritter, and W. R. Rouse. Role of the hudson-bay lowlands as a source of atmospheric methane. *Journal of Geophysical Research-Atmospheres*, 99(D1):1439–1454, 1994.

[268] J. L. Bubier, S. Frolking, P. M. Crill, and E. Linder. Net ecosystem productivity and its uncertainty in a diverse boreal peatland. *Journal of Geophysical Research-Atmospheres*, 104(D22):27683–27692, 1999.

[269] K.J. Dinsmore, M.F. Billett, U.M. Skiba, R.M. Rees, J. Drewer, and C. Helfter. Role of the aquatic pathway in the carbon and greenhouse gas budgets of a peatland catchment. *Global Change Biology*, 16(10):2750–2762, 2010.

[270] S.B. Verma, F.G. Ullman, D. Billesbach, R.J. Clement, J. Kim, and ES Verry. Eddy correlation measurements of methane flux in a northern peatland ecosystem. *Boundary-Layer Meteorology*, 58(3):289–304, 1992.

[271] T. Sachs, C. Wille, J. Boike, and L. Kutzbach. Environmental controls on ecosystem-scale CH_4 emission from polygonal tundra in the lena river delta, siberia. *Journal of Geophysical Research-Biogeosciences*, 113:G00A03, 2008.

[272] PC Van der Molen and TA Wijmstra. The thermal regime of hummock-hollow complexes on clara bog, co. offaly. *Biology and Environment: Proceedings of the Royal Irish Academy*, 94B(3):209–221, 1994.

[273] Z. Duan and S. Mao. A thermodynamic model for calculating methane solubility, density and gas phase composition of methane-bearing aqueous fluids from 273 to 523 k and from 1 to 2000 bar. *Geochimica Et Cosmochimica Acta*, 70(13):3369–3386, 2006.

[274] Patrick M. Crill, Karen B. Bartlett, John O. Wilson, Daniel I. Sebacher, Robert C. Harriss, John M. Melack, Sally MacIntyre, Lance Lesack, and Lesley Smith-Morrill. Tropospheric methane from an amazonian floodplain lake. *J. Geophys. Res.*, 93(D2):1564–1570, 1988.

[275] P. W. Ford, P. I. Boon, and K. Lee. Methane and oxygen dynamics in a shallow floodplain lake: the significance of periodic stratification. *Hydrobiologia*, 485(1-3):97–110, 2002.

[276] J. L. Bubier, T. R. Moore, and N. T. Roulet. Methane emissions from wetlands in the midboreal region of northern ontario, canada. *Ecology*, 74(8):2240–2254, 1993.

[277] J. M. Waddington, N. T. Roulet, and R. V. Swanson. Water table control of CH_4 emission enhancement by vascular plants in boreal peatlands. *Journal of Geophysical Research-Atmospheres*, 101(D17):22775–22785, 1996.

[278] S. MacIntyre, W. Eugster, and G.W. Kling. The critical importance of buoyancy flux for gas flux across the air-water interface. *Geophysical Monograph-American Geophysical Union*, 127:135–140, 2002.

[279] Sally MacIntyre, Anders Jonsson, Mats Jansson, Jan Aberg, Damon E. Turney, and Scott D. Miller. Buoyancy flux, turbulence, and the gas transfer coefficient in a stratified lake. *Geophys. Res. Lett.*, 37(24):L24604, 2010.

[280] N.T. Roulet, PM Crill, NT Comer, A. Dove, and RA Boubonniere. CO_2 and CH_4 flux between a boreal beaver pond and the atmosphere. *Journal of Geophysical Research*, 102(D24):29313–29,319, 1997.

[281] W. Eugster, G. Kling, T. Jonas, J.P. McFadden, A. Wuest, S. MacIntyre, and F.S. Chapin III. CO_2 exchange between air and water in an arctic alaskan and midlatitude swiss lake: Importance of convective mixing. *Journal of Geophysical Research*, 108(D12):4362, 2003.

[282] J.S. Read, D.P. Hamilton, A.R. Desai, K.C. Rose, S. MacIntyre, J.D. Lenters, R.L. Smyth, P.C. Hanson, J.J. Cole, and P.A. Staehr. Lake-size dependency of

wind shear and convection as controls on gas exchange. *Geophysical Research Letters*, 39(9):L09405, 2012.

[283] A. Rutgersson, A. Smedman, and E. Sahle. Oceanic convective mixing and the impact on air-sea gas transfer velocity. *Geophys. Res. Lett.*, 38(2):L02602, 2011.

[284] A. Joabsson, T. Christensen, and B Wallen. Vascular plant controls on methane emissions from northern peatforming wetlands. *Trends in Ecology and Evolution*, 14(10):385–388, 1999.

[285] LA Morrissey, DB Zobel, and GP Livingston. Significance of stomatal control on methane release from-dominated wetlands. *Chemosphere*, 26(1-4):339–355, 1993.

[286] D. Lloyd, K.L. Thomas, J. Benstead, K.L. Davies, S.H. Lloyd, J.R.M. Arah, and K.D. Stephen. Methanogenesis and CO_2 exchange in an ombrotrophic peat bog. *Atmospheric Environment*, 32(19):3229–3238, 1998.

[287] K.L. Thomas, J. Benstead, K.L. Davies, and D. Lloyd. Role of wetland plants in the diurnal control of CH_4 and CO_2 fluxes in peat. *Soil Biology and Biochemistry*, 28(1):17–23, 1996.

[288] L. Askaer, B. Elberling, T. Friborg, C. J. Jørgensen, and B. U. Hansen. Plant-mediated CH_4 transport and C gas dynamics quantified in situ in a phalaris arundinacea-dominant wetland. *Plant Soil*, 343(1-2):287–301, doi:10.1007/s11104–011–0718–x, 2011.

[289] G.M. King. In situ analyses of methane oxidation associated with the roots and rhizomes of a bur reed, sparganium eurycarpum, in a maine wetland. *Applied and Environmental Microbiology*, 62(12):4548–4555, 1996.

[290] P. Roslev and G.M. King. Regulation of methane oxidation in a freshwater wetland by water table changes and anoxia. *Fems Microbiology Ecology*, 19(2):105–115, 1996.

[291] K.D. Long, L.B. Flanagan, and T. Cai. Diurnal and seasonal variation in methane emissions in a northern canadian peatland measured by eddy covariance. *Global Change Biology*, 16(9):2420–2435, 2010.

[292] V. Gupta, K.A. Smemo, J. B. Yavitt, and N. Basiliko. Active methanotrophs in two contrasting north american peatland ecosystems revealed using dna-sip. *Microbial Ecology*, 63:438–445, 2012.

[293] T.J. Popp, J.P. Chanton, G.J. Whiting, and N. Grant. Evaluation of methane oxidation in therhizosphere of a carex dominated fen in northcentral alberta, canada. *Biogeochemistry*, 51(3):259–281, 2000.

[294] S. C. Whalen. Biogeochemistry of methane exchange between natural wetlands and the atmosphere. *Environmental Engineering Science*, 22(1):73–94, 2005.

[295] R. Segers. Methane production and methane consumption: a review of processes underlying wetland methane fluxes. *Biogeochemistry*, 41(1):23–51, 1998.